



TECHNISCHE  
UNIVERSITÄT  
WIEN

DISSERTATION

---

# Measurement of the prompt $\chi_{c1}$ and $\chi_{c2}$ polarizations at CMS

---

AUSGEFÜHRT ZUM ZWECKE DER ERLANGUNG DES AKADEMISCHEN GRADES  
EINES DOKTORS DER TECHNISCHEN WISSENSCHAFTEN  
UNTER DER LEITUNG VON

Univ.Doz. Dipl.-Ing. Dr.techn. Claudia Wulz  
und

Dipl.-Ing. Dr.techn. Ilse Krätschmer  
als verantwortlich mitwirkende Assistentin

am Atominstitut der Technischen Universität Wien (E141)  
in Zusammenarbeit mit dem Institut für Hochenergiephysik (HEPHY)  
der Österreichischen Akademie der Wissenschaften (ÖAW)

eingereicht an der  
TECHNISCHEN UNIVERSITÄT WIEN  
FAKULTÄT FÜR PHYSIK

von

Dipl.-Ing. Thomas Madlener, BSc.  
Matrikelnummer: 00926219

Wien, am 17. Dezember 2019



Die approbierte gedruckte Originalversion dieser Dissertation ist an der TU Wien Bibliothek verfügbar.  
The approved original version of this doctoral thesis is available in print at TU Wien Bibliothek.

# Kurzfassung

Die Bildung von Bindungszuständen aus Quarks, sogenannte Hadronen, durch die starke Wechselwirkung ist noch nicht vollständig verstanden. Quarkonia sind Bindungszustände aus einem Quark und seinen Antiquark ( $q\bar{q}$ ) und stellen ideale Versuchsobjekte zur Untersuchung der Produktionsmechanismen von Hadronen dar. In der momentan gängigen theoretischen Beschreibung im Zuge der Nicht-Relativistischen QuantenChromodynamik (NRQCD) wird die Entstehung von Quarkonia in die Entstehung eines anfänglichen  $q\bar{q}$  Paares und dessen darauf folgende Entwicklung zu einem gebundenen Zustand faktorisiert. Während der erste Schritt im Rahmen von perturbativen Methoden der QCD berechenbar ist, werden für den zweiten Schritt experimentelle Messungen der Produktionswechselwirkungsquerschnitte und der Polarisation von Quarkonia benötigt.

Seit dem Start des [Large Hadron Collider \(LHC\)](#) Programmes sind eine Vielzahl an solchen Quarkonium Messungen veröffentlicht worden. Die Eigenschaften der  $S$ -Wellen Zustände sind mittlerweile, vor allem bei zentraler Rapidität und hohen transversen Impulsen, sehr gut vermessen. Andererseits existieren nur wenige experimentelle Resultate für  $P$ -Wellen Zustände. Insbesondere die Polarisation dieser Zustände wurde bisher nicht gemessen.

Phänomenologische Studien haben, aufbauend auf den veröffentlichten Resultaten der LHC Experimente, überraschend einfache Muster in der Entstehung von Quarkonia gefunden. Diese Muster befinden sich im krassen Gegensatz zu den komplexen Mischungen aus Prozessen die in der NRQCD berücksichtigt werden. Trotzdem stimmen Berechnungen und Messungen sehr gut überein. Die Studien machen eine klare Vorhersage für die Polarisation der  $\chi_{c1}$  und  $\chi_{c2}$  Mesonen: Sie sind groß und vor allem entgegengesetzt.

In dieser Dissertation wird die erste Polarisationsmessung der prompten  $\chi_{c1}$  und  $\chi_{c2}$  Mesonen präsentiert. Dafür werden Daten verwendet die 2012 vom CMS experiment am LHC in Proton-Proton Kollisionen bei einer Schwerpunktsenergie von  $\sqrt{s} = 8$  TeV gesammelt wurden und einer integrierten Luminosität von  $19.1 \text{ fb}^{-1}$  entsprechen. Die  $\chi_c$  Mesonen werden über ihren Strahlungszерfall  $\chi_c \rightarrow J/\psi\gamma$  rekonstruiert. Hierbei, wird das Photon verwendet um zwischen  $\chi_{c1}$  und  $\chi_{c2}$  Zuständen zu unterscheiden. Eine Messung der Verhältnisse der Produktionswechselwirkungsquerschnitte der  $\chi_{c2}$  im Vergleich mit den  $\chi_{c1}$  Zuständen als Funktion des polaren und azimuthalen Winkels des Myonzerfalles des  $J/\psi$  wird verwendet um die relative Polarisation zu bestimmen. Die Parameter  $\Delta\lambda_\vartheta \equiv \lambda_\vartheta^{\chi_{c2}} - \lambda_\vartheta^{\chi_{c1}}$  und  $\Delta\lambda_\varphi \equiv \lambda_\varphi^{\chi_{c2}} - \lambda_\varphi^{\chi_{c1}}$ , zusammen mit unteren Grenzen für den Parameter  $\lambda_\vartheta^{\chi_{c1}}$ , werden in drei Bereichen des transversen Impulses des  $J/\psi$ , 8–12, 12–18 und 18–30 GeV, gemessen.

Für den azimuthalen Polarisationsunterschied,  $\Delta\lambda_\varphi$  werden keine signifikant von Null verschiedene Werte gemessen. Die Resultate für  $\Delta\lambda_\vartheta$ , hingegen, deuten auf starke und gegensätzliche polare Polarisierungen hin. Vergleiche der Messungen mit analytischen Kurven zeigen, dass ein unpolarisiertes Szenario, in dem beide Zustände die gleiche Polarisation aufweisen, unwahrscheinlich ist, während die Messungen mit den Vorhersagen auf Basis der NRQCD übereinstimmt.



Die approbierte gedruckte Originalversion dieser Dissertation ist an der TU Wien Bibliothek verfügbar.  
The approved original version of this doctoral thesis is available in print at TU Wien Bibliothek.

# Abstract

The process of how quarks are bound into hadrons by the strong interaction is not yet fully understood. Quarkonia, bound states of a heavy quark and its antiquark ( $q\bar{q}$ ), are ideal probes to study hadron formation. In the currently prevalent theoretical framework of [Non-Relativistic Quantum Chromodynamics \(NRQCD\)](#) the production of quarkonia is factorized into two separate steps, the formation of an initial  $q\bar{q}$  pair and its subsequent evolution into the bound quarkonium state. While the first part can be calculated within perturbative QCD, the second step depends on inputs from experiments, quarkonium cross section and polarization measurements.

With the advent of the [Large Hadron Collider \(LHC\)](#) physics program a multitude of quarkonium cross section and polarization measurements has recently become available. While the cross sections and polarizations of all  $S$ -wave states are by now well measured, especially at mid-rapidity and high transverse momenta, experimental results on  $P$ -wave states are scarce. In particular, no measurements of the polarization for any  $P$ -wave state exists.

Phenomenological studies using the published results of the LHC experiments have observed remarkably simple patterns in the production of the studied quarkonia. These are in striking contrast with the complexity of the mixture of processes that are considered in the NRQCD approach. Nevertheless, calculations made within the NRQCD framework are able to reproduce the measurements very well. This seeming disparity between the simplicity of the data and the complexity of the theory comes with a clear-cut prediction, the polarizations of the  $\chi_{c1}$  and  $\chi_{c2}$  mesons should be large and, more importantly, opposite.

This dissertation presents the first measurement of the polarizations of the prompt  $\chi_{c1}$  and  $\chi_{c2}$  mesons using data collected in 2012 by the CMS experiment at the LHC in proton-proton collisions at a center-of-mass energy of  $\sqrt{s} = 8$  TeV corresponding to a total integrated luminosity of  $19.1 \text{ fb}^{-1}$ . The  $\chi_c$  mesons are reconstructed via their radiative  $\chi_c \rightarrow J/\psi\gamma$  decay, where the photon is used to identify the  $\chi_{c1}$  and  $\chi_{c2}$  states. A measurement of the relative polarization in the helicity frame is performed via the analysis of  $\chi_{c2}$  over  $\chi_{c1}$  cross section ratios as a function of the polar and azimuthal angle of the dimuon decay of the associated  $J/\psi$ . The parameters  $\Delta\lambda_\vartheta \equiv \lambda_\vartheta^{\chi_{c2}} - \lambda_\vartheta^{\chi_{c1}}$  and  $\Delta\lambda_\varphi \equiv \lambda_\varphi^{\chi_{c2}} - \lambda_\varphi^{\chi_{c1}}$  are reported together with lower bounds for the parameter  $\lambda_\vartheta^{\chi_{c1}}$  in three ranges of  $J/\psi$  transverse momentum, 8–12, 12–18 and 18–30 GeV.

While no significant deviation from zero is found for the azimuthal anisotropy difference,  $\Delta\lambda_\varphi$ , the results for  $\Delta\lambda_\vartheta$  suggest strong and opposite polar anisotropies for the prompt  $\chi_{c1}$  and  $\chi_{c2}$  mesons. A comparison of the measured cross section ratios with the expected analytic shapes reveals that the measurement disfavors the unpolarized scenario, where both states have the same polarization, but is in agreement with the NRQCD prediction.



Die approbierte gedruckte Originalversion dieser Dissertation ist an der TU Wien Bibliothek verfügbar.  
The approved original version of this doctoral thesis is available in print at TU Wien Bibliothek.

---

## Acknowledgements

Four years after starting my PhD studies, this thesis represents the end of an intensive and remarkable journey. Thanking everybody that contributed not only to my academic but also to my personal growth during this time is nigh on impossible. Nevertheless, I will try to mention the most important persons here.

My PhD project was funded through the Austrian Science Fund (FWF) project P28411-N36. I would like to thank HEPHY and its director Jochen Schieck for giving me the opportunity to pursue my research during the last years. I am especially grateful to Claudia Wulz for her supervision and counsel. Special thanks also to Wolfgang Adam, our group leader for the majority of my PhD studies, for fruitful discussions and always being available for any kind of questions.

I would like to extend my deepest gratitude to Ilse Krätschmer, who not only made my PhD project possible in the first place, but who was also always available for any kind of advice, in academic and personal matters. Ilse was the one who introduced me to the CMS collaboration and to data analysis in high energy physics, and I would not have been able to do all of this work without her.

I want to thank the other members of the “quarkonium polarization team” Carlos Lourenço, Pietro Faccioli and João Seixas. It was through countless discussions and their patience that this endeavour has come to a successful end. Only through their endless support was I able to learn about, and understand the intricacies of quarkonium production and polarization measurements. I would like to further thank Jakob Necker, who had to “endure” my supervision during the research for his Master thesis, and Mariana Araújo. Both contributed to the development of the analysis software framework and have helped in various ways in the analysis of the data. I owe a dedicated thank-you to Carlos for his role as contact person for the presented analysis, enabling a timely publication for this thesis, and also for some very insightful discussions concerning career planing on both a personal as well as a professional level.

I would like to thank my fellow students who have been there since the start, Johannes, Lukas, Max, Willi, Matthias, Philipp and Wolfgang, just to name a few. I also want to include Erica in this group, even though I only had the pleasure to share an office with her for slightly more than two years. You have made the last years an unforgettable time, partly through productive discussions about physics and life in general but also, and maybe even more importantly, by providing the sometimes necessary option of distraction and banter.

I want to thank all the persons who have “volunteered” to proofread my thesis. All of them are already listed above for some other reasons, and have provided valuable comments and lead to a considerably improved manuscript in the end.

On a personal level I want to extend my gratitude to the people outside of my academic bubble, mainly to my housemates of the past few years, but also other good friends, who have kept the scales between physics and the “real world” balanced. Matthias, Harald, Christian, Laurin, Alex and Corinna, *thank you very much*, you have made the last few years a truly wonderful time for me.

---

I am also extremely grateful to my family: My mother, Renate, my father, Alfred and my two siblings, Sarah and Christoph. You have always been there with unconditional support and I would not be where I am today without you. Mama, Däta, Sarah und Christoph, I ka ned gnuag mal Danke saigo, ohne ü hätt das seachar nüd rät tau.

Finally, I would like to thank Kati, who has become one of the most important persons in my life, and who has been on the ride with me for the latter half of my PhD. With your patience and kindness you have made the downs less dire and the ups even more enjoyable. Thank you for accepting me with all my quirks and for lifting my spirits when necessary.

THANK YOU, DANKE, GRAZIE, MERCI, DANKSCHÖA



# Contents

<b>1</b>	<b>Introduction</b>	<b>1</b>
<b>2</b>	<b>Quarkonium Physics</b>	<b>7</b>
2.1	Quarkonium spectra . . . . .	7
2.2	Quarkonium production . . . . .	10
2.2.1	Non-Relativistic Quantum Chromodynamics . . . . .	11
2.2.2	Color-Singlet Model . . . . .	14
2.2.3	Color Evaporation Model . . . . .	15
2.2.4	Fragmentation function approach . . . . .	15
2.3	Quarkonium polarization . . . . .	16
2.3.1	Considerations in polarization measurements . . . . .	18
2.3.2	Polarization of $\chi$ mesons . . . . .	20
2.4	Current experimental status . . . . .	21
2.5	Phenomenological interpretation of the experimental results . . . . .	22
2.6	Prediction of the $\chi_{cJ}$ polarization . . . . .	25
2.7	Summary - Novelty of this thesis . . . . .	27
<b>3</b>	<b>Experimental Setup</b>	<b>29</b>
3.1	Large Hadron Collider . . . . .	29
3.2	Compact Muon Solenoid . . . . .	32
3.2.1	Inner tracking system . . . . .	35
3.2.2	Electromagnetic Calorimeter . . . . .	37
3.2.3	Hadron Calorimeter . . . . .	38
3.2.4	Superconducting magnet . . . . .	38
3.2.5	Muon system . . . . .	39
3.2.6	Trigger and data acquisition systems . . . . .	40
3.3	Quarkonium reconstruction at CMS . . . . .	44
3.3.1	Dimuon triggers . . . . .	45
3.3.2	Muon reconstruction and identification . . . . .	46
3.3.3	Photon conversion reconstruction . . . . .	47
<b>4</b>	<b>Upgrade of the BPH Quarkonium Triggers in Run II</b>	<b>51</b>
4.1	General considerations for the trigger strategy . . . . .	52
4.2	The status of the quarkonium triggers in 2016 . . . . .	53
4.2.1	Extrapolation of trigger rates to expected 2017 data taking conditions . . . . .	55
4.3	Studies for updating L1 seeds . . . . .	56
4.4	Studies for updating HLT paths . . . . .	60

4.5	Performance of the triggers . . . . .	62
<b>5</b>	<b>Measurement of the <math>\chi_{c1}</math> and <math>\chi_{c2}</math> Polarization</b>	<b>65</b>
5.1	Analysis strategy . . . . .	66
5.1.1	Relative polarization measurement . . . . .	66
5.1.2	Experimental considerations and challenges . . . . .	68
5.1.3	Validation of the analysis strategy . . . . .	70
5.2	Data samples and event selection . . . . .	71
5.2.1	Simulated event samples . . . . .	74
5.2.2	Fast MC generation . . . . .	75
5.3	Studies using simulated events . . . . .	78
5.3.1	Results in the absence of azimuthal anisotropies . . . . .	78
5.3.2	Results in the presence of azimuthal anisotropies . . . . .	79
5.4	Yield extraction . . . . .	81
5.4.1	Fit model . . . . .	82
5.4.2	Simultaneous binned fits . . . . .	83
5.5	Acceptance times efficiency corrections . . . . .	86
5.6	Bayesian extraction of polarization parameters . . . . .	91
5.7	Checks for systematic effects . . . . .	92
5.7.1	Signal peak fit model . . . . .	95
5.7.2	Background continuum fit model . . . . .	96
5.7.3	Acceptance times efficiency corrections . . . . .	97
5.7.4	Prompt selection . . . . .	97
5.7.5	KVF probability cut . . . . .	97
5.7.6	Evaluation of the systematic uncertainties . . . . .	98
5.8	Discussion of the results . . . . .	99
5.9	Summary . . . . .	102
<b>6</b>	<b>Conclusions</b>	<b>105</b>
<b>A</b>	<b>Other Approaches to <math>\chi_c</math> Polarization Measurements</b>	<b>109</b>
A.1	Likelihood based approach . . . . .	110
A.1.1	Analysis framework . . . . .	110
A.1.2	Preliminary results . . . . .	112
A.1.3	Investigation of possible sources for unphysical behaviour . . . . .	112
A.1.4	Gained insights . . . . .	118
A.2	Measurement relative to $J/\psi$ from $B^\pm \rightarrow J/\psi K^\pm$ decays . . . . .	119
A.2.1	Measurement principle . . . . .	119
A.2.2	Event selection and mass fitting . . . . .	121
A.2.3	Preliminary results . . . . .	122
A.2.4	Gained insights . . . . .	123
<b>B</b>	<b>Trigger Details for Run II</b>	<b>125</b>

<b>C</b>	<b>Supplementary Information for the Data Analysis</b>	<b>129</b>
C.1	Studies using simulated events . . . . .	129
C.2	Simultaneous binned fits results . . . . .	131
C.3	Systematic variations summary figures . . . . .	138
<b>Bibliography</b>		<b>149</b>
<b>Acronyms</b>		<b>165</b>
<b>List of Figures</b>		<b>169</b>
<b>List of Tables</b>		<b>175</b>
<b>Curriculum Vitae</b>		<b>176</b>

Die approbierte gedruckte Originalversion dieser Dissertation ist an der TU Wien Bibliothek verfügbar.  
 The approved original version of this doctoral thesis is available in print at TU Wien Bibliothek.



Die approbierte gedruckte Originalversion dieser Dissertation ist an der TU Wien Bibliothek verfügbar.  
The approved original version of this doctoral thesis is available in print at TU Wien Bibliothek.

# Introduction

The difference between screwing around and science is writing it down.

---

*(Adam Savage, "MythBusters", Ep. "Bouncing Bullet")*

The [Standard Model of Particle Physics](#) (SM) was first formulated in the sixties and seventies of the 20th century [1–3]. It classifies all observed particles so far and describes their interactions via the electromagnetic force, the weak force as well as the strong force. The SM comprises twelve fundamental spin- $\frac{1}{2}$  fermions<sup>i</sup> and the spin-1 bosons which are responsible for mediating the described forces. Additionally, it predicts the presence of the Higgs boson which allows the intermediate vector bosons to gain mass. The discovery of the Higgs boson in 2012 [4, 5], by then the last missing piece of the SM, marks the great success of the SM in describing the interactions of sub-atomic particles. An overview of the fundamental particles and their interactions as described by the SM is shown in Fig. 1.1.

Even though the SM is one of the most successful theoretical models in physics and it has predicted a large number of experimental results, it is considered an incomplete theory today as it has several shortcomings. Most importantly it does not include the fourth fundamental force, gravity. Due to the negligible relative strength of the gravitational force compared to the other three forces it is presumed that this has no effect for particle physics. Other shortcomings include the fact that neutrinos have masses, implied by the observation of neutrino oscillations [7, 8], even though neutrinos are considered massless in the SM. Furthermore, the SM does not provide a candidate for dark matter, whose existence is motivated by the observed deviations from expected rotational curves of galaxies, gravitational lensing and others [9]. These imperfections of the SM are just briefly highlighted here, but will not be addressed in any way in the context of the present thesis.

In mathematical terms the SM is a renormalizable quantum field theory based on a local  $SU(3) \times SU(2) \times U(1)$  gauge symmetry. The  $SU(2) \times U(1)$  gauge symmetry governs the unification of the electromagnetic and the weak force into the electroweak force. It is mediated by the  $Z^0$  and the  $W^\pm$  bosons and the photon respectively. Via

---

<sup>i</sup>The description of the corresponding anti-particles, with equal mass but opposite quantum numbers, including electric charge, is implied.

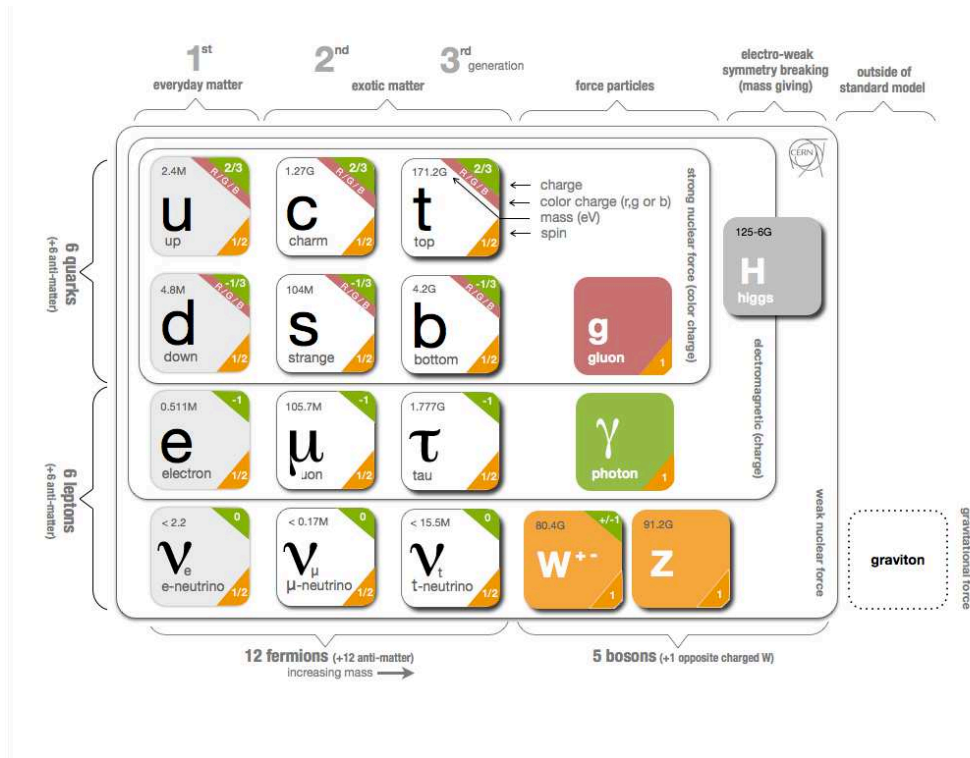


Figure 1.1: Particles and forces described by the SM [6].

the mechanism of *spontaneous symmetry breaking* an additional field is introduced which manifests itself in the presence of the Higgs boson and lets the  $Z^0$  and  $W^\pm$  bosons acquire a non-zero mass [10–12].

The  $SU(3)$  symmetry is the basis for the quantum field theory, [Quantum Chromodynamics \(QCD\)](#) [13], describing the strong interaction between the quarks and its mediators, the eight massless gluon fields. Only the quarks and the gluons carry color charge and participate in the strong interaction. The strong force binds the quarks into nucleons and nucleons into atomic nuclei. Thus, it keeps our visible world together at the innermost level.

Although the dynamics of the strong interaction are described in a self-consistent way by QCD, concrete calculations are only possible under specific conditions. This is closely related to the fact that gluons, mediating the strong force, themselves carry color charge and are, thus, self-interacting. This leads to the phenomenon of *asymptotic freedom*, also referred to as the *running of the strong coupling constant*  $\alpha_s$  [14, 15]. As a consequence perturbative QCD calculations as an expansion of  $\alpha_s$  are limited to processes at high energies, involving high momentum transfers at short distances where  $\alpha_s$  is small. In these *hard scattering* processes the interaction between quarks and gluons becomes small. On the other hand, at low energies and long distances, in the realm of *soft QCD*, the interaction between quarks and gluons becomes strong and the expansion breaks down, leading to the phenomenon of *quark confinement*, which ensures that only color singlet states are ever visible.

---

Since processes that lead to QCD bound states, so called *hadrons*, are characterized by low momentum transfers [16, 17], they cannot be easily accessed with perturbative QCD calculations. However, if only heavy quarks,  $q$ , i.e. charm or bottom quarks, denoted as  $c$  and  $b$  respectively, are involved this issue can be mitigated. QCD bound states of a heavy quark and its corresponding antiquark ( $c\bar{c}$  and  $b\bar{b}$ ) are called *quarkonia*. It is conjectured that due to the heavy quark masses, the production of these quarkonium states can be factorized into two separate steps which occur at two distinct time scales. The production of the initial quark-antiquark pair  $q\bar{q}$  is governed by short-distance parton-level strong interaction processes and can be calculated within perturbative QCD. During the subsequent hadronization into the bound quarkonium state this initial  $q\bar{q}$  pair undergoes long-distance strong interactions, which are part of the non-perturbative QCD sector.

**Non-Relativistic Quantum Chromodynamics (NRQCD)** [18] is a QCD-inspired effective field theory that leverages this factorization and which allows to calculate measurable observables, despite the importance of the non-perturbative effects for the description of quarkonium production. The initial quark-antiquark pair is produced as a superposition of various “pre-resonant”  $q\bar{q}$  states, characterized by different spin, angular momentum and color eigenstates, depending on the production mechanism. The evolution into the bound quarkonium state is described by so called **Long-Distance Matrix Elements (LDMEs)**, which are supposedly process independent constant parameters that contain all the non-perturbative physics. They determine the relative importance of the individual  $q\bar{q}$  states with respect to the full quarkonium cross section. Direct calculations of the LDMEs are in principle possible in lattice QCD or in the limit of using simplified model assumptions, but presently remain out of reach. Thus, they have to be determined from fits to experimental data, limiting the predictive power of NRQCD.

Different experimentally accessible physics observables depend on the values of the LDMEs, and can consequently be used to determine the latter by comparing theoretical calculations with measured data. The two most important kinds of observables are the production cross sections and the polarizations, which reveal information about the preferred spin alignment. Cross section measurements at the Tevatron experiments CDF [19–21] and D0 [22] contributed strongly to the acceptance of color octet contributions as they are used in the NRQCD approach [23]. However, subsequent polarization measurements at the same experiments [24–26] showed only small polarizations that were in stark disagreement with the NRQCD prediction [27] of fully transverse polarizations at high transverse momentum,  $p_T$ . Furthermore, the measurements were plagued by the fact that they were mutually inconsistent and could not be reliably interpreted. The latter issue of this so called “quarkonium polarization puzzle” has since been identified as being related to an inadequate analysis strategy, and a more robust methodology for polarization measurements has been proposed which allows to obtain reliable and unambiguous quarkonium polarization measurement results [28–32].

Since the start of the **Large Hadron Collider (LHC)** physics program, a multitude of measurements of quarkonium cross sections and polarizations has been made

available by the LHC experiments, extending to previously unexplored regions in  $p_T$ . Using available measurements in a consistent manner, giving equal importance to polarization and cross section measurements, several phenomenological studies have been done [33–37]. Taking into account the inescapable correlations between the quarkonium polarization and the acceptance corrections necessary in a cross section measurement, these studies have shown that it is indeed possible to consistently describe the measured cross sections and the measured vanishing polarizations within the NRQCD framework at high- $p_T$ . The patterns that can be extracted from the mid-rapidity measurements are characterized by a remarkable simplicity which is in striking contrast to the variegated mixture of processes that are at play in the NRQCD factorization approach. Nevertheless, calculations made in the NRQCD framework are able to reproduce the measurements very well, through a seemingly miraculous cancellation of terms [33, 37]. Even more, using the  $\chi_{c1}(1P)$  over  $\chi_{c2}(1P)$  cross section ratio measurements published by ATLAS [38] and CMS [39], it is possible to make predictions about the polarization of the  $\chi_{c1}(1P)$  and the  $\chi_{c2}(1P)$  [35] which are the last puzzle pieces in the quest for the first full picture of charmonium production at hadron colliders. Surprisingly, the predictions for the  $\chi_{cJ}(1P)$  polarizations defy the unpolarized pattern observed in all available  $S$ -wave quarkonium polarization measurements at mid-rapidity and high- $p_T$  and instead are of significant size and, more importantly, of opposite sign for the  $J = 1$  and  $J = 2$  state. This arguably represents the most important benchmark for the NRQCD approach today.

This thesis presents the development of a novel approach for measuring the relative polarization of the  $\chi_{c2}(1P)$  and  $\chi_{c1}(1P)$  states and the application of this approach to obtain the first measurement of  $P$ -wave quarkonium polarizations using data taken by the CMS experiment in proton-proton (pp) collisions at a center of mass energy  $\sqrt{s} = 8$  TeV in 2012. The main goal of the newly developed approach is to be as insensitive to possible experimental effects as possible. These effects include so called acceptance and efficiency effects that are introduced during the reconstruction of the  $\chi_c$  states via their radiative decay to a  $J/\psi$  and a photon, and the subsequent dimuon decay of the  $J/\psi$ . The author is one of the main contributors to the development of the presented analysis strategy and the implementation of the necessary software tools.

The basics of the physics of quarkonia and their production is introduced in Chapter 2. It gives an introduction to the NRQCD framework and other theoretical models that have been or are still in use to describe quarkonium production. An overview of the most recent experimental results regarding quarkonium production and polarization provided by the LHC experiments is presented before a brief review of a subset of phenomenological studies which use these results.

Chapter 3 describes the experimental setup, including a description of the LHC accelerator and the CMS detector focusing on those sub-detectors that are most important for the study of quarkonium states. The reconstruction techniques, including the trigger strategy, relevant for this thesis are also discussed.

Studies that were performed for updating the triggers used to collect data in 2017 and 2018 that can be used for quarkonium production measurements are presented



---

in Chapter 4. While this chapter is not related to the measurement of the  $\chi_c$  polarizations, it provides some additional insights into the considerations that have to be taken into account when designing the trigger strategy for polarization measurements. The author was strongly involved in developing the updated trigger strategy and the updated triggers play a crucial role in future quarkonium production measurements. Hence, this chapter can also serve as future reference.

The newly developed approach for the relative polarization measurement is described in detail in Chapter 5 together with its application to measure the  $\chi_c$  polarization in data collected in pp collisions at  $\sqrt{s} = 8$  TeV during the 2012 data taking period. The analysis strategy is validated using simulated events. The data analysis has been performed *blinded* until it has been extensively scrutinized by the CMS collaboration. The chapter gives a detailed report of possible systematic effects that have been considered before presenting the results and discussing them in the context of the current status of phenomenological studies. The results of this analysis have been submitted to PRL [40].

In the spirit of not only showing the final results but also the evolution from less successful attempts, a brief overview of other attempts that were investigated is given in Appendix A. Although none of these attempts were used in the end, they proved to be important stepping stones towards the final analysis strategy. Moreover, the author hopes, or at least would like to believe, that other scientists might be able to draw useful conclusions from these attempts.

Throughout the thesis natural units with  $\hbar = c = 1$  are used. Thus, energy, mass and momentum are all measured in GeV if not specified otherwise.



Die approbierte gedruckte Originalversion dieser Dissertation ist an der TU Wien Bibliothek verfügbar.  
The approved original version of this doctoral thesis is available in print at TU Wien Bibliothek.

# Quarkonium Physics

In physics, you don't have to go around making trouble for yourself - nature does it for you.

*(Frank Wilczek)*

Quarkonia are states bound by the strong force consisting of a heavy quark and its antiquark. These mesons are divided into two systems depending on the flavour of the heavy quark, the charmonium family for  $c\bar{c}$  states and the bottomonium family for  $b\bar{b}$  states. Top quarks do not form bound states, since they decay electroweakly before a bound state can form, due to their heavy masses. The  $J/\psi$  was the first quarkonium state that was discovered in 1974 almost simultaneously by groups at the [Brookhaven National Laboratory \(BNL\)](#) [41] and at the [Stanford Linear Accelerator Complex \(SLAC\)](#) [42]. Shortly after the discovery the newly found state was identified as a bound state of  $c\bar{c}$  [43], thus proving the existence of the then only conjectured charm quark. Only three years later the first member of the bottomonium family, the  $\Upsilon(1S)$ , was also discovered and marked the first observation of a particle containing a bottom quark [44].

## 2.1 Quarkonium spectra

The members of the two different quarkonium families occur in different quantum states and are characterized by the quantum numbers describing the spin  $S$ , the angular momentum  $L$ , the total angular momentum  $J = L + S$  and the principal quantum number  $n$ . The possible configurations are either denoted as  $J^{PC}$ , with parity  $P = (-1)^{L+1}$  and charge conjugation  $C = (-1)^{L+S}$  or using the so called spectroscopic notation  $n^{2S+1}L_J$ . Figures 2.1 and 2.2 show the subset of charmonium and bottomonium states relevant for this thesis, as well as a subset of the decays occurring within the two families. Inter-family decays of the form  $b\bar{b} \rightarrow c\bar{c}$  are negligible [45]. The spectra are restricted to the  $CP$ -even states with  $J^{++}$  and  $J^{--}$ , with masses below the open-heavy-flavour thresholds. The  $CP$ -odd  $0^{-+}$  ( $\eta_c$  and  $\eta_b$ ) and  $1^{+-}$  ( $h_c$  and  $h_b$ ) below these thresholds are omitted, since they will not be dis-

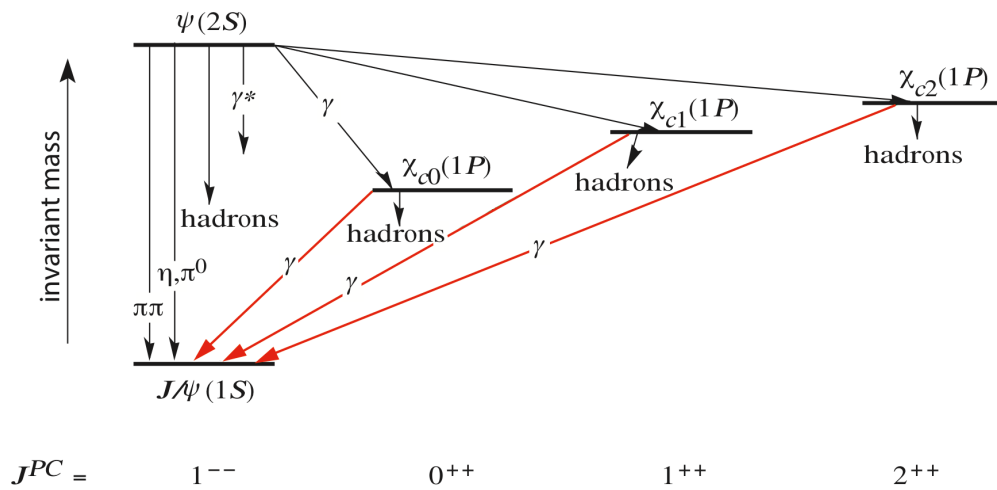


**Figure 2.1:** Charmonium spectrum and a subset of decays of the CP-even states below the open-charm threshold. Adapted from Ref. [45].

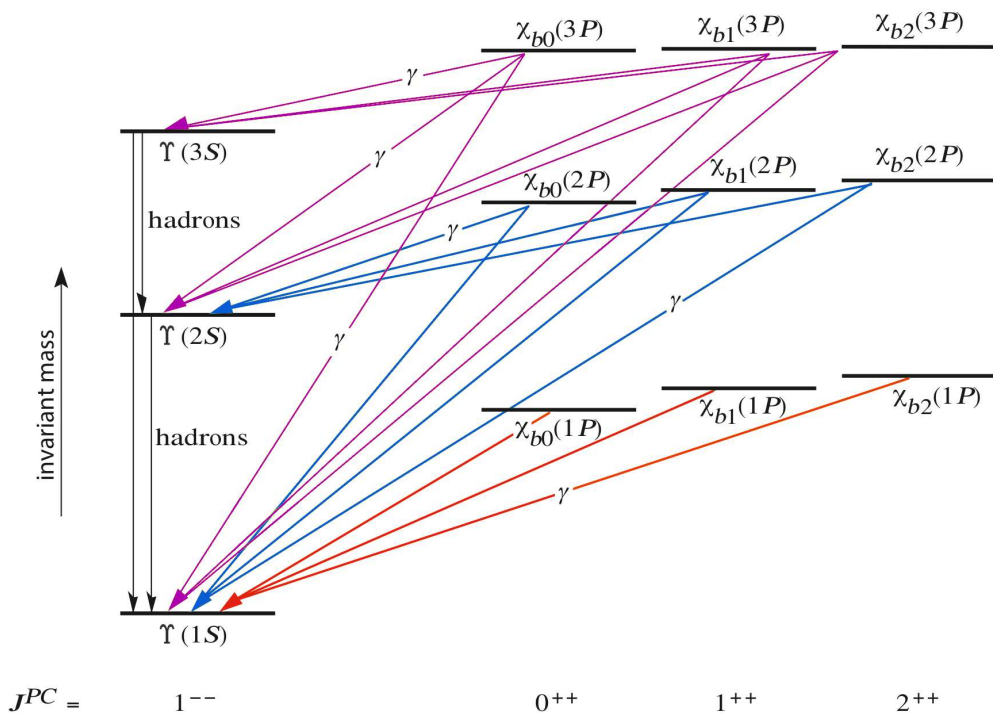


**Figure 2.2:** Bottomonium spectrum and a subset of decays of the CP-even states below the open-bottom threshold. Adapted from Ref. [45].

cussed in this thesis. The spectra can be divided into two categories, the  $S$ -wave states ( $L = 0$ ) and the  $P$ -wave states ( $L = 1$ ).

The considered  $S$ -wave states are the  $J^{PC} = 1^{--}$  vector mesons  $J/\psi$  and its radial excitation  $\psi(2S)$ <sup>i</sup> and the  $\Upsilon(1S)$  and its radial excitations  $\Upsilon(2S)$  and  $\Upsilon(3S)$ . In the charmonium family  $S$ -wave states are collectively denoted as  $\psi(nS)$  with  $n = 1, 2$ , whereas the ones of the bottomonium family are denoted as  $\Upsilon(nS)$  with  $n = 1, 2, 3$ . The  $P$ -wave states are the  $J^{PC} = J^{++}$  pseudovector mesons  $\chi_{cJ}(1P)$ <sup>ii</sup> and  $\chi_{bJ}(1P)$  and its radial excitations  $\chi_{bJ}(2P)$  and  $\chi_{bJ}(3P)$ , appearing in triplets corresponding to  $J = 0, 1, 2$ . While the majority of the just described states has been known for a relatively long time, the  $\chi_{bJ}(3P)$  state has only been discovered in 2012 [46, 47] and its triplet structure has only been confirmed recently [48].

At hadron colliders the experimentally most important decay of the  $S$ -wave states is the *dimuon* channel,  $\psi(nS) \rightarrow \mu\mu$ <sup>iii</sup> and  $\Upsilon(nS) \rightarrow \mu\mu$ , with branching fractions of 5.9 % ( $J/\psi$ ), 0.8 % ( $\psi(2S)$ ), 2.5 % ( $\Upsilon(1S)$ ), 1.9 % ( $\Upsilon(2S)$ ) and 2.2 % ( $\Upsilon(3S)$ ) [45]. The  $P$ -wave states are usually reconstructed using their radiative decays to  $S$ -wave states  $\chi_{cJ} \rightarrow J/\psi\gamma$  and  $\chi_{bJ}(nS) \rightarrow \Upsilon(mS)\gamma$  for  $n \geq m$ , with branching fractions spanning from around 1 % up to about 34 % ( $\chi_{c1}(1P) \rightarrow J/\psi\gamma$ ) depending on the involved states [45]. An overview over the currently measured properties of the stated particles is given in Table 2.1.

**Table 2.1:** Properties of quarkonium states seen in Figs. 2.1 and 2.2 [45]

Meson	$J^{PC}$	$n^{2S+1}L_J$	Mass / MeV	Full Width
$J/\psi$	$1^{--}$	$1^3S_1$	$3096.900 \pm 0.006$	$92.9 \pm 2.8$ keV
$\chi_{c0}(1P)$	$0^{++}$	$1^3P_0$	$3414.74 \pm 0.30$	$10.8 \pm 0.6$ MeV
$\chi_{c1}(1P)$	$1^{++}$	$1^3P_1$	$3510.67 \pm 0.05$	$0.84 \pm 0.04$ MeV
$\chi_{c2}(1P)$	$2^{++}$	$1^3P_2$	$3556.17 \pm 0.07$	$2.00 \pm 0.11$ MeV
$\psi(2S)$ or $\psi'$	$1^{--}$	$2^3S_1$	$3686.097 \pm 0.010$	$286 \pm 16$ keV
$\Upsilon(1S)$	$1^{--}$	$1^3S_1$	$9460.30 \pm 0.26$	$54.02 \pm 1.25$ keV
$\chi_{b0}(1P)$	$0^{++}$	$1^3P_0$	$9859.44 \pm 0.42 \pm 0.31$	-
$\chi_{b1}(1P)$	$1^{++}$	$1^3P_1$	$9892.78 \pm 0.26 \pm 0.31$	-
$\chi_{b2}(1P)$	$2^{++}$	$1^3P_2$	$9912.21 \pm 0.26 \pm 0.31$	-
$\Upsilon(2S)$	$1^{--}$	$2^3S_1$	$10023 \pm 0.31$	$31.98 \pm 2.63$ keV
$\chi_{b0}(2P)$	$0^{++}$	$2^3P_0$	$10232.50 \pm 0.40 \pm 0.50$	-
$\chi_{b1}(2P)$	$1^{++}$	$2^3P_1$	$10255.46 \pm 0.22 \pm 0.50$	-
$\chi_{b2}(2P)$	$2^{++}$	$2^3P_2$	$10268.65 \pm 0.22 \pm 0.50$	-
$\Upsilon(3S)$	$1^{--}$	$3^3S_1$	$10355.2 \pm 0.5$	$20.32 \pm 1.85$ keV
$\chi_{b1}(3P)$	$1^{++}$	$3^3P_1$	$10513.41 \pm 0.41 \pm 0.53$	-
$\chi_{b2}(3P)$	$2^{++}$	$3^3P_2$	$10524.02 \pm 0.57 \pm 0.53$	-

<sup>i</sup>Sometimes also referred to as  $\psi'$ .

<sup>ii</sup>From here on the  $\chi_{cJ}(1P)$  will be denoted as  $\chi_{cJ}$  only.

<sup>iii</sup>Since quarkonia are chargeless states the short notation  $\mu\mu$  for  $\mu^+\mu^-$  is commonly used and the opposite charge of the muons is implied.

The  $S$ -wave quarkonium states have decay times in the order of  $10^{-20}$ – $10^{-21}$  s, while the  $P$ -wave quarkonia states have decay times in the order of  $10^{-22}$ – $10^{-23}$  s<sup>iv</sup>. Consequently, the quarkonium states travel only very small distances in the order of femto- to pico-meters before they decay and all decays are classified as quasi-instantaneous or **prompt (PR)**. Due to these short decay times it is currently not possible to experimentally distinguish between directly produced quarkonia and decay products of heavier quarkonium states, so called *feed-down decays*. While it is in principle possible to separate such feed-down decays from directly produced quarkonia, by reconstructing all decay products of the heavier states, such an approach is in general not really feasible in the challenging environment of hadron collisions. The feed-down contributions can make up a considerable fraction of the observed states, e.g. for  $J/\psi$  mesons around 8 % are from  $\psi(2S)$  decays and around 25 % have their origin in  $\chi_{cJ}$  decays [38, 49]. The identification of  $P$ -wave quarkonium states in samples of lighter  $S$ -wave states is possible by requesting an additional photon in the dimuon final state, thus fully reconstructing the radiative decay of the  $P$ -wave quarkonia.

In the case of the charmonium system an additional **non-prompt (NP)** component, stemming from decays of heavier  $b$ -hadrons, has to be considered as well. However, since the average decay time is in the order of pico-seconds [45], these decays can be identified experimentally via the displacement of the secondary vertex which is in the order of 100  $\mu\text{m}$ .

Since the available samples of prompt  $S$ - and  $P$ -wave events always comprise a mixture of directly produced states and feed-down contributions, the properties of the directly produced quarkonium states have to be disentangled from the measured prompt properties using knowledge about the feed-down fractions and the properties of heavier quarkonium states. Conversely, the feed-down structure also allows to make predictions about certain unmeasured properties if enough information about other states and the feed-down fractions is present, as will be seen later.

## 2.2 Quarkonium production

Due to the large masses of the involved quarks and the inherent symmetry and simplicity of the quark-antiquark system quarkonia are ideal laboratories to study QCD. They are model systems to test the interplay of perturbative and non-perturbative aspects of QCD. A precise understanding of quarkonium production helps in understanding hadron formation, the process in which the strong interaction binds quarks into hadronic bound states, in general. An assumption that underpins almost all theoretical treatments of quarkonium production under discussion nowadays is that the production of quarkonia can be factorized into two steps, the production of an initial  $q\bar{q}$  pair and the subsequent evolution of the pair into the bound state. The main differences between the approaches are essentially in the treatment of the sec-

<sup>iv</sup>Only the decay times for the  $\chi_{cJ}$  states have been measured so far for  $P$ -wave quarkonia.

ond step, the so called hadronization, although some differences in the formation of the initial  $q\bar{q}$  pair are also introduced sometimes [50].

Given the large masses of the  $c$ - and  $b$ -quarks, the relative (anti-)quark velocity  $v$  in the bound quarkonium state is  $v^2 \approx 0.3$  in case of charmonium and  $v^2 \approx 0.1$  in case of bottomonium. Thus, quarkonia can be treated as non-relativistic bound states. Such states are identified by at least three different intrinsic momentum scales:  $m_q$  – the heavy-quark mass,  $m_q v$  – the momentum of the heavy-quark or antiquark in the quarkonium rest frame and  $m_q v^2$  – the binding energy of the quark-antiquark pair [16]. The production of the initial  $q\bar{q}$  pair occurs at a timescale  $\propto 1/m_q$  while the evolution into the physically observable bound state takes of the order of  $1/(m_q v^2)$  [18]. Intuitively one would expect that short-distance and long-distance effects can be separated if the two timescales are well separated. For the bottomonium this condition is well fulfilled and also in the charmonium system it holds reasonably well. However, for light hadrons the factorization of the production breaks down, because the timescales are no longer well separated. Thus, the study of quarkonium production offers unique opportunities to understand hadron formation and to study strong interactions involving long-distance, non-perturbative effects.

The currently prevalent theoretical framework describing inclusive quarkonium production is [Non-Relativistic Quantum Chromodynamics \(NRQCD\)](#) [18]. Other theoretical models currently under discussion are, among others, the [Color-Singlet Model \(CSM\)](#) [51], the [Color Evaporation Model \(CEM\)](#) [52, 53] and the fragmentation function approach [54–56]. In the following the focus will be put on NRQCD, while the other approaches will only be briefly mentioned and the reader is referred to summaries in the literature [16, 50] and the references therein for further information.

### 2.2.1 Non-Relativistic Quantum Chromodynamics

NRQCD is an effective field theory introduced in 1995 [18] and is presently the most rigorous and general theoretical approach to quarkonium production. It relies on the assumption that quarkonium production can be split into two separate steps, the formation of an initial  $q\bar{q}$  pair and its subsequent evolution into a bound quarkonium state. The inclusive production cross section for any directly produced quarkonium state  $\mathcal{Q}$  in the NRQCD factorization approach can be formulated as [16]

$$\sigma(\mathcal{Q}) = \sum_{\{n\}} \mathcal{S}[q\bar{q}(\{n\})] \cdot \langle \mathcal{O}^{\mathcal{Q}}(\{n\}) \rangle. \quad (2.1)$$

The so called [Short-Distance Coefficients \(SDCs\)](#)  $\mathcal{S}[q\bar{q}(\{n\})]$  describe the production of the initial quark-antiquark pair in a given quantum state  $\{n\} = {}^{2S+1}L_J^{[C]}$ , with  $C \in \{1, 8\}$ , the color multiplicity. The [Long-Distance Matrix Elements \(LDMEs\)](#)  $\langle \mathcal{O}^{\mathcal{Q}}(\{n\}) \rangle$  govern the evolution of the initial state with quantum numbers  $\{n\}$  into the bound quarkonium state  $\mathcal{Q}$  with possibly different quantum numbers. The sum runs over all possible intermediate  $q\bar{q}$  states  $\{n\}$ , including [color-octet \(CO\)](#) ( $C = 8$ ) and [color-singlet \(CS\)](#) ( $C = 1$ ) configurations. While the SDCs are calculable using perturbative QCD, the LDMEs, not calculated directly, are conjectured to be

universal constants that encompass all long-distance and, thus, non-perturbative effects. These include the non-perturbative emission of soft-gluons that are necessary to reach a color neutral final state from a CO initial  $q\bar{q}$  pair, illustrated in Fig. 2.3. Although the formalism explicitly allows for “colored” intermediate states, only the final color-neutral bound state is physically observable.

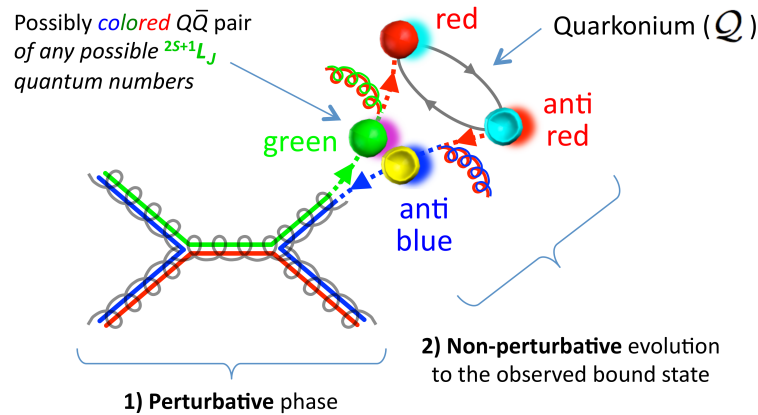


**Figure 2.3:** Illustration of the assumed NRQCD factorization in quarkonium production; the perturbative production of the possibly colored initial  $q\bar{q}$  pair (1) and the subsequent evolution into the color neutral bound quarkonium state  $Q$  via the non-perturbative emission of soft gluons (2) [57].

The *NRQCD factorization theorem* described above is widely accepted today, but has not yet been completely and rigorously proven. Currently proofs for the factorization exist up to *next-to-next-to-leading order* (NNLO) in the strong coupling constant  $\alpha_s$  [55, 56, 58]. While NRQCD can in principle address the binding step rigorously, the central issue in proving NRQCD factorization is establishing that this binding step leads to universal LDMEs.

### Short-Distance Coefficients

The SDCs  $\mathcal{S}[q\bar{q}(\{n\})]$  can be calculated using perturbative QCD approaches by expanding in powers of  $\alpha_s$ . They represent the inclusive partonic cross sections necessary to produce a  $q\bar{q}$  state with quantum numbers  $\{n\}$ , convolved with parton distribution functions. Hence, they are process-dependent and different for different collision systems and energies. They are functions that account for the kinematic dependence of the production cross sections. An SDC must not be in general individually observable, it may even be negative, as long as the sum over all partial cross sections remains physically meaningful. Each SDC term has its own calculable contribution to the angular shape of the quarkonium decay distribution, described by the polarization parameters  $\vec{\lambda} = (\lambda_\theta, \lambda_\phi, \lambda_{\theta\phi})$  (the quarkonium polarization concept is introduced in Sec. 2.3) corresponding to each SDC. Figure 2.4 shows the kinematic dependence of several SDCs corresponding to different intermediate  $\{n\}$  states in



Eq. (2.1). The different contributions have significantly different kinematic dependences that also lead to very characteristic behaviours of the polarization parameter  $\lambda_\vartheta$ .

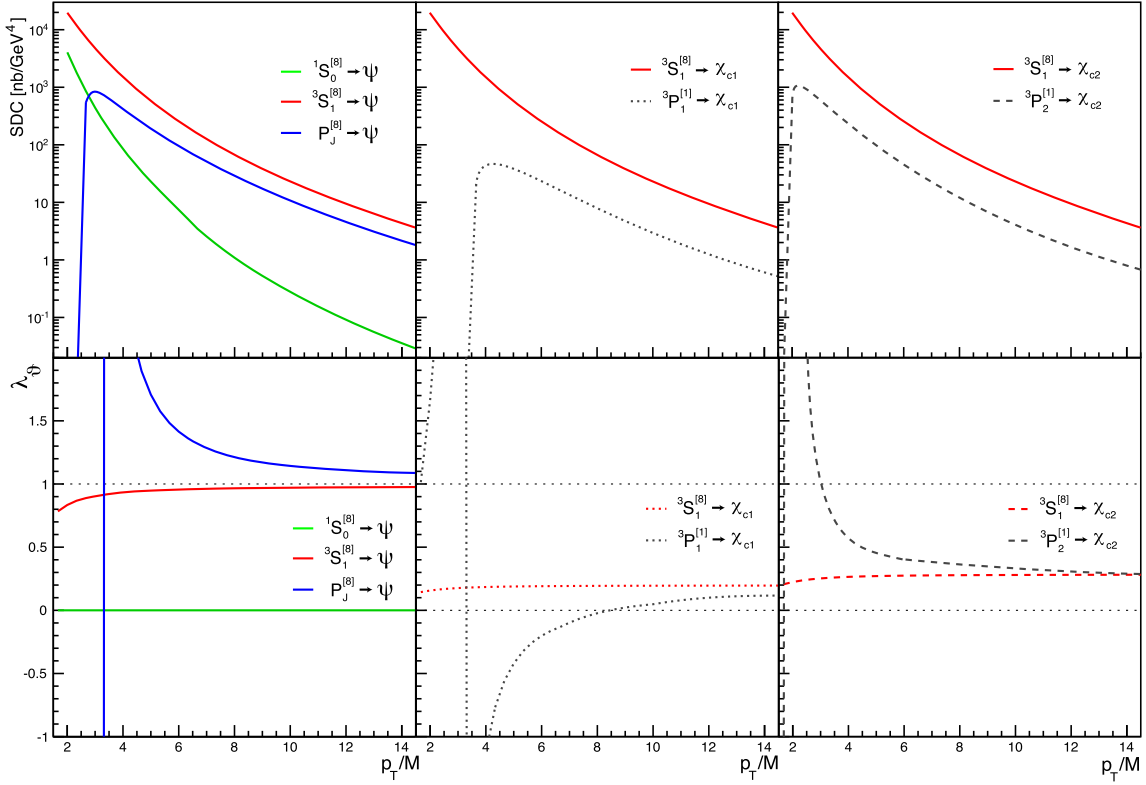


**Figure 2.4:** SDCs (top) and corresponding  $\lambda_\vartheta$  in the helicity frame (bottom) for the main contributions in the NRQCD factorization approach to directly produced  $\psi$  mesons (left) and for  $J/\psi$  from  $\chi_{c1}$  (center) and  $\chi_{c2}$  (right) decays, calculated at NLO [59–61] as a function of  $p_T/M$ . The  $^3P_J^{[8]}$  and  $^3P_{1,2}^{[1]}$  SDC functions are multiplied by  $m_c^2$ , the squared mass of the charm quark. They are plotted with flipped signs, since they become negative at high  $p_T/M$  [34].

### Long-Distance Matrix Elements

The LDMEs  $\langle \mathcal{O}^{\mathcal{Q}}(\{n\}) \rangle$  can be interpreted as the probability that a given initial  $q\bar{q}$  pair in the quantum state  $\{n\}$  evolves into a bound quarkonium state  $\mathcal{Q}$ . In NRQCD they are assumed to be universal constants, i.e. independent of the  $q\bar{q}$  kinematics and the collision system and energy. Since calculations of the LDMEs within QCD are not currently available they have to be estimated from fits to experimental measurements.

In principle the sum in Eq. (2.1) runs over all possible intermediate states  $\{n\}$ , which would entail having to calculate an infinite number of SDCs along with determining an equally infinite number of LDMEs. However, in practice, the LDMEs can be organized according to *velocity scaling rules*, such that the sum in Eq. (2.1)

can be seen as a double expansion in powers of  $\alpha_s$  and  $v$ . Due to the small velocities  $v$  in the quarkonium state, a strong suppression of partial cross sections  $\mathcal{S}[\text{q}\bar{\text{q}}(\{n\})] \cdot \langle \mathcal{O}^{\mathcal{Q}}(\{n\}) \rangle$  characterized by large powers of  $v$  is expected. Although this strong suppression of certain LDMEs could potentially be compensated by large values of the corresponding SDCs, the expansion is generally truncated at order  $v^4$ . While neglecting higher order terms in the velocity expansion is well justified in the bottomonium case due to the heavy mass of the bottom quark, the series may converge more slowly in case of the charmonium system or for excited states, as the relative velocity  $v$  is less small in excited states compared to the ground state [62].

Several slightly differing velocity scaling rules exist in the literature, a fairly common definition is given in Table 2.2 which also highlights the relevant LDMEs for  $S$ -wave and  $P$ -wave quarkonium production. The resulting intermediate states that are considered for  $S$ -wave quarkonium production are the CS state  ${}^3S_1^{[1]}$  and the three CO states  ${}^3S_0^{[8]}$ ,  ${}^3S_1^{[8]}$  and  ${}^1P_J^{[8]}$ . For  $P$ -wave quarkonium production only the CS state  ${}^3P_J^{[1]}$  and the CO state  ${}^3S_1^{[8]}$  are expected to give sizable contributions.

**Table 2.2:** Relative scaling of the LDMEs  $\langle \mathcal{O}^{\mathcal{Q}}(\{n\}) \rangle$  in powers of  $v$  for different quantum states  $\{n\} = {}^{2S+1}L_J^{[C]}$  of the intermediate  $\text{q}\bar{\text{q}}$  pair. The expected scaling is stated separately for vector meson states with  $J^{PC} = 1^{--}$  and pseudovector states with  $J^{PC} = J^{++}$ , split into LDMEs related to CS and CO states [63]. The relevant LDMEs are stated in bold.

$J^{PC} = 1^{--}$				
	${}^1S_0^{[C]}$	${}^3S_1^{[C]}$	${}^1P_1^{[C]}$	${}^3P_J^{[C]}$
color-singlet, $\mathcal{C} = 1$	$v^8$	<b><math>\mathbf{1}</math></b>	$v^8$	$v^8$
color-octet, $\mathcal{C} = 8$	<b><math>\mathbf{v^4}</math></b>	<b><math>\mathbf{v^4}</math></b>	$v^8$	<b><math>\mathbf{v^4}</math></b>
$J^{PC} = J^{++}$				
	${}^1S_0^{[C]}$	${}^3S_1^{[C]}$	${}^1P_1^{[C]}$	${}^3P_J^{[C]}$
color-singlet, $\mathcal{C} = 1$	$v^6$	$v^6$	$v^{10}$	<b><math>\mathbf{v^2}</math></b>
color-octet, $\mathcal{C} = 8$	$v^6$	<b><math>\mathbf{v^2}</math></b>	$v^6$	$v^6$

## 2.2.2 Color-Singlet Model

The **Color-Singlet Model (CSM)** was one of the first models for quarkonium production and was proposed already shortly after the discovery of the  $J/\psi$ . This model assumes that the initial  $\text{q}\bar{\text{q}}$  pair is already produced with the same quantum numbers  $\{n\}$  as the final quarkonium state  $\mathcal{Q}$ . It can be obtained from NRQCD as a special case for the production of CP-even states when only the CS intermediate states, i.e.  ${}^3S_1^{[1]}$  for  $S$ -wave quarkonia or  ${}^3P_J^{[1]}$  for the  $P$ -wave quarkonia respectively, are considered.

The CSM has been considered as describing quarkonium production reasonably well until the early 1990s [51], when it became more and more apparent that the

experimentally measured cross sections were significantly higher than the predicted ones. In case of the feed-down free  $\psi(2S)$  cross section measured by the [Collider Detector at Fermilab \(CDF\)](#) the discrepancy between experiment and theory amounted to a factor of 50 [20], and came to be known as the “CDF  $\psi(2S)$  anomaly”.

In the CSM the CS LDMEs are accessible to theoretical calculations and can be related to and fixed by measurements of the decay rates of the quarkonium states [16]. Taking this into account the CSM is a model without any free parameters. Roughly a decade ago the first [next-to-leading order \(NLO\)](#) and [NNLO](#) calculations in  $\alpha_s$  appeared and revealed that these contributions are significantly larger than the ones in [leading order \(LO\)](#) at high energies [16, 50]. This has somewhat resurrected the possibility of the CSM describing important production mechanisms. However, it is not apparent that the expansion in  $\alpha_s$  converges. Regardless of all these considerations the CSM also exhibits inconsistencies in the description of  $P$ -wave quarkonium production that can only be compensated by considering CO terms in the NRQCD factorization approach [16, 50].

### 2.2.3 Color Evaporation Model

The principle of quark-hadron duality forms the basis for the [Color Evaporation Model \(CEM\)](#) [52, 53]. It assumes that the production cross section of a quarkonium state is directly related to the one of producing a  $q\bar{q}$  pair in a mass region that allows for the evolution into a bound quarkonium state. This mass region is defined by the kinematical threshold of producing a quark pair,  $2m_q$ , and the one to create the lightest open-heavy-flavour hadron pair,  $2m_H$ . One free parameter per quarkonium state is introduced to account for the process-independent probability of the pair hadronizing into the given quarkonium state [16, 50]. The main assumption of the CEM is that the initial  $q\bar{q}$  pair can be produced in a quantum state  $\{n\}$  that is essentially decorrelated from the one of the quarkonium state  $\mathcal{Q}$ , as  $\{n\}$  is assumed to be modified by several non-perturbative emissions of soft gluons that color neutralize the initial state, hence the eponymous “color evaporation”.

Although the CEM has some success in phenomenological approaches, it also suffers from some discrepancies in transverse momentum spectra and most importantly offers no way of describing quarkonium polarization [16, 50]. However, some of these issues have recently received some attention in the framework of an [improved CEM \(ICEM\)](#), which addresses some of the issues and also incorporates the possibility of predicting quarkonium polarization [64–68].

### 2.2.4 Fragmentation function approach

Some of the more recent developments in the theoretical description of inclusive quarkonium production have happened in the so called fragmentation function approach [54–56]. For quarkonium production with  $p_T \gg m_q$  the cross section is written as a sum of single-parton production cross sections convolved with single-parton fragmentation functions [69]. All the information about the incoming state is included

in the parton production cross section. The parton fragmentation functions correspond to probability distributions of the non-perturbative evolution of a  $q\bar{q}$  pair into an actual quarkonium state [16]. The fragmentation function approach provides a convenient way to organize the contributions to the quarkonium production cross section as a function of  $m_q/p_T$ , which might be more expedient than the organization in powers of  $\alpha_s$  in NRQCD [16, 50].

It also possibly represents the first step towards a proof of the NRQCD factorization as it also provides a way to express the fragmentation functions as a sum of NRQCD LDMEs [54–56] under the assumption that the NRQCD factorization is valid. The approach can be seen as a way of reorganizing the sum in Eq. (2.1) and it provides a systematic method for resumming potentially large logarithms of  $p_T/m_q$ , which might make the  $\alpha_s$  expansion more convergent [16].

## 2.3 Quarkonium polarization

Even though the different contributions with different quantum numbers  $\{n\}$  to the total cross section in Eq. (2.1) cannot be individually measured, conclusions on the properties of the initial  $q\bar{q}$  pair can be drawn from measuring one of the variables summarized in  $\{n\}$ . Specifically, it is possible to measure the alignment of the total angular momentum vector  $\vec{J}$  with respect to a quantization axis  $z$ . Vector mesons with  $J = 1$ , such as the  $S$ -wave quarkonia, can be observed in three possible eigenstates of the angular momentum component  $J_z = 0, \pm 1$  with respect to a quantization axis  $z$ . An  $S$ -wave quarkonium state can be described as a superposition of the three eigenstates [29]

$$|\mathcal{Q}\rangle = a_{+1}|+1\rangle + a_{-1}|-1\rangle + a_0|0\rangle, \quad (2.2)$$

where  $a_i$ , for  $i \in \{+1, -1, 0\}$  are the amplitudes of the individual components. If the probability of finding the quarkonium state  $\mathcal{Q}$  in a given  $J_z$  eigenstate is the same for all possible values of  $J_z$ , the quarkonium is said to be *unpolarized*. If the  $J_z = \pm 1$  or the  $J_z = 0$  eigenstates are preferred, the quarkonium is referred to as *transversely* or *longitudinally* polarized respectively<sup>v</sup>.

The geometrical shape of the angular distribution of the two-body decay products in the  $\mathcal{Q}^{3S_1} \rightarrow \mu\mu$  decay reflects the polarization of the quarkonium state. The measurement of the angular distribution requires the definition of a reference frame in the quarkonium rest frame with respect to which the momentum of one of the decay products can be expressed<sup>vi</sup>. Figure 2.5 illustrates how the polar angle  $\vartheta$  and the azimuthal angle  $\varphi$  of the positively charged lepton are defined.

Exploiting basic quantum mechanical considerations, requiring helicity and parity conservation, the most general observable angular decay distribution of a vector

<sup>v</sup>This is a somewhat misleading, but commonly used, nomenclature which originates in the fact that the  $S$ -wave quarkonia share the quantum numbers ( $1^{--}$ ) of the photon [29].

<sup>vi</sup>The decay products are emitted back-to-back in the quarkonium rest frame.

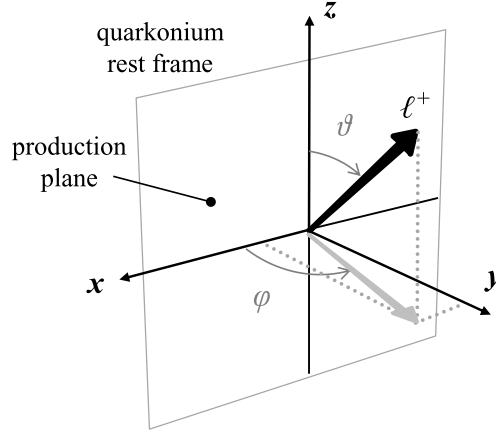


**Figure 2.5:** Coordinate system used to define the polar angle  $\vartheta$  and the azimuthal angle  $\varphi$  of the positively charged lepton  $l^+$ , here a  $\mu^+$ , with respect to a quantization axis  $z$  [29].

meson in a dilepton decay can be written as [29]

$$W(\cos \vartheta, \varphi | \vec{\lambda}) = \frac{3}{4\pi(3 + \lambda_\vartheta)} \left( 1 + \lambda_\vartheta \cos^2 \vartheta + \lambda_\varphi \sin^2 \vartheta \cos 2\varphi + \lambda_{\vartheta\varphi} \sin 2\vartheta \cos \varphi \right), \quad (2.3)$$

where  $\vec{\lambda} = (\lambda_\vartheta, \lambda_\varphi, \lambda_{\vartheta\varphi})$  are the reference frame dependent polarization parameters. The polar anisotropy parameter  $\lambda_\vartheta$  is negative (positive) for longitudinal (transverse) polarization. The unpolarized case is characterized by an isotropic angular decay distribution  $\vec{\lambda} = (0, 0, 0)$ . It has to be noted, that no combination of  $a_0$ ,  $a_{+1}$  and  $a_{-1}$  exists that leads to this special case, such that the decay of a  $J = 1$  state is never intrinsically isotropic. Consequently, only a non-trivial physical polarization scenario, with a lucky mixture of different contributing subprocesses leads to unpolarized  $S$ -wave quarkonium states [29].

The  $x$ - $z$ -plane of the reference frame is defined by the production plane which is spanned by the momenta of the colliding beams  $\vec{b}_1$  and  $\vec{b}_2$  in the quarkonium rest frame. The  $y$ -axis is defined to be orthogonal to the production plane, in direction of  $\vec{b}_1 \times \vec{b}_2$  as seen in the quarkonium rest frame. Different conventions are used for defining the orientation of the  $z$ -axis to make the definition of the reference frame unique. The two definitions used in this thesis are the helicity (HX) and the Collins-Soper (CS) frame [70]. In the HX frame the  $z$ -axis coincides with the momentum direction of the quarkonium in the center-of-mass of the colliding beams, while in the CS frame the  $z$ -axis is defined as bisector of the angle of one beam and the opposite angle of the other beam momentum in the quarkonium rest frame. The definition of the production plane and of the  $z$ -axes for the two described reference frames can be seen in Fig. 2.6.

In cases where more than one subprocess contributes to the production mechanism of a quarkonium, or more general, if  $N$  samples of vector quarkonia with possibly

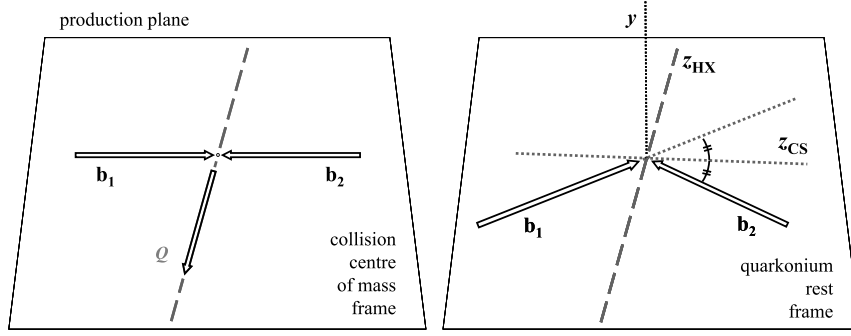


**Figure 2.6:** Definition of the production plane (left) and the quantization axis  $z$  for the HX and the CS frame (right). Adapted from Ref. [29].

different angular decay distributions  $W(\cos\vartheta, \varphi|\vec{\lambda}^{(i)})$  are merged, the resulting total angular decay distribution can be written as the weighted sum of all contributing distributions

$$W(\cos\vartheta, \varphi|\vec{\lambda}') = \sum_{i=1}^N f^{(i)} W(\cos\vartheta, \varphi|\vec{\lambda}^{(i)}), \quad (2.4)$$

where  $f^{(i)}$  is the relative weight of the  $i$ -th sample in the mixture. The resulting effective polarization parameters  $\vec{\lambda}'$  can be calculated via [29]

$$\vec{\lambda}' = \frac{\sum_{i=1}^N \frac{f^{(i)}}{3+\lambda_\vartheta^{(i)}} \vec{\lambda}^{(i)}}{\sum_{i=1}^N \frac{f^{(i)}}{3+\lambda_\vartheta^{(i)}}}. \quad (2.5)$$

These relations are characterized by attributing a larger weight to longitudinal contributions than to transverse ones. This can be demonstrated by calculating the resulting value for  $\lambda_\vartheta$  for a mixture of a fully transverse ( $\lambda_\vartheta = +1$ ) and a fully longitudinal ( $\lambda_\vartheta = -1$ ) sample with equal weights,  $f^{(i)} = 0.5$ . Intuition would predict an unpolarized mixed sample with  $\lambda_\vartheta = 0$  in this case, however, calculating the effective polar anisotropy parameter actually yields  $\lambda'_\vartheta = -1/3$ .

### 2.3.1 Considerations in polarization measurements

A useful concept is the one of the *natural polarization frame* which is defined as the frame in which the polar anisotropy parameter  $\lambda_\vartheta$  is maximal, the azimuthal anisotropy parameter  $\lambda_\varphi$  is minimal, and  $\lambda_{\vartheta\varphi}$  vanishes [31]. Using the condition that the absolute value of  $\lambda_\vartheta$  never exceeds one regardless of the chosen reference frame it is possible to derive so called positivity constraints for  $\lambda_\varphi$  and  $\lambda_{\vartheta\varphi}$  [32]. The allowed regions for the  $\vec{\lambda}$  phase space are shown in Fig. 2.7 as grey shapes. Since the

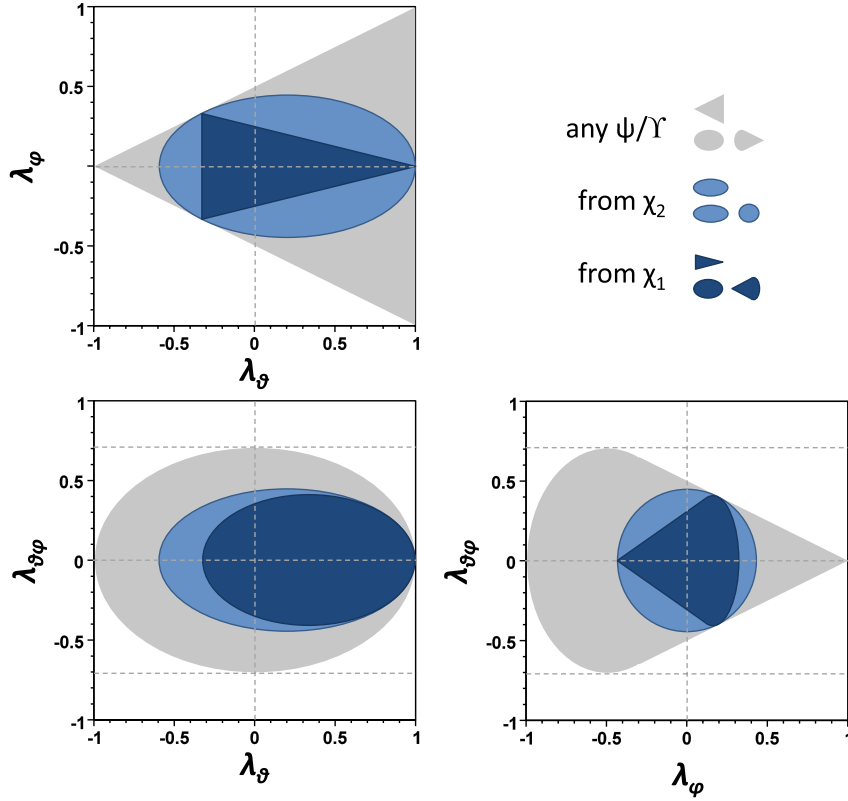


**Figure 2.7:** Allowed regions for the polarization parameters of the dilepton angular decay distribution of  $1^{--}$  (grey) and  $J^{++}$  quarkonia, with  $J = 1, 2$  (dark and light blue) respectively [71].

subprocesses considered in quarkonium production possibly have different kinematic dependencies, encoded in the respective SDCs (see Fig. 2.4), the relative importance of a given subprocess can change as a function of the kinematics of the produced quarkonium. Consequently, also the natural frame might exhibit a dependency on the quarkonium kinematics and this intrinsic kinematic dependence is a feature of the produced quarkonium state. In contrast, an external kinematic dependence can be introduced by the fact that the reference frame adopted in the measurement not necessarily coincides with the natural frame. This is not a feature of the production mechanism under study but a purely experimental effect.

Early polarization measurements from the Tevatron experiments, CDF and D0, were plagued by several shortcomings in the measurement process leading to the paradox situation that the measurements of the  $J/\psi$  polarization measured by the CDF experiment in Run I [24] and Run II [25] exhibited differences that could not be attributed to the small differences in the experimental setup. Also the stark difference in the measurements of the  $\Upsilon(1S)$  polarization by the CDF [72] and D0 [26] experiments could not be explained by the difference in rapidity coverage. Addi-

tionally a discrepancy between the experimental data and the predictions from, then state-of-the-art, LO NRQCD [27] was observed and dubbed the “polarization puzzle”.

The shortcomings of the measurements have been pointed out and addressed in a series of papers [28–32] and have since formed the basis of new polarization measurements. Most importantly, the authors advocate to make use of the full experimentally available information by simultaneously measuring all three or at least the polar and azimuthal polarization parameters. The above mentioned measurements have only determined  $\lambda_\vartheta$  in one reference frame which makes the model independent interpretation of the results almost impossible [29]. By providing results that give information about the polar and the azimuthal direction, a model independent interpretation is made possible. They also introduce frame-invariant parameters [31] that allow for a better control of systematic effects and characterize the shape of the angular distribution irrespectively of the specific reference frame chosen by the analyst. A commonly used frame-invariant parameter is

$$\tilde{\lambda} = \frac{\lambda_\vartheta + 3\lambda_\varphi}{1 - \lambda_\varphi}. \quad (2.6)$$

Measurements of these frame-invariant parameters also allow to identify the intrinsic kinematic dependence and to distinguish them from external dependencies introduced by the measurement.

### 2.3.2 Polarization of $\chi$ mesons

The measurement of the  $P$ -wave quarkonia, the  $\chi$  mesons, is in principle more challenging experimentally than the one of the  $S$ -wave quarkonia discussed above. The major challenge is the presence of the photon in the  $Q^{3P_J} \rightarrow Q^{3S_1}\gamma$  decay which is very difficult to reconstruct and measure reliably (see Sec. 3.3.3 for more details on how the photons of the radiative decay are reconstructed). Nevertheless measuring the  $P$ -wave polarization is a crucial experimental ingredient, since directly produced  $\chi$  mesons and directly produced  $\psi$  or  $\Upsilon$  mesons have different angular momentum and parity properties and are the results of different partonic subprocesses.

The direct way of measuring the  $\chi$  polarization is to measure the angular decay distribution of the  $Q^{3S_1}\gamma$  system in the  $Q^{3P_J}$  system. This would entail having to know the photon reconstruction efficiencies and kinematic properties very precisely in order to be able to reliably measure the polarization. However, it has been shown in Ref. [71] that the angular decay distribution of the  $Q^{3S_1} \rightarrow \mu\mu$  decay in the  $Q^{3S_1}$  rest frame approximates well the angular decay distribution of the  $Q^{3P_J} \rightarrow Q^{3S_1}\gamma$  decay in the  $Q^{3P_J}$  rest frame, for sufficiently high  $Q^{3P_J}$  momenta. The bias associated to this approximation is negligible for momentum ranges accessible at the CMS experiment. Hence, the measurement of the  $\chi$  polarization can be done in exactly the same manner as the one for the  $S$ -wave quarkonium states by measuring the angular decay distribution of the dimuon decay. The only difference is that the  $Q^{3S_1}$  states have to be identified as coming from a  $Q^{3P_J}$  decay by reconstructing the invariant mass of the  $Q^{3S_1}\gamma$  system.



The interpretation of the measured polarization parameters in terms of quantum mechanical eigenstates is less straightforward for the  $J^{++}$   $P$ -wave  $\chi$  states compared to the  $1^{--}$   $S$ -wave quarkonium states. In the latter case a fully longitudinal (transverse) polarization, with  $\lambda_\vartheta = -1$  ( $\lambda_\vartheta = +1$ ) corresponds to a pure  $J_z = 0$  ( $J_z = \pm 1$ ) eigenstate. On the contrary, a value of  $\lambda_\vartheta = +1$  corresponds to the  $J_z = 0$  state for the  $\chi_1$  and to  $J_z = \pm 2$  for the  $\chi_2$ , two very different quantum mechanical states [71]. The allowed regions for the polarization parameters can be calculated similarly to the ones for the  $S$ -wave quarkonia and are also shown as blue shapes in Fig. 2.7. The relations defining these regions for the  $\chi_1$  case are [71]

$$\begin{aligned} -\frac{1}{3} \leq \lambda_\vartheta \leq 1, \quad |\lambda_\varphi| \leq \frac{1 - \lambda_\vartheta}{4}, \quad \frac{9}{4} \left( \lambda_\vartheta - \frac{1}{3} \right)^2 + 6\lambda_{\vartheta\varphi}^2 \leq 1, \\ |\lambda_{\vartheta\varphi}| \leq \frac{\sqrt{3}}{2} \left( \lambda_\varphi + \frac{1}{3} \right), \quad (6\lambda_\varphi - 1)^2 + 6\lambda_{\vartheta\varphi}^2 \leq 1 \text{ for } \lambda_\varphi > \frac{1}{9} \end{aligned} \quad (2.7)$$

and for the  $\chi_2$  [71]

$$\frac{5}{16} \left( \lambda_\vartheta - \frac{1}{5} \right)^2 + \lambda_\varphi^2 + \lambda_{\vartheta\varphi}^2 \leq \frac{1}{5}. \quad (2.8)$$

This results in the following physically allowed ranges in one-dimensional projections:  $\lambda_\vartheta^{\chi_{c1}} \in [-\frac{1}{3}, 1]$ ,  $\lambda_\varphi^{\chi_{c1}} \in [-\frac{1}{3}, \frac{1}{3}]$ ,  $\lambda_\vartheta^{\chi_{c2}} \in [-\frac{3}{5}, 1]$  and  $\lambda_\varphi^{\chi_{c2}} \in [-\frac{1}{\sqrt{5}}, \frac{1}{\sqrt{5}}]$  which will be used in Chapter 5.

## 2.4 Current experimental status

Since the start of the LHC physics program a multitude of measurements of quarkonium cross sections and polarizations has been made available by all four LHC experiments, CMS, ATLAS, LHCb and ALICE that supplement earlier measurements by the Tevatron experiments CDF and D0:

- The prompt production cross sections of  $J/\psi$  and  $\psi(2S)$  have been measured by CMS [73–75], ATLAS [76–78], LHCb [79–84], ALICE [85–90], CDF [20, 91–93] and D0 [22, 94] at various collision energies and in different kinematic regions.
- Cross section measurements for the  $\Upsilon(nS)$ , where  $n = 1$  or  $n = 1, 2, 3$  have been reported by CMS [75, 95], ATLAS [77, 96], LHCb [82, 97–100], ALICE [88, 89], CDF [19, 101, 102] and D0 [103] at various collision energies and in different kinematic regions.
- Polarization measurements of the promptly produced  $J/\psi$  and  $\psi(2S)$  have been released by CMS [104], LHCb [105, 106], CDF [107, 108] and for the  $J/\psi$  only by ALICE [107, 108].
- The  $\Upsilon(nS)$  for  $n = 1, 2, 3$  polarizations have been measured by CMS [109], LHCb [110] and CDF [102, 111].

For each promptly produced  $S$ -wave quarkonium state at least one cross section and one polarization measurement exists in different kinematic  $p_T$  and rapidity windows as well as for different center-of-mass energies  $\sqrt{s}$  of the colliding (anti-)protons. The production cross sections are determined up to slightly above 100 GeV in  $p_T$  at central rapidity and up to 30 GeV in  $p_T$  at forward rapidity with some differences in reach for the different  $S$ -wave states. The polarization measurements are usually reported with slightly less coverage of the high  $p_T$  regions due to their statistically more demanding nature. All polarization measurements at mid-rapidity and high- $p_T$  consistently report small and constant values for the polarization parameters that are compatible with an (almost) unpolarized production of the  $S$ -wave states. Figure 2.8 shows the polarization parameters of the prompt  $J/\psi$  and  $\psi(2S)$  mesons measured by CMS [104] as a function of  $p_T$  in different rapidity bins. A subset of the available cross section measurements of different  $S$ -wave states as well as for the  $\chi_{c1}$  and  $\chi_{c2}$  is discussed in Sec. 2.5 and shown in Fig. 2.9.

The progress on  $P$ -wave state measurements at hadron colliders has been mainly focused on the measurement of relative cross sections of the  $J = 2$  states with respect to the  $J = 1$  states [39, 113–117] or measurements of feed-down contributions from the  $P$ -wave to the  $S$ -wave states [21, 118–121], although ATLAS has reported a prompt cross section measurement for the  $\chi_{c1}$  and  $\chi_{c2}$  individually as well [38]. Even though these measurements provide extremely useful information, necessary for the interpretation of the results for the feed-down affected  $S$ -wave states, no measurement of the  $P$ -wave polarization is available to date. This thesis presents the measurement of the relative  $\chi_{c2}(1P)$  and  $\chi_{c1}(1P)$  polarizations and, thus, also the first polarization measurement of any  $P$ -wave quarkonium state in hadron collisions. The  $\chi_c$  polarization is one of the last missing pieces to have a full picture of the charmonium system and constitutes a crucial test for the NRQCD factorization approach, as will be explained in Sec. 2.6.

## 2.5 Phenomenological interpretation of the experimental results

The experimental progress has been accompanied by similar efforts of the theoretical community, and NLO NRQCD calculations of SDCs are now available [59–61, 122]. These have been used in different fitting strategies to extract corresponding LDMEs [61, 112, 122–124] using mainly the measured cross sections as input and comparing the resulting predicted polarization with the measured data results as test of the theory. While these results are in general able to describe the cross section as a function of  $p_T$ , they predict significantly polarized quarkonium production, in contradiction with the measured data. However, as it was pointed out in Ref. [33], ignoring the polarization measurements completely in such fits does not only mean ignoring available information but can also lead to inconsistencies, since the acceptance corrections that need to be applied in cross section measurements strongly depend on

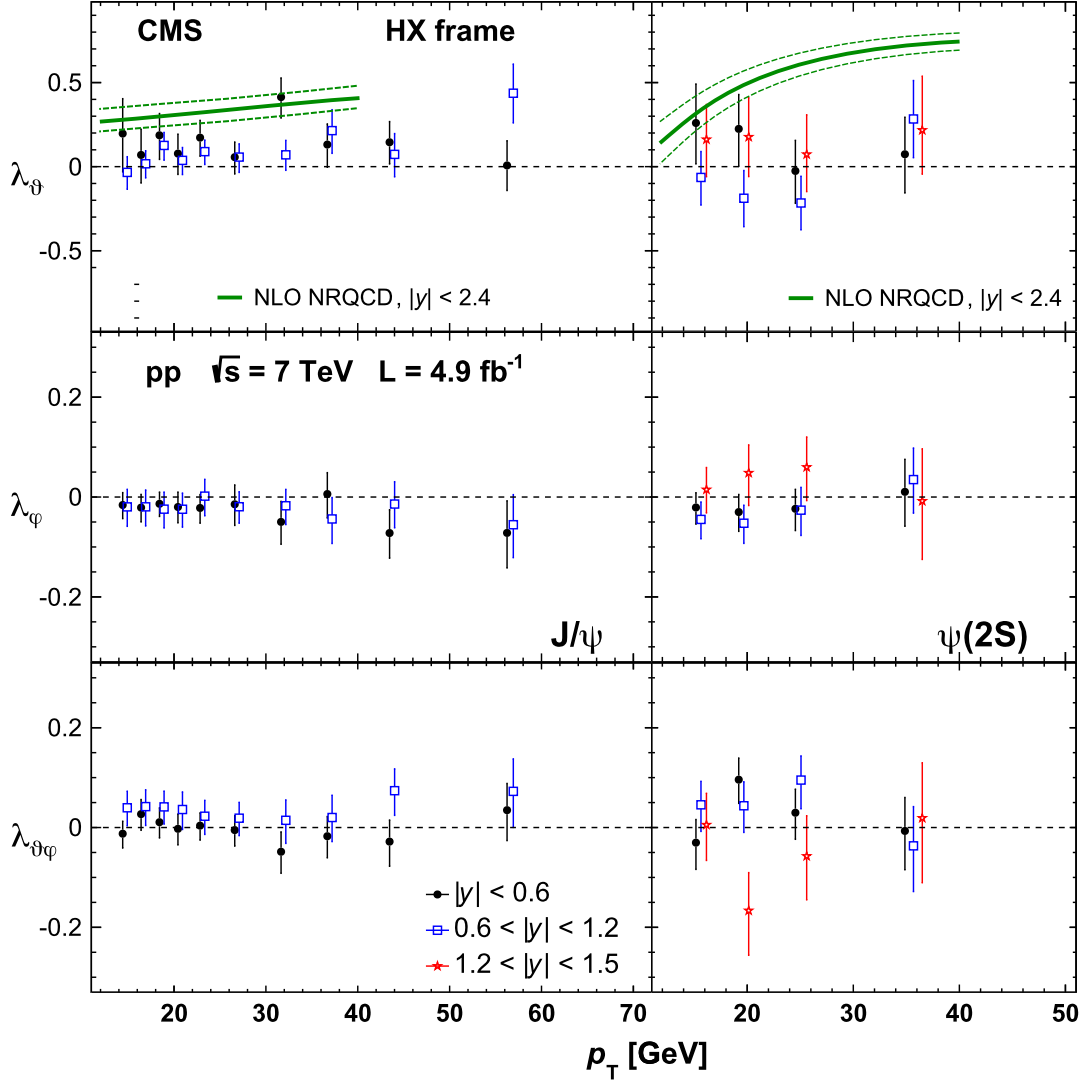


**Figure 2.8:** Polarization parameters  $\lambda_\theta$ ,  $\lambda_\phi$  and  $\lambda_{\theta\phi}$  in the HX frame for prompt  $J/\psi$  and  $\psi(2S)$  mesons as a function of  $p_T$  and  $|y|$  measured by the CMS collaboration at  $\sqrt{s} = 7$  TeV [104]. The green curves represent calculations of  $\lambda_\theta$  in NLO NRQCD [112]. Adapted from Ref. [104].

the assumed polarization of the measured quarkonium state. Most importantly, fits done in the past extended down to the lowest measured  $p_T$  values, while perturbative calculations of the SDCs have only limited validity at very low  $p_T$ .

The approach followed in Ref. [33], where data below a certain  $p_T$  threshold are excluded and cross section measurements are iteratively reweighted, taking into account the measured polarization, indeed shows that it is possible to derive LDMEs corresponding to NLO SDCs in such a way that cross section and polarization measurements can be described consistently for the  $\Upsilon(3S)$  and  $\psi(2S)$ . The approach not only solves the “quarkonium polarization puzzle”, seemingly arising in other

approaches due to not adequately addressing known limitations in the existing perturbative calculations, but can also be seen as a strong sign that the factorization of short- and long-distance effects underpinning NRQCD works.

The data-driven considerations presented in Sec. 3 of Ref. [33] have been extended to completely data-driven approaches considering more quarkonium states and measurements at different collision energies in Refs. [34, 36, 37]. These analyses reveal a surprisingly simple pattern. The cross sections of all promptly produced quarkonia seem to follow a universal pattern in the shapes as a function of  $p_T/M$ , the mass rescaled  $p_T$  distribution, where  $M$  is the mass of the corresponding quarkonium state. Figure 2.9 shows a comparison of different  $S$ - and  $P$ -wave quarkonium differential cross section measurements together with a fit using the data for which  $p_T/M > 2$  and imposing the same shape for all states only allowing for normalization differences between the different states. The shape is described by the functional form, first introduced by the HERA-B collaboration [125]

$$f(p_T/M) \propto \frac{p_T}{M} \left( 1 + \frac{1}{\beta - 2} \frac{(p_T/M)^2}{\gamma} \right)^{-\beta}, \quad (2.9)$$

where  $\gamma$  defines the shape in the low- $p_T$  region and  $\beta$  characterizes the high- $p_T$  region instead.

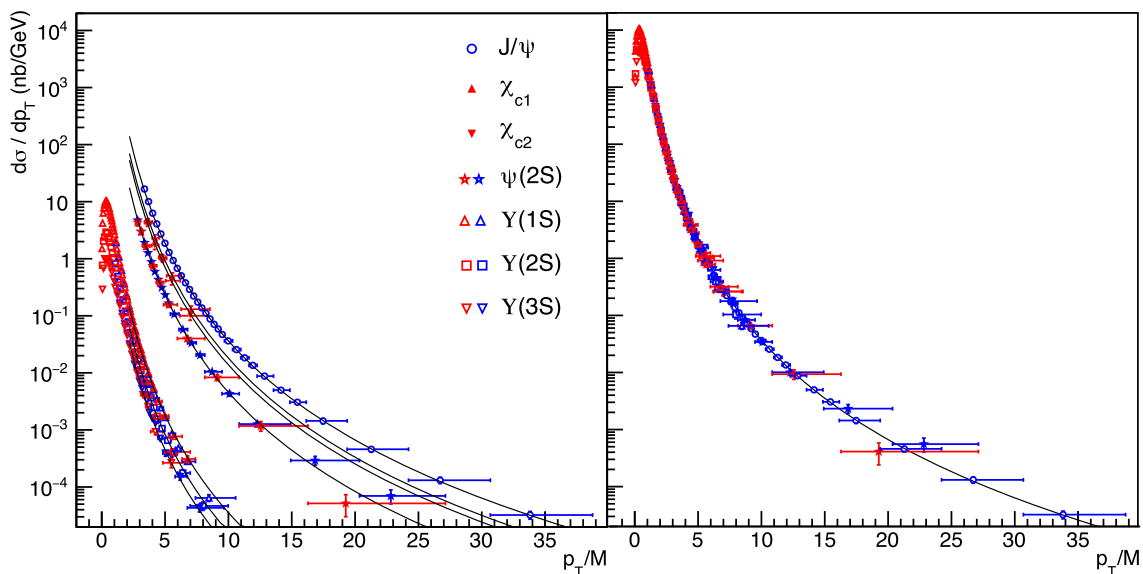


**Figure 2.9:** Prompt cross sections at mid-rapidity as a function of  $p_T/M$  for different quarkonium states measured in pp collisions at  $\sqrt{s} = 7$  TeV by ATLAS (red markers) [38, 77, 96] and CMS (blue markers) [73, 95]. The curves are determined by a simultaneous fit to all data (with  $p_T/M > 2$ ) with equal shape but normalizations specific for each state (left panel) or adjusted to the  $J/\psi$  points (right panel) [34].

The fact that the  $P$ -wave and the  $S$ -wave states exhibit very similar kinematic behaviours is a priori not expected within the NRQCD factorization approach, since their production proceeds through intermediate  $q\bar{q}$  states with different quantum numbers  $\{n\}$  with very different kinematic properties (see Fig. 2.4). Furthermore, different  $S$ -wave states are affected by different feed-down contributions. While the prompt  $\psi(2S)$  are always directly produced, the  $J/\psi$  and  $\Upsilon(nS)$  states receive significant feed-down contributions from  $\chi_c$  and  $\chi_b$  decays respectively. The fact that the intrinsic complexity of the NRQCD approach with its variegated mixture of sub-processes can still be made compatible with the simple patterns observed in data may not be seen as pure coincidence. The fine-tuning of the LDMEs, necessary to cancel unobserved differences between states may be an indication that the present formulation of NRQCD does not naturally reflect physical symmetries which exist at least in the mid-rapidity and high- $p_T$  limit, where the universal kinematic patterns become apparent [34, 37].

## 2.6 Prediction of the $\chi_{cJ}$ polarization

Different predictions for the  $\chi_{cJ}$  polarizations exist in the literature [35, 60, 126]. However, here the focus is put on the ones presented in Ref. [35], since it is the only one that rigorously takes into account the correlation between cross section and polarization measurements, whereas the other references ignore acceptance correlation effects when determining LDMEs.

The measured prompt polarizations of the  $S$ -wave states are all very similar, as shown in Fig. 2.10 for the  $J/\psi$ ,  $\psi(2S)$  and  $\Upsilon(1S)$ , even though they are affected by vastly different feed-down contributions,  $\simeq 25\%$  [38, 49],  $0\%$  and  $\simeq 40\%$  [120] respectively. Under the assumption that the directly produced  $S$ -wave mesons have very similar production mechanisms, indicated by the observed identical  $p_T/M$  shapes of the differential cross sections, the sum of the  $\chi_{c1}$  and  $\chi_{c2}$  feed-down contributions can only have a small influence on the prompt  $J/\psi$  polarization [35].

Taking into consideration the sensitivity to the assumed polarization hypothesis of the measured  $\chi_{c2}/\chi_{c1}$  cross section ratio it is possible to extract a prediction for the polarizations of the  $\chi_{c1}$  and  $\chi_{c2}$ . The cross section ratio and polarizations of the  $\chi_{c1,2}$  are functions of one common parameter in the NRQCD approach [35]

$$K_\chi = \frac{1}{m_c^2} \frac{\langle \mathcal{O}^{\chi_{c0}}({}^3P_0^{[1]}) \rangle}{\langle \mathcal{O}^{\chi_{c0}}({}^3S_1^{[8]}) \rangle}, \quad (2.10)$$

with  $\langle \mathcal{O}^{\chi_{c0}}(\{n\}) \rangle$  denoting the LDME corresponding to different intermediate states with quantum number  $\{n\}$  and  $\chi_{c0}$  as final state. The parameter  $K_\chi$  enters the  $\chi$  production cross section  $\sigma_J$  and the spin-density matrix elements  $\sigma_J^{ij}$  via [35]

$$\sigma_J^{(ij)} \propto (2J+1) \left[ \mathcal{S}^{(ij)}({}^3S_1^{[8]}) + K_\chi m_c^2 \mathcal{S}^{(ij)}({}^3P_J^{[1]}) \right], \quad (2.11)$$

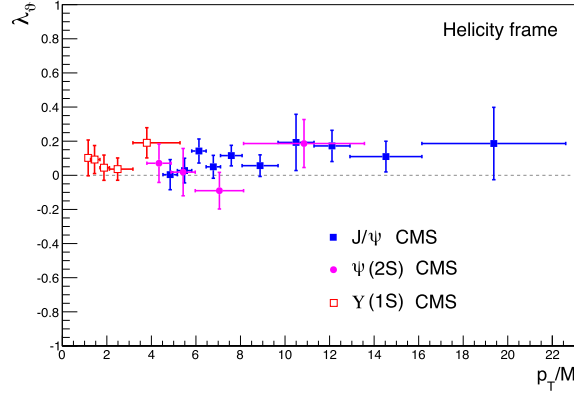


**Figure 2.10:** Polar anisotropy parameter  $\lambda_\vartheta$  in the HX frame measured by CMS in pp collisions at  $\sqrt{s} = 7$  TeV for prompt  $J/\psi$ ,  $\psi(2S)$  [104] and  $\Upsilon(1S)$  [109]. Values corresponding to different rapidity ranges have been averaged assuming uncorrelated systematic uncertainties [34].

where  $\mathcal{S}^{(ij)}$  denotes the SDC or its spin projection corresponding to a quantum state  $\{n\}$ . The polarization parameter  $\lambda_\vartheta$  can be calculated from the spin projections as [35]

$$\lambda_\vartheta^{\chi_{c1}} = \frac{\sigma_1^{00} - \sigma_1^{11}}{\sigma_1^{00} + 3\sigma_1^{11}} \quad \text{and} \quad \lambda_\vartheta^{\chi_{c2}} = \frac{-3\sigma_2^{00} - 3\sigma_2^{11} + 6\sigma_2^{22}}{5\sigma_2^{00} + 9\sigma_2^{11} + 6\sigma_2^{22}}. \quad (2.12)$$

The parameter  $K_\chi$  can be determined from the measured  $\chi_{c2}/\chi_{c1}$  ratios by ATLAS [38] and CMS [39] by calculating the polarizations of the  $\chi_{c1}$  and  $\chi_{c2}$  corresponding to the value of  $K_\chi$  using NLO SDCs. This polarization hypothesis can then be used to correct the measured ratio with the appropriate acceptance corrections, corresponding to the polarization hypothesis. The corrected measured ratio is then used to calculate a  $\chi^2$  value with respect to the predicted ratio corresponding to the  $K_\chi$  value. Recording the  $\chi^2$  value for different  $K_\chi$  values allows to determine the central value and its uncertainty, which can in turn be used to predict  $\lambda_\vartheta$  for the  $\chi_{c1}$  and  $\chi_{c2}$  [35] in an iterative procedure. The results of the fit are shown in Fig. 2.11 (top), where the  $\chi_{c2}/\chi_{c1}$  ratios reported by ATLAS and CMS are shown together with the corresponding theory fit in grey bands. While the theory fit and the measured data points agree reasonably, but not very satisfactorily if unpolarized acceptance corrections are used, a considerable improvement is achieved by using the matching NRQCD polarization conjecture.

The predictions for the polarizations of the  $\chi_{c1}$  and  $\chi_{c2}$  corresponding to the results of the fit, using inputs from NRQCD in the form of NLO SDCs, are shown in Fig. 2.11 (bottom). Interestingly, the predicted polarizations defy the universal and (almost) unpolarized patterns observed up until now in polarization measurements of the  $S$ -wave states. With decreasing  $p_T/M$ ,  $\lambda_\vartheta$  tends to the extreme physically allowed values  $\lambda_\vartheta^{\chi_{c1}} \rightarrow +1$  and  $\lambda_\vartheta^{\chi_{c2}} \rightarrow -\frac{3}{5}$ . Even though these limits correspond to very different decay angular distributions, the corresponding angular momentum configuration is the pure  $J_z = 0$  for both states.

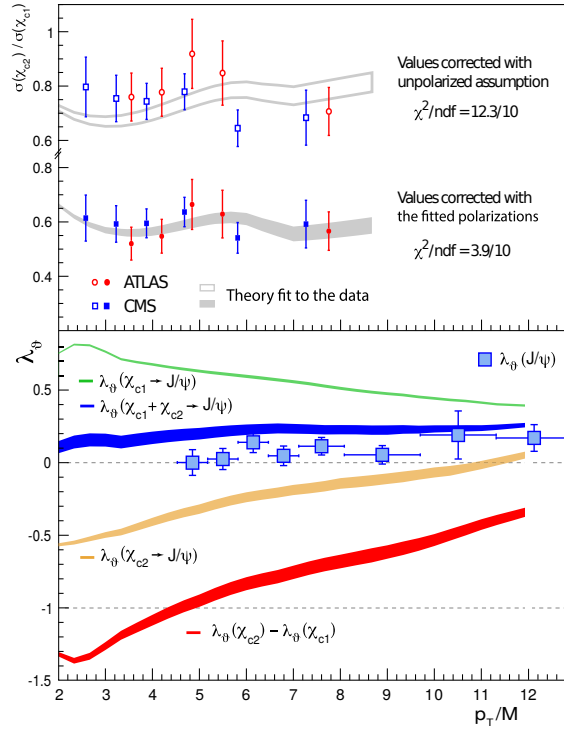


**Figure 2.11:** (Top)  $\chi_{c2}/\chi_{c1}$  cross section ratio measured by ATLAS [38] and CMS [39] with acceptance corrections corresponding to unpolarized production (open markers) and “best-fit polarizations” (filled markers) and accompanying theory fit (grey bands). (Bottom) Predicted  $\chi_{c1}$  (green band) and  $\chi_{c2}$  (yellow band)  $\lambda_\vartheta$  polarization parameter in the HX frame as a function of  $p_T/M$  as well as the predicted  $\chi_{c2} - \chi_{c1}$  difference (red band) and the  $J/\psi$  polarization from the weighted feed-down contributions (blue band) in comparison with the prompt  $J/\psi$  polarization measurement by CMS [104]. The bands reflect the uncertainties of  $K_\chi$  [35].

## 2.7 Summary - Novelty of this thesis

The experimental situation of the  $P$ -wave states is somewhat lagging behind the one of the  $S$ -wave states. While in the latter case an almost complete experimental picture is available nowadays, the former case is still lacking some key measurements. This is of course also rooted in the fact that measurements of the  $P$ -wave states are in general more difficult because they pose several challenges. The states belonging to one  $P$ -wave triplet are much closer to each other in the invariant mass spectrum, requiring excellent energy resolution for all the decay products to be able to disambiguate between the  $J = 0, 1, 2$  states. Furthermore, the most prominent decay, the radiative transition into lower energy  $S$ -wave states, requires the accurate reconstruction of the photon, a very challenging task in the messy collision events of hadron colliders.

One of the still missing key measurements is the polarization of promptly produced  $P$ -wave states in hadron collisions.

Even though the NRQCD approach has received a lot of attention from the theoretical community and recent years have brought forward a multitude of measurements of quarkonium cross sections and polarizations, a confirmation of the factorization of short- and long-distance effects at the basis of the approach is still lacking. Recent phenomenological analyses [33–37] have revealed surprisingly simple patterns in the measurements. These findings are in striking contrast to the complex structure of NRQCD, where different subprocesses with different kinematic dependencies contribute to quarkonium production. Only a fortuitous cancellation of different effects in the NRQCD framework would lead to such simple observable patterns. Nevertheless, calculations performed in the NRQCD framework are able to reproduce the measurements very well. Moreover, they come with a precise prediction [35] that can be viewed as one of the most important benchmark for the theory today: the  $\chi_{c1}$  and  $\chi_{c2}$  have strong and opposite polarizations. Particularly, the difference between the  $\chi_{c2}$  and  $\chi_{c1}$  polarization, expressed through  $\Delta\lambda_\vartheta = \lambda_\vartheta^{\chi_{c2}} - \lambda_\vartheta^{\chi_{c1}}$ , is predicted to exceed  $-1$  if the  $p_T$  of the decay  $J/\psi$  is below 15 GeV.

This thesis presents the first measurement of  $P$ -wave quarkonium polarization in hadron collisions in the form of the relative prompt  $\chi_{c2} - \chi_{c1}$  polarization.



# Experimental Setup

The test of all knowledge is experiment. Experiment is the sole judge of scientific truth.

---

(Richard Feynman, *They Feynman Lectures on Physics*)

The *European Organization for Nuclear Research* ([CERN](#), French: *Organisation européenne pour la recherche nucléaire*)<sup>i</sup>, located at the Swiss-French border in Geneva operates the world's largest particle physics laboratory. It was established in 1954 and currently has 23 member states and seven associate member states. Additionally, five states and international organizations have observer status [127]. CERN houses various particle accelerators and decelerators (see Fig. 3.1) which provide a number of experiments with the necessary particles at their desired energy levels. CERN has played a major role in several seminal discoveries of SM particles, for example the discovery of the  $W^\pm$  and  $Z^0$  bosons in 1983 [128–131] and the last missing predicted particle, the Higgs boson, in 2012 [4, 5], and also is the birth place of the World Wide Web (www) [132]. The currently most powerful and largest particle accelerator, the [Large Hadron Collider \(LHC\)](#), is also located at CERN and will be described in a bit more detail below. The [CMS](#) experiment at the LHC will also be briefly introduced with an emphasis on the most important components for this thesis. More detailed and extensive descriptions of the LHC and CMS can be found in Refs. [133] and [134–136] respectively.

## 3.1 Large Hadron Collider

The LHC is a superconducting hadron accelerator and collider with a nominal design center-of-mass energy  $\sqrt{s} = 14$  TeV for proton-proton (pp) collisions. Installed in the 26.7 km circumference tunnel, which previously housed the [Large Electron-Positron Collider \(LEP\)](#), the most powerful lepton accelerator to date that was in operation until 2000 and subsequently dismantled, the LHC tunnel is situated between 45 and 170 m below ground. Apart from protons the LHC is also designed to be able to

---

<sup>i</sup>The abbreviation is derived from the name of the council mandated with the foundation of the organization, *Conseil européen pour la recherche nucléaire*.

accelerate lead ions. Even xenon-xenon collisions have been achieved in 2017 [137]. Nevertheless, the focus here will be on pp collisions recorded during the 2012 data taking period, as part of the so called *LHC Run I*, and to a lesser extent on *LHC Run II* starting in 2015 and ending in 2018.

The LHC is the last element in a chain of machines sequentially increasing the energy of the accelerated nucleons shown in Fig. 3.1. Protons are accelerated in so called *bunches* containing in the order of  $N_b \sim 1.15 \cdot 10^{11}$  protons each. After obtaining protons by stripping electrons off of hydrogen atoms and accelerating them up to 50 MeV in the **LINear ACcelerator 2 (LINAC2)** and subsequently up to 1.4 GeV in the **Proton Synchrotron Booster (PSB)**, these bunches are formed in the **Proton Synchrotron (PS)**. Here they are accelerated up to 25 GeV before they are transferred to the **Super Proton Synchrotron (SPS)** where the acceleration up to 450 GeV takes place before the protons are fed into and accumulated in the LHC ring in two counter-circulating beams until the design value of  $n_b = 2808$  bunches per beam is reached. After fully filling the LHC the bunches are accelerated up to the desired collision energy. The full process of filling the LHC and accelerating the protons to the design energy of 7 TeV takes about 36 minutes under ideal conditions. The beams can be kept in “collision mode” for several hours until the beam intensity becomes too low and a new fill is started [133].

The beam lines in which the bunches travel are arranged such that there are four main collision points along the LHC ring. Around these collision points the main experiments at the LHC are built:

- **A Large Ion Collider Experiment (ALICE)** [138]

The ALICE experiment is mainly designed to study the physics of strongly interacting matter and the emergence of the quark-gluon plasma at extreme energy densities and temperatures in heavy-ion collisions. It is designed to cope with the extremely high multiplicity of charged particle tracks occurring in heavy-ion collisions, but cannot operate at the same instantaneous luminosity conditions as ATLAS and CMS during pp collisions.

- **A Toroidal LHC AparatuS (ATLAS)** [139]

With a 25 m diameter and 44 m of length the ATLAS detector is the largest of the four LHC experiments. It is a general purpose detector, similar to CMS, addressing wide range of physics questions. Both experiments complement each other and serve as independent experiments to confirm possible discoveries of each other.

- **Compact Muon Solenoid (CMS)** [136]

CMS is another general purpose experiment with a slightly different design philosophy than ATLAS, which will be described in more detail in Sec. 3.2.

- **Large Hadron Collider beauty (LHCb)** [140]

LHCb is a specialized b-physics experiment designed to measure primarily the interactions of b-hadrons and parameters of CP violation. It also provides measurements of quarkonium cross sections and polarizations at forward rapidity.

In between the experimental caverns radio frequency cavities for acceleration and energy loss compensation, beam cleaning facilities and the beam dump are located. The particles are kept on their circular track using superconducting dipole magnets and the beams are focused using quadrupole magnets.

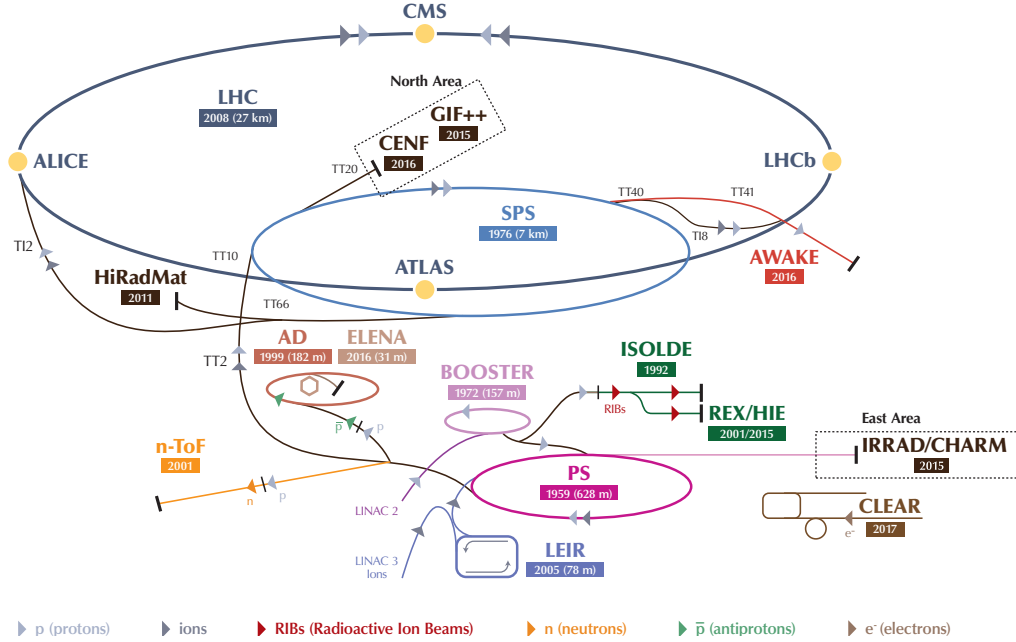


**Figure 3.1:** Overview of the CERN accelerator complex. The PSB is labeled *BOOSTER* in this illustration. Adapted from Ref. [141].

The expected average number of events per second with a given cross section  $\sigma$  occurring at a particle accelerator can be calculated as

$$N = L \cdot \sigma, \quad (3.1)$$

where  $L$  is the instantaneous luminosity, one of the most important parameters describing a particle accelerator. It is defined as

$$L = \frac{N_b^2 n_b \nu_r \gamma}{4\pi \epsilon_n \beta^*} F, \quad (3.2)$$

where  $\nu_r$  is the revolution frequency,  $\gamma$  the relativistic gamma factor,  $\epsilon_n$  the normalized transverse beam emittance,  $\beta^*$  the beta function at the collision point and  $F$  the geometric luminosity reduction factor accounting for the reduction of the effective beam size due to the beam crossing angle at the interaction point [133]. The LHC was designed to reach values of  $L = 10^{34} \text{ cm}^{-2} \text{ s}^{-1}$ , but has exceeded this design goal by more than a factor of two by the end of 2018 [142, 143] as can be seen in Fig. 3.2. The total amount of data delivered by the LHC or collected by the LHC experiments is denoted by the so called integrated luminosity, defined as

$$\mathcal{L}_{\text{int}} = \int L(t) dt. \quad (3.3)$$

It is usually given in units of  $\text{fb}^{-1}$  ( $= 10^{15} \text{b}^{-1}$ )<sup>ii</sup> or  $\text{pb}^{-1}$  ( $= 10^{12} \text{b}^{-1}$ ). It relates the average number of occurrences of a process with a given cross section to the amount of collected data. For example, in a dataset of size  $1 \text{fb}^{-1}$  on average one event of a process with a cross section of  $1 \text{fb}$  will be found. From the start of Run I in 2011 to the end of Run II in 2018 the LHC has delivered  $192.3 \text{fb}^{-1}$  to CMS of which  $177.7 \text{fb}^{-1}$  have been recorded [143] as shown in Fig. 3.3 (left).

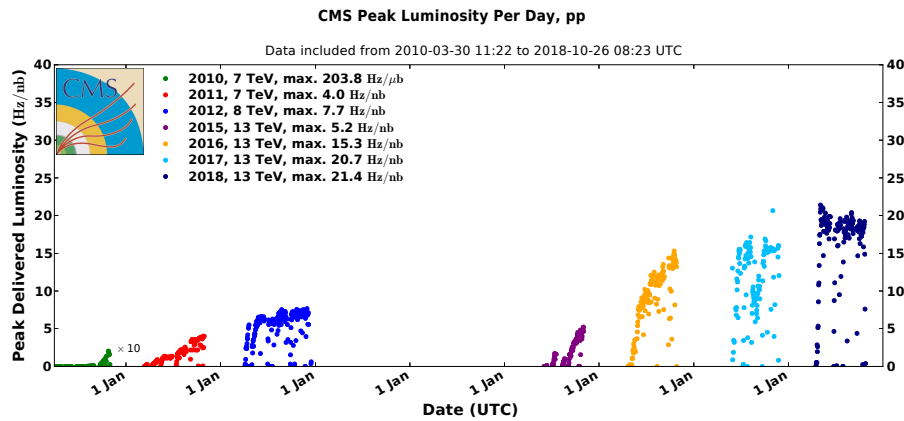


**Figure 3.2:** Peak instantaneous luminosity ( $10^{34} \text{cm}^{-2} \text{s}^{-1} = 10 \text{Hz nb}^{-1}$ ) in pp collisions vs time for Run I (2010–2012) and Run II (2015–2018) [143].

At every bunch crossing the probability that more than one pp collision occurs at CMS is non-negligible. This phenomenon is labeled **pile-up** (PU) and in 2012 the average number of interaction per bunch crossing at CMS was around 21 [143]. The PU increases with increasing center-of-mass energy and instantaneous luminosity. The PU distribution for different data taking periods is shown in Fig. 3.3 (right), where the increased PU is clearly visible for the later data taking periods.

## 3.2 Compact Muon Solenoid

Located in Cessy, France, the **Compact Muon Solenoid** (CMS) experiment is a general purpose particle detector designed to cover a wide range of physics topics. With a length of 21.6 m, a diameter of 14.6 m and a mass of 12500 t [136]. The overall layout of the CMS detector is shown in Fig. 3.4. It follows the typical onion like structure of modern particle physics experiments at particle colliders where different layers are designed to measure the energy and momentum of particles exploiting specific properties. The central feature is the eponymous solenoid providing a 3.8 T magnetic field. Enclosed therein are the silicon pixel and strip trackers, the **Electromagnetic Calorimeter** (ECAL) and the **Hadron Calorimeter** (HCAL). Outside the solenoid the

<sup>ii</sup>*barn* is a unit to measure cross sections widely used in particle and nuclear physics and is defined as  $1 \text{b} = 10^{-24} \text{cm}^{-2}$ .

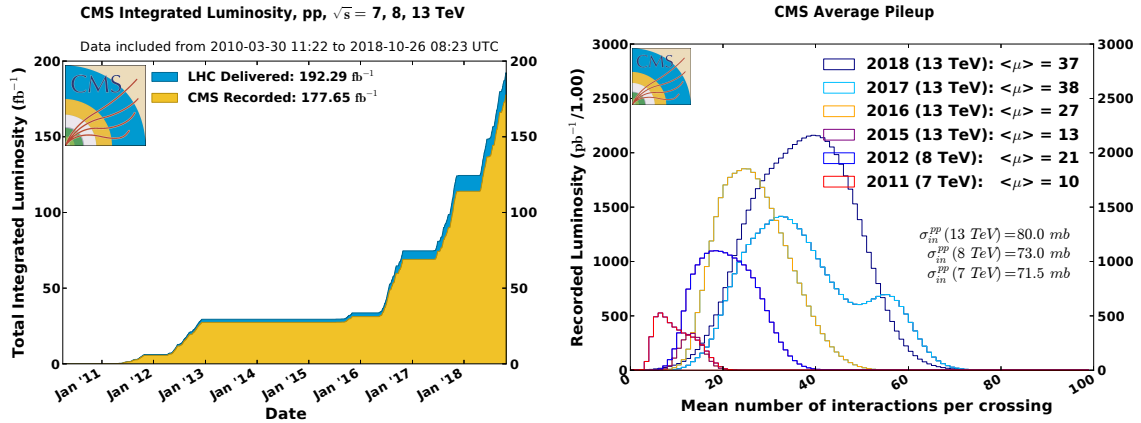


**Figure 3.3:** Cumulative luminosity delivered by the LHC and recorded by CMS in pp collisions vs. time (left) and distribution of pile-up for different data taking periods (right) in Run I (2010–2012) and Run II (2015–2018) [143].

muon detection system is integrated into the steel return yoke for the magnetic field, which accounts for more than 95 % of the total weight of CMS.

The silicon trackers accurately measure the positions and momenta of charged particles while the energies of all particles are determined by the calorimeters. Electrons and photons deposit their energy in the ECAL, whereas hadrons are contained within the HCAL. Muons are the only particles able to penetrate the solenoid and to reach the muon chambers of the muon system where they are detected. In this way different particles can be identified by the signature they leave in the CMS detector, as illustrated in Fig. 3.5.

Before discussing the different subsystems of the CMS detector in more details some conventions and the adopted coordinate system need to be defined. The origin of the coordinate system is defined to be in the nominal **interaction point (IP)** of CMS and the  $x$ -axis of the right handed coordinate system points towards the center of the LHC ring, the  $y$ -axis vertically upwards and the  $z$ -axis along the direction of the beam running counterclockwise. The polar angle  $\theta$  is measured from the  $z$ -axis and the azimuthal angle  $\phi$  is measured from the  $x$ -axis in the  $x$ - $y$ -plane [134]. Commonly, the pseudorapidity, defined as

$$\eta = -\ln\left(\tan\frac{\theta}{2}\right), \quad (3.4)$$

is used instead of the polar angle. For highly energetic particles with  $E \gg m$  it is a good approximation of the Lorentz-invariant rapidity [45]

$$y = \frac{1}{2} \ln \frac{E + p_z}{E - p_z} = \ln \frac{\sqrt{m^2 + p_T^2} \cosh^2 \eta + p_T \sinh \eta}{\sqrt{m^2 + p_T^2}}, \quad (3.5)$$

where  $p_T$  is the so called transverse momentum, the momentum in the plane transverse to the beam-axis and  $p_z$  is the part of the momentum along it.

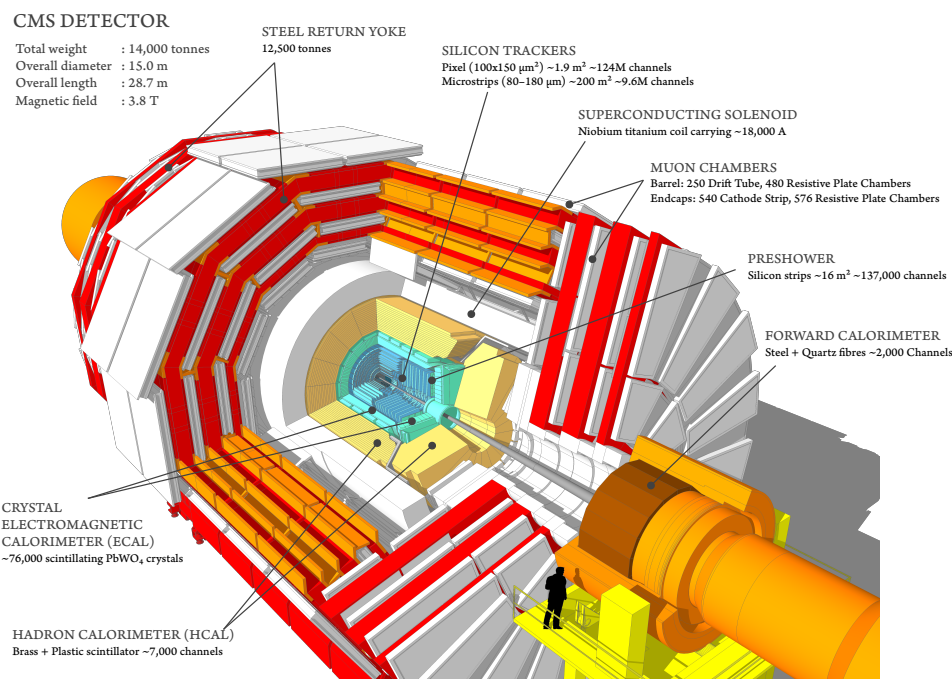


**Figure 3.4:** Layout of the CMS experiment after the upgrade of the pixel detector at the end of 2016 (see text). The inner tracker is surrounded by the ECAL and HCAL as well as the solenoid. The outermost parts are the muon chambers interleaved with the steel return yokes [144, 145].

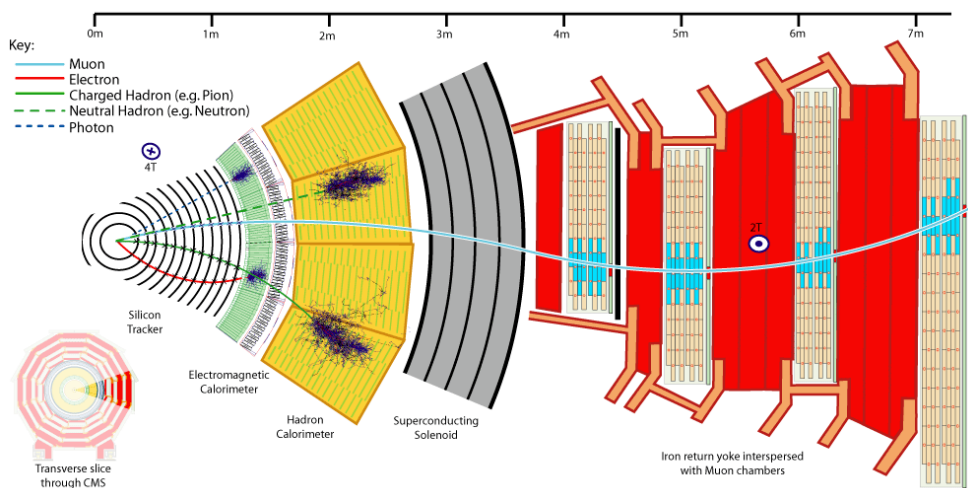


**Figure 3.5:** Illustration of particle identification in CMS in a slice of the transverse view of the detector [146].

The collision point of two partons is denoted as the **primary vertex (PV)** and is inside the **beam spot (BS)**, the region approximating the overlap region of the two proton bunches. Long-lived particles, like e.g. b-hadrons produced in the PV travel a certain distance before decaying and it is possible to extract information about a **secondary vertex (SV)**.

### 3.2.1 Inner tracking system

The innermost part of the CMS detector is the inner tracking system consisting of silicon pixel and silicon strip sensors. Using position sensitive sensors it is designed to provide efficient and accurate measurements of charged particle trajectories which allows the precise reconstruction of charged particle momenta and vertices, both PVs and SVs. The tracking system covers a pseudorapidity range  $|\eta| \leq 2.5$  and is split into two parts, the pixel tracker and the strip tracker. The layout of the inner tracking system is shown in Fig. 3.6.

The tracking system has to cope with the challenging conditions posed by the LHC. At the instantaneous design luminosity in each bunch crossing an average of 1000 charged particles hit the tracker. This requires fast response times and high granularity. Additionally the tracker has to be radiation hard to withstand the severe radiation caused by the intense particle flux. Finally, it should have minimal material budget in order to limit processes that could bias the trajectory reconstruction like multiple scattering, nuclear interactions, bremsstrahlung or photon conversions. To meet all these requirements the tracker is entirely silicon based [136].

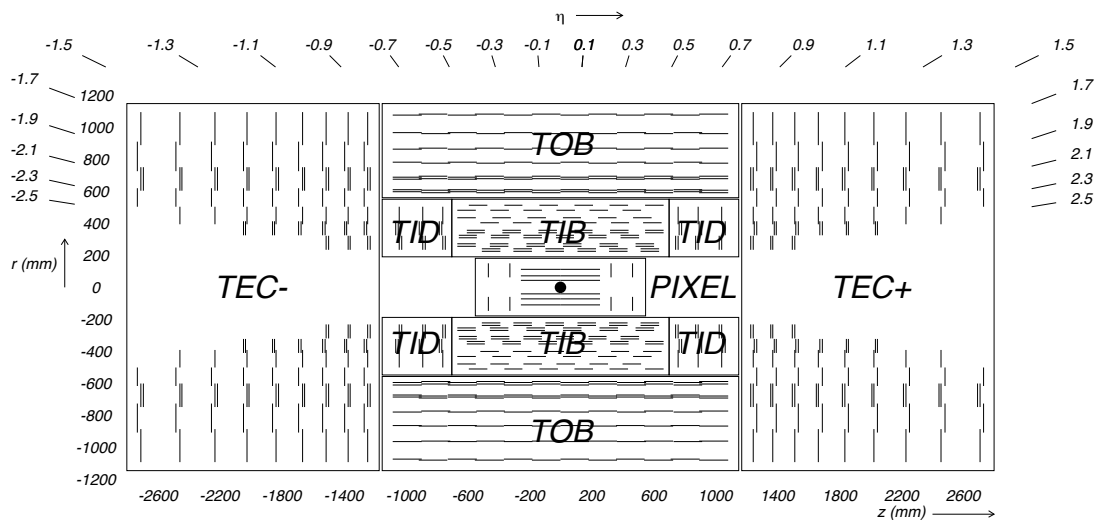


**Figure 3.6:** Schematic layout of the inner tracking system before the Phase I upgrade of the pixel detector. Each line represents a detector module and double lines indicate back-to-back modules [136].

## Pixel tracker

The CMS pixel detector, providing two-dimensional position measurements, is the innermost subsystem installed closest to the beam pipe. It is composed of the barrel pixel detector (BPix) and the endcap pixel detector (FPix). During the data taking period relevant for this thesis the former comprises three layers of pixel detector modules with sensor cells of  $100 \times 150 \mu\text{m}^2$ , placed at approximate radii of 4.4, 7.3 and 10.2 cm. Each layer is approximately 54 cm long. The BPix is complemented by the four disks of the FPix that are located at  $z = \pm 34.5$  and  $\pm 46.5$  cm. This arrangement of pixel modules ensures that at least three pixel layers are hit almost everywhere in the covered pseudorapidity region up to  $|\eta| = 2.5$  [136]. The geometric layout can be seen in Figs. 3.6 and 3.7. In total the pixel tracker had 66 million pixels and covers about  $1 \text{ m}^2$  of area, before it was upgraded.

The pixel detector of CMS was designed to efficiently record with high precision under the conditions corresponding to the nominal design values of the LHC. However, due to the excellent performance of the LHC, the instantaneous luminosity design goal was exceeded by a factor of two and consequently the number of PU events per bunch crossing was exceeding the design value of 25. To still be able to perform equally well or even better in these operating conditions the so called Phase I upgrade of the pixel detector was performed between the end of the 2016 and the start of the 2017 data taking period.

The complete original pixel detector was replaced by a new one, featuring four barrel layers and three endcap disks and newly designed readout chips, in just a few months. This remarkably quick replacement was only possible due to the modular design of the CMS detector. The newly installed pixel detector is characterized by higher tracking efficiencies, lower rates of misidentifying tracks and lower data loss. It is foreseen to withstand the increased luminosity conditions of the LHC until 2023 [147]. The layout of the upgraded pixel detector in comparison with the original one is shown in Fig. 3.7. The number of pixels is increased to 124 million and the covered active area doubles to about  $2 \text{ m}^2$ .

## Strip tracker

The silicon strip tracker is built from silicon strip modules and constitutes the outer layers of the tracking system. Similar to the pixel tracker it consists of modules arranged in layers in the barrel and disks in the endcap regions. The barrel part is further split into the **Tracker Inner Barrel (TIB)**, close to the pixel detector, and the **Tracker Outer Barrel (TOB)**, as can be seen in Fig. 3.6. In total 10 layers are arranged in the barrel extending up to a radius of 1.1 m. The endcap region is similarly separated into the **Tracker Inner Disk (TID)**, consisting of three disks, and the **Tracker Endcap (TEC)** consisting of nine disks. In the inner regions of the tracker the expected particle flux allows typical module sizes of  $10 \text{ cm} \times 80 \mu\text{m}$ . At larger radii,  $r > 55 \text{ cm}$ , the even further decreased flux allows the installation of modules



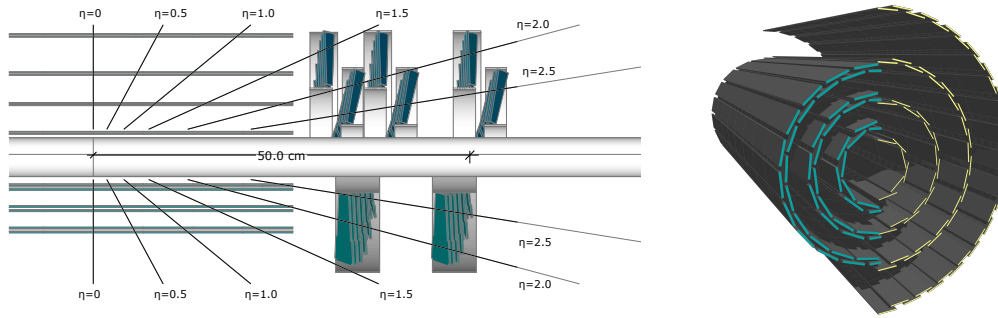


**Figure 3.7:** Conceptual layout comparing the disks and layers of the original and the upgraded pixel detectors. In the  $y$ - $z$  view (left) the upper half and in the  $x$ - $y$  view (right) the right half corresponds to the upgraded layout of the pixel detector [147].

with typical strip sizes of  $25\text{ cm} \times 180\text{ }\mu\text{m}$ . In total the area of the strip tracker has 9.3 million strip modules and covers an area of  $198\text{ m}^2$  [136].

Some of the layers also feature so called double sided strip sensors, where two strip sensors are added to each other back-to-back tilted by a small angle. This allows to also measure the  $z$ -coordinate in the barrel and the  $r$ -coordinate in the disk respectively. These layers are indicated by double lines in Fig. 3.6.

### 3.2.2 Electromagnetic Calorimeter

The CMS **Electromagnetic Calorimeter (ECAL)** is a hermetic homogenous calorimeter consisting of 75848 lead tungstate ( $\text{PbWO}_4$ ) crystals, of which 61200 are mounted in the barrel part and the remaining ones in the two endcaps [136]. It is placed between the inner tracking system and the HCAL. The main task of the ECAL is the energy reconstruction of photons and electrons. The extremely dense but optically clear lead tungstate crystals scintillate when electrons and photons pass through. High-energy photons and electrons produce a cascade of lower energy photons and electrons, a so called “electromagnetic shower”, mainly via pair production by photons or bremsstrahlung by electrons. This process continues until either the energy of the photons drops below the threshold for pair production or ionization processes start to dominate. The atoms of the lead tungstate crystals are ionized by the charged particles in the electromagnetic shower and the subsequent de-excitation of the atoms yields scintillation light that is collected and converted into an electric signal in photodiodes.

The shape and size of an electromagnetic shower are characterized by the *radiation length*  $X_0$  and the related *Molière radius*  $r_M$ . The radiation length is a material specific characteristic that gives the mean distance over which an electron loses all but  $1/e$ , where  $e$  is Euler’s number, of its initial energy by bremsstrahlung or  $7/9$  of the mean free path for pair production of a high energy photon [45]. The Molière

radius describes the transverse evolution of an electromagnetic shower. On average 95 % of the total energy of the initial particle are contained within a cylinder of radius  $2r_M$ . PbOW<sub>4</sub> has a radiation length of 0.89 cm and a Molière radius of 2.2 cm [134].

The crystals used in the barrel region (EB) are 23 cm, corresponding to 25.8 times  $X_0$ , in length and have a front facing area of  $22 \times 22 \text{ mm}^2$ . The EB covers the pseudorapidity range  $|y| < 1.479$ . The two endcap disks of the ECAL (EE) consist of crystals that are 22 cm, 24.9 times  $X_0$ , long and that have a front face of  $28.6 \times 22 \text{ mm}^2$ . They cover the region up to  $|\eta| < 3$ . In order to be able to better distinguish between highly energetic single photons and pairs of close electron pairs two preshower detectors, covering the pseudorapidity range  $1.653 < |\eta| < 2.6$  are installed. They consist of two lead disks interleaved with silicon strip detectors.

The energy resolution  $\sigma_E$  of the EB for electrons has been measured in beam tests [148] to be

$$\frac{\sigma_E}{E} = \frac{2.8\%}{\sqrt{E(\text{GeV})}} \oplus \frac{12\%}{E(\text{GeV})} \oplus 0.3\%. \quad (3.6)$$

Here the three contributions correspond to a stochastic, noise and constant term respectively. The energy resolution for photons varies between 1 % and 2.5 % in the EB and between 2.5 % and 4 % in the EE, depending on whether they convert before reaching the ECAL [149]. For electrons an energy resolution between below 2 %, for well measured electrons in the EB, and up to 5 %, for electrons in the EE is achieved [150].

### 3.2.3 Hadron Calorimeter

The **Hadron Calorimeter (HCAL)** is installed between the ECAL and the solenoid of CMS. Consisting of several absorbing brass layers interleaved with plastic scintillator layers it is a sampling calorimeter providing energy measurements of hadrons like protons, neutrons, pions or kaons. Brass has been chosen as absorber material for most of the HCAL due to the short nuclear interaction length of 16.8 cm [136]. This complete containment is important for measurements of very weakly interacting particles that have the experimental signature of an energy imbalance, so called *missing energy*.

The hadron calorimeter endcap covers the range  $1.3 < |\eta| < 3$  and roughly 34 % of all particles are produced in this pseudorapidity range. The very forward region  $3 < |\eta| < 5$  is instrumented with the hadronic forward calorimeters, installed 11.2 m away from the interaction point. It provides measurements of energetic forward jets, which are an experimental signature for various interesting final state topologies [136].

### 3.2.4 Superconducting magnet

The eponymous superconducting solenoid is the central feature of the CMS detector. It provides a nearly homogenous magnetic field of 3.8 T which is necessary to reconstruct the charges and the momenta of charged particles from 1 GeV up to roughly

1 TeV. Made from a high purity aluminum stabilized Niobium-Titanium conductor the CMS solenoid has a 6.3 m bore, is 12.5 m long and weighs 220 t. At full current 2.6 GJ of energy are stored in the magnet. The field lines are closed by the steel return yoke, weighing 10000 t, which is interleaved with the muon detectors [136].

### 3.2.5 Muon system

Efficient and accurate muon reconstruction is crucial for CMS as many experimental signatures, including those used in studies of quarkonium physics, involve muons in their final state. The muon system serves three basic purposes; identifying muons, improving the measurement of muon momenta and triggering the readout of interesting events. Given the large material budget that particles coming from the interaction region have to pass through before they reach the muon stations, all particles but the weakly interacting muons and neutrinos are assumed to be stopped in the calorimeters or the solenoid. Hence, only the charged muons will leave a trace in the muon detectors.

Similar to the other subdetectors the muon system is divided into a cylindrical barrel region and two endcap disks. A quarter of the geometrical layout is shown in Fig. 3.8. The total active area covered by the muon system is around 25000 m<sup>2</sup>. Due to this large area that has to be covered also the financial costs of the detectors had to be considered when choosing the detector technology. Thus, the muon system consists of reliable and robust gaseous detectors [134].

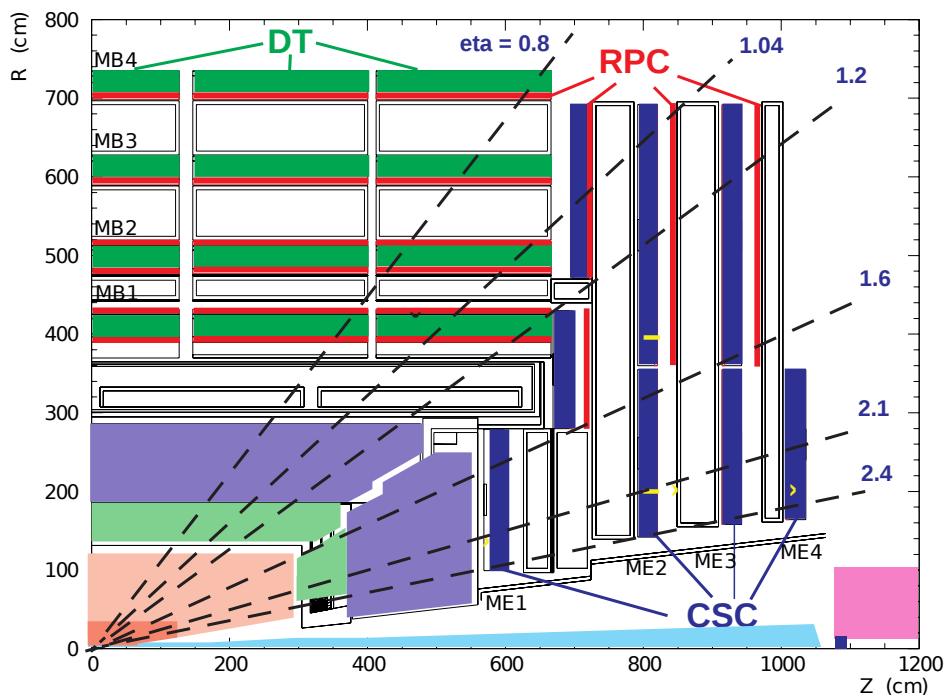


Figure 3.8: One quarter of the layout of the muon systems in CMS [134].

In the barrel region, where the magnetic field is uniform and muon rates are relatively low, **drift tubes (DTs)** are used, organized in four stations and placed between the layers of the steel return yoke. The endcap region is characterized by large muon rates and a non-uniform magnetic field. Here **cathode strip chambers (CSCs)** organized in four disks are used, again interspersed with the layers of the steel return yoke plates. The CSCs are oriented perpendicular to the beam line and complete the range of the muon system up to  $|\eta| < 2.4$ , resulting in an almost full geometrical coverage. Additionally a third kind of detector, the **resistive plate chambers (RPCs)**, are placed both in the barrel and part of the endcap region. While they have a worse spatial resolution than the DTs and CSCs, they have a very fast response and an excellent time resolution. The latter is exploited by the trigger system to identify the correct bunch crossing. Six and four layers of RPCs are installed in the barrel and in the endcap region respectively [134].

### Drift Tube Chambers

The **DT** chambers are filled with a mixture of 85 % argon and 15 %  $\text{CO}_2$ . A muon entering the gas chamber ionizes gas molecules along its path and the resulting ions and electrons drift to their respective electrodes. Using the drift time, precisely determined with the help of the surrounding RPCs, and the known drift-velocity the muon trajectory through the DT can be reconstructed. A resolution of 100  $\mu\text{m}$  in position and 1 mrad in the radial direction can be reached [134].

### Cathode Strip Chambers

The **CSCs** are multiwire proportional chambers that can operate in non-uniform magnetic fields and at high rates. In CMS they have trapezoidal shape and consist of six anode wire layers interleaved among seven cathode panels and are filled with a mixture of 40 % argon, 50 %  $\text{CO}_2$  and 10 %  $\text{CF}_4$ . A muon entering the CSC ionizes the gas molecules and induces a fast signal in the anode wires, which is used for triggering, while the slower cathode signal provides better spatial resolution, typically around 200  $\mu\text{m}$  in position and 20 mrad in direction. In total 486 CSCs are installed in both endcaps [134].

### Resistive Plate Chambers

The **RPCs** are parallel plate gaseous detectors filled with a mixture of 96.2 %  $\text{C}_2\text{H}_2\text{F}_4$ , 3.5 %  $\text{C}_4\text{H}_{10}$  and 0.3 %  $\text{SF}_6$ . They are operated in avalanche mode and have a time resolution in the order of 1 ns and are able to unambiguously determine the bunch crossing associated to a muon track [134].

## 3.2.6 Trigger and data acquisition systems

At the nominal design parameters the bunch spacing in the LHC is 25 ns corresponding to a bunch crossing frequency of 40 MHz for pp collisions. The high frequency

combined with the fact that typically tens of collisions take place at each bunch crossing, leading to PU, makes it impossible to read out, process and store each event, which have a size of around around 1 MB. To reduce the rate to a manageable level a sophisticated two-tiered online trigger system is used to only select physically interesting events that will be processed and stored for further analysis. The hardware-based [Level-1 \(L1\)](#) trigger reduces the rate in a first step before the second step is done by the [high-level trigger \(HLT\)](#) which runs on an online computer farm. After the HLT the event rate is reduced to  $\mathcal{O}(100\text{ Hz})$ . Accepted events are forwarded to mass storage devices and high-level analysis objects are identified in the reconstruction process.

## L1 Trigger

The [Level-1](#) trigger is responsible for reducing the event rate from the 40 MHz bunch crossing rate of the LHC to around 100 kHz, the maximal readout frequency of the full event information from the detector front-end electronics. Using only information of the muon systems and the calorimeters, the L1 trigger has to form a decision whether to keep or discard an event in less than 4  $\mu\text{s}$ , including the required time for propagating the signals from the detector to the trigger electronics [151]. Due to these strict low latency limits the L1 trigger is hardware based and uses [Field Programmable Gate Arrays \(FPGAs\)](#) and [Application Specific Integrated Circuits \(ASICs\)](#) to run simple algorithms in parallel. Only if the L1 trigger reaches a positive decision a full detector readout is triggered and the event is further processed by the HLT [136]. The following description is valid for the L1 trigger that was operated during Run I, since that is most relevant for the data analysis of this thesis, and some of the details have changed during the upgrade of the L1 trigger.

Because of constraints posed by the FPGAs and ASICs the L1 trigger operates in a *divide and conquer* approach, where first so called trigger primitives are reconstructed locally based on the hits in the muon detectors (DTs, CSCs and RPCs) as well as on the energy deposits in the calorimeters. These trigger primitives are then combined into physics objects like muons, electrons or photons, jets and various energy sums before they are used in a final global stage, the [Global Trigger \(GT\)](#), where the decision on whether to accept or reject an event is made.

Before being merged in the GT, the triggers based on inputs from the muon system and the ones based on calorimeter inputs are processed independently of each other as shown in Fig. 3.9. Local segments built from signals in the DTs and CSCs are combined to muon tracks in the corresponding track finders, where estimates for  $p_T$  and  $\eta$  as well as a quality indicator are used for sorting the tracks before passing them on to the [Global Muon Trigger \(GMT\)](#). The RPC hits are used in a pattern matching algorithm and the best resulting tracks are directly sent to the GMT. The GMT receives 16 tracks in total, 4 each from the DT and CSC track finders and 8 from the RPC trigger, and utilizes the overlap of the different regional trigger systems to improve the  $p_T$  resolution and to identify and merge candidates that were found by two subsystems. Finally, the GMT ranks the different candidates according to

their reconstruction quality and transverse momentum and the best four candidates are propagated to the GT. A similar approach is followed in the calorimeter, where first trigger primitives are collected into calorimeter regions, which are then used in the Global Calorimeter Tower to compute the highest four transverse momentum isolated and non-isolated electrons/photons, four forward, central and  $\tau$  jets of highest transverse momentum, the total transverse energy and the missing jet transverse energy.

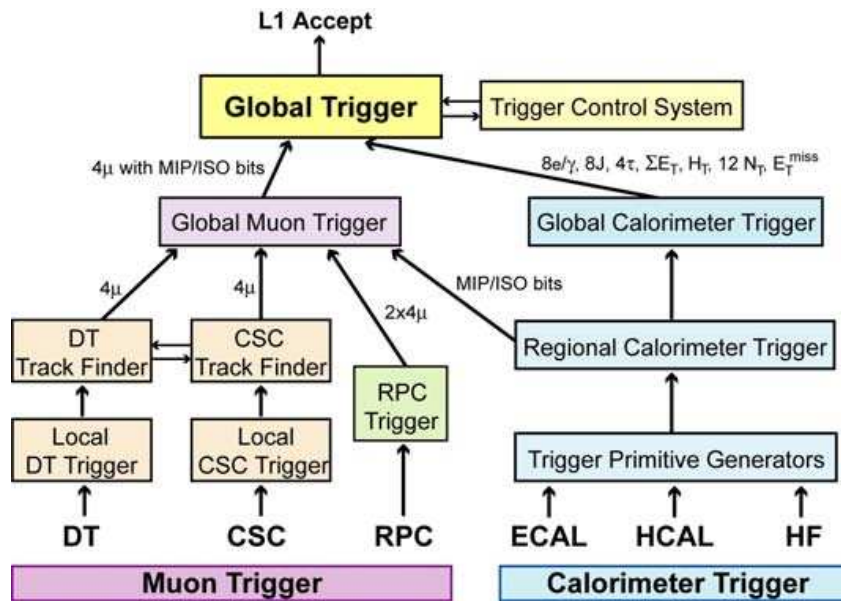


**Figure 3.9:** Architecture of the L1 trigger at CMS during LHC Run I [136].

Based on these inputs and a list of programmable algorithms the GT forms a decision on whether or not to accept an event. Algorithms, also called *L1 seeds*, can make use of the inputs to the GT and of simple algorithms combining two or more inputs to, for example, select two oppositely charged muons with a large enough  $p_T$  or within a given  $|\eta|$  region. Since the resolution of the primitively reconstructed objects at L1 is not comparable to the one that can be achieved at the HLT or during offline reconstruction, these thresholds are normally chosen with large enough margins to only minimally affect the offline analysis. Each L1 seed can also be prescaled by an integer factor  $n$  to throttle its rate by only accepting every  $n$ -th event. These prescale factors can be assigned individually to each L1 seed and are defined in different prescale columns, each corresponding to a different instantaneous luminosity range. A complete list of such algorithms and corresponding prescale values is called a *L1 menu* [152].

The final decision of the GT is the combined *final-OR* signal of all individual algorithms. Consequently, if any of the L1 seeds in a L1 menu yields a positive decision the event will be accepted, regardless of the decision of all other seeds.

## Upgrade of the L1 Trigger for Run II

In order to still be able to effectively operate in the challenging conditions posed by the above design performance of the LHC a major overhaul of the L1 trigger was necessary. Simply raising the trigger thresholds of the L1 seeds to combat the increased rate due to the increased instantaneous luminosity and PU would have a significant negative impact on the physics performance of CMS. To avoid this, several new features were introduced in the L1 trigger upgrade for Run II [153]:

- PU subtraction for jet finding and electromagnetic object isolation algorithms
- Improved identification of hadronic  $\tau$  leptons
- Improved position and transverse momentum resolution for muon tracks
- Increased number of possible algorithms that fit into a L1 menu (from 128 to up to 512 algorithms)
- Di-object invariant mass calculation.

The L1 trigger was upgraded during the [Long Shutdown \(LS\) 1](#), commissioned in 2015, which was the first year of data taking in Run II, and replaced the old system completely in 2016.

## High-Level Trigger

The [high-level trigger \(HLT\)](#) receives all events that are accepted by the L1 trigger and has to reduce the rate from 100 kHz down to  $\mathcal{O}(100\text{ Hz})$ , where the limiting factor is the processing of the output data downstream of the HLT, including storage and prompt reconstruction. The HLT has access to the full detector data, including the signals from the tracking detectors, and runs on a processor farm consisting of commercial CPUs. The reconstruction modules and selection filters used at the HLT are part of the software framework that is also used in offline reconstruction. Hence, the HLT can already partially leverage the better reconstruction algorithms that are available during offline reconstruction. To limit the time spent for each event the regions in which the time intensive reconstruction algorithms are run, are determined from information available from the L1 trigger or from parts of the algorithms that are less costly to run.

Similar to the L1 trigger various so called *HLT paths* are collected in the HLT menu. However, unlike the L1 trigger the number of HLT paths that can be used is not limited by the used hardware, but mainly by the time it takes to run all paths in parallel. Different HLT paths cover different parts of the CMS physics program, but it is possible that paths share the results of different reconstruction steps. In general an HLT path consists of a chain of several reconstruction modules interleaved with selection filters. The first reconstruction module starts off from a list of one or more L1 seeds and only starts further processing if the logical expression connecting them is

fulfilled. More and more complex reconstruction steps are run with the aim to, as soon as possible, determine whether to continue or immediately abort the reconstruction to not waste precious computing resources. Only if the final selection filter of a given HLT path is passed, an event is considered as accepted by this path. Events that are accepted by the HLT are sent to storage and offline reconstruction. Only these events can be used for offline analysis as all other events are discarded [152].

To alleviate some constraints placed on the HLT output rate it is possible to omit the prompt reconstruction directly after data taking and process the recorded data at a later time, when more computing resources are available. This technique of so called *data parking* was used during the 2012 data taking period, which was followed by the LS 1, where computing resources previously in use for prompt reconstruction became available. This allowed to almost double the HLT output rate and was especially advantageous for the trigger paths focused on quarkonia.

### 3.3 Quarkonium reconstruction at CMS

As already mentioned in Sec. 2.1 the experimentally most important decay mode of  $S$ -wave quarkonia at CMS is the decay into a pair of oppositely charged muons. Since also the  $P$ -wave quarkonia are reconstructed in their radiative decay to  $S$ -wave quarkonia, the reconstruction of quarkonia in CMS starts by triggering on such dimuons and then using the corresponding events for the offline analysis. In the following the general trigger strategy and reconstruction techniques that were used for obtaining the samples used in the data analysis presented in Chapter 5 will be briefly described. The description given here is kept very general and applies to all quarkonium states recorded during the 2012 data taking period. The selection criteria specific to the  $\chi_c$  polarization measurement presented in this thesis are given in Chapter 5.

The reconstruction of the quarkonium states does not differ from the reconstruction of other states in high energy physics experiments. Possible candidates are built by combining the known decay products to obtain the original particle from which they emerged. In case of  $S$ -wave quarkonia this is as simple as combining pairs of oppositely charged muons within the mass region of the quarkonium. For the  $P$ -wave states these muon pairs have to be combined with an additional photon. Since many photons and muons that do not originate from a quarkonium decay are produced in hadron collisions the identification, in particular the corresponding photon of the  $P$ -wave states, is one of the main challenges.

Considering all possible combinations will lead to an overwhelming *combinatorial background* consisting of random combinations of the decay products. To filter out the majority of these random combinations different techniques are employed. For  $S$ -wave quarkonium states, reconstructed in the CMS experiment, it is required that the two muons forming a possible candidate fulfill some basic quality requirements, have charges of opposite sign and that they have their origin in a common vertex. The latter can be achieved by requiring a minimum distance of closest approach or also



by using a so called vertex fit that imposes that the two tracks are compatible with coming from the same vertex. It is then possible to obtain a sample of candidates with a very small combinatorial background contribution, where specific states can simply be selected by imposing an invariant mass range on the possible candidates. For the reconstruction of  $P$ -wave quarkonia only the selected dimuon pairs from the  $S$ -wave candidate reconstruction are then combined with reconstructed photons. Similar requirements as before are then used to again reduce the contributions from random combinations.

The rejection of combinatorial background and also the mass resolution can be further improved by doing a so called **Kinematic Vertex Fit (KVF)** in which several constraints can be imposed. All the decay products have to originate in the same vertex, the mass of the dimuon pair is constrained to the world average value of the  $S$ -wave state appearing in the radiative decay, while the photon mass is constrained to be compatible with zero. By constraining the dimuon mass to the world average value, the effects of the dimuon mass resolution on the  $P$ -wave candidate mass resolution can be minimized. This can in principle also be achieved by calculating

$$\tilde{M}^{\mu\mu\gamma} = M^{\mu\mu\gamma} - M^{\mu\mu} + M^{Q^3S_1}, \quad (3.7)$$

where  $M^{Q^3S_1}$  is the world average value for the  $Q^3S_1$  state [45].

### 3.3.1 Dimuon triggers

Selecting quarkonia at the trigger level is a challenging task in the conditions found at CMS. On the one hand, the two muons of a low  $p_T$  quarkonium decay are hard to distinguish from the high rate of soft muons originating in hadronic jets. On the other hand, for high  $p_T$  quarkonium decays the two muons are spatially not very well separated and can be mistaken for a single muon by the L1 trigger system. While both of these issues could be mitigated at the HLT the rate restrictions require a careful choice of strategy already at the L1 trigger.

Using single muon L1 triggers as seeds for the HLT paths is not feasible because the necessary  $p_T$  thresholds to keep the rates manageable are too high. Consequently, a double muon trigger is already used at L1, specifically in 2012 the `L1_DoubleMu0er_HighQ` seed was used. It accepts events with at least two muons without any requirements on their transverse momentum or charge, where both muons are within  $|\eta| < 2.1$  and are of high quality. In 2012 it seeded three kinds of HLT paths for inclusive quarkonia:

- `HLT_DimuonX_Jpsi`, with X=8 and 10
- `HLT_DimuonX_PsiPrime`, with X=5 and 7
- `HLT_DimuonX_Upsilon`, with X=5 and 7.

These paths implement the same requirements and only differ in the dimuon invariant mass ranges and minimum transverse momentum they select. The minimum  $p_T$  in GeV of the dimuon is denoted by the  $X$  in the name of the trigger paths. Other requirements at the HLT mainly aim to reduce the rate of combinatorial background. While no further kinematic constraints than already present at L1 are placed on the single muons, the two muons forming a dimuon pair must have opposite charge and originate from the same vertex. To select dimuons where both muons originate from the same vertex two criteria are put into place. The distance of closest approach between the two muons has to be less than 5 mm and the  $\chi^2$  probability of a dimuon vertex fit has to be larger than 0.5 %. The invariant mass selection at the HLT is defined to be loose enough around the nominal masses of the different quarkonium states to not discard any signal candidates and to have a wide enough mass region to still be able to define sideband regions, which are dominated by combinatorial background and used to separate signal from background.

In 2012 a data sample corresponding to about  $20 \text{ fb}^{-1}$  was collected using these trigger paths. The collected data sample can be used for quarkonium polarization and cross section measurements down to relatively low  $p_T$ .

### 3.3.2 Muon reconstruction and identification

The standard CMS muon reconstruction in pp collisions [134] starts by independently reconstructing tracks in the inner tracker, so called “tracker tracks”, and in the muon system, defined as “standalone muon tracks”. Two different reconstruction approaches are then used based on these inputs. They are only briefly summarized here, more details can be found in Ref. [154].

**Global muon reconstruction** So called “global muons” are reconstructed in an “outside-in” approach. Each standalone muon track is matched to a tracker track by extrapolating both to a common surface and comparing the track parameters on that surface. A global muon track is obtained by refitting the combined hits from both tracks.

**Tracker muon reconstruction** “Tracker muons” are reconstructed using an “inside-out” approach, where all tracker tracks satisfying some mild kinematic requirements are extrapolated to the muon stations. If at least one matching segment, a short stub consisting of DT or CSC hits, is found the corresponding tracker track is labeled as tracker muon. Contrary to the global muons the tracker muon is not updated with the additional information available from the muon system.

The overall muon reconstruction efficiency of muons produced in pp collisions at CMS with sufficiently high momenta and within the geometrical acceptance is about 99 % [154]. Muon candidates that are reconstructed as both a global and a tracker muon are merged into a single candidate if they share the same tracker track. Depending on the needs of the physics analysis different selection criteria can be applied

to the reconstructed muons to strike the necessary balance of detection efficiency and purity. Such requirements are referred to as *muon identification* (muon ID).

### 3.3.3 Photon conversion reconstruction

In radiative decays of  $P$ -wave to  $S$ -wave quarkonia,  $Q^3 P_J \rightarrow Q^3 S_1 \gamma$ , a photon has to be reconstructed in addition to the two muons from the dimuon decay of the  $S$ -wave states. Several challenges arise in this reconstruction. Firstly, the mass differences between the  $P$ -wave and  $S$ -wave states are in the order of hundreds of MeV and are in general below 500 MeV leading to photons with low energies and transverse momenta as shown in Fig. 3.10 (left). Secondly, the mass difference between the  $J = 1$  and  $J = 2$  states is even lower in the range of tens of MeV [45] (Table 2.1). Consequently, the photons in radiative  $P$ -wave quarkonium decays must be reconstructed with an excellent energy resolution in order to be able to have the necessary invariant mass resolution of the  $\mu\mu\gamma$  system to separate the  $J = 1$  and  $J = 2$  states.

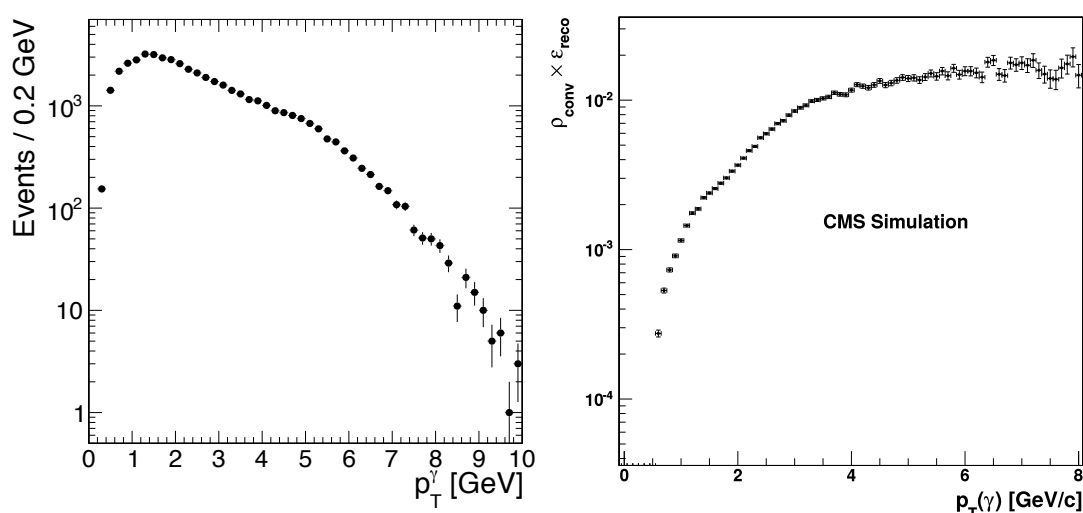


**Figure 3.10:** Photon  $p_T$  distribution (left) observed in the data collected during the 2012 data taking period and used in the analysis in Chapter 5. Convolution of conversion probability and reconstruction efficiency as function of the photon  $p_T$  (right) estimated from simulations assuming 2011 CMS data taking conditions [155].

In principle two possibilities exist to reconstruct photons in the CMS detector, either from the energy deposited in the ECAL or through the conversion into an  $e^+e^-$  pair in the silicon tracker. The major drawback of the standard photon reconstruction procedures is that the relative energy resolution scales with the photon energy, which makes them well suited for the reconstruction of highly energetic photons, like the ones in  $H \rightarrow \gamma\gamma$  decays [149]. In order to achieve the necessary relative energy resolution in the order of  $10^{-3}$  converted photons can also be reconstructed relying solely on information of the silicon trackers.

Photons can convert into an  $e^+e^-$  pair through pair production processes, which are the dominant processes for the interaction of the photon with the material of the silicon tracker for photon energies occurring in the radiative decays of  $P$ -wave quarkonia. The conversion probability is basically independent of the photon energy in this case and only depends on the amount of material that a photon passes through on its trajectory [45].

Converted photons are reconstructed exploiting the characteristics of the conversion process. The opposite sign electron pair originating from a secondary vertex, the possibly highly displaced **conversion vertex (CV)**, must have an invariant mass compatible with zero and the momenta of the electrons must be parallel at the CV. The two trajectories open only in the transverse plane due to the magnetic field geometry. Since the two photons do not have to share the photon energy equally the resulting electron momenta can be highly asymmetric and it is possible that one or both of the electrons with low transverse momentum do not even reach the ECAL, so that using tracker only information is the sole possibility to reconstruct very low energy photons.

The reconstruction of converted photons starts from a collection of low  $p_T$  general tracks by combining tracks that have opposite charges assigned to them and satisfy basic quality criteria. Similar to the dimuon reconstruction additional topological constraints are placed on these combinations to reject random combinations. These constraints include, among others, a minimum transverse impact parameter, a maximum distance of closest approach in the transverse plane and a maximum opening angle in the longitudinal plane [156, 157]. Selected pairs are then used in a three dimensional **KVF** that imposes the invariant mass to be zero and the tracks to be parallel at the CV. The collection of pairs for which the fit converges and gives a reasonable  $\chi^2$  probability is retained for further analysis [157]. Figure 3.11 shows the spatial distribution in the transverse plane of the CVs corresponding to these converted photons. The individual layers of the silicon tracker layers as well as the off-centered beam pipe are clearly visible.

Due to the excellent performance of the silicon tracker a mass resolution of around 6 MeV for  $\chi$  candidates built with photons reconstructed with this tracker only conversion technique can be reached. However, the overall efficiency of the approach is very small because of the low conversion probability combined with the low reconstruction efficiency of low  $p_T$  electron tracks. The total conversion reconstruction efficiency, obtained by convolving the conversion probability and the reconstruction efficiency, is shown in Fig. 3.10 (right) as a function of the photon  $p_T$ . It reaches a plateau for  $p_T > 5$  GeV at a few percent but drops steeply for lower transverse momenta.

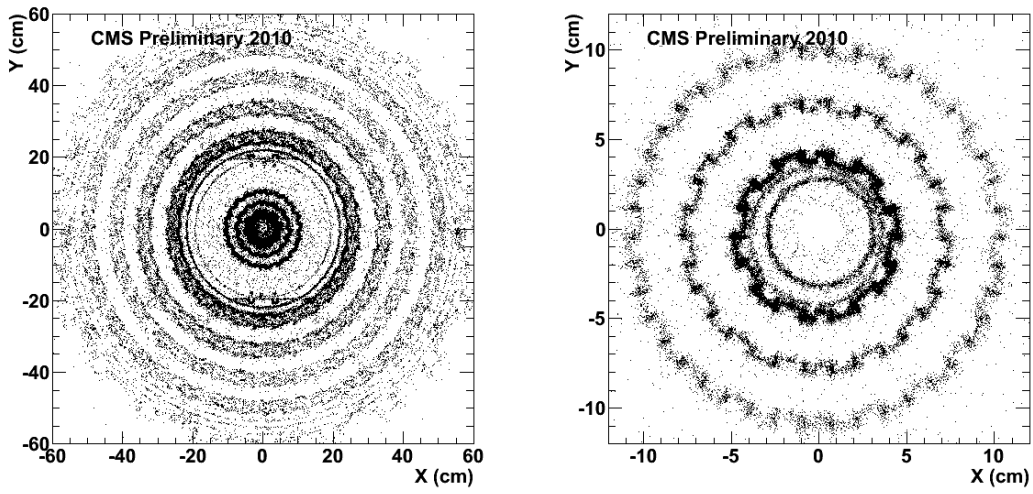


**Figure 3.11:** Spatial distribution of photon conversion vertices in the transverse plane for  $|z| < 26$  cm with increasing zoom level from left to right [157].



Die approbierte gedruckte Originalversion dieser Dissertation ist an der TU Wien Bibliothek verfügbar.  
The approved original version of this doctoral thesis is available in print at TU Wien Bibliothek.

# Upgrade of the BPH Quarkonium Triggers in Run II

“The light works,” he said, indicating the window, “the gravity works,” he said, dropping a pencil on the floor. “Anything else we have to take our chances with.”

*(Douglas Adams, Dirk Gently's Holistic Detective Agency)*

The performance of the LHC started to exceed its nominal design values shortly after the beginning of the 2016 data taking period, as can be seen in Fig. 3.2. Already before that the target luminosity of the LHC was increased to  $L = 2 \cdot 10^{34} \text{ cm}^{-2} \text{ s}^{-1}$  and the expected pile-up at CMS was in the order of 50–60 interactions per bunch crossing.

For the start of the Run II data taking period in 2015 the trigger<sup>i</sup> menu was largely based on the one that was used at the end of Run I in 2012, with some adjustments to keep the increased rate due to the increased center-of-mass energy,  $\sqrt{s} = 13 \text{ TeV}$  in Run II versus  $\sqrt{s} = 8 \text{ TeV}$  at the end of Run I, under control. Especially for the quarkonium trigger paths, falling under the responsibility of the B-physics (BPH) group in CMS, no special studies were conducted for the 2016 data taking periods and the main adaptations to cope with the increased rates were to either simply increase the  $p_T$  thresholds to an acceptable level or even to introduce prescale factors at the HLT. The extended technical stop between the 2016 and 2017 data taking periods, which was also used to replace the pixel detector, provided CMS with the necessary time to completely review the trigger strategies used at L1 and at the HLT in order to make the best use of the available bandwidth exploiting all of the improvements that had been introduced since Run I. This chapter gives a brief summary of selected efforts and their results to obtain an updated quarkonium related trigger strategy at CMS for the 2017 and 2018 data taking periods. The states that are covered by these triggers are the  $\phi(1020)$ ,  $J/\psi$ ,  $\psi(2S)$  and the  $\Upsilon(nS)$ , with  $n = 1, 2, 3$ , mesons.

<sup>i</sup>Throughout this chapter trigger path and the shorter form trigger are used interchangeably. The distinction between an L1 algorithm and an HLT trigger path will also be handled in a rather relaxed way as most concerns are valid for both.

## 4.1 General considerations for the trigger strategy

Several considerations factor into the decision whether to include a proposed trigger path in the trigger menu. In the following discussion a trigger is used as a generic term to describe both an HLT trigger path as well as an L1 algorithm, since similar considerations apply to both. Furthermore, a trigger has to be seen as a combination of an L1 algorithm and the HLT path that is seeded by it. Some changes to either end of the combination might require alterations to the other.

Obviously, the most important factor whether a trigger can be included in the trigger menu is the rate of the proposed trigger path or L1 algorithm, since that is in the end the limiting factor for the whole trigger system. Two different rate definitions are in use when performing trigger studies, the *total rate* and the *pure rate*. While the total rate just measures how many events a given trigger accepts per second, the pure rate is a measure for the number of events that are only recorded by that trigger. Thus, the pure rate is the more interesting number for the inclusion of a new trigger in an existing menu as it gives an estimate of the rate increase due to the new trigger. Since considerable overlaps exist between different triggers it is vital to properly define the *baseline* menu with respect to which the pure rate is measured to get reliable estimates for the actual pure rate. Quarkonium triggers usually aim to collect events with comparably low  $p_T$ , where the overlap with other trigger paths is very small and consequently the pure rate is the main limiting factor.

Other important characteristics are the *purity* and the *efficiency* of the trigger. The purity is defined as the fraction of events that are collected by a given trigger that are also used in the offline analysis. The efficiency on the other hand is the fraction of generated events that are also recorded by the trigger. In quarkonium analyses the purity is usually rather high because the meson masses are known and so suitable selections, mainly based on the invariant masses of the trigger objects, are possible. The efficiency of the L1 algorithms usually has the largest impact for quarkonium analyses.

The *timing* of an HLT path is also crucial to ensure that a trigger decision can be reached within the necessary time constraints. The timing is measured on a dedicated CPU farm with comparable hardware to the one that is used at the HLT CPU farm. The timing measurement always yields a distribution of run-time for a given HLT path until an event is either accepted or rejected. For the simple dimuon triggers that are used for quarkonia, timing constraints are usually only a minor concern, because they require only little reconstruction effort. However, as soon as track reconstruction or even more complicated reconstruction steps are used in an HLT path, timing can become a major concern.

Finally, it should be possible to monitor the different selection criteria during online data taking and to determine efficiencies for them from the recorded data. This necessitates the development of several so called monitoring and efficiency triggers alongside the main triggers. These auxiliary triggers will collect data using high prescale factors, which are tuned such that enough data are collected for the necessary studies while keeping the trigger rates as low as possible. Although no trigger will



be incorporated into the trigger menu without an accompanying monitoring strategy, this strategy will not be discussed here for the sake of brevity.

Table 4.1 gives an overview of commonly used selections that are applied at the HLT level and how these selections are encoded into the name of the HLT trigger paths. The naming scheme is not strictly enforced by CMS but based on convention to facilitate quickly grasping the overall selections that a trigger imposes on the data it collects. It is possible that some details that influence the selection, e.g. the fine tuning of certain threshold values, are changed throughout a data taking period. Such changes do usually not significantly change the behavior of a given trigger, and if significant changes are introduced the name of the trigger is changed to reflect the new behavior. Small differences in the collected data samples can also be introduced by changes in the conditions under which the data are collected, even if the trigger remains unchanged.

## 4.2 The status of the quarkonium triggers in 2016

Several triggers with the aim of collecting data samples containing different quarkonium states were in place during the 2016 data taking period. They can be grouped into three different categories by the L1 seeds they are using. Although they have a considerable overlap, each category also covers a specific phase space region not easily accessible to the others and by doing so enables analyses with specific requirements. In order to keep the discussion short the focus will be on the  $J/\psi$  triggers, but the differences to the triggers covering the other quarkonium states are mainly limited to the invariant mass windows they select. An overview over all quarkonium related triggers and the effective integrated luminosity<sup>ii</sup> collected with each trigger during the 2016 data taking period is given in Table B.1 in Appendix B.

### Inclusive triggers

Various inclusive triggers covering the mass windows of the  $J/\psi$ ,  $\psi(2S)$  and the  $\Upsilon(nS)$  mesons were used to collect data samples containing candidate events in the dimuon decay channel. These inclusive triggers feature comparably high dimuon  $p_T$  thresholds, but do not put any other strong constraints onto the candidates at the HLT level. They are seeded by a combination of `DoubleMu` L1 algorithms, requiring the presence of two muons at the L1 trigger level. In this case the two muons could be of any charge combination and had to fulfill asymmetric  $p_T$  requirements which makes these triggers harder to use in polarization measurements because the asymmetric requirements have to be taken into account explicitly. For symmetric requirements on the two muons this is not the case and both muons can be treated equally regardless of their charge. In case of the  $J/\psi$  the  $p_T$  threshold for the only unrescaled inclusive trigger that was active for the whole data taking period was at 20 GeV.

<sup>ii</sup>If a trigger runs with a prescale factor the luminosity for which the trigger was “effectively active” reduces by the same factor.

**Table 4.1:** Overview of the selection criteria for different quarkonium trigger paths encoded in the name of the trigger paths. A trigger path generally starts with one of the two described generic filter modules and possibly combines it with other more specific filters. Even though the filters are presented separately here, almost all of these selections are applied in one trigger module at the HLT.

Generic filters	
DimuonX	Generic dimuon trigger filter (see e.g. Sec. 3.3.1), seeded by a <b>DoubleMu</b> L1 seed, imposing, among others, the following constraints: <ul style="list-style-type: none"> <li>• Dimuon vertex <math>\chi^2</math> probability <math>&gt; 0.5</math> %</li> <li>• DCA between the two muons <math>&lt; 5</math> mm</li> <li>• Dimuon <math>p_T^{\mu\mu} &gt; X - 0.1</math> GeV</li> </ul>
MuX_TkMu0	Generic dimuon trigger seeded by a <b>SingleMu</b> L1 algorithm using a tracker muon, reconstructed at the HLT, as second muon without a minimum $p_T$ requirement. Imposing: <ul style="list-style-type: none"> <li>• <math>p_T^\mu &gt; X - 0.1</math> GeV (for the muon matched to the L1 muon)</li> <li>• <math> y^{\mu\mu}  &lt; 2.5</math></li> <li>• Maximum distance along the beamline, <math>\Delta z &lt; 2</math> mm, between the two muons</li> </ul>
Barrel	Restricting the Dimuon rapidity to the central region of the detector: $ y^{\mu\mu}  < 1.25$
dEta_X	Maximum $\Delta\eta$ between the two muons: $ \eta^{\mu^+} - \eta^{\mu^-}  < X/10$
Seagulls	Only selects dimuons that bend away from each other in the magnetic field: $\Delta\phi < 0$ , where $\Delta\phi \equiv \phi^{\mu^+} - \phi^{\mu^-}$
etaXpY	Restricting the dimuon pseudo rapidity to $ \eta^{\mu\mu}  < X.Y$
yXpY	Restricting the dimuon rapidity to $ y^{\mu\mu}  < X.Y$
noCorrL1	Trigger paths seeded by <b>DoubleMu</b> L1 seeds without any correlation requirements between the two muons at L1.
Mass window selection filters	
Jpsi	$2.9 < M^{\mu\mu} < 3.3$ GeV
PsiPrime	$3.35 < M^{\mu\mu} < 4.05$ GeV
Psi	$2.9 < M^{\mu\mu} < 4.05$ GeV
Upsilon	$8.5 < M^{\mu\mu} < 11.5$ GeV
Onia	$2.8 < M^{\mu\mu} < 11.5$ GeV <sup>a</sup>
Phi	$0.85 < M^{\mu\mu} < 1.2$ GeV

<sup>a</sup>For the 2016 data taking period the upper bound was 12 GeV.

## Barrel triggers

For each of the mass windows covered by an inclusive trigger a second, so called *barrel trigger* was in place. These triggers restrict the absolute rapidity of the collected dimuon candidate events in order to be able to lower the  $p_T$  thresholds. Additionally, they are seeded by **DoubleMu** L1 algorithms with symmetric requirements on the two muons. In this case the muons had to have opposite charge, be in the geometrical region  $|\eta| < 1.6$  and have an  $\eta$  difference smaller than 1.8 at L1. Apart from the different L1 seeds and the different kinematic windows they cover, these triggers are equivalent to the inclusive triggers described above. Since they do not place any  $p_T$  requirements onto the single muons at L1 or at HLT they are well suited for quarkonium polarization studies. However, due to the lower  $p_T$  thresholds and the corresponding increased trigger rates they were either run with a prescale factor or were disabled for the last part of the data taking period with the highest instantaneous luminosities in case of the  $J/\psi$  meson. Thus, they did not collect as many data as the inclusive triggers in the 2016 data taking period.

## Single muon based triggers

A third category of triggers was run to collect data samples for the measurement of quarkonium properties. These triggers were based on **SingleMu** L1 seeds which require the presence of only one muon at L1 with relatively high  $p_T$  thresholds to keep the L1 rate under control. At HLT these muons were paired with a second muon, reconstructed using the silicon tracker, and retained if the two muons were spatially close and their invariant mass compatible with a loose mass window covering the whole mass range from the  $J/\psi$  mass up to the  $\Upsilon(nS)$  mass region. By construction these triggers allow the study of extremely imbalanced dimuon decays, and are challenging for polarization measurements for similar reasons as the inclusive triggers described above. Nevertheless, since these triggers are seeded by single muon L1 seeds, some issues arising from using double muon L1 seeds can be partly mitigated. These issues arise mainly because the L1 trigger is not able to resolve two muons if they are spatially not well separated, which results in the two muons being mistaken for only one muon. These effects become noticeable for high- $p_T$  quarkonium decays.

### 4.2.1 Extrapolation of trigger rates to expected 2017 data taking conditions

In order to get a first estimate of the trigger rates for the 2017 data taking period a data sample collected under special conditions as well as dedicated simulated event samples, so called **Monte Carlo** (MC) samples, are used. The data samples were collected at the end of the 2016 data taking period using a specialized trigger menu that does not impose any additional requirements at the HLT other than a prescale factor to bring down the data output to a manageable rate. These samples allow

studies of different HLT paths as long as the used L1 algorithms were in the L1 menu at the time of data taking. The MC samples aimed to reproduce a broad spectrum of physics processes, mimicking the ones occurring in *minimum bias*<sup>iii</sup> data. By simulating the trigger for the MC samples, respectively re-evaluating the HLT trigger decision on the data samples the rates corresponding to different instantaneous luminosity and PU conditions can be determined. From these measurements the rates are extrapolated to the expected conditions in the 2017 data taking period.

Figure 4.1 (left) shows the rates obtained from the dedicated 2016 data samples as a function of average PU for a subset of all available quarkonium related triggers. The behavior as a function of PU is in general well behaved and exhibits a linear dependency. From this and similar considerations for the dependency on the instantaneous luminosity it is trivial to extrapolate the expected rates to the expected instantaneous luminosity of  $2.0 \cdot 10^{34} \text{ cm}^{-2} \text{ s}^{-1}$  and  $\langle PU \rangle = 58$  in 2017 conditions. The results of this extrapolation are shown in Fig. 4.1 (right) where also a first estimate of the impact of an increased dimuon  $p_T$  threshold with respect to the one of 2016 is shown. This extrapolation shows that a simple increase of the  $p_T$  thresholds will have a serious impact on the availability of low  $p_T$  quarkonium data and that other means have to be explored to further reduce the rates under 2017 data taking conditions.

### 4.3 Studies for updating L1 seeds

The studies to estimate the efficiencies of different triggers have been conducted using signal only MC samples of unpolarized  $J/\psi$ ,  $\psi(2S)$  and  $\Upsilon(1S)$  respectively. The efficiency is always defined based on the offline selection, i.e. it is the fraction of the events that pass the offline selection which also satisfy all trigger requirements. For the studies concerning the update of the L1 algorithms, the offline selection has been adapted to effectively reflect the requirements that are usually imposed at the HLT level. This approach allows to better separate the changes to the L1 seeds from other effects. The requirements introduced at the HLT are in general very similar to the ones used in the offline analysis of quarkonium cross section and polarization measurements.

Studies have shown that a high quality requirement on the single muons at L1 has only a negligible influence on the efficiency for the quarkonium states that are reconstructed via their dimuon decay. This so called *single quality* requirement, denoted as **SQ** in algorithm names, is thus used for all L1 algorithms aiming to trigger on single muon and double muon event signatures for quarkonium related triggers.

<sup>iii</sup>Minimum bias data samples are data samples collected using special L1 algorithms which only require that any collision has occurred during a bunch crossing. *Zero bias* data samples are even less restrictive and the only condition is that a bunch crossing was detected in the CMS detector. Such samples are usually not useful for physics studies, since they contain only a vanishing number of “interesting” events. However, for detector performance related studies, such as estimates of L1 rates from data, they are an invaluable tool.

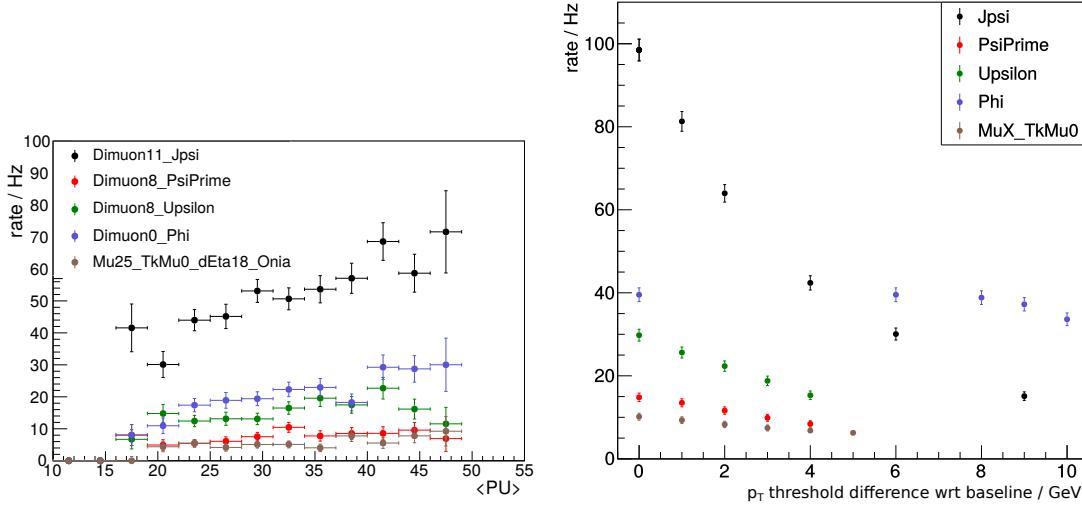


**Figure 4.1:** Trigger rate as function of average PU for different trigger paths determined from special data samples collected in 2016 (left) and estimated trigger rates from extrapolation to expected conditions during the 2017 data taking period for different  $p_T$  thresholds (right). The  $x$ -axis denotes the increase in GeV of the threshold w.r.t. the baseline threshold from the left panel. Information about the requirements of the different triggers encoded in their name is given in Table 4.1.

Requiring single quality muons leads to a rate reduction of around 30 % over the whole  $|\eta|$  range. Another requirement that leads to a roughly 50 % rate reduction, while introducing only a small efficiency degradation, is the opposite charge requirement for the two muons for double muon L1 seeds. This *opposite sign* requirement is denoted as OS in the L1 algorithm names.

As already briefly mentioned in Sec. 3.2.6 the upgrade of the L1 trigger for Run II also introduced the possibility of more elaborate correlations between two trigger objects. The correlations that are most important for the quarkonium related triggers are the already mentioned opposite charge requirement, the possibility to constrain two muons to be inside an angular cone and the possibility to constrain the invariant mass of a combination of two muons. The invariant mass of highly relativistic pairs of particles can be calculated as

$$M^2 = 2p_{T,1}p_{T,2} (\cosh(\eta_1 - \eta_2) - \cos(\phi_1 - \phi_2)), \quad (4.1)$$

where  $p_{T,i}$ ,  $\eta_i$  and  $\phi_i$  are the transverse momentum, pseudorapidity and azimuthal angle of the suspected decay products measured at the decay vertex. The angular cone is defined using the variable  $\Delta R = \sqrt{(\Delta\eta)^2 + (\Delta\phi)^2}$ , where  $\Delta\eta$  and  $\Delta\phi$  are the differences in pseudorapidity and azimuthal angle of the two muons. The distributions for the invariant dimuon mass and the  $\Delta R$  variable, obtained from background-free simulated event samples, for the  $J/\psi$ ,  $\psi(2S)$  and  $\Upsilon(1S)$  states at the L1 are shown in Fig. 4.2. While the distributions for the  $J/\psi$  and the  $\psi(2S)$  mesons are very similar

due to their similar mass and the coarse resolution achievable at the L1, the ones for the  $\Upsilon(1S)$  are considerably different. Thus, L1 algorithms using either of these two criteria will have to use different threshold values for selecting the charmonium states compared to the bottomonium states. These requirements are denoted using either `Mass` or `dR` in the algorithm names, where, for example, `dRMaxXpY` denotes a  $\Delta R < X.Y$  selection and `MassXtoY` selects invariant masses between  $X$  and  $Y$  GeV.

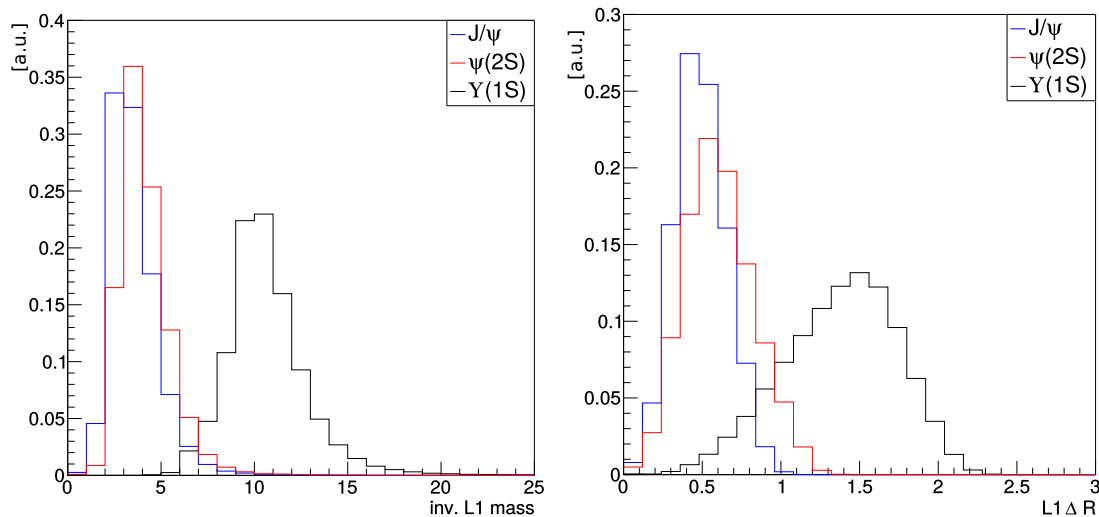


**Figure 4.2:** Invariant dimuon mass distribution (left) and  $\Delta R$  distribution (right) for  $J/\psi$ ,  $\psi(2S)$  and  $\Upsilon(1S)$  mesons at the L1, obtained from simulated event samples.

For the quarkonium related trigger paths the effects on the angular decay distributions introduced by different L1 algorithm are of particular interest, especially for those that are used in the barrel trigger paths as they cover the kinematic region which is usually used for polarization measurements at CMS. The efficiencies as a function of the angular variables in the HX frame are shown in Fig. 4.3 for the  $J/\psi$  and  $\Upsilon(1S)$  samples. Interestingly, the azimuthal direction seems to be more affected than the polar direction in both cases. Furthermore, the invariant mass and  $\Delta R$  requirements have a rather small impact on the shape of the efficiency as a function of the angular variables. On the other hand, a restriction on  $|\eta|$  of the L1 muon candidates, denoted by `erXpY` for  $|\eta| < X.Y$ , clearly shapes the  $\varphi^{\text{HX}}$  efficiency. This is especially visible for the  $\Upsilon(1S)$  state shown in the bottom row of Fig. 4.3.

The proposals for updated L1 algorithms were collected and coordinated within the BPH group to have a consistent and concise set of L1 seeds that cover the broadest possible physics range for the analyses that fall under the responsibility of the BPH group. The considerations presented above and results from similar studies in the context of other analyses led to the following final set of L1 algorithms related to quarkonium analyses that were proposed and accepted:

- `L1_DoubleMu0er1p5_SQ_OS_dRMax_1p4` - A L1 seed requiring two muons of opposite charge within the range  $|\eta| < 1.5$  and a separation smaller than  $\Delta R < 1.4$ ,

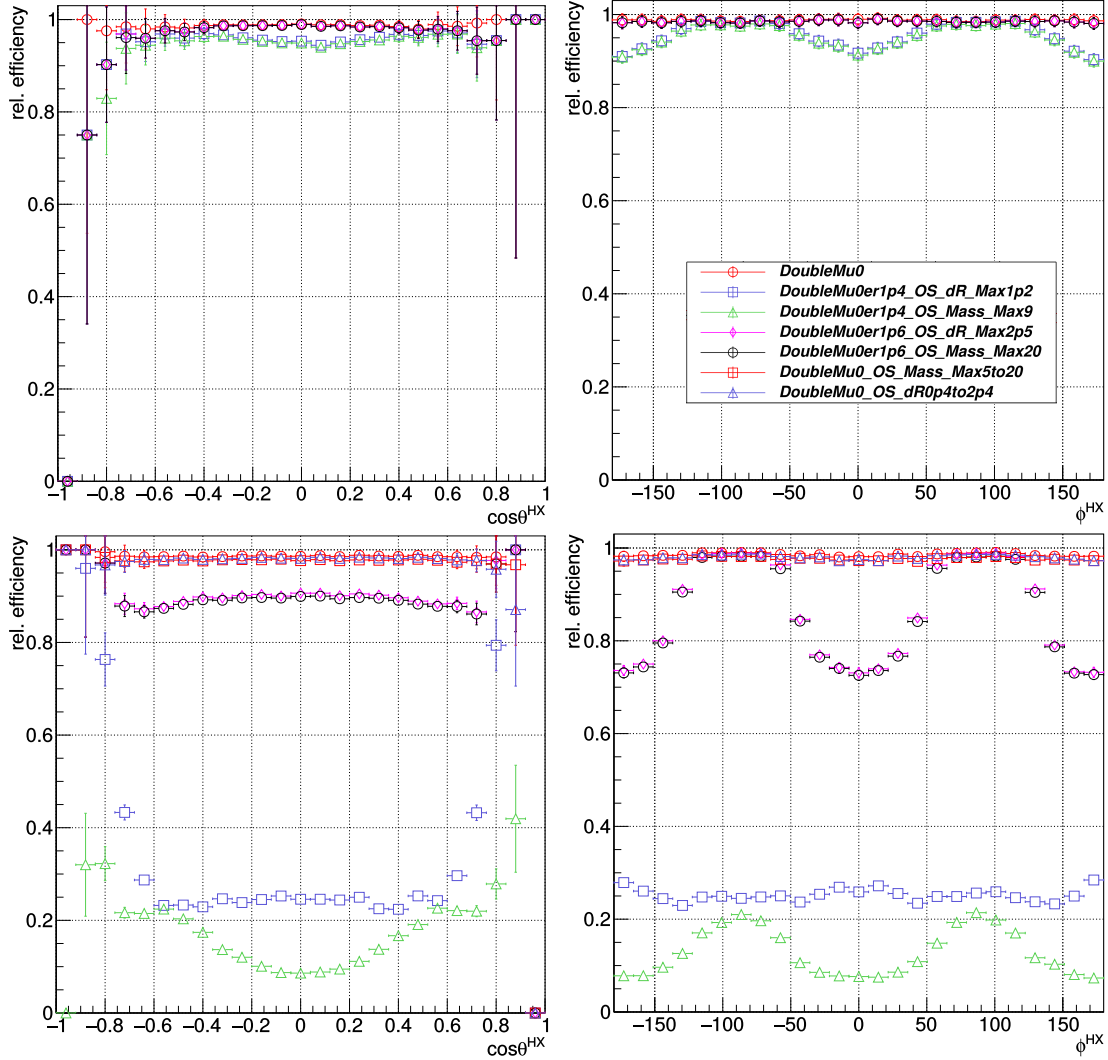


**Figure 4.3:** L1 efficiencies of different L1 algorithms as a function of  $\cos \vartheta^{\text{HX}}$  (left) and  $\varphi^{\text{HX}}$  (right) for  $J/\psi$  (top) and  $\Upsilon(1S)$  (bottom) mesons. The presented algorithms represent different possible combinations of the selections described in the text and the chosen threshold values for the different requirements are close to the ones that have been used in the end.

without any  $p_T$  requirements used in the barrel triggers aiming for the charmonium resonances. The  $\Delta R$  requirement was chosen over the invariant mass because it leads to slightly lower rates, while not impacting the physics performance. A backup with a slightly stricter pseudorapidity requirement of  $|\eta| < 1.4$  was also placed in the menu in case the rates were becoming too large for leaving the nominal L1 seed unrescaled.

- **L1\_DoubleMu4p5er2p0\_SQ\_OS\_Mass7to18** - A L1 algorithm requiring two oppositely charged muons with a minimum  $p_T$  of 4.5 GeV within the pseudo-rapidity range  $|\eta| < 2.0$ , where the invariant mass of the pair has to be in the range  $7 < M^{\mu\mu} < 18$  GeV. This seed is used in the barrel trigger covering the  $\Upsilon(nS)$  resonances. In this case the large coverage in  $|\eta|$ , necessary for not impacting the polarization measurements, required a significant increase on the minimum  $p_T$  of the muons. The value of 4.5 GeV was chosen in accordance with the  $p_T$  threshold at the HLT. In this case the invariant mass requirement proved to lead to lower rates compared to the  $\Delta R$  requirement at comparable efficiency.
- **L1\_DoubleMu4p0\_SQ\_OS\_dRMax1p2** - L1 algorithm selecting two muons of opposite charge muons with a minimum  $p_T$  of 4 GeV within a cone of  $\Delta R < 1.2$  used for the inclusive charmonium paths, covering the full  $\eta$  range with higher dimuon  $p_T$  thresholds at the HLT. A backup algorithm with an increased muon  $p_T$  threshold of 4.5 GeV was also included in the menu.
- **L1\_DoubleMu8\_SQ** - An algorithm selecting two muons with a comparably high  $p_T$  threshold of 8 GeV but without imposing any further criteria on the muons. This allows its usage in HLT paths with a high dimuon  $p_T$  threshold without any correlations between the two muons at L1.

## 4.4 Studies for updating HLT paths

The main concern at the HLT level was to reduce the pure rate of the barrel triggers as far as possible while keeping the lowest possible dimuon  $p_T$  thresholds. Since, the instantaneous luminosity will only further increase in the future these efforts were aiming at making some complementary low  $p_T$  dimuon data samples available for future studies at least in the central rapidity region. For the inclusive trigger paths other considerations as, for example, the consistency of the trigger thresholds over the whole Run II data taking period or collecting more data covering a wider rapidity range at the cost of a higher  $p_T$  threshold, were the driving forces for the final decision on the trigger thresholds and selection criteria. The thresholds for the single muon seeded dimuon paths were mainly dictated by the available L1 single muon seeds. An overview of the set of quarkonium related triggers that were online during the 2017 data taking period is given in Table B.2 in Appendix B. The following discussion focuses on the studies conducted for the barrel trigger paths.



In order to avoid timing issues for trigger paths at the HLT, object reconstruction is done centrally as far as possible so that different trigger paths can use the products of only a few time-consuming reconstruction modules to avoid reconstructing the same physical object multiple times in different trigger paths. Due to the upgrade of the pixel tracker the muon reconstruction sequences had to be updated to accommodate for the additional available pixel layer. These efforts were done taking into account the requirements of several analyses using muons in their trigger strategy to ensure a very good efficiency for multiple different trigger paths. The quarkonium related trigger paths also use this central muon reconstruction.

As a consequence the dimuon paths targeting quarkonium decays have very few handles that can be leveraged to reduce the rate. Most of these handles involve reducing the kinematic coverage in one way or another by either reducing the rapidity range or increasing the  $p_T$  thresholds. One other option is to reject so called *cowboy* dimuon decays where the two muons bend towards each other in the magnetic field and only accepting *seagull* dimuons where the muons bend away from each other. From a physics point of view the two decays are equivalent, however, from a trigger and detector point of view cowboy dimuons are harder to reconstruct since the chance that the two muons are mistakenly reconstructed as one single muon by the L1 trigger is non-negligible. Thus, only accepting seagull dimuons at the HLT potentially simplifies the offline analysis and allows for an almost 50 % rate reduction as shown in Fig. 4.4. A similar strategy has already been used for collecting quarkonium events during the 2011 data taking period [104].

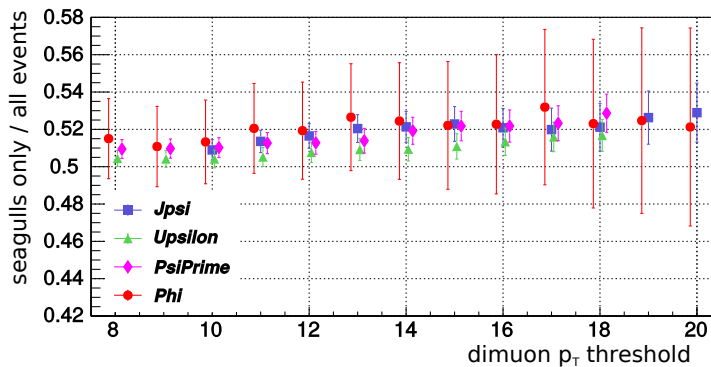


**Figure 4.4:** Rate reduction factor by selecting only seagull dimuon decays at the HLT as function of the dimuon  $p_T$  threshold. The points are slightly shifted along the horizontal axis for better visibility.

Taking all other proposals of the BPH group into account to form a baseline menu with respect to which pure rates could be determined, the dimuon  $p_T$  thresholds were chosen as low as possible. An overview of the proposed and accepted thresholds is given in Table 4.2 together with rate estimates obtained from MC samples assuming 2017 data taking conditions.

Additionally to the triggers that replace or update triggers that were already present for the 2016 data taking period a new set of inclusive quarkonium trigger

**Table 4.2:** Dimuon  $p_T$  thresholds for the dimuon barrel HLT paths, respectively single muon  $p_T$  thresholds for the single muon seeded dimuon HLT paths and their estimated total rates assuming 2017 data taking conditions ( $L = 2 \cdot 10^{34} \text{ cm}^{-2} \text{ s}^{-1}$ ,  $54 < \text{PU} < 58$ ).

Path name	rate / Hz	min. $p_T$ /GeV
HLT_Dimuon20_Jpsi_Barrel_Seagulls	$13.5 \pm 1.7$	19.9
HLT_Dimuon10_PsiPrime_Barrel_Seagulls	$6.0 \pm 1.1$	9.9
HLT_Dimuon10_Upsilon_Barrel_Seagulls	$9.3 \pm 1.5$	9.9
HLT_Dimuon14_Phi_Barrel_Seagulls	$14 \pm 1.7$	13.9
HLT_Mu30_TkMu0_Onia	$7.6 \pm 0.8$	29.9
HLT_Mu25_TkMu0_Phi	$5.1 \pm 0.6$	24.9

paths was proposed and accepted. These triggers are seeded by algorithms without any correlations between the two muons, e.g. opposite sign or invariant mass requirements, at L1, only requiring the presence of two muons. These paths are similar in strategy to the earliest quarkonium triggers that were in use during the 2010 data taking period where the instantaneous luminosity was low enough to only impose very loose requirements on the objects. The main difference is that the single muon  $p_T$  threshold at L1 was raised to 8 GeV and that the dimuon  $p_T$  thresholds at the HLT were raised significantly to between 18 and 25 GeV depending on which quarkonium state is targeted. These paths collect some higher  $p_T$  quarkonium data that are not affected by any possible bias introduced by the correlation requirements between the two muons at L1 that went undetected during the studies conducted for the upgrade of the trigger strategy.

## 4.5 Performance of the triggers

All of the proposed triggers went online at the start or shortly after the start of the 2017 data taking period with the exception of the inclusive quarkonium triggers seeded by L1 algorithms without correlations. Since the corresponding L1 algorithm was only implemented in a later L1 menu, these triggers went online at the end of August 2017 and collected slightly more than half of the available integrated luminosity. Summary tables of the available triggers and the corresponding collected integrated luminosities for the 2016, 2017 and 2018 data taking periods are listed in Appendix B.

The rate estimates from the MC samples proved to be not very far off the ones that were later measured during data collecting in pp collisions. The rates of three of the HLT paths listed in Table 4.2 are shown in Fig. 4.5 versus the time of day for one run of CMS data taking that was chosen mainly based on its length. During this run  $540 \text{ pb}^{-1}$  of the delivered  $563 \text{ pb}^{-1}$  were recorded by CMS [158]. The highest instantaneous luminosity was  $1.56 \cdot 10^{34} \text{ cm}^{-2} \text{ s}^{-1}$  which also explains why the observed rates are lower than the estimated rates for the HLT\_Mu30\_TkMu0\_Onia and the HLT\_Dimuon20\_Jpsi\_Barrel\_Seagulls paths. On the other hand, the estimated

rate for the `HLT_Dimuon10_Upsilon_Barrel_Seagulls` path is as high as estimated, even though the estimates are for a higher instantaneous luminosity. Thus, in this case the rates are underestimated from the studies conducted using MC samples. Nevertheless, overall the rate estimates proved to be rather reliable and all proposed triggers remained online unprescaled for the whole 2017 data taking period. During the 2018 data taking period the rates for the barrel triggers covering the  $J/\psi$  and  $\psi(2S)$  resonances became too high and were disabled but the inclusive trigger paths remained unprescaled.

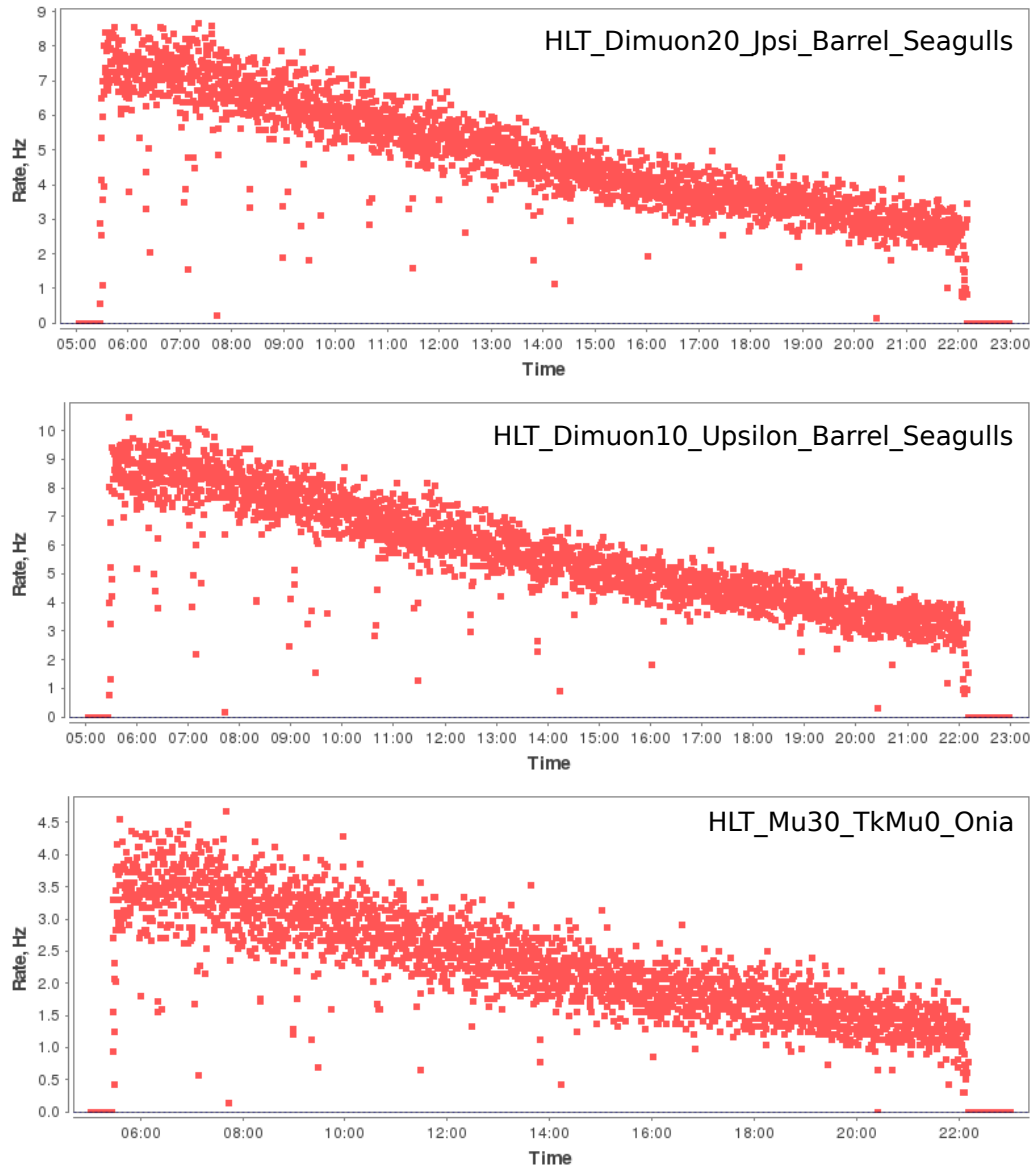
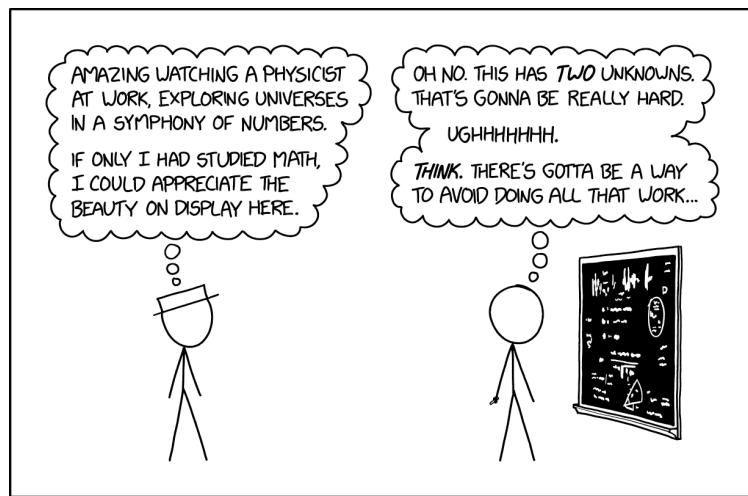


**Figure 4.5:** Rates for three HLT paths vs. time of day during run 304144 of CMS data taking at the end of September 2017 [158].

A lack of manpower made quarkonium polarization measurements using data collected in Run II impossible and for the analysis presented in Chapter 5 only data from Run I were used. The main reason for this is the significantly lower  $p_T$  threshold of the  $J/\psi$  triggers used for collecting the data. However, data collected by some of the updated triggers have been used for other quarkonium analyses, most notably for the confirmation of the triplet structure of the  $\chi_{bJ}(3P)$  [48], which also marks the first measurement by CMS using the full Run II data.

# Measurement of the $\chi_{c1}$ and $\chi_{c2}$ Polarization



(<https://xkcd.com/2207/>)

Measuring the polarization of any quarkonium state by determining the decay angular distribution given in Eq. (2.3) poses several challenges that need to be adequately addressed in order to avoid introducing any bias in the data analysis. This chapter presents the measurement of the  $\chi_{c1}$  and  $\chi_{c2}$  polarizations, the challenges arising in the measurement and how they have been addressed.

The measurement is done in the HX frame and uses data collected in pp collisions in 2012 at a center-of-mass energy of  $\sqrt{s} = 8$  TeV. More details about the used data samples and the event selection are outlined in Sec. 5.2 after first giving an overview of the analysis strategy. Section 5.3 shows the results of studies that have been done using simulated events to validate the analysis strategy. The extraction of the  $\chi_{c1}$  and  $\chi_{c2}$  yields from the data samples and the necessary corrections to account for some effects introduced by the experimental setup are presented in Secs. 5.4 and 5.5, respectively. The extraction of the polarization parameters from the yields is described in Sec. 5.6, before Sec. 5.7 gives the results of systematic checks that were

conducted to estimate systematic uncertainties. Finally, in Sec. 5.8 the results are presented and discussed in the context of predictions based on the phenomenological interpretation of previous measurements summarized in Sec. 2.6.

## 5.1 Analysis strategy

As discussed in Sec. 2.3.2, measuring the polarization of a  $\chi_{cJ}$  state is equivalent to measuring the polarization of the  $J/\psi$  appearing in the radiative  $\chi_{cJ} \rightarrow J/\psi\gamma$  decay. Hence, the polarization measurement is done by studying the decay angular distribution, given by Eq. (2.3), of the dimuon decay  $J/\psi \rightarrow \mu\mu$ . The photon is only used to resolve the  $\chi_{c1}$  and  $\chi_{c2}$  signals in the  $\chi_c$  mass distribution to identify  $J/\psi$  stemming from  $\chi_{c1}$  and  $\chi_{c2}$  decays.

The dimuon angular decay distribution,  $W(\cos\vartheta, \varphi|\vec{\lambda})$ , is shaped by the event selection, including the one imposed by the trigger, as well as reconstruction efficiencies. These shaping effects have to be taken into account in order to obtain an unbiased polarization measurement. While it is in principle possible to account for the shaping effects on the angular decay distribution by precisely measuring the reconstruction efficiencies of the decay particles, as well as determining the effects of the event selection, such an approach has proven notoriously difficult in the case of the  $\chi_{cJ}$  polarization measurement at CMS. A brief description of some other attempts and why they cannot be used is given in Appendix A. Thus, a different approach has been developed which is essentially insensitive to these effects.

### 5.1.1 Relative polarization measurement

Instead of measuring the polarization of the  $\chi_{c1}$  and  $\chi_{c2}$  separately, a relative measurement of one state with respect to the other is performed. In the limit of identical selection and reconstruction effects for the two states, the previously mentioned shaping effects cancel and the measurement becomes insensitive to the event selection and reconstruction efficiencies. The study of the small deviations from this ideal situation, due to the slightly different masses of the  $\chi_{c1}$  and  $\chi_{c2}$  states, is the central part of the analysis. Specifically, the polarization of the  $\chi_{c2}$  relative to the one of the  $\chi_{c1}$  is measured by determining the ratio of the corresponding dimuon decay angular distributions,

$$R(\cos\vartheta, \varphi|\vec{\lambda}^{\chi_{c2}}, \vec{\lambda}^{\chi_{c1}}) = \frac{W(\cos\vartheta, \varphi|\vec{\lambda}^{\chi_{c2}})}{W(\cos\vartheta, \varphi|\vec{\lambda}^{\chi_{c1}})}. \quad (5.1)$$

Here the numerator distribution is measured from  $J/\psi$ 's appearing in  $\chi_{c2}$  decays, whereas the denominator distribution is measured from  $J/\psi$ 's appearing in  $\chi_{c1}$  decays. Due to the limited size of the available data samples a joint two-dimensional measurement of all the relevant parameters is not possible and the two angles  $\cos\vartheta$

and  $\varphi$  are considered separately. The relevant ratio functions are

$$R(\cos \vartheta | \lambda_{\vartheta}^{\chi_{c2}}, \lambda_{\vartheta}^{\chi_{c1}}) = \frac{\int W(\cos \vartheta, \varphi | \vec{\lambda}^{\chi_{c2}}) d\varphi}{\int W(\cos \vartheta, \varphi | \vec{\lambda}^{\chi_{c1}}) d\varphi} \propto \frac{1 + \lambda_{\vartheta}^{\chi_{c2}} \cos^2 \vartheta}{1 + \lambda_{\vartheta}^{\chi_{c1}} \cos^2 \vartheta} \quad (5.2)$$

and

$$R(\varphi | \vec{\lambda}^{\chi_{c2}}, \vec{\lambda}^{\chi_{c1}}) = \frac{\int W(\cos \vartheta, \varphi | \vec{\lambda}^{\chi_{c2}}) d\cos \vartheta}{\int W(\cos \vartheta, \varphi | \vec{\lambda}^{\chi_{c1}}) d\cos \vartheta} \propto \frac{1 + \kappa^{\chi_{c2}} \cos 2\varphi}{1 + \kappa^{\chi_{c1}} \cos 2\varphi}, \quad (5.3)$$

with

$$\kappa = \frac{3 - \cos \vartheta_{\max}^2}{3 + \lambda_{\vartheta} \cos \vartheta_{\max}^2} \lambda_{\varphi} \quad . \quad (5.4)$$

In this case  $\cos \vartheta_{\max}$  denotes the symmetric integration boundaries around zero that are used in Eq. (5.3). The integration in Eq. (5.2) spans the complete domain of  $\varphi$ .

To obtain the ratios described in Eqs. (5.2) and (5.3) from the collected data samples the ratio of the  $\chi_{c2}$  over  $\chi_{c1}$  yields is determined as a function of the polar and azimuthal angles in the HX frame,  $|\cos \vartheta^{\text{HX}}|$  and  $\varphi^{\text{HX}}$ . The HX frame is used because it is the frame that is closest to the natural polarization frame for  $pp \rightarrow c\bar{c}X$  processes in the kinematic region that is accessible to the CMS experiment. Furthermore, since both the polar and the azimuthal dimensions are measured, a model independent interpretation is still possible, even if the HX frame does not coincide with the natural polarization frame. How this would manifest in the present measurement is illustrated in Fig. 5.1, which shows the kinematic dependence of the observable polarization parameters in the HX frame if the CS frame is the natural polarization frame. In particular, the azimuthal anisotropy parameter  $\lambda_{\varphi}$  becomes strongly negative, and almost reaches the physically allowed lower bound of  $-1/\sqrt{5}$  (see Sec. 2.3.2).

Since the  $\chi_{c1}$  and the  $\chi_{c2}$  have slightly different masses, it is natural to expect that the effects introduced by the event selection and reconstruction efficiencies will also be slightly different for the two states. To address these small differences *acceptance times efficiency corrections* are applied that take into account the differences between the  $\chi_{c1}$  and the  $\chi_{c2}$  states. A detailed description of how these corrections are determined and applied is given in Sec. 5.5, where it will also be shown that these corrections mainly only lead to changes of the normalization of the yield ratios. Because all of the information about the polarization lies in the shape of the observed yield ratio, such a global shift of the normalization does not change the extracted values of the polarization parameters.

While the approach of a relative polarization measurement has the advantage of not being sensitive to shaping effects introduced during the event selection and reconstruction, some drawbacks have to be mentioned. When only using the projections onto the  $\cos \vartheta$  and  $\varphi$  directions as defined in Eqs. (5.2) and (5.3), no information about the parameter  $\lambda_{\vartheta\varphi}$  can be extracted in the measurement. Furthermore, constraining the other polarization parameters of both states simultaneously is not possible without using some prior knowledge. However, none of these drawbacks lead to any major issues and the results remain model-independent and provide useful new information for the understanding of quarkonium production.

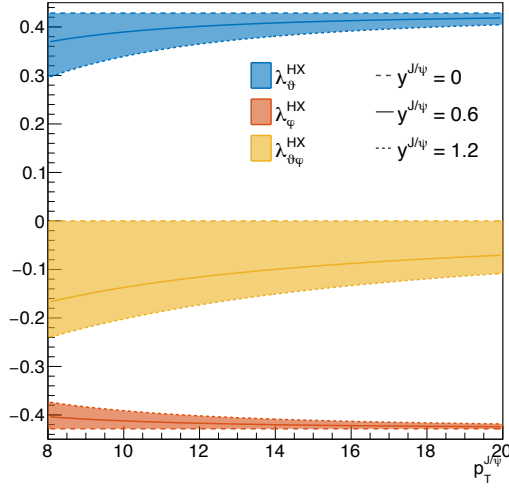


**Figure 5.1:** Dependence of polarization parameters  $\vec{\lambda}^{\text{HX}}$  on  $p_T^{J/\psi}$  for the polarization scenario corresponding to  $\vec{\lambda}^{\text{CS}} = (-\frac{3}{5}, 0, 0)$ . The bands reflect the rapidity range  $|y^{J/\psi}| < 1.2$  for  $\lambda_\theta$  and  $\lambda_\varphi$  and the range  $0 < y^{J/\psi} < 1.2$  for  $\lambda_{\theta\varphi}$ , where the sign flip in the rapidity also introduces a sign flip in  $\lambda_{\theta\varphi}$ .

Since, determining all polarization parameters of both states simultaneously is not possible, the analysis focuses on measuring the differences in polarization parameters,  $\Delta\lambda_\theta \equiv \lambda_\theta^{\chi_{c2}} - \lambda_\theta^{\chi_{c1}}$  and  $\Delta\lambda_\varphi \equiv \lambda_\varphi^{\chi_{c2}} - \lambda_\varphi^{\chi_{c1}}$ , as well as deriving two-dimensional confidence regions for  $lth^{\chi_{c2}}$  vs.  $\lambda_\theta^{\chi_{c1}}$ . With these measurements several currently open questions can be addressed as will be discussed in Sec. 5.8.

### 5.1.2 Experimental considerations and challenges

In order to be less sensitive to statistical fluctuations the analysis is performed using so called *folded angles*, defined as

$$(\cos\vartheta_{\text{fold}}, \varphi_{\text{fold}}) = \begin{cases} (-\cos\vartheta, 180^\circ + \varphi) & \text{if } -180^\circ < \varphi < -90^\circ \\ (\cos\vartheta, \varphi) & \text{if } 0^\circ < \varphi < 90^\circ \\ (\cos\vartheta, -\varphi) & \text{if } -90^\circ < \varphi < 0^\circ \\ (-\cos\vartheta, 180^\circ - \varphi) & \text{if } 90^\circ < \varphi < 180^\circ \end{cases} \quad (5.5)$$

This folding procedure uses the four-fold  $\varphi$  symmetry that the angular decay distribution must obey and allows to use a finer binning in  $\varphi_{\text{fold}} \in [0^\circ, 90^\circ]$ . Since the projection onto the polar direction of the angular distribution is symmetric in  $\cos\vartheta$ , as can be seen from Eq. (5.2), the analysis is performed using the absolute value of  $\cos\vartheta$ . Hence, the folding of the angles has no effect on the polar dimension, since it only affects the sign. In the following the usage of the folded angle definition is im-



plied and the *fold* subscript will be omitted from the angles when they are mentioned in the text for better readability.

As already mentioned in Sec. 2.1 the collected data samples comprise a mixture of promptly produced  $\chi_c$  candidates as well as a NP contribution from decays of heavier b-hadrons. This NP contamination can be reduced by selecting an event sample consisting mainly of promptly produced candidates via the distance between the primary vertex and the dimuon decay vertex.

To determine the  $\chi_{c1}$  and  $\chi_{c2}$  yields from the collected data sample it is necessary to unfold the two states from a combinatorial background and from each other. The combinatorial background, introduced during the reconstruction of the  $\chi_c$  candidates, consists mainly of random  $J/\psi\gamma$  combinations and is already reduced by the event selection described in Sec. 5.2. The mass resolution achieved by CMS in the reconstruction of the radiative decay leads to a small but considerable overlap between the two states, which has to be taken into account in the yield determination. The fit to the invariant mass distribution that is performed to separate the two states from each other and from the combinatorial background is described in detail in Sec. 5.4.

Among the main challenges in quarkonium polarization analyses are the effects on the dimuon angular decay distribution introduced by the limited acceptance and the reconstruction efficiencies of the detector. The latter can normally be determined either from simulation or from data that have been collected with special trigger paths. However, single muon reconstruction efficiencies at CMS are determined as a function of muon  $p_T^\mu$  and  $|\eta^\mu|$  so that such efficiencies have to be transformed appropriately to make them usable in the  $(\cos\vartheta, \varphi)$  angular space in which the analysis is done. Furthermore, there are some correlations between the two muons that are not reflected in the simple product of the single muon efficiencies, summarized in a so called  $\rho$ -factor, which is normally only accessible in simulated events.

The limited acceptance of the detector, mainly due to a minimal  $p_T^\mu$  that is necessary for muons to reach the muon detectors, leads to severe restrictions in the coverage of the 2D angular phase space as illustrated in Fig. 5.2. The loss of angular phase space coverage can be intuitively understood by considering following situation. In the HX frame, the  $z$ -axis with respect to which the polar angle  $\cos\vartheta$  is measured is defined as the direction of the quarkonium momentum in the center-of-mass (laboratory) frame. Hence in the case of  $|\cos\vartheta^{\text{HX}}| \approx 1$ , one of the two muons will have its momentum almost aligned with the momentum of the mother  $J/\psi$ , while the momentum of the other muon will point into almost the opposite direction in the rest frame of the  $J/\psi$ , as shown using red arrows in Fig. 5.2 (left). If this system is boosted to the center-of-mass frame, the muon with the momentum almost aligned with the  $J/\psi$  momentum will have a very high momentum, whereas the second muon will only have a very low momentum, as illustrated in Fig. 5.2 (right). Since the muons are reconstructed in the center-of-mass frame and muons with low momenta are more likely to be lost due to a minimum requirement on  $p_T^\mu$ , it is also more likely to lose events with high values of  $|\cos\vartheta^{\text{HX}}|$ . On the other hand, in events with small  $|\cos\vartheta^{\text{HX}}|$  values both muons will have almost equal momenta in the center-of-mass frame and are, thus, less likely to be lost.

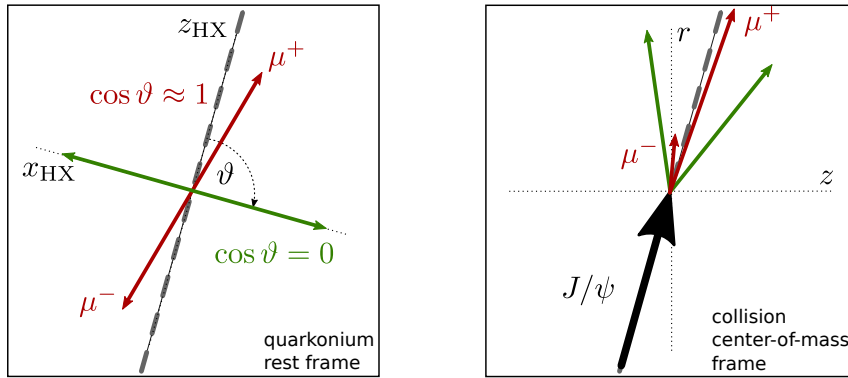


**Figure 5.2:** Illustration of how large values of  $|\cos \vartheta^{\text{HX}}|$  lead to imbalanced muon momenta in the center-of-mass laboratory frame whereas small values lead to muons with similar momenta. The left panel shows what the emission of the two decay muons looks like in the quarkonium rest frame for two extreme values of  $|\cos \vartheta^{\text{HX}}|$ , while the right panel shows the observable muon momenta after boosting the quarkonium system to the laboratory frame.

In the HX frame this leads to a steep drop-off of reconstructed events at high values of  $|\cos \vartheta^{\text{HX}}|$  leading to very narrow  $|\cos \vartheta^{\text{HX}}|$  distributions, especially at low dimuon  $p_{\text{T}}^{J/\psi}$ . Figure 5.3 (left) shows how increasingly higher requirements on the minimal  $p_{\text{T}}^{\mu}$  lead to increasingly narrower  $|\cos \vartheta^{\text{HX}}|$  distributions for the 12–18 GeV  $p_{\text{T}}^{J/\psi}$  range. For the azimuthal direction the effect of a minimum  $p_{\text{T}}^{\mu}$  requirement is small in the HX frame, as can be seen from Fig. 5.3 (center). In other frames, for example the CS frame, these acceptance losses lead to holes in the 2D angular space, as shown in Fig. 5.3 (right). Such holes in the acceptance space where the boundary is a function of both angular variables are very hard to properly take into account when measuring only the one-dimensional projections. This also motivates the choice of the HX frame as measurement frame from an experimental point of view.

The incomplete coverage of  $|\cos \vartheta^{\text{HX}}|$  by the reconstructed data is already reflected in the definition of the ratios of the one-dimensional angular distribution projection onto the azimuthal direction in Eq. (5.3), where it appears in the symmetric integration boundaries as  $\cos \vartheta_{\text{max}}$ . For the measurement of  $\Delta\lambda_{\varphi}$  it is only necessary to properly define  $\cos \vartheta_{\text{max}}$  when selecting the data that are used to obtain the yield ratios. For the measurement of the  $\lambda_{\vartheta}$  parameters and  $\Delta\lambda_{\vartheta}$  the choice of  $\cos \vartheta_{\text{max}}$  is in principle inconsequential. However, data at high  $|\cos \vartheta^{\text{HX}}|$  has more discriminatory power for the extraction of polarization parameters. This poses a significant challenge on the precise determination of  $\Delta\lambda_{\vartheta}$  and the  $\lambda_{\vartheta}$  parameters.

### 5.1.3 Validation of the analysis strategy

To validate the basic assumption that the acceptance and efficiency effects indeed cancel in the relative polarization measurement studies using simulated events, which

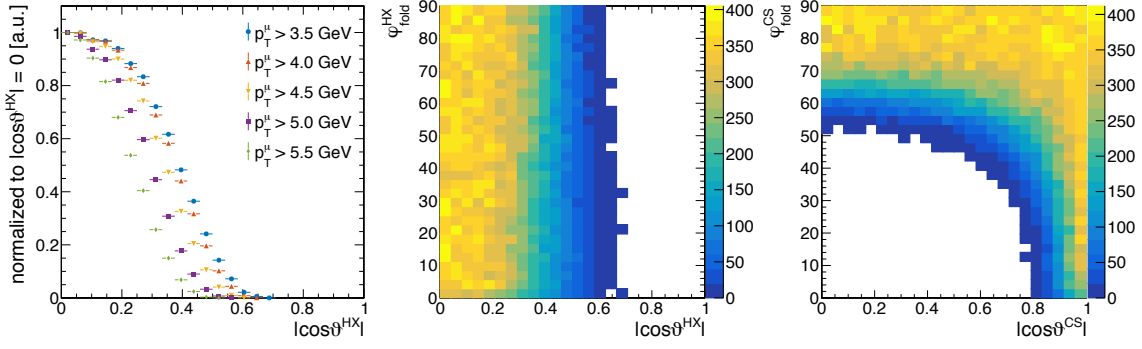


**Figure 5.3:** Normalized  $|\cos \vartheta^{\text{HX}}|$  distributions for increasingly stricter  $p_{\text{T}}^{\mu}$  requirements (left) and two-dimensional ( $|\cos \vartheta|, \varphi$ ) angular distributions in the HX (center) and CS (right) frame obtained from all candidate events in the  $p_{\text{T}}^{J/\psi}$  range 12–18 GeV after applying all nominal event selection criteria (Sec. 5.2).

will be described in more detail in Sec. 5.3, have been used. During these studies it was also verified that small residual differences between the  $\chi_{c1}$  and  $\chi_{c2}$  states can be taken into account using efficiency and acceptance corrections, such that an unbiased measurement of the polarization parameters is possible for all physically allowed polarization scenarios. The analysis of the data samples is done independently of these studies. Only the acceptance times efficiency corrections are determined from simulated event samples.

After the validation step, the analysis of the data samples has been carried out in a *blinded* fashion, in order not to reveal, and thus possibly bias, the physics results. The *unblinding* of the results only took place after the analysis procedure had been scrutinized and blessed by the members of the CMS BPH group. In the case of this analysis a deterministic but unknown random constant was introduced during the extraction of the polarization parameters described in Sec. 5.6 prior to the unblinding. Furthermore, comparisons of specific polarization scenarios to the measured  $\chi_{c2}$  over  $\chi_{c1}$  yield ratios, as presented during the discussion of the results in Sec. 5.8, were only carried out after the blessing of the analysis procedure.

These blinding procedures have proven to be successful in concealing the final result until after the analysis procedure has been properly validated and scrutinized. Since the blinding procedures are of no further interest and do not influence the final results in any way, they will only be mentioned here, but not during the following presentation and discussion of the analysis procedure and its results.

## 5.2 Data samples and event selection

The data sample used in the analysis has been collected in pp collisions at  $\sqrt{s} = 8$  TeV at the CMS experiment in 2012 and corresponds to an integrated luminosity

of  $19.1 \text{ fb}^{-1}$ . The data were collected using the `HLT_Dimuon8_Jpsi` trigger described in Sec. 3.3.1 which requires that the invariant mass of the dimuon pair is in the range 2.8–3.35 GeV, the dimuon absolute rapidity is in the region  $|y^{\mu\mu}| < 1.25$  and that the dimuon  $p_T^{\mu\mu}$  is above 7.9 GeV. Additionally, the dimuon vertex fit  $\chi^2$  probability has to be larger than 0.5 % and the distance of closest approach has to be below 0.5 cm.

The offline reconstruction of  $\chi_c$  candidates follows the procedure described in Sec. 3.3. First the muons and photons are selected independently before  $J/\psi$  candidates and finally the  $\chi_c$  candidates are built and selected. The muons are required to match the ones that triggered the event readout and have to satisfy the *Soft Muon ID* [159] which ensures efficient high quality muon reconstruction at low  $p_T^\mu$ . In particular, the muon tracks must satisfy high-purity track requirements [160] as well as have at least five hits in the silicon tracker, of which at least one has to be in the pixel layers. The track from the inner tracker is extrapolated and matched to segments in the DT or CSC chambers, where the distance between the extrapolated track and at least one segment has to be less than 3 cm or 3 times its uncertainty in local  $X$  and  $Y$  coordinates. The distance from the interaction point must be smaller than 20 cm along the beam line and must not exceed 0.3 cm in the transverse plane. Additionally, a minimum  $p_T^\mu$  of 3.5 GeV is imposed and all muon tracks must be within the range  $|\eta^\mu| < 1.6$ . Oppositely charged muon pairs satisfying these requirements are combined to  $J/\psi$  candidates. For the analysis all  $J/\psi$  candidates that have  $8 < p_T^{J/\psi} < 30$  GeV and  $|y^{J/\psi}| < 1.2$  are selected without imposing any requirements on the invariant dimuon mass.

Promptly produced  $J/\psi$  candidates are selected via their pseudo-proper<sup>i</sup> decay length [74], from here on referred to simply as the *lifetime*,

$$c\tau = l = L_{xy} \cdot m^{\mu\mu} / p_T^{J/\psi}, \quad (5.6)$$

where  $m^{\mu\mu}$  and  $p_T^{J/\psi}$  are the invariant mass and the transverse momentum of the  $J/\psi$  candidate and  $L_{xy}$  is the most probable decay length in the transverse plane, defined as

$$L_{xy} = \frac{\mathbf{u}^T \sigma^{-1} \mathbf{x}}{\mathbf{u}^T \sigma^{-1} \mathbf{u}}. \quad (5.7)$$

Here  $\mathbf{x}$  is the vector in the transverse plane connecting the dimuon vertex and the primary vertex,  $\mathbf{u}$  is the unit vector of the dimuon  $p_T^{J/\psi}$  and  $\sigma$  is the sum of the covariance matrices of the dimuon vertex and the PV under consideration. Only candidates for which the lifetime divided by its uncertainty,  $\sigma_{c\tau}$ , is below 2.5 are used in the analysis. With this requirement on the *lifetime significance* only about 1 % of prompt signal events but the majority of the contributions from NP decays are rejected. The dimuon mass and lifetime significance distributions of all selected events without any lifetime significance selection applied is shown in Fig. 5.4. The

<sup>i</sup>The word “pseudo” in this definition stems from the fact that only the  $J/\psi$  but not all decay products of the decaying b-hadron are reconstructed. Hence, the kinematics of the b-hadron, and consequently the boost to the laboratory frame, are only approximated by the  $J/\psi$  kinematic properties.

mass distribution exhibits a nice peak around the nominal  $J/\psi$  mass and only a negligible combinatorial background combination. The NP contribution, estimated from fitting a simple exponential function to the lifetime significance distribution for  $|\text{ct}|/\sigma_{\text{ct}} > 7$  and extrapolating to the region below 2.5, is around 6 %. Possible effects of this negligible contamination are assessed in systematic checks that are described in Sec. 5.7.

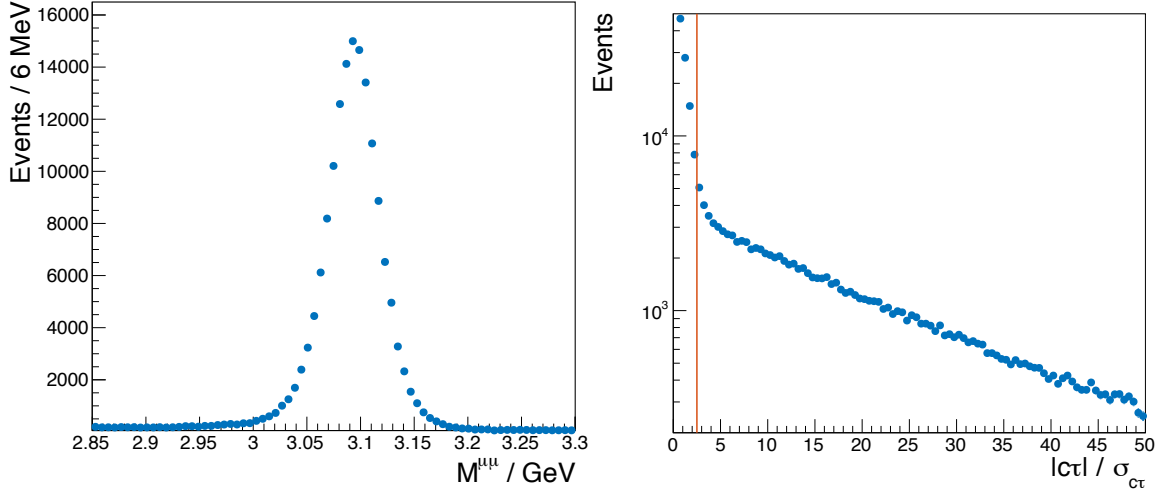


**Figure 5.4:** Invariant dimuon mass distribution (left) and lifetime significance distribution (right) after applying all selections but the lifetime significance. The vertical line in the lifetime significance distribution denotes the nominal threshold value of 2.5 used for selecting prompt events.

The photons are independently reconstructed via their conversion into pairs of oppositely charged electrons in the material of the silicon tracker, described in Sec. 3.3.3 and already successfully used in Refs. [39, 117]. One of the two oppositely charged tracks must have at least four tracker hits, while the other must have three or more. The  $\chi^2$  probability of the two-track KVF, imposing zero mass and a common vertex, must be greater than 0.05 %. Contributions from  $\pi^0$  Dalitz decays are suppressed by requiring that the conversion vertex is more than 1.5 cm away from the geometrical center of the detector in the transverse plane. Furthermore, the photons are required to have  $|\eta^\gamma| < 1.5$  and  $p_T^\gamma > 400$  MeV. The electron tracks of the converted photon have to satisfy the same high-purity track quality requirements [160] as the muon tracks used for the reconstruction of the  $J/\psi$  candidates.

$\chi_c$  candidates are then obtained by combining  $J/\psi$  candidates and photons if the distance along the beam axis between the dimuon vertex and the extrapolated photon trajectory is smaller than 5 mm. A four-track KVF using the muon and electron tracks is performed, imposing the world average  $J/\psi$  mass [45] on the dimuon and zero mass on the photon. Only  $\chi_c$  candidates for which the fit converges and yields a  $\chi^2$  probability larger than 1 % and with an invariant mass in the range between 3.2

and 3.75 GeV are kept for the analysis. The analysis is performed in three ranges of dimuon  $p_T^{J/\psi}$ , 8–12, 12–18 and 18–30 GeV, which contain 103, 106 and 45 thousand  $\chi_c$  candidates respectively after applying all selection criteria.

To determine the  $\chi_{c2}$  over  $\chi_{c1}$  yield ratio as a function of  $|\cos\vartheta^{\text{HX}}|$  or  $\varphi^{\text{HX}}$  the selected events are split into bins of  $|\cos\vartheta^{\text{HX}}|$  or  $\varphi^{\text{HX}}$ . Along the azimuthal  $\varphi^{\text{HX}}$  direction six equidistant bins between 0 and  $90^\circ$  are used. The  $\cos\vartheta_{\text{max}}$  values that are used to properly define the integration boundaries are 0.225, 0.45 and 0.625 in the three  $p_T^{J/\psi}$  ranges. These values are chosen such that the acceptance times efficiency corrections become minimal, while not rejecting significant portions of the available data samples. The binning in  $|\cos\vartheta^{\text{HX}}|$  is defined to use the bin-borders 0, 0.075, 0.15, 0.225, 0.3, 0.375, 0.45, 0.625 in the 12–18 GeV  $p_T^{J/\psi}$  range, resulting in seven  $|\cos\vartheta^{\text{HX}}|$  bins. In the lowest  $p_T^{J/\psi}$  range, covering 8–12 GeV, the last bin has to be dropped because the acceptance is negligible and no data is available. In the highest  $p_T^{J/\psi}$  range, covering 18–30 GeV, the first two bins as well as the third and the fourth bin have to be merged, resulting in five bins with borders 0, 0.15, 0.3, 0.375, 0.45, 0.625, to make the best use of the available data.

### 5.2.1 Simulated event samples

To verify that no bias is introduced in the relative measurement studies using simulated events in various polarization scenarios, covering any physically allowed polarization, have been used. Due to the design of the CMS detector with a minimal material budget in the silicon tracker and the reconstruction of the photons via the tracker only conversion technique, described in Sec. 3.3.3, the combined probability of a conversion to occur and to be subsequently reconstructed is extremely low. Thus, generating sufficiently large event samples using the full detector simulation, from here on referred to as *Full MC*, in different polarization scenarios is extremely time-consuming and computationally expensive. Instead a *Fast MC* simulation with all necessary features has been implemented and used for the simulation based studies.

To obtain a Full MC sample events are first generated, then decayed to their final state particles before the detector response to these final state particles is simulated. Specifically in the case of this analysis, a so called *particle gun* is used, where the initial states are generated according to a desired  $p_T$  and rapidity distribution and with masses and widths set to the current world average values [45] (see Table 2.1). These initial states are then decayed using PYTHIA6 [161] and the propagation and interactions of the decay products in the detector is simulated using the GEANT4 [162] software framework, after which the reconstruction of the generated events follows the same path as data recorded in collisions. This gives in general a reasonable agreement between simulated samples and data samples collected during pp collisions, but the simulation of the detector response is extremely time consuming. Since the conversions of photons into a pair of two electrons only takes place in this late step and it is not possible to predict for which generated event the conversion will occur it is basically impossible to significantly speed up this simulation process for  $\chi_c$  studies.

The Full MC samples that have been used to validate the Fast MC generation have been generated assuming an unpolarized production of the  $\chi_{c1}$  and  $\chi_{c2}$  states. The samples contained no background of any kind and all generated particles are directly produced, i.e. there is no NP contamination and also no feed-down from  $\psi(2S)$ . An equal number of  $\chi_{c1}$  and  $\chi_{c2}$  states has been generated assuming a flat pseudorapidity distribution in the range  $|\eta^{X_c}| < 1.4$  and with a  $p_T^{X_c}/m^{X_c}$  distribution according to Eq. (2.9) using the values  $\beta = 3.4$  and  $\gamma = 0.635$  [34] in the range  $2.6 < p_T^{X_c}/m^{X_c} < 22.5$ .

The Full MC samples are processed using the same reconstruction sequence as the data samples recorded in pp collisions. Hence, the same selection criteria as described above are applied to the Full MC samples, apart from the lifetime selection. This leads to samples containing approximately 35 (39), 37 (40) and 14 (15) thousand reconstructed and selected  $\chi_{c1}$  ( $\chi_{c2}$ ) events in the three  $p_T^{J/\psi}$  ranges. The slightly different numbers of reconstructed and selected events for the two states are due to the slightly different acceptance times efficiency for the two states.

### 5.2.2 Fast MC generation

In order to get sufficiently large event samples for studying all possible polarization scenarios the Fast MC simulation, based on the calculations in Ref. [71], uses realistic single muon and photon reconstruction efficiencies [163, 164] and emulates reconstruction effects by smearing the generated muon and photon momenta.

The momenta are smeared according to

$$\vec{p}' = \frac{p + \delta p}{p} \vec{p}, \quad (5.8)$$

where  $p$  is the total momentum and  $\delta p$  is drawn from a normal distribution centered around zero in case of the muons and from a **Crystal Ball (CB)** distribution [165]. The CB function features a Gaussian core and a tail on the left side of this core describing radiative energy losses. For the photon momentum smearing the parameters are chosen such that the Gaussian core is centered at zero. The width of the normal distribution and the Gaussian core as well as the tail parameters of the CB distribution have been chosen such that the smeared mass distribution of the generated  $\chi_c$  and  $J/\psi$  mesons roughly matches the one observed on data. However, it has also been found that the exact values of these parameters do not influence the angular distribution significantly.

Examples of single muon and photon reconstruction as a function of  $|\eta|$  and  $p_T$  that are used for the Fast MC sample generation are shown in Fig. 5.5 and Fig. 5.6 respectively. Both figures show the reconstruction efficiencies that are used to obtain the nominal results as a function of  $p_T$  as well as alternative efficiencies that are used to probe systematic effects, which will be discussed in more details in Sec. 5.7. The used photon efficiencies are only dependent on  $p_T^\gamma$ , while the muon reconstruction efficiencies have different  $p_T^\mu$  dependencies in different  $|\eta^\mu|$  regions. The efficiency curves include all effects that influence the reconstruction, including the trigger selection

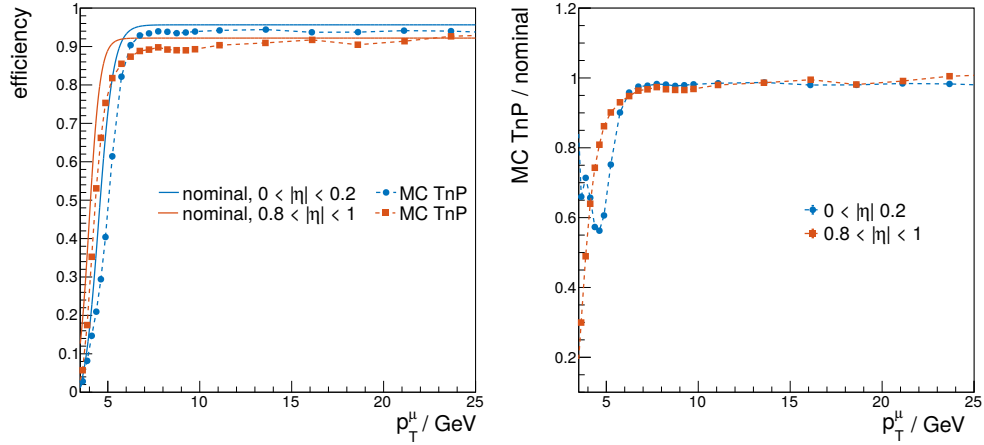


**Figure 5.5:** Single muon reconstruction efficiencies (left) as a function of  $p_T^\mu$  for two  $|\eta^\mu|$  ranges and ratios between the alternative and the nominal curve (right). The solid curves in the left panel correspond to the parametrized reconstruction efficiencies determined from data using the Tag-and-Probe (TnP) method, while the dashed lines correspond to the unparametrized reconstruction efficiencies obtained from MC samples using the same TnP method as for the data samples [163]. For the generation of the Fast MC samples the parametrized data efficiencies are used, while the alternative MC TnP efficiencies are used for the evaluation of systematic effects (see Sec. 5.7).

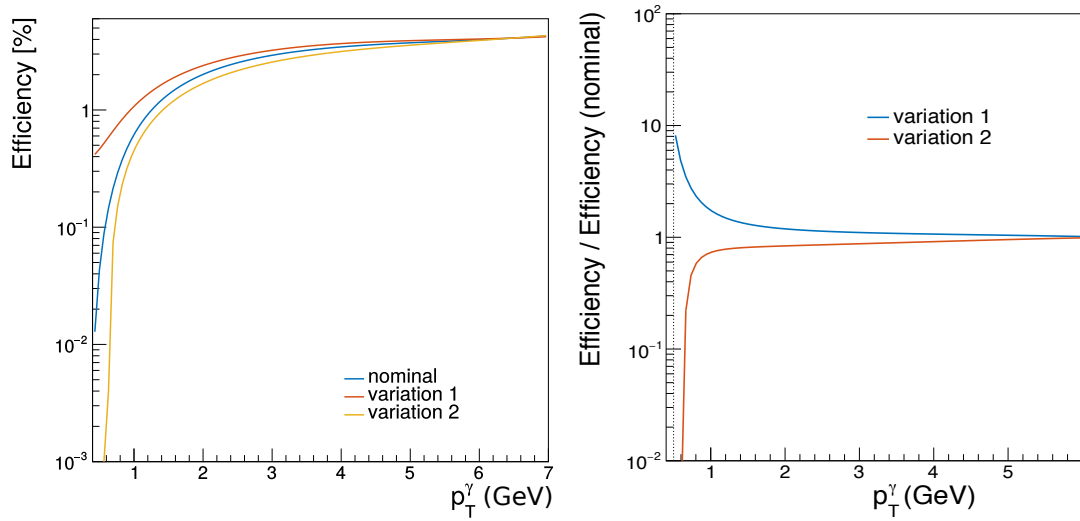


**Figure 5.6:** Photon reconstruction efficiencies (left) as a function of  $p_T^\gamma$  and ratios between the alternative curves and the nominal curve (right). The blue curve in the left panel corresponds to the nominal  $|\eta^\gamma|$  integrated parametrized photon efficiency determined for the 2012 data taking period [164], and is used for the Fast MC generation. The red and yellow curves correspond to variations of this parametrization and are used to probe systematic effects (see Sec. 5.7).



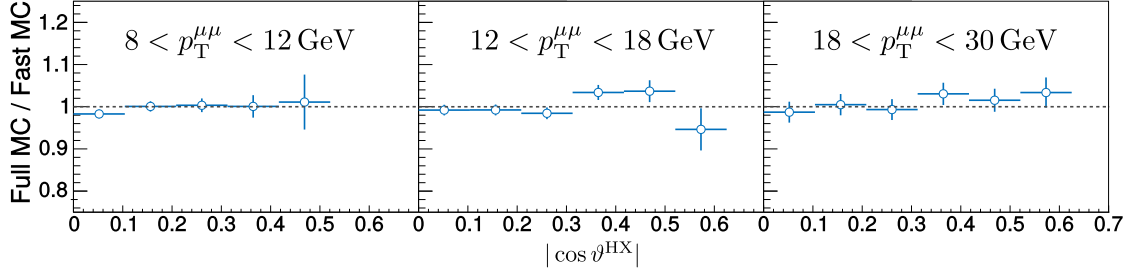


**Figure 5.7:** Ratio  $R(\cos\vartheta)$  obtained from a Full MC and a Fast MC sample generated assuming unpolarized  $\chi_{c1}$  and  $\chi_{c2}$  in three different  $p_T^{\mu\mu}$  ranges (left to right): 8–12, 12–18 and 18–30 GeV.

and muon ID for the muons, as well as the track and other quality requirements applied in the muon and photon reconstruction.

The single muon and photon efficiencies are used to assign a “reconstruction weight” for each event. It is determined as the product of the single muon and photon efficiencies, evaluated at the relevant  $p_T$  and  $|\eta|$  values. This procedure yields a realistic description of the reconstruction effects on a statistical basis without having to go through a detailed detector simulation.

A comparison of the ratios of  $\chi_{c2}$  over  $\chi_{c1}$  yields as a function of  $|\cos\vartheta^{\text{HX}}|$  obtained from a Full MC and from a Fast MC sample generated using the same generation settings and assuming unpolarized production is shown in Fig. 5.7 in the form of the ratio between Full MC and Fast MC in three different  $p_T^{J/\psi}$  ranges. Both MC generations use equivalent selection criteria. Within the limited statistical precision available in the Full MC sample a good agreement between Fast MC and Full MC is found, validating the approach of the statistical approximation of the reconstruction effects taken in the Fast MC generation.

For the studies using simulated event samples obtained from the Fast MC generation, the following generation settings are used. The  $\chi_c$  candidates are generated such that they follow a uniform rapidity distribution in the range  $|y^{\chi_c}| < 1.3$  and the  $p_T^{\chi_c}/m^{\chi_c}$  distribution is the same as the one that has been used for the Full MC sample generation. The  $p_T^{\chi_c}/m^{\chi_c}$  ranges in which the events are generated are adapted according to the  $p_T^{J/\psi}$  ranges that are used in the data analysis, to avoid generating too many events outside of the kinematic range under study. In all three  $p_T^{J/\psi}$  ranges the lower bound is chosen such that the minimal  $p_T^{\chi_c}$  is 0.5 GeV below the minimal  $p_T^{J/\psi}$ . The upper bound is chosen to correspond to  $p_T^{\chi_c} < 70$  GeV independently of the  $p_T^{J/\psi}$  range under consideration. This procedure ensures that the  $p_T^{J/\psi}$  distribution remains unchanged by the generation settings, while avoiding to generate too many events that are outside of the considered phase space.

Only events in which the photons have  $p_T^\gamma > 400$  MeV and  $|\eta^\gamma| < 1.5$ , both muons have  $p_T^\mu > 3.5$  GeV and  $|\eta^\mu| < 1.6$  and the dimuon rapidity is within  $|y^{J/\psi}| < 1.2$  are selected for the studies using simulated events. All selections are applied after smearing the muon and photon momenta.

## 5.3 Studies using simulated events

Simulated event samples generated using the Fast MC procedure are used to validate the analysis method and to verify that an unbiased measurement is possible for all physically allowed polarization scenarios. Two different kinds of studies are performed. First, event samples generated without azimuthal anisotropies are analyzed to check that the  $\chi_{c2}$  over  $\chi_{c1}$  yield ratios as a function of  $|\cos \vartheta^{\text{HX}}|$  can be extracted reliably. Second, the ratios as a function of  $|\cos \vartheta^{\text{HX}}|$  and  $\varphi^{\text{HX}}$  are studied using event samples generated with polar and azimuthal anisotropies to validate the analysis procedure also for polarization scenarios that are theoretically less motivated.

Since only prompt signal events are generated, independently for the  $\chi_{c1}$  and  $\chi_{c2}$  states, effects related to the unfolding of the signal states from each other as well as the combinatorial background contribution and the NP contamination are not probed in these studies. Nevertheless, the corrections for the acceptance times efficiency effects are taken into account. Some additional information on the studies presented in the following sections can be found in Appendix C.1.

### 5.3.1 Results in the absence of azimuthal anisotropies

As the HX frame is the frame that is closest to the natural frame for the  $\chi_c$  polarization measurement in the kinematic range accessible to CMS, the samples for the studies in absence of azimuthal anisotropies are generated assuming the HX frame as natural frame, i.e.  $\lambda_\varphi = \lambda_{\varphi\varphi} = 0$ . To verify that the analysis approach is unbiased for any conceivable polarization scenario, event samples produced with the most extreme physically allowed polarizations as well as the unpolarized scenario are analyzed. The  $\lambda_\vartheta$  values corresponding to these scenarios are

- $\lambda_\vartheta^{\chi_{c1}} = \lambda_\vartheta^{\chi_{c2}} = 0$  (unpolarized)
- $\lambda_\vartheta^{\chi_{c1}} = -\frac{1}{3}$ ,  $\lambda_\vartheta^{\chi_{c2}} = +1$  (maximal positive polarization difference)
- $\lambda_\vartheta^{\chi_{c1}} = +1$ ,  $\lambda_\vartheta^{\chi_{c2}} = -\frac{3}{5}$  (maximal negative polarization difference).

These values can be easily understood from the positivity constraints shown in Fig. 2.7 and defined in Eqs. (2.7) and (2.8).

Using these samples it is possible to show that in the absence of azimuthal anisotropies the reconstruction effects and event selection criteria cancel completely in the relative polarization measurement as long as the measurement is done in small enough  $p_{\text{T}}^{J/\psi}$  windows. The exceptionally good cancellation of the reconstruction, acceptance and efficiency effects in the  $\chi_{c2}$  over  $\chi_{c1}$  yield ratios as function of  $|\cos \vartheta^{\text{HX}}|$  are shown in Fig. 5.8, where the ratio is compared to the expected shape computed analytically from Eq. (5.2). In all three of the polarization scenarios described above, the yield ratio as a function of  $|\cos \vartheta^{\text{HX}}|$  is in perfect agreement with the expected shape. The normalization of the analytical shapes, which is irrelevant for the polarization measurement, is obtained from a fit to the data points. The small differences between

the  $\chi_{c2}$  and  $\chi_{c1}$  mesons manifest mainly in a shift of this normalization. For the unpolarized scenario the normalization would be expected to be exactly one if an equal number of  $\chi_{c1}$  and  $\chi_{c2}$  mesons is generated. A close look to the normalization of the unpolarized curve (blue) in Fig. 5.8 shows that the overall acceptance times efficiency is slightly larger for the  $\chi_{c2}$  than for the  $\chi_{c1}$  shifting the value of the normalization to slightly above 1. This is readily understood by the fact that the  $\chi_{c2}$  is the heavier of the two states and the emitted photons have higher energy on average.

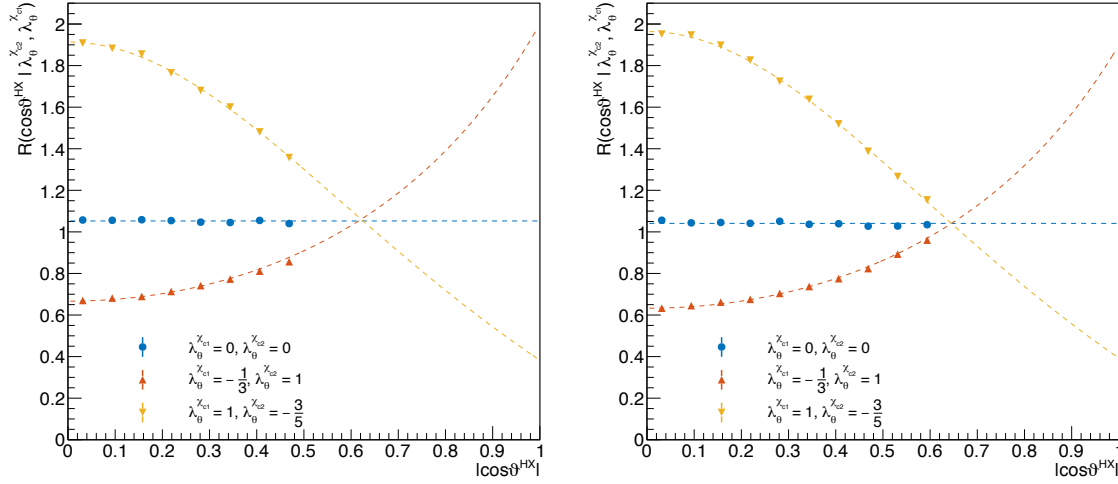


**Figure 5.8:** Ratios of  $\chi_{c2}$  over  $\chi_{c1}$  yields as a function of  $|\cos\vartheta^{\text{HX}}|$  in the  $p_{\text{T}}^{\text{J}/\psi}$  ranges 12–14 GeV (left) and 16–20 GeV (right) for three polarization scenarios with polar but no azimuthal anisotropies (different colors) in comparison with the shapes expected from analytic expressions.

The checks have been done in other  $p_{\text{T}}^{\text{J}/\psi}$  ranges as well as with differently shaped  $p_{\text{T}}$  and  $|\eta|$  dependent single muon and photon efficiencies. Figures 5.9 and 5.10 show the results in the same  $p_{\text{T}}^{\text{J}/\psi}$  ranges as here, but comparing the results when using variations of the single muon and photon reconstruction efficiencies as shown in Figs. 5.5 and 5.6 for the generation of the Fast MC samples. As expected from the observed perfect cancellation of the acceptance times efficiency effects, using different efficiencies in the Fast MC generation does not change the results. However, the cancellation is only perfect for narrow  $p_{\text{T}}^{\text{J}/\psi}$  ranges which are not feasible for the available sample sizes in the data analysis. The acceptance times efficiency corrections start to become more important when integrating over larger  $p_{\text{T}}^{\text{J}/\psi}$  ranges.

### 5.3.2 Results in the presence of azimuthal anisotropies

Previous quarkonium polarization measurements have all reported vanishing or negligible azimuthal polarization parameters [104–110]. Additionally, the HX frame is

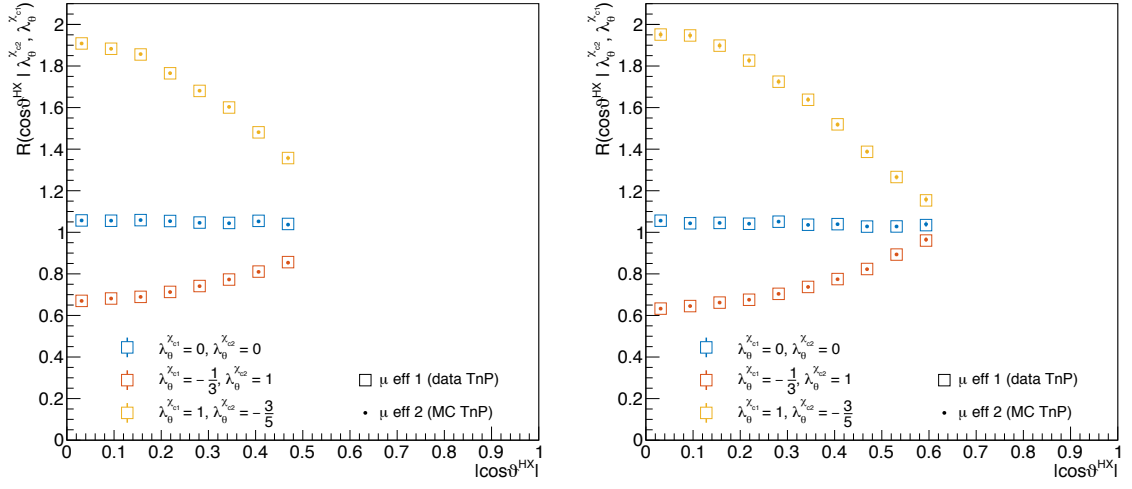


**Figure 5.9:** Ratios of  $\chi_{c2}$  over  $\chi_{c1}$  yields as a function of  $|\cos \vartheta^{\text{HX}}|$  in the  $p_{\text{T}}^{J/\psi}$  ranges 12–14 GeV (left) and 16–20 GeV (right) for three polarization scenarios with polar but no azimuthal anisotropies (different colors) comparing the values obtained with different single muon reconstruction efficiencies.

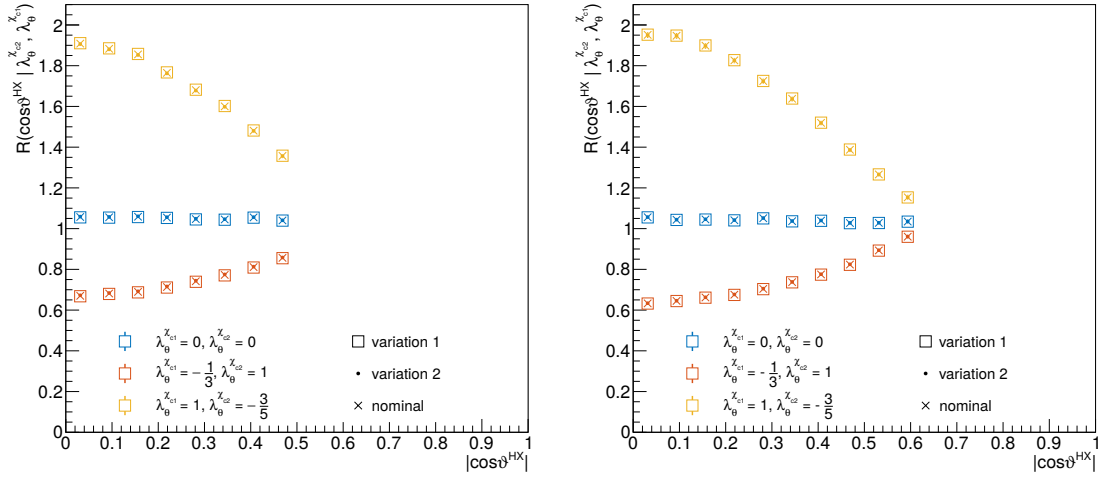


**Figure 5.10:** Ratios of  $\chi_{c2}$  over  $\chi_{c1}$  yields as a function of  $|\cos \vartheta^{\text{HX}}|$  in the  $p_{\text{T}}^{J/\psi}$  ranges 12–14 GeV (left) and 16–20 GeV (right) for three polarization scenarios with polar but no azimuthal anisotropies (different colors) comparing the values obtained with different photon reconstruction efficiencies.

the best motivated natural frame for charmonium production at CMS. Nevertheless, it is important to verify that the analysis approach still works in the presence of such azimuthal anisotropies. The samples that were used in the following checks have been generated using the same polarization scenarios as previously but using the CS frame as natural frame. Hence, they serve as a proxy for various things. Firstly, the natural polarization frame and the measurement frame do no longer coincide and any purely polar anisotropy in the natural frame will lead to a mixture of polar and azimuthal anisotropies in the measurement frame. Secondly, since the analytic transformations from the CS frame to the HX frame depend on the  $J/\psi$  kinematics [29], the samples will also have an intrinsic kinematic dependency. Both effects are illustrated in Fig. 5.1 for one of the used extreme polarization scenarios, where  $\vec{\lambda}^{\text{CS}} = (-\frac{3}{5}, 0, 0)$ .

In order to be able to compare the results with the expected analytical shapes the polarization parameters have to be transformed from the CS frame to the HX frame. This is achieved by fitting the generated two-dimensional  $(\cos \vartheta^{\text{HX}}, \varphi^{\text{HX}})$  distributions in the corresponding kinematic regions of the  $J/\psi$ .

If azimuthal anisotropies are present, the acceptance times efficiency corrections have a small effect on the  $\chi_{c2}$  over  $\chi_{c1}$  yield ratios as a function of  $|\cos \vartheta^{\text{HX}}|$  and  $\varphi^{\text{HX}}$ , even for small  $p_{\text{T}}^{J/\psi}$  ranges. Figure 5.11 shows the comparison of the yield ratios, both before and after corrections, to the analytically expected shapes obtained from Eqs. (5.2) and (5.3) for the  $p_{\text{T}}^{J/\psi}$  range between 12 and 14 GeV. Even for the most extreme polarization scenarios where the CS frame is the natural frame, the corrected ratios agree well with the expected analytical shape. In all cases the difference between the corrected and uncorrected ratios are visible but rather small, indicating that also in the presence of azimuthal anisotropies the acceptance times efficiency effects already cancel to the largest extent, even without taking them into account explicitly.

The differences between corrected and uncorrected ratios become larger at lower  $p_{\text{T}}^{J/\psi}$  values and smaller at higher  $p_{\text{T}}^{J/\psi}$  values. However, for all tested  $p_{\text{T}}^{J/\psi}$  ranges the corrected yield ratios agree well with the expected analytical shapes as can be appreciated from the additional figures provided in Appendix C.1, Figs C.1 and C.2.

In summary, the studies done with simulated events corresponding to the most extreme physically allowed polarization scenarios obtain from Fast MC simulations have shown that the basic assumption that reconstruction effects cancel to the largest extent in the relative measurement holds. Even for the most general polarization scenarios with polar and azimuthal anisotropies an unbiased measurement is possible.

## 5.4 Yield extraction

Determining the prompt  $\chi_{c1}$  and  $\chi_{c2}$  from the collected data samples poses some challenges as mentioned in Sec. 5.1.2. Two issues need to be solved in this case. First, a contribution from NP  $J/\psi$  decays has to be taken into account. This, is already addressed at the data selection stage by imposing a lifetime significance selection onto the data sample that rejects the majority of the NP decays while keeping almost all

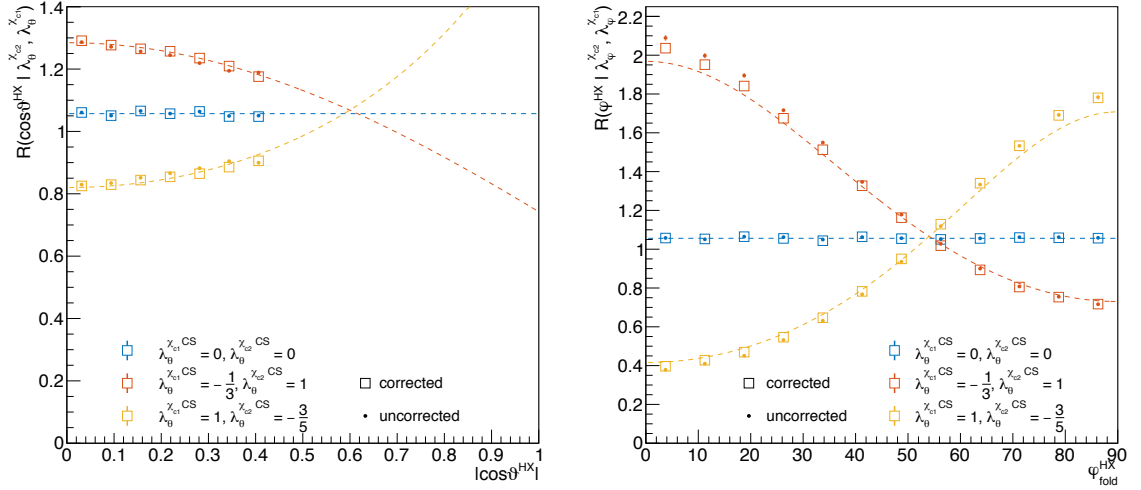


**Figure 5.11:** Ratios of  $\chi_{c2}$  over  $\chi_{c1}$  yields as a function of  $|\cos \vartheta^{\text{HX}}|$  (left) and  $\varphi^{\text{HX}}$  (right) evaluated with event samples generated assuming the CS frame as natural frame and measured in the HX frame comparing the results with and without applying acceptance times efficiency corrections, for the  $p_{\text{T}}^{J/\psi}$  range 12–14 GeV.

prompt events. The second challenge is the combinatorial background consisting mainly of combinations of  $J/\psi$  with random photons and the overlap of the  $\chi_{c1}$  and  $\chi_{c2}$  peaks due to the resolution of the detector. The ratio between the  $\chi_{c2}$  and  $\chi_{c1}$  yields are determined in bins of  $|\cos \vartheta^{\text{HX}}|$  or in bins of  $\varphi^{\text{HX}}$  through an extended unbinned maximum likelihood fit to the  $\chi_c$  candidate mass distribution.

### 5.4.1 Fit model

The model used to extract the  $\chi_{c2}$  over  $\chi_{c1}$  yield ratio is a superposition of three peaks corresponding to the  $\chi_{c0}$ ,  $\chi_{c1}$  and  $\chi_{c2}$  states and an underlying smooth continuum background describing the mass distribution of random  $J/\psi$  and photon combinations:

$$\mathcal{M}(m) = N^{\chi_{c0}} \cdot \mathcal{M}_{\chi_{c0}}(m) + N^{\chi_{c1}} \cdot \mathcal{M}_{\chi_{c1}}(m) + N^{\chi_{c2}} \cdot \mathcal{M}_{\chi_{c2}}(m) + N^{\text{bg}} \cdot \mathcal{M}_{\text{bg}}(m), \quad (5.9)$$

where  $m$  is the  $\chi_c$  candidate mass, and  $N$  denotes the number of events observed for each component.

The  $\chi_{c1}$  and  $\chi_{c2}$  peaks are described using a [double-sided Crystal Ball \(DSCB\)](#) function, a distribution with a Gaussian core described by the parameters  $\mu$  and  $\sigma$  and two radiative tails on either side of the core described by two tail parameters

$n_{L,R}$  and  $\alpha_{L,R}$  each. It is defined as

$$\mathcal{M}_{\text{DSCB}}(m) = \begin{cases} \exp(-\frac{1}{2}u^2) & \text{if } -\alpha_L < u < \alpha_R, \\ \exp(-\frac{1}{2}\alpha_L^2) \left[ \frac{\alpha_L}{n_L} \left( \frac{n_L}{\alpha_L} - \alpha_L - u \right) \right]^{-n_L} & \text{if } u < -\alpha_L, \\ \exp(-\frac{1}{2}\alpha_R^2) \left[ \frac{\alpha_R}{n_R} \left( \frac{n_R}{\alpha_R} - \alpha_R + u \right) \right]^{-n_R} & \text{if } u > \alpha_R, \end{cases} \quad (5.10)$$

with  $u = \frac{m-\mu}{\sigma}$ .

The broad and small  $\chi_{c0}$  bump is described by a Voigtian distribution, a convolution of a normal distribution and a Breit-Wigner distribution. Hence, it has three parameters,  $\mu^{\chi_{c0}}$  and  $\sigma^{\chi_{c0}}$  and the Breit-Wigner width  $\Gamma^{\chi_{c0}}$ .

The smooth continuum background distribution is parametrized by an exponential function, describing the high-mass region using the exponential parameter  $\lambda^{\text{bg}}$ , multiplied by a saturation term providing the necessary low-mass turn down, defined by the parameters  $\mu^{\text{bg}}$  and  $\sigma^{\text{bg}}$ :

$$\mathcal{M}_{\text{bg}}(m) = \left[ 1 + \text{erf} \left( \frac{m - \mu^{\text{bg}}}{\sigma^{\text{bg}}} \right) \right] \cdot \exp(m \cdot \lambda^{\text{bg}}), \quad (5.11)$$

where erf is the error function.

## 5.4.2 Simultaneous binned fits

The analysis is performed independently in each of the three  $p_{\text{T}}^{\text{J}/\psi}$  ranges and also as a function of  $|\cos \vartheta^{\text{HX}}|$  and  $\varphi^{\text{HX}}$ . In each  $p_{\text{T}}^{\text{J}/\psi}$  range the sample is divided into several bins of  $|\cos \vartheta^{\text{HX}}|$  or  $\varphi^{\text{HX}}$ , defined in Sec. 5.2, depending on whether the  $\chi_{c2}$  over  $\chi_{c1}$  ratio is determined as a function of  $|\cos \vartheta^{\text{HX}}|$  or  $\varphi^{\text{HX}}$ . The resulting mass distributions are then fitted simultaneously by minimizing the joint negative log-likelihood, which is simply defined as the sum of all negative log-likelihoods of the considered bins. This results in six independent simultaneous fits, one for each of the two angular dimension in the three  $p_{\text{T}}^{\text{J}/\psi}$  ranges under consideration.

The model described in Eq. (5.9) has 18 parameters defining its shape and another four parameters for the yields of the individual components. Considering the limited number of candidate events in the data sample it is natural to expect that the results will be affected by statistical fluctuations if the fit model has too many free parameters. To improve the reliability and stability of the fits and to decrease the sensitivity to statistical fluctuations some reasonable relations between the individual parameters are introduced.

First, the parameters of the Gaussian core of the barely visible  $\chi_{c0}$  peak are fixed relative to the ones of the  $\chi_{c1}$  peak and the Breit-Wigner width is fixed to the world average value, 10.4 MeV [45]. The relations for the Gaussian core parameters are

$$\begin{aligned} \mu^{\chi_{c0}} &= (\mu^{\chi_{c1}} - M^{\text{J}/\psi}) \frac{M^{\chi_{c0}} - M^{\text{J}/\psi}}{M^{\chi_{c1}} - M^{\text{J}/\psi}} + M^{\text{J}/\psi}, \\ \sigma^{\chi_{c0}} &= \sigma^{\chi_{c1}} \frac{M^{\chi_{c0}} - M^{\text{J}/\psi}}{M^{\chi_{c1}} - M^{\text{J}/\psi}}, \end{aligned} \quad (5.12)$$

where  $M^X$  is the world average value for state  $X$  [45]. These relations take into account that the two peaks are affected by similar effects leading to a proportional shift of their mean values, sometimes also referred to as *photon energy scale* [48], and to a similarly proportional broadening of their widths. Additionally, the  $\chi_{c0}$  yields are fixed to the  $\chi_{c1}$  yields in each  $|\cos \vartheta^{\text{HX}}|$  or  $\varphi^{\text{HX}}$  bin via the relations

$$\begin{aligned} N^{\chi_{c0}}/N^{\chi_{c1}} &= r_{\vartheta}/(1 + \delta_{\vartheta} \cos^2 \vartheta^{\text{HX}}) \\ N^{\chi_{c0}}/N^{\chi_{c1}} &= r_{\varphi}/(1 + \delta_{\varphi} \sin 2\varphi^{\text{HX}}), \end{aligned} \quad (5.13)$$

where  $r_{\vartheta}$ ,  $r_{\varphi}$ ,  $\delta_{\vartheta}$  and  $\delta_{\varphi}$  are free parameters determined in the simultaneous fit. These relations can be derived from Eqs. (5.2) and (5.3) by imposing that the  $\chi_{c0}$  is unpolarized<sup>ii</sup> and can be interpreted as describing the polarization difference between the  $\chi_{c0}$  and  $\chi_{c1}$  state.

The  $\chi_{c1}$  and  $\chi_{c2}$  signal peaks each have six parameters defining their shape. The two parameters of each tail are highly correlated and trying to determine both can lead to unstable fits. Additionally, the right tail is almost negligible and its parameters are hard to determine from the measured data distributions. Thus, some preliminary studies have been done using Full MC signal-only samples. From these studies the parameter values for the right tails and one of the parameters of the left tail are determined and fixed. Furthermore, reasonable simple analytical relations of the shape parameters as function of  $|\cos \vartheta^{\text{HX}}|$  and  $\varphi^{\text{HX}}$  have been derived from these studies. This allows to reduce the number of free parameters as the simple analytical relations are described by two free parameters at most. The studies using simulated events were used to validate that imposing such relations is possible and to find the most suitable analytical relations. The parameters of the imposed relations are determined during the simultaneous fit of the measured mass distributions and the only MC based input to the fits are the values of some of the tail parameters.

In a similar fashion simple functional relations were obtained for the shape of the smooth continuum background from studies using only the mass sidebands, excluding the mass region covering the  $\chi_c$  signal between 3.365 and 3.6 GeV. Again, the final values of the parameters are only determined in the simultaneous fits of the measured mass distributions and not from the results of these preliminary studies.

The set of possible relations describing the functional dependency of shape parameters on  $|\cos \vartheta^{\text{HX}}|$  or  $\varphi^{\text{HX}}$  are

- *fixed* - The value of the parameter is fixed and not varied during the fit.
- *free* - No inter-bin dependency is imposed and the parameter can vary freely in all bins.
- *constant* - One value for the parameter independent of  $|\cos \vartheta^{\text{HX}}|$  or  $\varphi^{\text{HX}}$  is determined during the simultaneous fit to the mass distributions in all bins.

<sup>ii</sup>A quarkonium state with  $J = 0$  is always produced unpolarized.



- *linear* - A linear dependency, defined by two parameters that are determined during the simultaneous fit, is imposed for the parameter. The linear function is evaluated at the mean value of  $|\cos \vartheta^{\text{HX}}|$  or  $\varphi^{\text{HX}}$  in the corresponding bin.

The final set of relations has been decided during preliminary tests using a data sample consisting of all selected events in the range  $12 < p_{\text{T}}^{\text{J}/\psi} < 30$  GeV. Different sets of relations have been tested and the Akaike Information Criterion [166, 167] and the Bayesian Information Criterion [168] have been used to determine the best set of relations. These information criteria can be used to select a model from a set of related models and give a relative measure of the quality of different models based on the maximum observed likelihood in the fit. Both aim to select the model which best describes the data while penalizing models with many free parameters. The two criteria are very similar and only differ in the penalty assigned for the number of free parameters in the model.

Table 5.1 gives an overview of the relations imposed on the shape parameters used for the fits in bins of  $|\cos \vartheta^{\text{HX}}|$ . A subset of all parameters is also shown in Fig. 5.12 where the parameter values obtained from simultaneous fits without imposed relations are compared to the functional relations obtained from simultaneous fits when they are imposed. The values obtained from the fits without imposed relations and the obtained functional relations agree nicely. Hence, introducing these relations should lead to results less affected by statistical fluctuations without biasing the results of the fits. For the fits in bins of  $\varphi^{\text{HX}}$  all linear relations are replaced by constant relations and additionally  $\sigma^{\chi_{c2}}$  is fitted to a constant. Consequently,  $\lambda^{\text{bg}}$  is the only parameter that can vary freely in all bins.

The yields of the individual components are free parameters in all bins except for the ones of the  $\chi_{c0}$ , which are related to the ones of the  $\chi_{c1}$ , as previously described. It has been verified that imposing these relations has no influence on the results of the fit. Since the parameter of interest is in fact the  $\chi_{c2}$  over  $\chi_{c1}$  yield as a function of  $|\cos \vartheta^{\text{HX}}|$  or  $\varphi^{\text{HX}}$ , the  $\chi_{c2}$  yields are defined with respect to the  $\chi_{c1}$  yields and the value of  $N^{\chi_{c2}}/N^{\chi_{c1}}$  is determined in the simultaneous fits without imposing any constraints.

All these considerations lead to a fit model that is able to describe the observed mass distributions well while not being too sensitive to statistical fluctuations. The mass distribution for one  $|\cos \vartheta^{\text{HX}}|$  bin in the  $p_{\text{T}}^{\text{J}/\psi}$  range 12–18 GeV overlaid with the results of the simultaneous fit is shown in Fig. 5.13. The mass distributions and fit results in all other  $|\cos \vartheta^{\text{HX}}|$  and  $\varphi^{\text{HX}}$  bins for all  $p_{\text{T}}^{\text{J}/\psi}$  ranges can be found in Appendix C.2. No systematic trends are visible in the distribution of the pulls and even the largest pulls are barely larger than two. The  $\chi^2/\text{ndf}$  values are computed using the data points in all  $|\cos \vartheta^{\text{HX}}|$  or  $\varphi^{\text{HX}}$  bins and are summarized in Table 5.2 for all  $p_{\text{T}}^{\text{J}/\psi}$  ranges. All six individually performed simultaneous fits yield reasonable  $\chi^2/\text{ndf}$  values. The variation in the number of degrees of freedom in the  $|\cos \vartheta^{\text{HX}}|$  fits can be understood from the fact that a different number of bins is used in each  $p_{\text{T}}^{\text{J}/\psi}$  range.

**Table 5.1:** Functional relations imposed on the shape parameters of the mass model described in Eq. (5.9) for the simultaneous fits in bins of  $|\cos \vartheta^{\text{HX}}|$  and  $\varphi^{\text{HX}}$ .

component	parameter	relation	
		$ \cos \vartheta^{\text{HX}} $	$\varphi^{\text{HX}}$
$\chi_{c0}$	$\mu^{\chi_{c0}}$	related to $\mu^{\chi_{c1}}$ , Eq. (5.12)	
	$\sigma^{\chi_{c0}}$	related to $\sigma^{\chi_{c1}}$ , Eq. (5.12)	
	$\Gamma^{\chi_{c0}}$	fixed, 10.4 MeV (world average) [45]	
background	$\mu^{\text{bg}}$	linear	constant
	$\sigma^{\text{bg}}$	linear	constant
	$\lambda^{\text{bg}}$	free	
$\chi_{c1}$	$n_R^{\chi_{c1}}$	fixed (MC), 2.5	
	$\alpha_R^{\chi_{c1}}$	fixed (MC), 2.021	
	$n_L^{\chi_{c1}}$	fixed (MC), 3.2	
	$\alpha_L^{\chi_{c1}}$	constant	
	$\mu^{\chi_{c1}}$	linear	constant
	$\sigma^{\chi_{c1}}$	linear	constant
$\chi_{c2}$	$n_R^{\chi_{c2}}$	fixed (MC), 2.5	
	$\alpha_R^{\chi_{c2}}$	fixed (MC), 2.219	
	$n_L^{\chi_{c2}}$	fixed (MC), 3.2	
	$\alpha_L^{\chi_{c2}}$	constant	
	$\mu^{\chi_{c2}}$	constant	
	$\sigma^{\chi_{c2}}$	free	constant

## 5.5 Acceptance times efficiency corrections

Acceptance and efficiency effects introduce correlations between the two angular dimensions that possibly also depend on the  $J/\psi$  kinematics as described in Sec. 5.1.2. To take into account the multi-dimensionality of the problem, three-dimensional acceptance times efficiency maps are defined as

$$\mathcal{A}(\cos \vartheta^{\text{HX}}, \varphi^{\text{HX}}, p_{\text{T}}^{\text{J}/\psi}) = \frac{(\cos \vartheta^{\text{HX}}, \varphi^{\text{HX}}, p_{\text{T}}^{\text{J}/\psi}) \text{ at reconstruction level}}{(\cos \vartheta^{\text{HX}}, \varphi^{\text{HX}}, p_{\text{T}}^{\text{J}/\psi}) \text{ at generation level}}. \quad (5.14)$$

The acceptance times efficiency correction maps are obtained using unpolarized Fast MC samples and are used to obtain an event-by-event correction weight, determined as  $1/\mathcal{A}(\cos \vartheta^{\text{HX}}, \varphi^{\text{HX}}, p_{\text{T}}^{\text{J}/\psi})$ , that is then applied to get acceptance and efficiency corrected  $\chi_{c2}$  over  $\chi_{c1}$  yield ratios as a function of  $|\cos \vartheta^{\text{HX}}|$  and  $\varphi^{\text{HX}}$ . To properly take into account the small differences between the  $\chi_{c1}$  and  $\chi_{c2}$  states two correction maps, one per state, are used.

The maps are finely binned in  $\cos \vartheta^{\text{HX}}$ ,  $\varphi^{\text{HX}}$  and  $p_{\text{T}}^{\text{J}/\psi}$ . The  $\cos \vartheta^{\text{HX}}$  dimension is divided into 80 equidistant bins between  $-1$  and  $1$ , while the  $\varphi^{\text{HX}}$  dimension is split into 24 bins of equal width in the range  $\varphi^{\text{HX}} \in [0^\circ, 90^\circ]$ . These binning definitions

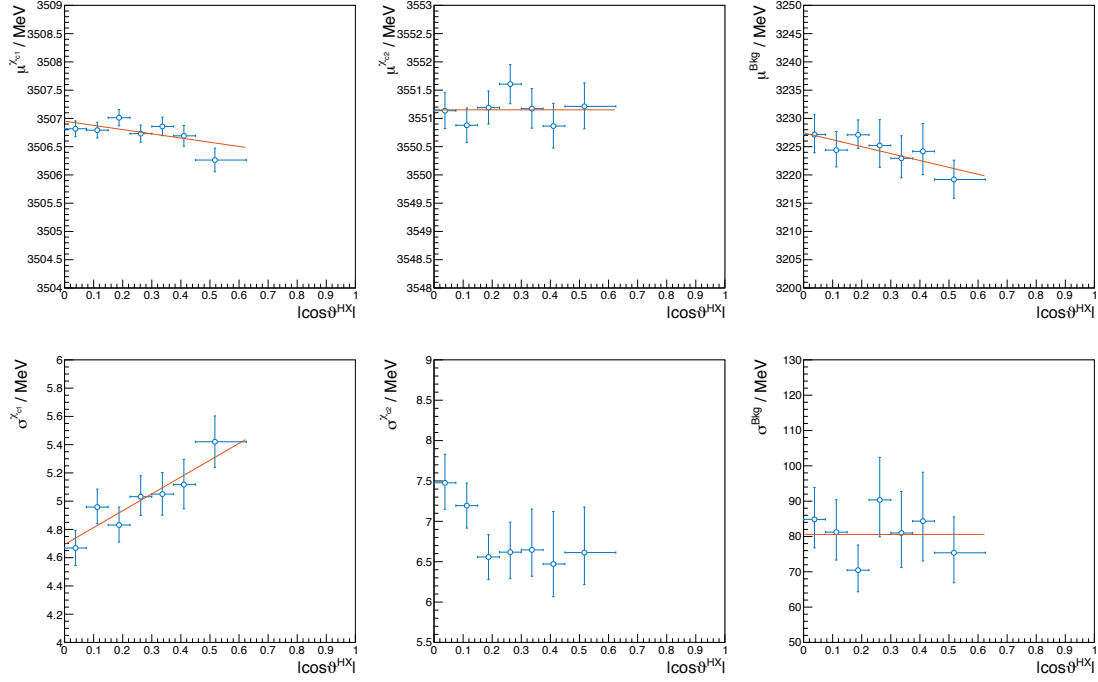


**Figure 5.12:** Several shape parameters of the model used to fit the mass distributions as determined from preliminary fits to mass spectra obtained from an enlarged data sample in the  $p_{\text{T}}^{\text{J}/\psi}$  range 12–30 GeV. The points reflect the values obtained from fits where the parameters were left free. The lines correspond to the resulting relations obtained during the simultaneous fits where the relations have been imposed.

ensure that the bin borders used in the simultaneous mass fits coincide with bin borders of the acceptance times efficiency correction maps. The  $p_{\text{T}}^{\text{J}/\psi}$  bins have a width 1 GeV up to a  $p_{\text{T}}^{\text{J}/\psi}$  of 18 GeV, above which they are 4 GeV wide.

Since the single muon and photon efficiencies are inputs to the Fast MC generation which is used to obtain the samples from which the correction maps are determined, it is vital to check that the exact details of these inputs only have a negligible influence on the results. This is one of the major goals of the presented analysis strategy as the precise determination of the reconstruction efficiencies is not always straight forward and is usually very work intensive. To verify that no precise knowledge about the actual reconstruction efficiencies is necessary two different correction maps have been generated. Once the same efficiencies have been used for the generation of the correction maps and the test samples and once different efficiencies have been used for generating the correction maps. As can be seen in Fig. 5.14 the results do not change significantly when different efficiencies are used for acceptance times efficiency corrections. Again, this is not completely unexpected as the analysis strategy strives to minimize such effects. Figures C.3 and C.4 in Appendix C.1 show that these conclusions hold independently of the considered  $p_{\text{T}}^{\text{J}/\psi}$  range.

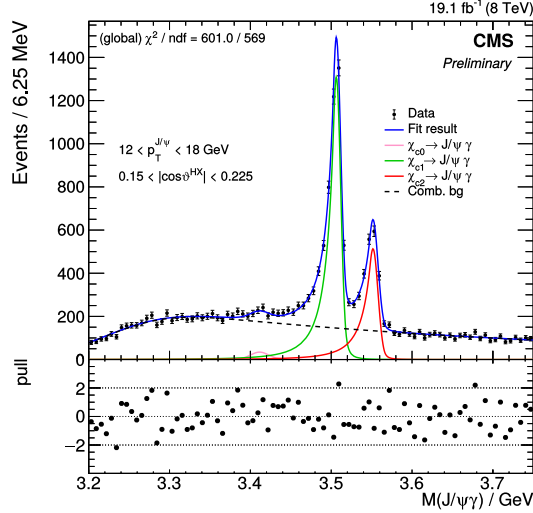


**Figure 5.13:** Top panel: Invariant mass distribution of the  $\chi_c$  candidates in the range  $0.15 < |\cos \vartheta^{\text{HX}}| < 0.225$ , for the 12–18 GeV  $p_{\text{T}}^{\text{J}/\psi}$  range. Bottom panel: Corresponding pull distribution computed as difference between the data and the fitted curve divided by the uncertainty of the data.

**Table 5.2:** Resulting  $\chi^2/\text{ndf}$  for the simultaneous fits in bins of  $|\cos \vartheta^{\text{HX}}|$  and  $\varphi^{\text{HX}}$  in the three  $p_{\text{T}}^{\text{J}/\psi}$  ranges.

$p_{\text{T}}^{\text{J}/\psi} / \text{GeV}$	$\chi^2/\text{ndf}$	
	$ \cos \vartheta^{\text{HX}} $	$\varphi^{\text{HX}}$
8–12	476/486	478/494
12–18	601/569	508/494
18–30	351/403	490/494

The fits to the  $\chi_c$  candidate mass distributions provide the  $\chi_{c2}$  over  $\chi_{c1}$  yield ratio. However, this raw yield ratio is not yet corrected for acceptance and efficiency effects. The major challenge in case of the measured mass distributions is the identification of the  $\chi_{c1}$  and  $\chi_{c2}$  states, which is no longer as trivial as it was the case for the studies using simulated events. This is solved by assigning each event a probability of being a  $\chi_{c1}$  or a  $\chi_{c2}$  meson on the basis of its  $\chi_c$  candidate mass,  $m$ , using the corresponding ratio of the fitted mass models

$$\mathcal{P}_{\chi_{cJ}}(m) = \mathcal{M}_{\chi_{cJ}}(m) / \mathcal{M}(m), \quad \text{with } J = 1, 2. \quad (5.15)$$

The acceptance and efficiency corrected yield in each  $|\cos \vartheta^{\text{HX}}|$  or  $\varphi^{\text{HX}}$  bin is then calculated as

$$N^{\chi_{cJ}} = \sum_{i=1}^N \mathcal{P}_{\chi_{cJ}}(m_i) / \mathcal{A}_{\chi_{cJ}}(\cos \vartheta_i^{\text{HX}}, \varphi_i^{\text{HX}}, p_{\text{T},i}^{\mu\mu}), \quad (5.16)$$

where  $N$  is the number of events in the corresponding  $|\cos \vartheta^{\text{HX}}|$  or  $\varphi^{\text{HX}}$  bin and  $m_i$ ,  $\cos \vartheta_i^{\text{HX}}$ ,  $\varphi_i^{\text{HX}}$  and  $p_{\text{T},i}^{\mu\mu}$  are the corresponding values for the  $i$ -th event. This

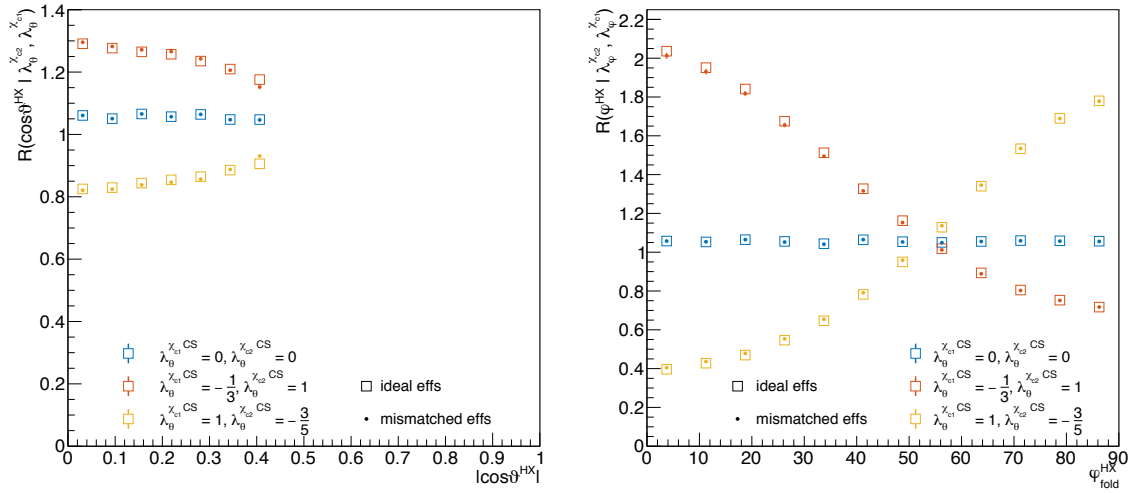


**Figure 5.14:** Ratios of  $\chi_{c2}$  over  $\chi_{c1}$  yields as a function of  $|\cos \vartheta^{\text{HX}}|$  (left) and  $\varphi^{\text{HX}}$  (right) evaluated with corrections maps computed with different reconstruction efficiencies, for the  $p_{\text{T}}^{J/\psi}$  range 12–14 GeV. For the “ideal effs” the same efficiencies are used in the generation of the correction maps and the test samples whereas in case of the “mismatched effs” two different sets of efficiencies have been applied.

calculation has to be done twice, once for  $J = 1$  and once for  $J = 2$  each time using the corresponding correction map.

This approach has the additional advantage that all candidates are considered, even background events as the sum in Eq. (5.16) runs over all events. However, only events with non-vanishing probabilities of being either a  $\chi_{c1}$  or a  $\chi_{c2}$  candidate contribute to the corrected yields. Candidate events which are clearly combinatorial background get assigned zero probability and are, thus, not counted for the corrected yields.

The relative uncertainty of the acceptance times efficiency corrected yield ratio is assumed to be the same as for the uncorrected yield ratio, which is obtained directly from the fit. The uncertainties of the correction are assumed to be negligible.

As already observed during the studies using simulated events, shown in Fig. 5.14, the effect of the acceptance times efficiency corrections on the yield ratio is small. Figure 5.15 shows the raw yield ratios and the corrected yield ratios as a function of  $|\cos \vartheta^{\text{HX}}|$  and  $\varphi^{\text{HX}}$  in the three considered  $p_{\text{T}}^{J/\psi}$  ranges. While the corrections lead to a clearly visible shift in the overall normalization of the yield ratios, the shape of the yield ratio remains effectively unchanged. The latter can easily be appreciated by comparing the scaled raw yield ratios and the corrected yield ratios in which case both have the same normalization. As the polarization measurement is insensitive to the absolute normalization of  $R(\cos \vartheta)$  and  $R(\varphi)$ , such normalization changes do not change the results of the analysis.

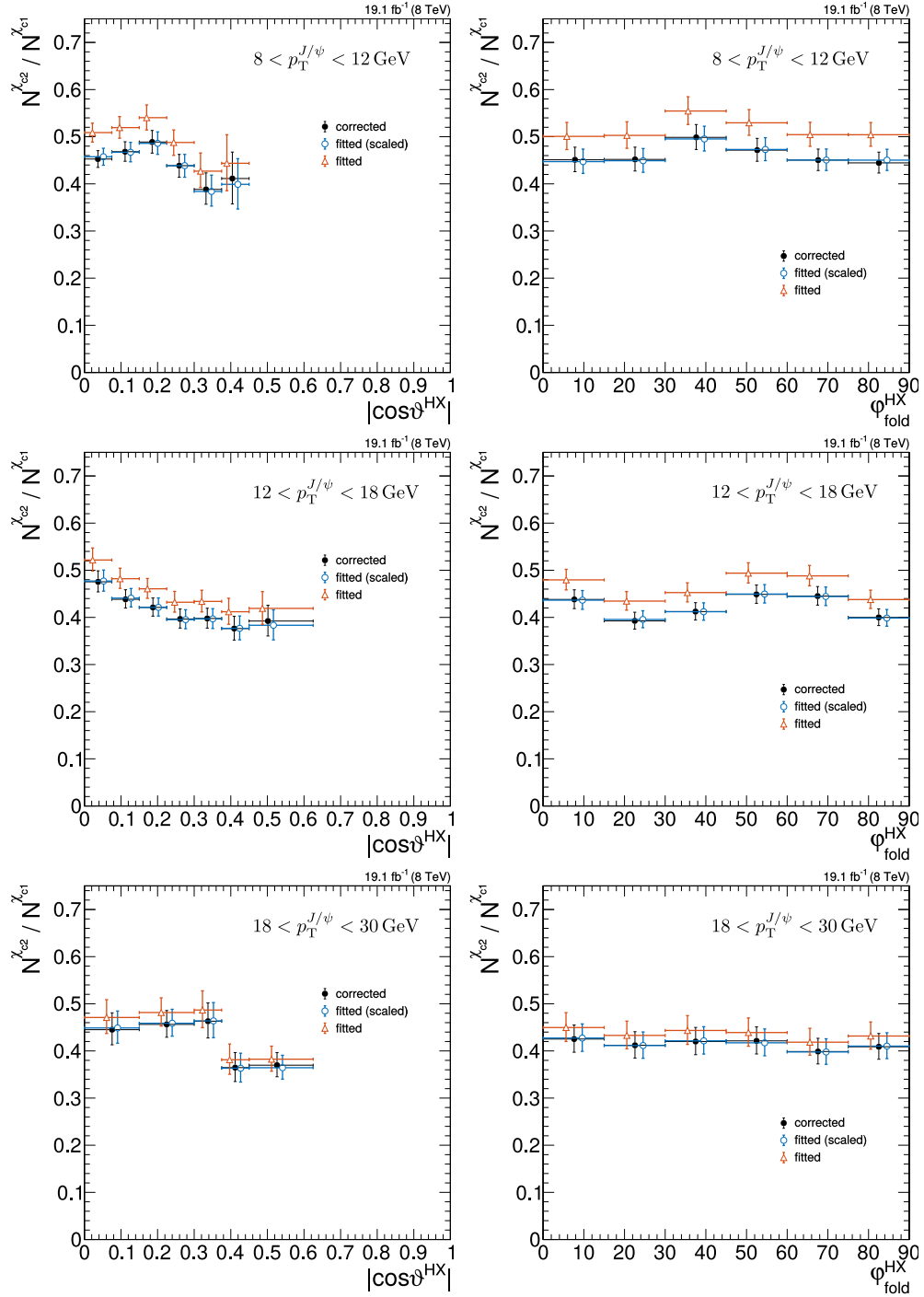


**Figure 5.15:** Ratios of  $\chi_{c2}$  over  $\chi_{c1}$  yields as a function of  $|\cos \vartheta^{\text{HX}}|$  (left) and  $\varphi^{\text{HX}}$  (right) for the three  $p_T^{J/\psi}$  ranges 8–12, 12–18 and 18–30 GeV (top to bottom). The three different sets of points correspond to the raw yields obtained from the simultaneous fits (“fitted”), after applying the acceptance times efficiency corrections (“corrected”) and to the fitted points scaled by a normalization factor (“fitted scaled”) to match the normalization of the corrected ratios. The blue and red points are shifted horizontally for better visibility.

## 5.6 Bayesian extraction of polarization parameters

The polarization parameters,  $\lambda_{\vartheta}^{\chi_{c1}}$ ,  $\Delta\lambda_{\vartheta}$ ,  $\lambda_{\varphi}^{\chi_{c1}}$  and  $\Delta\lambda_{\varphi} \equiv \lambda_{\varphi}^{\chi_{c2}} - \lambda_{\varphi}^{\chi_{c1}}$  are extracted from the measured and acceptance times efficiency corrected yield ratios using a Bayesian approach. The basis of the approach is the determination of a three-dimensional **posterior probability density** (PPD) depending on the normalization  $R_0$ ,  $\lambda_{\vartheta}^{\chi_{c1}}$  and  $\Delta\lambda_{\vartheta}$  ( $R_0$ ,  $\lambda_{\varphi}^{\chi_{c1}}$  and  $\Delta\lambda_{\varphi}$ ). From these 3D PPDs it is possible to obtain one-dimensional projections for each parameter which can in turn be used to determine central values and uncertainties or one-sided limits.

In order to determine the three-dimensional PPDs the corresponding three-dimensional parameter space is scanned. For each scanning point a weight  $w = \exp(-\frac{1}{2}\chi^2)$  is calculated, which is used to obtain the PPD as a weighted distribution of all scanned points. The  $\chi^2$  value is calculated between the measured yield ratios and the corresponding analytical functions which are defined in Eqs. (5.2) and (5.3). The scanning points are randomly generated according to their prior distributions.

For the overall normalization parameter  $R_0$ , which is not relevant for the measurement of the polarization parameters, no assumptions are made for the prior distribution. An importance sampling scheme has been adapted where the random values are drawn from a wide normal distribution around a central value which is taken as the value of the yield ratio in the first  $|\cos \vartheta^{\text{HX}}|$  or  $\varphi^{\text{HX}}$  bin. For each drawn value of  $R_0$  an importance sampling correction weight is determined as  $w_s = \text{No}(R_0|\mu, \sigma)$ , where  $\mu$  and  $\sigma$  are the central value and the width of the normal distribution used for importance sampling. The width is set to  $\sigma = 0.025$  and the central value  $\mu$  is chosen as the value of the corrected  $\chi_{c2}$  over  $\chi_{c1}$  yield ratio in the first  $|\cos \vartheta^{\text{HX}}|$  or  $\varphi^{\text{HX}}$  bin. The final weight for each generated scan point is given as  $w/w_s$ . In this way no constraints are placed on the value of  $R_0$  as the prior distribution can be interpreted as uniform in the range  $(-\infty, \infty)$ .

For the polarization parameters the only prior knowledge that is injected in the Bayesian approach are the physically allowed ranges of the parameters shown in Fig. 2.7 and defined in Eqs. (2.7) and (2.8). The prior distributions are generated assuming uniform distributions in these ranges:

- $\lambda_{\vartheta}^{\chi_{c1}} \sim \text{Un}(-\frac{1}{3}, 1)$
- $\lambda_{\vartheta}^{\chi_{c2}} \sim \text{Un}(-\frac{3}{5}, 1)$
- $\lambda_{\varphi}^{\chi_{c1}} \sim \text{Un}(-\frac{1}{3}, \frac{1}{3})$
- $\lambda_{\varphi}^{\chi_{c2}} \sim \text{Un}(-\frac{1}{\sqrt{5}}, \frac{1}{\sqrt{5}})$ .

The scanning points for the different parameters are generated independently from each other. The values for  $\Delta\lambda_{\vartheta} = \lambda_{\vartheta}^{\chi_{c2}} - \lambda_{\vartheta}^{\chi_{c1}}$ ,  $\kappa^{\chi_{c1}}$ , defined in Eq. (5.4), and  $\Delta\kappa = \kappa^{\chi_{c2}} - \kappa^{\chi_{c1}}$  are calculated using the generated values. Using these inputs the weight  $w$  is calculated for each multi-dimensional scanning point.

Figure 5.16 shows the resulting one-dimensional projections in the three  $p_T^{J/\psi}$  ranges for the parameters  $\Delta\lambda_\vartheta$  and  $\lambda_\vartheta^{\chi_{c1}}$ . A broad peak is present for all three  $p_T^{J/\psi}$  ranges in the projections for  $\Delta\lambda_\vartheta$ , covering mostly the negative part of the physically allowed range. For the lowest range from 8–12 GeV the peak is significantly broader than for the other two ranges. This is directly linked to the lower  $|\cos\vartheta^{\text{HX}}|$  coverage in this bin and also reflects the increased uncertainty on  $\lambda_\vartheta^{\chi_{c1}}$ . Nevertheless, a central value and a 68 % **confidence interval (CI)** can be trivially obtained from the median and the difference between the 0.16 and 0.84 quantiles of the projection in all three  $p_T^{J/\psi}$  ranges.

In the case of  $\lambda_\vartheta^{\chi_{c1}}$  the one-dimensional PPD projection does not exhibit a peak. However, compared to the uniformly distributed prior distribution the PPD shows a clear preference for larger values in the physically allowed range. Using the 0.1 quantile it is possible to determine a lower limit for  $\lambda_\vartheta^{\chi_{c1}}$  at the 90 % **confidence level (CL)**, which are also shown in Fig. 5.16 (right). In all three  $p_T^{J/\psi}$  ranges this lower limit is above zero, thus excluding about a quarter of the physically allowed range at the 90 % CL.

The results for  $\Delta\lambda_\varphi$  and  $\lambda_\varphi^{\chi_{c1}}$  are shown in Fig. 5.17. In this case a rather precise determination of  $\Delta\lambda_\varphi$  is possible as the corresponding projections of the 3D PPD exhibit a narrow peak almost centered at zero for all three  $p_T^{J/\psi}$  ranges. In contrast, the projection for  $\lambda_\varphi^{\chi_{c1}}$  reveals that basically no information about its actual value can be drawn from the yield ratios as a function of  $\varphi^{\text{HX}}$  as the PPD projection remains essentially flat in the complete physically allowed range.

## 5.7 Checks for systematic effects

Several sources of possible systematic effects have been investigated by checking how the results change when different aspects of the analysis are changed. The considered variations include changes to the fit model used for describing the  $\chi_{c1}$  and  $\chi_{c2}$  signal peaks and the continuum background, variations of the inputs used in the computation of the acceptance times efficiency corrections and changes to the threshold values of the lifetime significance and KVF probability selection criteria.

Only reasonable variations to the nominal settings were used to ensure that possible systematic effects are properly assessed without introducing a bias due to too extreme changes. For all of the variations under consideration the analysis was repeated. The obtained  $\Delta\lambda_\vartheta$  and  $\Delta\lambda_\varphi$  values and their uncertainties are compared to the values obtained using the nominal settings. Irrelevant changes are thus excluded. Only differences in the shape of the yield ratios are taken into account in the evaluation of the systematic uncertainties.

A pedagogical visualization of the systematic effects due to the variations of the acceptance times efficiency corrections for the yield ratio as a function of  $|\cos\vartheta^{\text{HX}}|$  in the  $p_T^{J/\psi}$  range between 12 and 18 GeV is shown in Fig. 5.18. While these results are useful for understanding the possible systematic effects, they are not actually used in



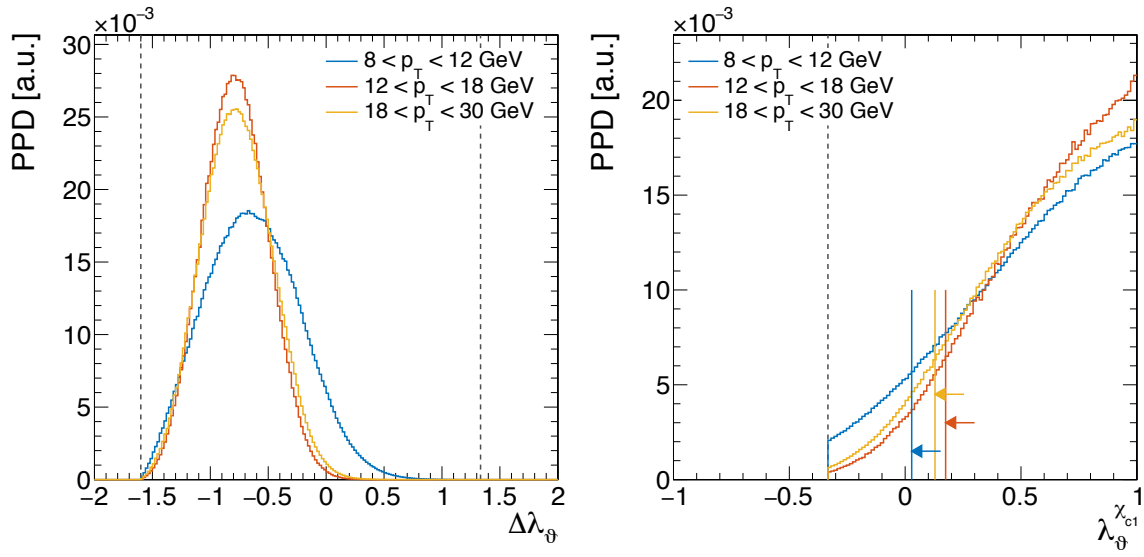


**Figure 5.16:** One-dimensional projections of the 3D PPD onto the variables  $\Delta\lambda_\phi$  (left) and  $\lambda_\phi^{\chi_{c1}}$  (right) for the three different  $p_T^{J/\psi}$  ranges. The vertical dashed lines indicate the physically allowed boundaries of the plotted parameters. The solid vertical lines denote the 90 % CL lower limits for  $\lambda_\phi^{\chi_{c1}}$ .

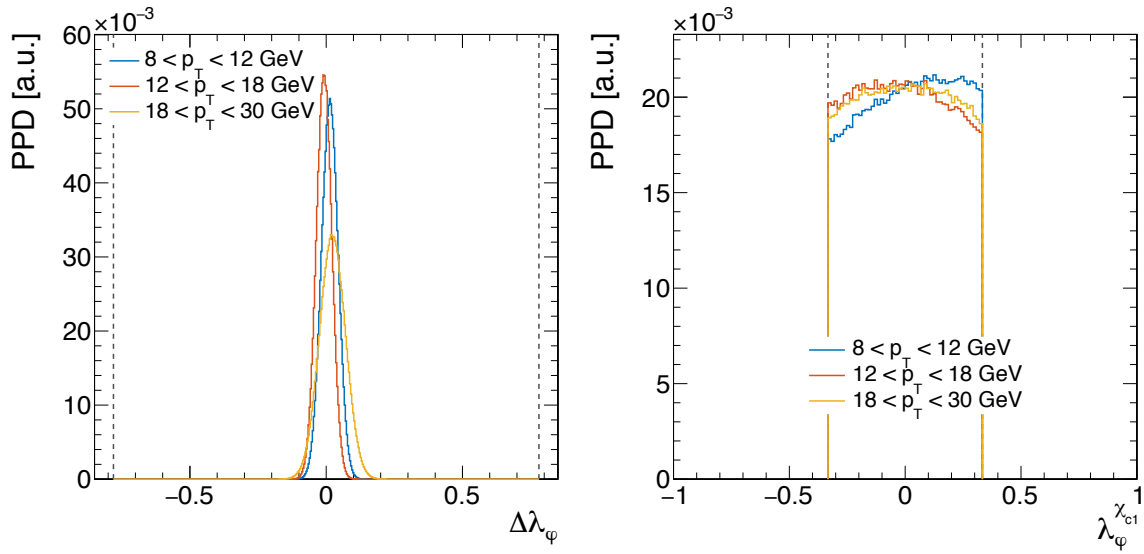


**Figure 5.17:** One-dimensional projections of the 3D PPD onto the variables  $\Delta\lambda_\phi$  (left) and  $\lambda_\phi^{\chi_{c1}}$  (right) for the three different  $p_T^{J/\psi}$  ranges. The vertical dashed lines indicate the physically allowed boundaries of the plotted parameters.

the determination of systematic uncertainties. Figure 5.18 (left) shows the  $\chi_{c2}$  over  $\chi_{c1}$  yield ratios after correcting them for acceptance and efficiency effects. The top left panel shows a direct comparison of the results and the different normalization scales introduced by the variations of the acceptance times efficiency corrections. However, when the variations are rescaled to have the same normalization as the nominal result the differences between the different variations almost vanish. This can be even better appreciated in the right panel of Fig. 5.18, which directly shows the relative difference of the variations with respect to the nominal results to more easily appreciate the actual changes in shape. In this case only one variation leads to visible changes in the order of 1 % in one of the  $|\cos \vartheta^{\text{HX}}|$  bins.

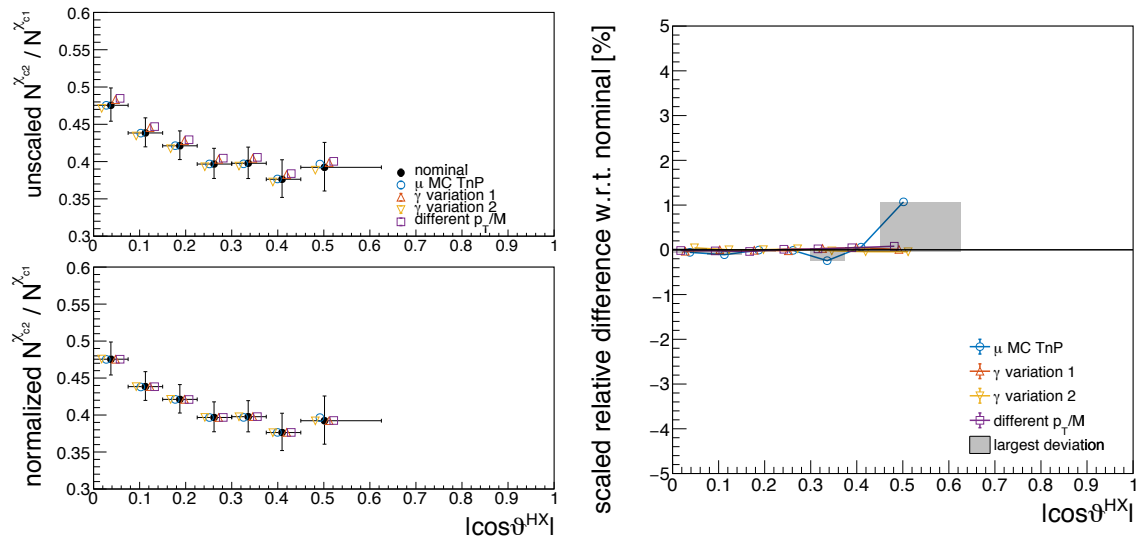


**Figure 5.18:** Comparison of the corrected yield ratio for different variations of the acceptance times efficiency corrections with (left, bottom panel) and without (left, top panel) scaling the variations to the nominal results. Relative difference between the scaled variations and the nominal results (right). The gray shaded area denotes the largest relative difference observed in each  $|\cos \vartheta^{\text{HX}}|$  bin.

The main drawback of this pedagogical approach is that it is hard to quantify the change introduced in  $\Delta\lambda_\vartheta$  or  $\Delta\lambda_\varphi$  by comparing the nominal ratio and the ones obtained using variations. For example, relative differences in the order of a few percent in a few  $|\cos \vartheta^{\text{HX}}|$  or  $\varphi^{\text{HX}}$  bins must not necessarily lead to large changes in  $\Delta\lambda_\vartheta$  or  $\Delta\lambda_\varphi$  if they appear in an essentially random “zig-zag” fashion. On the other hand, even very small relative differences can lead to significant changes in  $\Delta\lambda_\vartheta$  or  $\Delta\lambda_\varphi$  if they exhibit a monotonic behavior.

Thus, to actually quantify the magnitude of the changes introduced by different values the results of the Bayesian fit described in Sec. 5.6 are used. After the 3D PPDs have been determined for all variations the central value of  $\Delta\lambda_\vartheta$  or  $\Delta\lambda_\varphi$  and its uncertainties are determined from the 1D projections. From these the difference with respect to the nominal result is computed assuming fully correlated uncertainties. The

results of this procedure are visualized in Fig. 5.19 for the acceptance times efficiency correction variations. The left panel shows a comparison of the 1D projection of the PPD for the different variations, after shifting the projection by the central value of the nominal result. In this case all but one variation are virtually indistinguishable from the nominal result. This is also visible on the right panel where the differences between the nominal result and the variations are shown. All but one variation are indistinguishable from the nominal result and even the difference for this variation is small compared to the statistical uncertainty of the nominal result indicated by the red shaded bands.

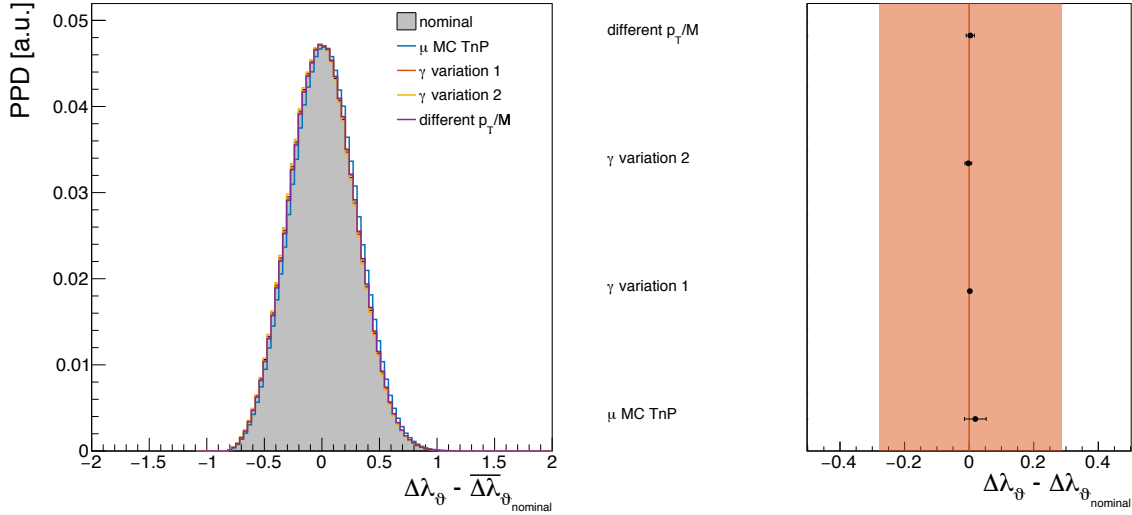


**Figure 5.19:** Comparison of the 1D projections of the 3D PPDs after shifting them by the nominal observed central value for  $\Delta\lambda_\theta$  (left) and the resulting difference in central value and its uncertainty (right). The red shaded band denotes the 68 % CI of the nominal result.

These results already show that the systematic uncertainties related to the acceptance times efficiency corrections will be small, as already anticipated from the results of the studies using simulated events. The details of the evaluation of the systematic uncertainties are discussed in Sec. 5.7.6. Before, all the tested variations will be briefly described. The figures showing the relative differences between the  $\chi_{c2}$  over  $\chi_{c1}$  yield ratios as a function of  $|\cos\vartheta^{\text{HX}}|$  or  $\varphi^{\text{HX}}$  have been placed in Appendix C.3. Figures showing the differences of  $\Delta\lambda_\theta$  and  $\Delta\lambda_\varphi$  with respect to the nominal results are also placed there and references to the corresponding figures are given in the sections describing the considered variations.

### 5.7.1 Signal peak fit model

The correct description of the  $\chi_{c1}$  and  $\chi_{c2}$  signal peaks in the simultaneous mass fits is a crucial detail of the analysis procedure as the results of the fits are used to

determine the acceptance and efficiency corrected  $\chi_{c2}$  over  $\chi_{c1}$  yield ratio from which the difference in the polarization parameters is estimated. The fit model remains unchanged in order to ensure an accurate description of the observed mass distributions. Instead, the main purpose of the variations of the signal peak model is to evaluate the sensitivity of the yield ratio on the exact description of the left and right tails of the DSCB model, defined in Eq. (5.10). Since, the peaks are partially overlapping details in the description of the tails potentially influence the cross-feed between the two signal peaks, which is expected to lead to the largest changes in the yield ratios.

Given that the right tail of both peaks is very small, its influence on the results is evaluated by simply removing it completely, effectively making the signal peak model a CB function. For the left tail, one of the tail parameters is fixed from MC studies. The effect of the left-tail parametrization is evaluated by replacing the default value of  $n_L = 3.2$  by four alternative values 2.8, 3.0, 3.4 and 3.6, which all still give a reasonable description of the signal peaks. To completely assess the possible effect of signal cross-feed from the left tail of the  $\chi_{c2}$  into the  $\chi_{c1}$  peak region, all possible combinations of the above mentioned variations are considered. These variations can be seen as rather conservative tests since they essentially assume that the effects that lead to the observed shapes of the signal peaks are different for the two states. The natural assumption would be that both signal shapes are affected by similar effects which would in turn cancel to some extent in the yield ratio.

Figures C.11 and C.16 show the comparison of the nominal results with all considered variations.

### 5.7.2 Background continuum fit model

The nominal shape of the continuum background as a function of  $|\cos \vartheta^{\text{HX}}|$  and  $\varphi^{\text{HX}}$  is identified by using only the sidebands of the measured spectra, excluding the intermediate signal region containing the  $\chi_{c0}$ ,  $\chi_{c1}$  and  $\chi_{c2}$  peaks. These studies show that all  $|\cos \vartheta^{\text{HX}}|$  and  $\varphi^{\text{HX}}$  bins can be described by almost identical shapes. In the nominal fit model only the parameter describing the high mass tail,  $\lambda^{\text{bg}}$ , is left free, while the two parameters describing the low-mass region,  $\mu^{\text{bg}}$  and  $\sigma^{\text{bg}}$ , are fitted either to constant values or to a linear dependency on  $|\cos \vartheta^{\text{HX}}|$  or  $\varphi^{\text{HX}}$ . But also the opposite choice of fitting  $\lambda^{\text{bg}}$  to a constant and leaving  $\mu^{\text{bg}}$  and  $\sigma^{\text{bg}}$  as free parameters is found to lead to a good description of the background shape. Consequently, this option is used as one variation of the background model.

Another variation is obtained by replacing the default model with a “power law times exponential” function, which has previously also been used in Refs. [39, 117], defined as

$$\mathcal{M}'_{\text{bg}}(m) = |m - q_0|^\alpha \cdot \exp[\beta(m - q_0)] . \quad (5.17)$$

Here  $\alpha$  is fitted to a constant, while  $\beta$  is left free in all bins. The low mass cut-off,  $q_0$ , is fixed to 3.2 GeV, a value determined from fits to the mass sidebands.

The comparison of the results of the variations and the nominal results can be found in Figs. C.12 and C.17.

### 5.7.3 Acceptance times efficiency corrections

As described in Sec. 5.3 the computation of the acceptance times efficiency corrections depends on the single muon and photon reconstruction efficiencies that are used as inputs for the generation of the Fast MC samples from which the correction maps are determined. Even though the studies using Fast MC samples have shown that the analysis is largely insensitive to the exact details of the used reconstruction efficiencies, different input efficiencies are used to assess how sensitive the measurement is to them. In case of the photon reconstruction efficiencies the nominal ones are replaced by two variations, one with a steeper turn-on curve and one with a flatter turn-on curve, shown in Fig. 5.6. For the muon reconstruction efficiencies the nominally used efficiencies determined from data samples using the Tag-and-Probe method are replaced by the corresponding efficiencies evaluated using Full MC samples, which exhibit a significantly different low  $p_T$  turn-on behavior, as can be seen in Fig. 5.5.

Independently, another variation is considered using alternative kinematic distributions in the Fast MC generation, with different  $p_T/M$  shapes for the  $\chi_{c1}$  and  $\chi_{c2}$  states. The difference in the  $p_T/M$  shapes is chosen to be compatible with the differences between the two states reported in Ref. [35]. Specifically,  $\beta = 3.56$  is used for the generation of the  $\chi_{c2}$  samples instead of the nominal value of 3.4, which corresponds to a difference between the two states covering the full range of the reported values and their uncertainties in Ref. [35].

The results of these variations in comparison with the nominal results are shown in Figs. C.13 and C.18.

### 5.7.4 Prompt selection

Prompt events are selected by rejecting  $\chi_c$  candidates with a lifetime significance larger than 2.5. Using this approach a small NP contamination remains in the sample which is expected to only have a negligible influence on the  $\chi_{c2}$  over  $\chi_{c1}$  yield ratios. To check that this is indeed the case, the cut value is changed from the default value of 2.5 to the alternative values of 2.0 and 3.0.

Figures C.14 and C.19 show how the yield ratios and consequently the values of  $\Delta\lambda_\psi$  and  $\Delta\lambda_\phi$  change under these variations.

### 5.7.5 KVF probability cut

The reconstruction of the  $\chi_c$  candidates is performed through a kinematic vertex fit of the two electron and two muon tracks, as described in Sec. 3.3. Since the reconstruction of the electron and muon tracks are done independently of each other, the chances of misidentifying one as the other are virtually non-existent. Hence, given reasonable descriptions of the reconstruction efficiencies of the conversion photon and the single muons, correlations between the two reconstruction processes can only be introduced by the KVF. For the nominal analysis a minimum  $\chi^2$  probability of 1 %

is used. To evaluate if the measurement is sensitive to this cut value it is repeated with three other cut values of 0.5, 2 and 3 %.

The effects of these variations on the results are shown in Figs. C.15 and C.20.

### 5.7.6 Evaluation of the systematic uncertainties

The results of the numerous variations that were considered are turned into systematic uncertainties corresponding to each of the previously mentioned categories following the recommendations of the CMS statistics committee. These recommendations are based on the ones that can be found in Ref. [169].

Specifically, all the variations that do not change the underlying sample may in principle be interpreted as actual changes to the procedure and are considered to be “modelling uncertainties”. These are the signal peak and continuum background model as well as the acceptance times efficiency variations. The largest absolute deviation of all variations in each of these categories is taken as the symmetric systematic uncertainty. On the contrary, variations in which the underlying sample is changed, in this case the prompt selection and the KVF probability cut, are considered to be “pass/fail tests”. Of the 30 studied variations that fall into this class, only one exceeds the  $2\sigma$  significance level, at  $2.3\sigma$ . Therefore, all checks are considered as passed and no corresponding systematic uncertainties are assigned.

Table 5.3 gives an overview of all the considered sources of systematic uncertainties and the corresponding values for  $\Delta\lambda_\vartheta$  and  $\Delta\lambda_\varphi$ . No dominant systematic uncertainty can be identified. The total systematic uncertainty is calculated as the sum in quadrature of the individual contributions. It is small compared to the statistical uncertainty which ranges between 0.28 and 0.40 for  $\Delta\lambda_\vartheta$  and between 0.03 and 0.05 for  $\Delta\lambda_\varphi$ .

**Table 5.3:** Systematic uncertainties on  $\Delta\lambda_\vartheta$  and  $\Delta\lambda_\varphi$ , for each of the three  $p_T^{J/\psi}$  ranges.

$p_T^{J/\psi}/\text{GeV}$	8–12	12–18	18–30
$\Delta\lambda_\vartheta$			
signal peak fit model	0.075	0.034	0.029
background continuum fit model	0.040	0.024	0.053
acceptance times efficiency corrections	0.029	0.019	0.047
prompt selection cut	–	–	–
KVF probability cut	–	–	–
$\Delta\lambda_\varphi$			
signal peak fit model	0.003	0.002	0.002
background continuum fit model	0.002	0.003	0.002
acceptance times efficiency corrections	0.003	0.002	0.001
prompt selection	–	–	–
KVF probability cut	–	–	–

## 5.8 Discussion of the results

The results of the Bayesian parameter extraction for  $\Delta\lambda_\vartheta$  and  $\Delta\lambda_\varphi$  are shown as a function of  $p_T^{J/\psi}$  in Fig. 5.20 and summarized in Table 5.4. Along the  $x$ -axis the points have been placed at the mean  $p_T^{J/\psi}$  value in each range. The results for both parameters are completely dominated by the statistical uncertainties, as can be appreciated by the barely visible blue bands in Fig. 5.20 and from the numerical values in Table 5.4.

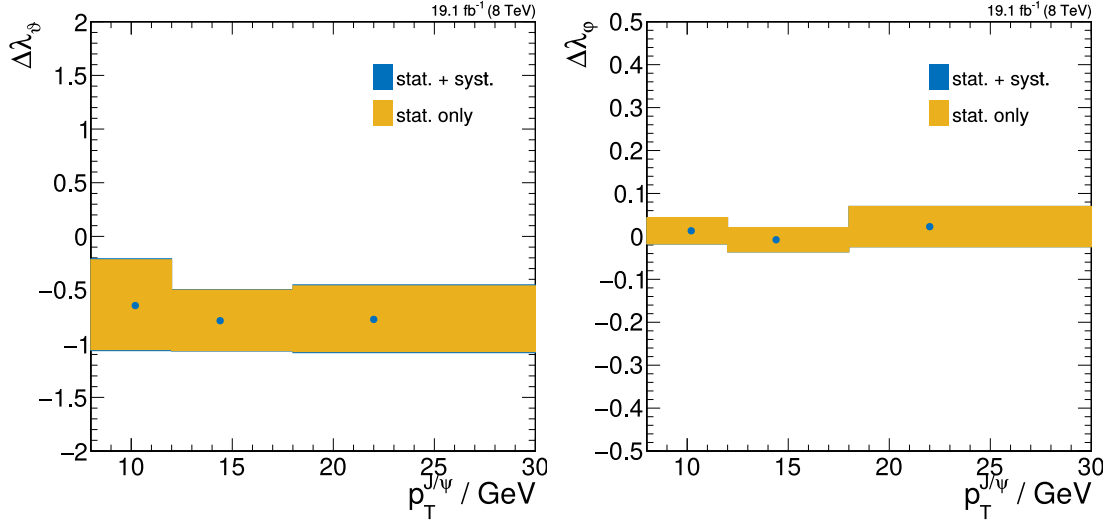


**Figure 5.20:** Values for  $\Delta\lambda_\vartheta$  (left) and  $\Delta\lambda_\varphi$  (right) as a function of  $p_T^{J/\psi}$ . The yellow bands represent statistical uncertainties at 68.3 % CL, while the blue bands represent the total uncertainty.

**Table 5.4:** Values for  $\Delta\lambda_\vartheta$  and  $\Delta\lambda_\varphi$  and their statistical and systematic uncertainties in the three different  $p_T^{J/\psi}$  ranges.

$p_T^{J/\psi} / \text{GeV}$	value	stat. uncer.	syst. uncer
$\Delta\lambda_\vartheta$			
8–12	-0.64	$\pm 0.42$	$\pm 0.09$
12–18	-0.79	$\pm 0.28$	$\pm 0.05$
18–30	-0.77	$\pm 0.31$	$\pm 0.08$
$\Delta\lambda_\varphi$			
8–12	0.013	$\pm 0.030$	$\pm 0.005$
12–18	-0.008	$\pm 0.028$	$\pm 0.004$
18–30	0.023	$\pm 0.047$	$\pm 0.003$

The measured values for  $\Delta\lambda_\varphi$  are compatible with being zero independently of  $p_T^{J/\psi}$ . Even though no information about the absolute values of  $\lambda_\vartheta^{Xc1}$  and  $\lambda_\vartheta^{Xc2}$  can be

extracted from the  $\chi_{c2}$  over  $\chi_{c1}$  yield ratios as a function of  $\varphi^{\text{HX}}$ , shown in Fig. 5.21 (left), the absence of azimuthal anisotropy differences is a strong indication for the HX frame to be close to the natural polarization frame. Polar polarization differences in other reference frames would lead to  $\Delta\lambda_\varphi$  being different from zero in the HX frame, which is not the case. Two exemplifying curves for large azimuthal anisotropy differences that would arise from extreme polar anisotropy differences in the CS frame are shown in Fig. 5.21 (left). The dotted (dash-dotted) line corresponds to the  $J_z^{\chi_{c1}} = J_z^{\chi_{c2}} = 0$  ( $J_z^{\chi_{c1}} = \pm 1, J_z^{\chi_{c2}} = \pm 2$ ) angular momentum configurations along the CS quantization axis.

In the  $\varphi^{\text{HX}}$  analysis the data extend over the full range from 0 to 90°. Contrary to this, the data coverage of  $|\cos\vartheta^{\text{HX}}|$  misses the high- $|\cos\vartheta^{\text{HX}}|$  edge, where different polarization scenarios can be more easily distinguished. Thus, the  $|\cos\vartheta^{\text{HX}}|$  coverage is the main limiting factor for the precision of the polar anisotropy parameter measurement. From the Bayesian parameter extraction only lower limits for  $\lambda_\vartheta^{\chi_{c1}}$  can be obtained from the projections of the PPDs shown in Fig. 5.16 (right). At 90 % CL these lower bounds are 0.03, 0.17 and 0.13 for the three consecutive  $p_{\text{T}}^{\text{J}/\psi}$  ranges. These bounds already indicate that J/ $\psi$  mesons produced in  $\chi_{c1}$  decays are transversely polarized, meaning that the  $\chi_{c1}$  mesons tend to be produced with angular momentum component  $J_z = 0$  along the helicity axis [71].

For the comparison of the  $\chi_{c1}$  over  $\chi_{c2}$  yield ratio as a function of  $|\cos\vartheta^{\text{HX}}|$ , shown in Fig. 5.21 (right), two specific polarization scenarios are used: the unpolarized scenario, corresponding to  $\lambda_\vartheta^{\chi_{c1}} = \lambda_\vartheta^{\chi_{c2}} = 0$ , and a scenario which uses the  $\lambda_\vartheta$  values listed in Table 5.5 in accordance with predictions obtained within the NRQCD framework [35] (as described in Sec. 2.6). A fit with free normalizations of the analytical shapes yields a  $\chi^2/\text{ndf}$  value of 31/15, corresponding to a  $\chi^2$  probability of only 0.9 % for the unpolarized scenario. On the other hand, the analytic shapes corresponding to the NRQCD scenario are able to describe the measured yield ratios nicely. The corresponding  $\chi^2/\text{ndf}$  values obtained from a fit with free normalization is 13/15 leading to a  $\chi^2$  probability of 58 %. The observed  $\chi^2/\text{ndf}$  values, and consequently the  $\chi^2$  probabilities, do not change significantly when repeating the procedure and considering  $\chi_{c2}$  over  $\chi_{c1}$  ratios obtained from the systematic variations described in Sec. 5.7.

**Table 5.5:** Values for  $\lambda_\vartheta^{\chi_{c1}}$  and  $\lambda_\vartheta^{\chi_{c2}}$  obtained from evaluating the NRQCD prediction bands in Fig. 2.11 from Ref. [35] at the mean value of the observed  $(p_{\text{T}}/M)^{\text{J}/\psi}$  in the three  $p_{\text{T}}^{\text{J}/\psi}$  ranges.

$p_{\text{T}}^{\text{J}/\psi} / \text{GeV}$	$(p_{\text{T}}/M)^{\text{J}/\psi}$	$\lambda_\vartheta^{\chi_{c1}}$	$\lambda_\vartheta^{\chi_{c2}}$
8–12	3.3	0.72	-0.48
12–18	4.7	0.65	-0.35
18–30	7.1	0.56	-0.19

The results of a simultaneous fit of the  $\chi_{c1}$  over  $\chi_{c2}$  yield ratios as a function of  $|\cos\vartheta^{\text{HX}}|$  in all three  $p_{\text{T}}^{\text{J}/\psi}$  ranges imposing  $p_{\text{T}}^{\text{J}/\psi}$  independent values of  $\lambda_\vartheta^{\chi_{c1}}$  and  $\lambda_\vartheta^{\chi_{c2}}$  is



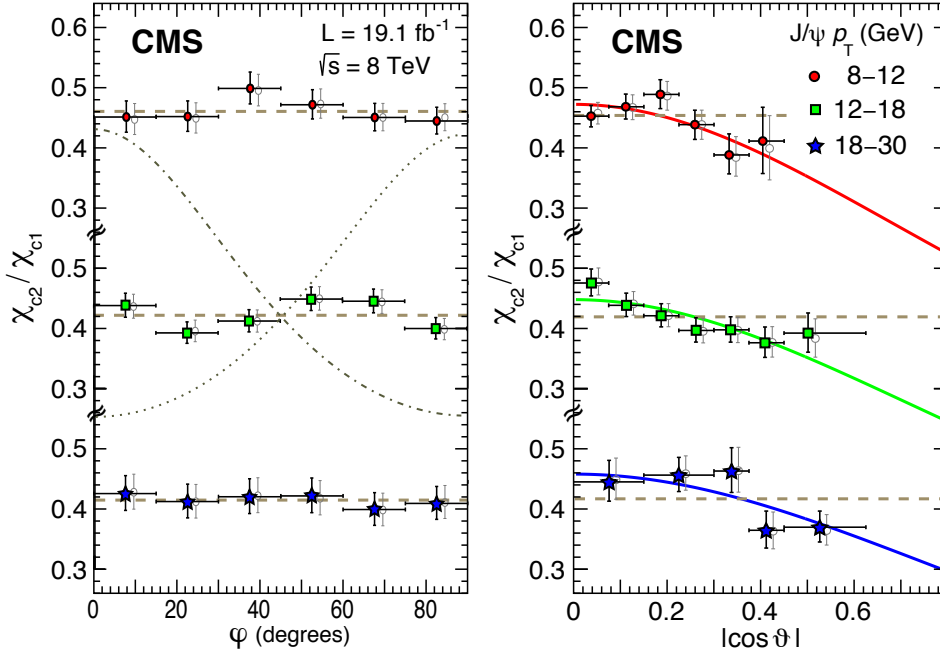


**Figure 5.21:** Ratios of  $\chi_{c2}$  over  $\chi_{c1}$  yields as a function of  $\varphi^{\text{HX}}$  (left) and  $|\cos \vartheta^{\text{HX}}|$  (right) for the three  $p_T^{J/\psi}$  ranges in comparison with different polarization scenarios: unpolarized (dashed), NRQCD predicted (solid) and two azimuthal anisotropy scenarios (dotted and dash-dotted) that would arise for maximal polar anisotropies in the CS frame. The grey markers show the values of the ratios before acceptance and efficiency corrections.

shown in Fig. 5.22. The contours are obtained from scanning the two  $\lambda_\vartheta$  parameters and the three independent normalizations to evaluate the  $\chi^2$  profiles corresponding to the 68.3 %, 95.5 % and 99.7 % CLs. The unpolarized scenario as well as more than half of the physically allowed region are excluded, as they are outside of the 99.7 % CL contour. This region also includes all cases where  $\lambda_\vartheta^{X_{c2}} \geq \lambda_\vartheta^{X_{c1}}$ , and the pure angular momentum configurations  $J_z^{X_{c2}} = \pm 2$  as well as  $J_z^{X_{c1}} = J_z^{X_{c2}} = \pm 1$ . The conclusion that the  $\chi_{c1}$  mesons are primarily produced in the  $J_z^{X_{c1}} = 0$  angular momentum state can also be drawn from these contours, similar to the findings from the Bayesian approach described above.

The correlation between  $\lambda_\vartheta^{X_{c2}}$  and  $\lambda_\vartheta^{X_{c1}}$ , already visible in Fig. 5.22, can be expressed through a simple parametrization:  $\lambda_\vartheta^{X_{c2}} = (-0.94 + 0.90\lambda_\vartheta^{X_{c1}}) \pm (0.51 + 0.05\lambda_\vartheta^{X_{c1}})$ ,  $(-0.76 + 0.80\lambda_\vartheta^{X_{c1}}) \pm (0.26 + 0.05\lambda_\vartheta^{X_{c1}})$  and  $(-0.78 + 0.77\lambda_\vartheta^{X_{c1}}) \pm (0.26 + 0.06\lambda_\vartheta^{X_{c1}})$ , in the three consecutive  $p_T^{J/\psi}$  ranges. These expressions are obtained from fits to the  $\chi_{c2}$  over  $\chi_{c1}$  yield ratios as a function of  $|\cos \vartheta^{\text{HX}}|$  where  $\lambda_\vartheta^{X_{c1}}$  is fixed and scanned over the positive range  $\lambda_\vartheta^{X_{c1}} \in [0, 1]$ . The perfect linear relation between  $\lambda_\vartheta^{X_{c2}}$  and  $\chi_{c1}$  that arises from these fits is shown in Fig. 5.23, where the central values of  $\lambda_\vartheta^{X_{c2}}$  are shown as a function of  $\lambda_\vartheta^{X_{c1}}$ . The uncertainties in the parametrizations include

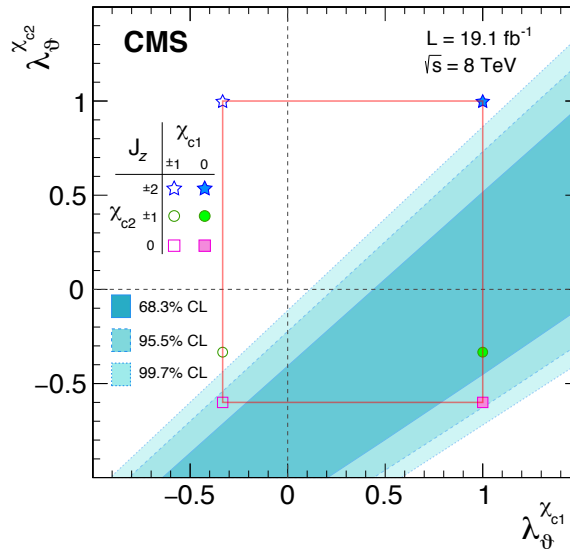


**Figure 5.22:** Two-dimensional contours for  $\lambda_{\theta}^{\chi_{c2}}$  vs.  $\lambda_{\theta}^{\chi_{c1}}$ , at the 68.3 %, 95.5 % and 99.7 % CLs, obtained from a simultaneous fit of the yield ratios as a function of  $|\cos \vartheta^{\text{HX}}|$  in all three  $p_{\text{T}}^{\text{J}/\psi}$  ranges. The physically allowed region (red rectangle) and six pure angular momentum configurations (markers) are also shown.

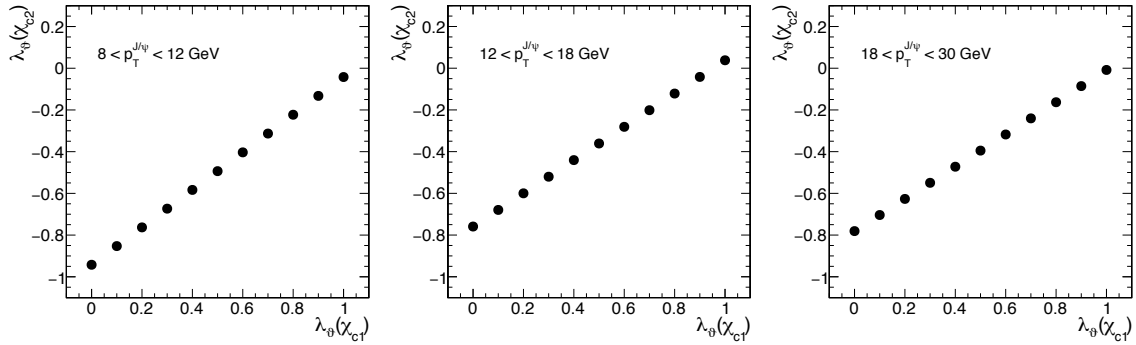
the systematic uncertainties, which are determined as described in Sec. 5.7.6. Hence, these values can be used to directly the results to different theoretical predictions.

Figure 5.24 shows the comparison to two different polarization scenarios, once with  $\lambda_{\theta}^{\chi_{c1}}$  values according to the NRQCD prediction [35], and once assuming unpolarized  $\chi_{c1}$  production. In the former case there is an overall good agreement with the predicted band for  $\lambda_{\theta}^{\chi_{c2}}$ , while the resulting values for the assumption  $\lambda_{\theta}^{\chi_{c1}} = 0$  lead to  $\lambda_{\theta}^{\chi_{c2}}$  significantly different from zero and with central values that are even outside of the physically allowed range.

## 5.9 Summary

The polarizations of the promptly produced  $\chi_{c1}$  and  $\chi_{c2}$  mesons are measured using a newly developed analysis approach where the relative  $\chi_{c2}$  over  $\chi_{c1}$  yields are obtained as a function of  $|\cos \vartheta^{\text{HX}}|$  and  $\varphi^{\text{HX}}$ . This method has proven to be unbiased and robust against all tested systematic effects. The data sample, recorded in pp collisions in 2012 at  $\sqrt{s} = 8$  TeV, corresponding to  $19.1 \text{ fb}^{-1}$  allowed for a precise measurement of  $\Delta\lambda_{\theta}$  and  $\Delta\lambda_{\varphi}$  over the whole covered  $p_{\text{T}}^{\text{J}/\psi}$  range from 8–30 GeV. The measured  $\Delta\lambda_{\varphi}$  values exhibit no trend as a function of  $p_{\text{T}}^{\text{J}/\psi}$  and are compatible with being zero. In the case of the measurement of  $\Delta\lambda_{\theta}$ , the reduced coverage of the  $|\cos \vartheta^{\text{HX}}|$  range is a major challenge.

The absence of azimuthal polarization differences indicates that the chosen measurement frame, the HX frame, is close to the natural polarization frame. The com-



**Figure 5.23:** Measured  $\lambda_\phi^{\chi_{c2}}$  values for different fixed values of  $\lambda_\phi^{\chi_{c1}}$  in the three  $p_T^{J/\psi}$  ranges (from left to right). For better visibility only the central values are shown.

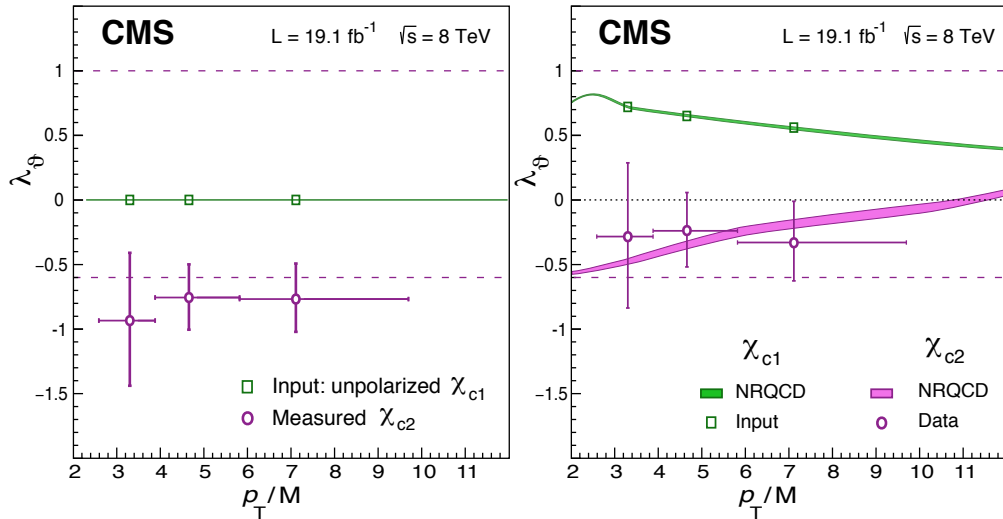


**Figure 5.24:** Measured  $\lambda_\phi^{\chi_{c2}}$  values as a function of  $(p_T/M)^{J/\psi}$  for  $\lambda_\phi^{\chi_{c1}}$  values fixed according to the unpolarized scenario (left) and the NRQCD scenario (right). The dashed horizontal lines show the physically allowed range of  $\lambda_\phi^{\chi_{c2}}$  from  $-0.6$  to  $1$ . The horizontal bars denote the width of the individual bins.

parison of the measured  $\chi_{c2}$  over  $\chi_{c1}$  yield ratios as a function of  $|\cos \vartheta^{\text{HX}}|$  with different polarization scenarios has revealed that the unpolarized scenario, corresponding to  $\lambda_{\vartheta}^{\chi_{c1}} = \lambda_{\vartheta}^{\chi_{c2}} = 0$  is strongly disfavored by the measurements, while a good agreement with the prediction in accordance with NRQCD based on the measurements of other quarkonium states and the  $\chi_{c2}$  over  $\chi_{c1}$  cross sections ratios, described in Sec. 2.6, can be observed.

The joint consideration of the  $\chi_{c2}$  over  $\chi_{c1}$  yield ratios as a function of  $|\cos \vartheta^{\text{HX}}|$  in all three  $p_{\text{T}}^{J/\psi}$  ranges, imposing  $p_{\text{T}}^{J/\psi}$  independent values of  $\lambda_{\vartheta}^{\chi_{c1}}$  and  $\lambda_{\vartheta}^{\chi_{c2}}$ , leads to the conclusion that the  $J/\psi$  from  $\chi_{c1}$  decays are significantly differently polarized than the ones from  $\chi_{c2}$  decays. Even though these two polarizations correspond to very different angular decay distributions, the corresponding angular momentum state is similar for both  $\chi_c$  states. Both are produced with a large  $J_z = 0$  component in the HX frame. Large contributions of the  $J_z = \pm 1$  component can be excluded for the  $\chi_{c1}$  mesons, while predominant production in the  $J_z = \pm 2$  configuration can be excluded for the  $\chi_{c2}$  mesons.

This measurement marks the first measurement of  $P$ -wave quarkonium polarization in hadron collisions and should trigger further progress in the understanding of the strong interaction and hadron formation.

# Conclusions

“And now his watch is ended,” the black brothers said, in solemn chant.

“And now his watch is ended,” Mormont echoed.

---

*(George R. R. Martin, A Storm of Swords - Samwell II)*

The quest for understanding hadron formation is still an active area of research. Quarkonium production represents an ideal probe to study how quarks bind into hadrons, as the heavy masses of the involved  $c$  and  $b$  quarks lead to a separation of the timescales at which the initial  $q\bar{q}$  pair is produced and at which it subsequently transforms into the bound state. This conjecture is the basis of the NRQCD factorization approach, the currently prevalent theoretical model describing quarkonium production. The production of the pre-resonant  $q\bar{q}$  state is described by a superposition of color-singlet and color-octet configurations calculable in the realm of perturbative QCD. The evolution of the initial state into the bound state is governed by constant, supposedly universal factors that have to be extracted from experimental measurements.

After a great initial success of the NRQCD factorization approach in describing the cross section measurements reported by the Tevatron experiments, the community became somewhat disillusioned when the first polarization measurements of the same experiments could not be reproduced by theoretical calculations. The experimental inconsistencies by which these polarization measurements were plagued were identified shortly before the advent of the LHC physics program, which allowed for consistent polarization measurements by the LHC experiments. In recent years the  $S$ -wave quarkonium states have received the most attention from an experimental point of view and today a multitude of cross-section and polarization measurements exists for the  $J/\psi$ ,  $\psi(2S)$  and  $\Upsilon(nS)$  states. Several LHC experiments have published cross sections and their ratios for the  $P$ -wave states, but no polarization measurement exists until now.

Updated phenomenological studies have revealed remarkably simple patterns in quarkonium production at the LHC that are in stark contrast to the variegated structure of the NRQCD factorization approach. Nevertheless, calculations performed in the NRQCD framework are able to reproduce the experimental measurements very

well, through a series of seemingly surprising cancellations of terms. Moreover, these considerations lead to a surprising prediction for the polarizations of the  $\chi_{c1}$  and  $\chi_{c2}$  mesons, which should be strong and, more importantly, opposite. As of today this arguably represents the most important benchmark for the NRQCD framework.

This thesis presented the first measurement of inclusively produced prompt  $P$ -wave quarkonium states by studying the decay angular distribution of the  $J/\psi$  in the radiative decays of  $\chi_{c1}$  and  $\chi_{c2}$  mesons. The measurement was performed on data collected by the CMS experiment in pp collisions at a center-of-mass energy  $\sqrt{s} = 8$  TeV during the 2012 data taking period. Using a newly developed analysis strategy the parameters  $\Delta\lambda_\varphi = \lambda_\varphi^{\chi_{c2}} - \lambda_\varphi^{\chi_{c1}}$  and  $\Delta\lambda_\vartheta = \lambda_\vartheta^{\chi_{c2}} - \lambda_\vartheta^{\chi_{c1}}$  were determined from the angular decay distributions of  $J/\psi$  mesons appearing in the radiative decays of the  $\chi_c$  states. The parameters are extracted using fits to the  $\chi_{c2}$  over  $\chi_{c1}$  yield ratios as a function of  $|\cos\vartheta^{\text{HX}}|$  and  $\varphi^{\text{HX}}$  in three  $p_{\text{T}}^{J/\psi}$  ranges, 8–12, 12–18 and 18–30 GeV. Furthermore, lower limits at 90 % CL were determined for the parameter  $\lambda_\vartheta^{\chi_{c1}}$ .

While  $\Delta\lambda_\varphi$  is compatible with being zero independently of  $p_{\text{T}}^{J/\psi}$ , the measured values of  $\Delta\lambda_\vartheta$  indicate strong and opposite polar anisotropies for the  $\chi_{c1}$  and  $\chi_{c2}$  mesons. The vanishing azimuthal anisotropy differences also serve as a cross-check of the assumption that the HX frame, in which the measurement is performed, is close to the natural polarization frame of the  $\chi_{c1}$  and  $\chi_{c2}$  mesons, as polar anisotropy differences in other frames lead to visible azimuthal polarization differences in the HX frame.

The combination of the measurements in the three  $p_{\text{T}}^{J/\psi}$  ranges indicates that the  $J/\psi$  mesons in  $\chi_{c1}$  decays are significantly differently polarized than the ones in  $\chi_{c2}$  decays. These results indicate that the  $\chi_{c1}$  and  $\chi_{c2}$  mesons are produced in similar angular momentum configurations. However, at the current level of precision it is not yet possible to exclude the possibility that they are produced in different configurations.

The measurement marks the first observation of inclusively produced quarkonium states with a non-zero polarization at mid-rapidity and high- $p_{\text{T}}$ , contrary to the already measured  $S$ -wave quarkonium polarizations. Comparisons of the measured  $\chi_{c2}$  over  $\chi_{c1}$  yield ratios as a function of  $|\cos\vartheta^{\text{HX}}|$  with analytical shapes corresponding to the unpolarized polarization scenarios have shown that the unpolarized scenario is strongly disfavored. On the other hand, the scenario predicted within the NRQCD framework from cross section ratio measurements are in agreement with the measured results.

The reported measurement will trigger further progress in the understanding of the strong interaction and hadron formation. They are the last missing ingredient to completing the full picture of quarkonium production for the charmonium family. With the information of recently published  $J/\psi$  and  $\psi(2S)$  cross section and polarization measurements as well as the cross section ratios between  $\chi_{c1}$  and  $\chi_{c2}$  and the newly available measurements of the relative polarization difference between the latter two states new theoretical calculations and phenomenological studies will

be able to more precisely constrain the production mechanisms of the  $\chi_{c1}$  and  $\chi_{c2}$  mesons. Moreover, the results will also allow for a better understanding of the impact of the  $\chi_c$  feed-down on  $J/\psi$  meson measurements. A more precise determination of the polarization of directly produced  $J/\psi$  mesons, which are affected by the, up until now unknown, polarization of the feed-down contributions from  $\chi_{c1}$  and  $\chi_{c2}$  decays will be possible.

One of the next logical experimental steps would be to extend the current measurements to data samples collected during Run II of the LHC. The data samples already collected during Run II correspond to an integrated luminosity of roughly  $150 \text{ fb}^{-1}$ . Combining the increased center-of-mass energy of  $\sqrt{s} = 13 \text{ TeV}$  and the increased instantaneous luminosity, quarkonium production yields are expected to be almost a factor of four larger than during Run I conditions. This makes it possible to extend the high- $p_T$  reach of future analysis using Run II data. However, the increase in instantaneous luminosity and center-of-mass energy is also accompanied by an increase in PU, which makes the reconstruction of quarkonium states more difficult. Especially the reconstruction efficiency of the converted photons in the tracker material of CMS is significantly affected by PU. Thus, the increase of available  $\chi$  candidate events will be lower than expected. Nevertheless, more precise measurements than currently available should be feasible, both for the  $S$ -wave as well as for the  $P$ -wave states.

The presented analysis strategy can in principle also be extended to the corresponding measurement of the polarizations of the  $\chi_b$  mesons. The necessary adaptations mainly concern the fit model used to extract the  $\chi_b$  yields from the invariant mass distribution. The major challenge for the measurement in the bottomonium family is the resolution of the  $J = 1$  and  $J = 2$  states for the  $\chi_{bJ}(mP)$  ( $m = 1, 2, 3$ ), which are much closer in mass than the  $\chi_{c1}$  and  $\chi_{c2}$  states. However, if this separation can be achieved sufficiently well for at least one of the three triplets in the bottomonium family, a more complete picture of quarkonium production will also be in reach for the bottomonium family, which is affected by a much more complicated feed-down structure compared to the charmonium family.

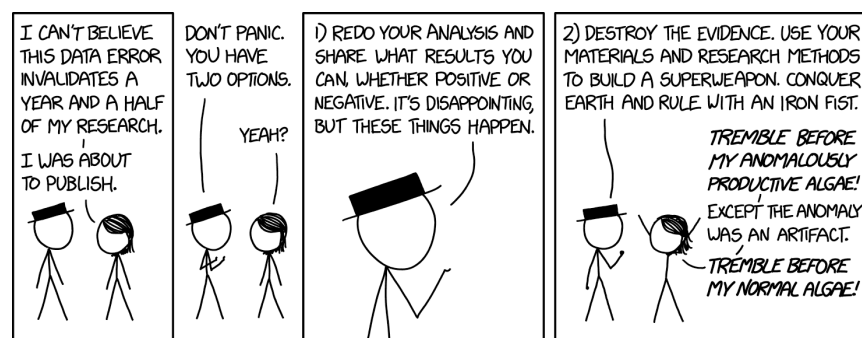
While the new polarization results seem to favor the NRQCD factorization approach, a few theoretical aspects of NRQCD still require a complete and rigorous proof. It is currently still not established that the LDMEs are truly universal. Experimentally, this can be tackled by measuring the production of quarkonium states in other collision systems or their production in association with other particles. ATLAS has already observed the production of  $J/\psi$  in association with  $W^\pm$  [170, 171] and  $Z^0$  [172] bosons. Once the universality of quarkonium production is understood, this knowledge can be applied to enhance the predictive power of the NRQCD factorization approach in other production channels, such as, for example, heavy-ion collisions. Future measurements of the couplings of the Higgs boson to  $b$  and  $c$  quarks also profit from an improved understanding of quarkonium production, as the process of  $H \rightarrow J/\psi\gamma$  is considered the golden channel for the measurement of the  $Hc\bar{c}$  coupling.



Die approbierte gedruckte Originalversion dieser Dissertation ist an der TU Wien Bibliothek verfügbar.  
The approved original version of this doctoral thesis is available in print at TU Wien Bibliothek.



# Other Approaches to $\chi_c$ Polarization Measurements



(<https://xkcd.com/2239>)

Unlike light following the shortest possible path in general relativity, scientific progress is seldomly achieved by not straying at least a little bit from the ideal path. In the case of the analysis presented in the main matter of this thesis, at least from a subjective point of view of the author, some of the steps that were taken in the “stumbling” towards the solution merit mentioning. Without even dreaming to imply that these missteps will turn out to be as important for the scientific progress as others have been in the past [173, 174], some of the insights gained from these intermediate steps might be useful for others, even if just to realize that behind many scientific successes there lies an, oftentimes undocumented, amount of failure [174–176].

This chapter will give an overview of two of the intermediate attempts that did not lead to a measurement of the  $\chi_{c1}$  and  $\chi_{c2}$  polarization. The descriptions of the different approaches will be held brief and details are mostly omitted in the spirit of giving the broader picture. Some parts of the discussion will also focus on the insights and understandings that could be gained from these endeavours. However, it also has to be stated that in hindsight some of the approaches have likely been abandoned too early to really gauge their general applicability. Hence, some of the issues that were discovered and are stated as reasons for moving to another approach seem a bit less impossible to overcome now than they have in the past.

## A.1 Likelihood based approach

The first attempts at measuring the polarization of the  $J/\psi$  in radiative  $\chi_{c1}$  and  $\chi_{c2}$  decays were aiming at reusing the likelihood based framework that has been originally developed for the measurement of the  $S$ -wave states at CMS [104, 109]. In the following only a brief description of the framework will be given, more detailed information about it can be found in Refs. [177, 178].

### A.1.1 Analysis framework

The framework using a likelihood based approach is fully data-driven and does not require any model-dependent inputs or assumptions to extract the polarization parameters from a data sample. The necessary inputs to the framework are

- The 4-momenta of the muons of a  $J/\psi$  decay, where the  $J/\psi$  have been suitably selected, such that the sample comprises mainly muons of interest. In the case of the polarization measurement of prompt  $\chi_{c1}$  and  $\chi_{c2}$  mesons two separate  $J/\psi$  samples are defined, selecting the respective decays using the invariant mass of the  $J/\psi\gamma$  system.
- The fraction of inclusive background events in the selected data sample,  $f_{\text{bg}}$  which includes all relevant background contributions. In general this includes the combinatorial background as well as NP contributions. For the  $\chi_{c1}$  an additional cross-feed component from  $\chi_{c2}$  decays can be considered as well.
- The  $(p_{\text{T}}^{J/\psi}, |y^{J/\psi}|, m^{J/\psi}, \cos\vartheta, \varphi)$  distribution of the inclusive background events, determined from sidebands.
- The dimuon efficiencies  $\varepsilon(\vec{p}_{\mu^+}, \vec{p}_{\mu^-})$  as a function of the muon momentum vectors in the laboratory frame. This is the only “external” input as it is not determined from the data sample under study.

A mass model very similar to the one described in Sec. 5.4 has been used in conjunction with a sophisticated lifetime model [104] to perform a two-dimensional unbinned maximum likelihood fit of the  $\chi_c$  mass and lifetime distributions. From the results of this fit, suitable mutually exclusive mass and lifetime regions are defined that are either dominated by mainly combinatorial background or non-prompt events or contain one of the signal components as illustrated in Fig. A.1. From the definition of these regions the background fraction,  $f_{\text{bg}}$ , and the  $(p_{\text{T}}^{J/\psi}, |y^{J/\psi}|, m^{J/\psi}, \cos\vartheta, \varphi)$  distribution of the inclusive background events are determined. Furthermore, the events belonging to the corresponding signal regions are selected.

From the selected event sample in each signal region, “background-like” events are removed based on a likelihood-ratio criterion. Likelihoods according to a background only hypothesis and according to the full event sample in the signal region are compared to decide whether an event is likely to be a background event. Given the statistical nature of this procedure, it is repeated several times to take into account statistical fluctuations.

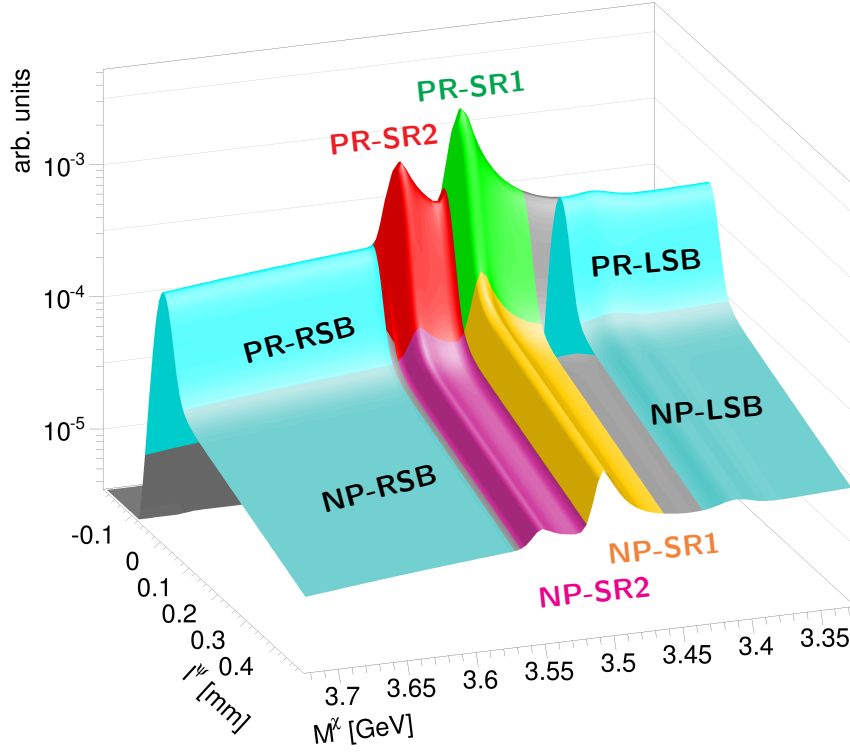


**Figure A.1:** Pedagogical illustration of the mass-lifetime distribution and different mass and lifetime regions obtained from the data sample under study. In the mass dimension the regions are defined as left and right sidebands (LSB and RSB) as well as the  $\chi_{c1}$  (SR1) and  $\chi_{c2}$  (SR2) signal regions. For each mass region a prompt (PR) and non-prompt (NP) lifetime region is defined.

The sample of events remaining after the background subtraction is considered background free. The likelihood of the polarization parameters taking into account acceptance and efficiency effects is defined as

$$\mathcal{L}(\vec{\lambda}) = \prod_i \mathcal{E}(\vec{p}_{\mu^+}^{(i)}, \vec{p}_{\mu^-}^{(i)} | \vec{\lambda}), \quad (\text{A.1})$$

where the *event probability* is given as

$$\mathcal{E}(\vec{p}_{\mu^+}, \vec{p}_{\mu^-} | \vec{\lambda}) = \frac{1}{\mathcal{N}(\vec{\lambda})} W(\cos \vartheta, \varphi | \vec{\lambda}) \cdot \varepsilon(\vec{p}_{\mu^+}, \vec{p}_{\mu^-}). \quad (\text{A.2})$$

The normalization  $\mathcal{N}(\vec{\lambda})$  is calculated as the integral over  $\cos \vartheta$  and  $\varphi$  of  $W \cdot \varepsilon$ . Since no closed form of the integral exists, the value of the integral is approximated with a simple MC procedure using events generated according to the acceptance times efficiency corrected  $(p_T^{J/\psi}, |y^{J/\psi}|, m^{J/\psi})$  distribution and uniformly in  $\cos \vartheta$  and  $\varphi$ .

The extraction of the polarization parameters  $\vec{\lambda}$  is done via a Bayesian [Markov Chain Monte Carlo \(MCMC\)](#) approach in which the full three-dimensional PPD is

obtained, assuming uniform priors. The sampling of the parameter space is done using a Metropolis-Hastings algorithm [179], where extracted parameter values are kept depending on the likelihood ratio with respect to the previously extracted parameter values. Due to the statistical nature of this sampling and the previously mentioned background subtraction the whole procedure is repeated 50 times and the PPDs from all individual extractions are merged. Thus, the uncertainty related to the random extractions of individual parameter sets is already included in the final PPD from which the parameter values are determined.

Uncertainties related to systematic effects are determined for different possible sources. They are directly incorporated into the PPD by smearing the PPD using a normal distribution centered at zero and a width corresponding to the size of the systematic uncertainty or using a uniform distribution covering the full range of possible values.

From the three-dimensional PPDs the values of the parameters are obtained using one-dimensional projections. The highest value of the projected PPD, the **most probable value (MPV)**, is used as the central value for the parameter. To minimize the influence of statistical fluctuations, a normal distribution is fitted to the one-dimensional projection in the vicinity of the MPV. The CLs at  $x\%$  for the parameters are estimated by identifying intervals containing the MPV and  $x\%$  of the one-dimensional PPD projection integrated over the full range.

### A.1.2 Preliminary results

The preliminary result for the polarization parameters are shown in Fig. A.2 as a function of  $p_T^{\chi_c}$ . While the values for  $\lambda_\varphi$  and  $\lambda_{\varphi\varphi}$  seem to be compatible with 0 independently of  $p_T^{\chi_c}$ , the values for  $\lambda_\theta$  exhibit a strong increasing trend with increasing  $p_T^{\chi_c}$ . Most importantly, the values are far outside the physically allowed region at low  $p_T^{\chi_c}$ . Severely underestimated systematic uncertainties can be excluded by comparing the values of the frame invariant parameter  $\tilde{\lambda}$  obtained in two different frames as shown in Fig. A.3, where the values obtained in the HX and the CS frame are compared for the two  $\chi_c$  states. No significant differences between the results from the two different frames are observed. Hence, the physically impossible values of  $\lambda_\theta$  observed at low  $p_T^{\chi_c}$  cannot be attributed to an obvious underestimation of a systematic effect.

### A.1.3 Investigation of possible sources for unphysical behaviour

Various possible sources are investigated in an attempt to identify reasons for the observation of physically impossible  $\lambda_\theta$  values. The studies are used to exclude, one by one, the different sources and will be described briefly below.

The physically impossible behavior observed in the  $J/\psi$  from radiative  $\chi_c$  decays is also observed in inclusive  $J/\psi$  samples. Thus, the majority of the tests are done using inclusive  $J/\psi$  samples because these samples are much larger and the results are less affected by statistical fluctuations. In some cases the statistically more precise results

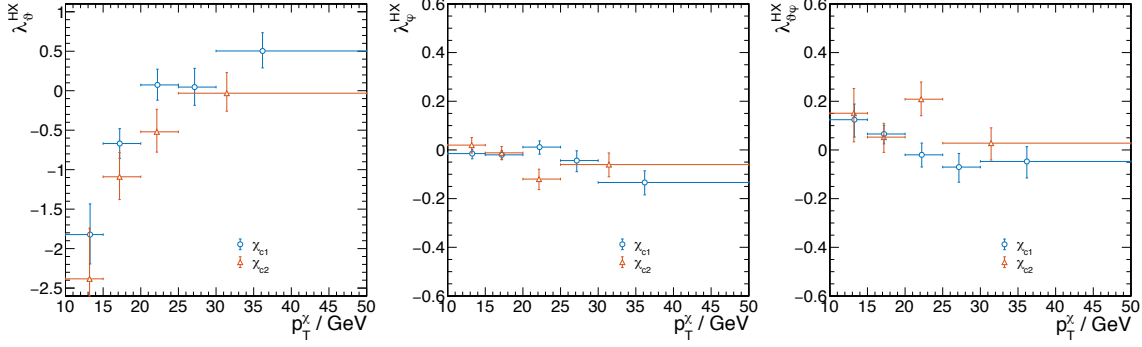


**Figure A.2:** Polarization parameters in the HX frame ( $\lambda_{\phi}$ ,  $\lambda_{\phi}$  and  $\lambda_{\phi\psi}$  from left to right) for the  $\chi_{c1}$  (blue) and the  $\chi_{c2}$  (red) as a function of  $p_T^{\chi}$ . The uncertainties do not include systematic effects.

are necessary to decide whether an effect could be due to an “unlucky” statistical fluctuation or whether it is indeed a systematic effect. Some of the tests also use data samples collected in 2011 that were used for the measurement of the prompt  $J/\psi$  polarization [104].

### MC closure tests

Simulated event samples with known polarizations are used to check whether a bias is introduced in the analysis procedure unintentionally. These checks are done with event samples containing only prompt  $\chi_{c1}$  and  $\chi_{c2}$  signal events as well as with samples containing only prompt  $J/\psi$  events. Consequently, these tests are not able to uncover any problems in the background subtraction procedure. Nevertheless, they serve as important checks to validate the analysis procedure in general. Neither for the  $\chi_c$  states nor the  $J/\psi$  any systematic bias is found in these MC closure tests.

### Dimuon efficiencies

The dimuon efficiencies,  $\varepsilon(\vec{p}_{\mu^+}, \vec{p}_{\mu^-})$ , are the only external input to the polarization framework. They are defined as the product of the single muon reconstruction efficiencies as well as a term taking into account possible correlations between the two muons introduced during the reconstruction, called  $\rho$ -factor. The  $\rho$ -factor has been found to become important only at relatively high  $p_T^{J/\psi}$  [104, 109].

The single muon reconstruction efficiencies are determined from dedicated data samples that are recorded simultaneously with the data samples that are used for physics analysis. The efficiencies are affected by statistical as well as systematic uncertainties as well. Hence, slightly different  $p_T^{\mu}$  and  $|\eta^{\mu}|$  dependencies are possible. The effects of these differences on the final results from inclusive  $J/\psi$  samples are tested. Additionally, the single muon reconstruction efficiencies that have been used for the measurement of the  $S$ -wave states using data collected in 2011 [104, 109]

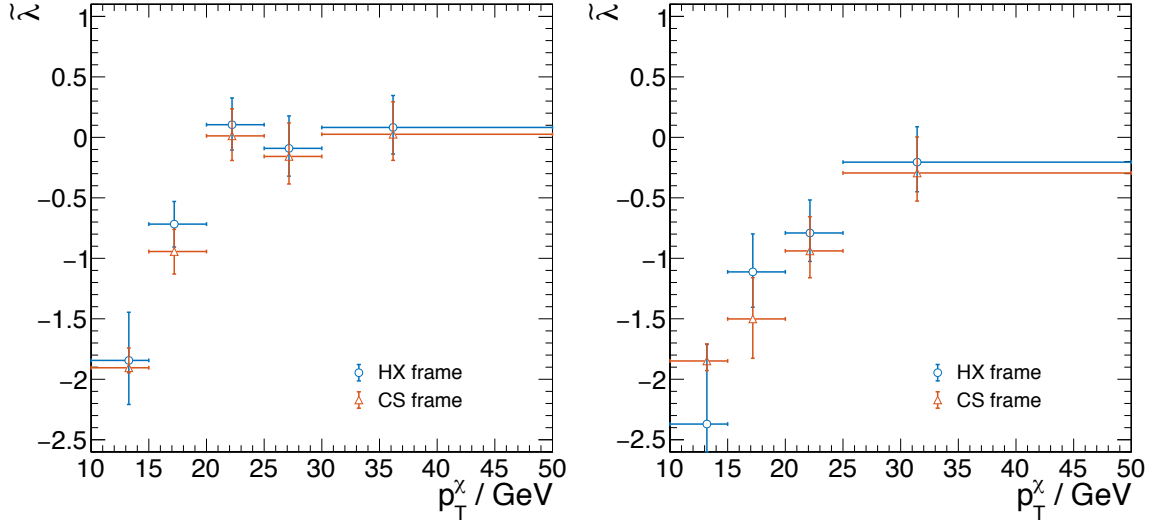


**Figure A.3:** Frame invariant parameter  $\tilde{\lambda}$  determined in the HX and CS frame for the  $\chi_{c1}$  (left) and the  $\chi_{c2}$  (right) as a function of  $p_T^{\chi_c}$ . The uncertainties do not include systematic effects.

replace the nominal reconstruction efficiencies for some tests. These efficiencies have been determined from data collected at  $\sqrt{s} = 7$  TeV in 2011. Since the running conditions between 2011 and 2012 have not changed significantly, the single muon reconstruction efficiencies exhibit very similar  $p_T^\mu$  and  $|\eta^\mu|$  dependencies.

Corrections related to the  $\rho$ -factor are determined from simulated event samples. The ratio of accepted and reconstructed events with respect to the generated events as a function of  $\cos\vartheta$ ,  $\varphi$  and the  $J/\psi$  kinematics is determined from these event samples.

Figure A.4 shows a comparison of the effects of different dimuon efficiencies on the results obtained from an inclusive  $J/\psi$  sample. While, variations of the single muon reconstruction efficiencies only have a small effect on the results, taking into account the dimuon correlations using the  $\rho$  factor significantly affects the results at high  $p_T^{J/\psi}$ . Even when using comparably large variations in the single muon reconstruction efficiencies the physically impossible  $\lambda_\vartheta$  trend at low  $p_T^{J/\psi}$  remains. These checks also rule out the possibility of a  $\cos\vartheta$  and  $\varphi$  dependent  $\rho$ -factor at low  $p_T^{J/\psi}$ , as no significant changes are observed at low  $p_T^{J/\psi}$ .

### Polarization extraction framework

Since none of the above checks have revealed any significant problems, a final check is done to exclude the possibility of an undiscovered problem in the polarization extraction framework. Such problems could arise from small changes that are introduced to the framework between the measurement of the  $S$ -wave quarkonium polarizations and the measurement of the  $P$ -wave quarkonium polarizations. These changes only con-

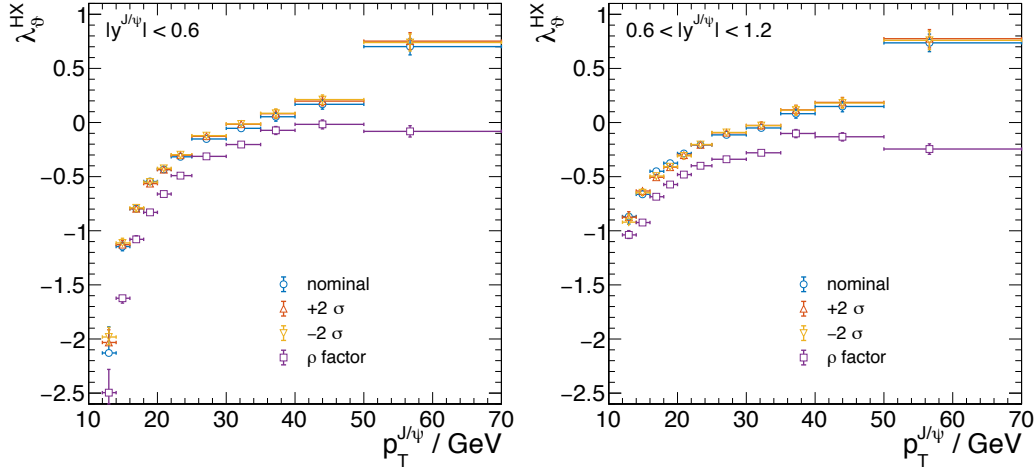


**Figure A.4:** Comparison of the effects of different dimuon efficiencies on the measured values of  $\lambda_{\phi}^{J/\psi}$  in the HX frame as a function of  $p_T^{J/\psi}$  in two rapidity ranges. The nominal (blue) points correspond to the results that are obtained when evaluating the dimuon efficiencies as product of the single muon reconstruction efficiencies at their nominal values. The  $\pm 2\sigma$  results are obtained when evaluating the single muon reconstruction efficiencies at their  $\pm 2\sigma$  uncertainty bands. The  $\rho$  factor (purple) values correspond to the results that are obtained when taking into account dimuon correlations in the dimuon efficiencies.

cern minor parts of the framework and should in principle not change the behaviour of the framework.

During the measurement of the  $S$ -wave states polarizations the polarization extraction framework has been extensively validated [104, 109, 177, 178]. Part of these validation checks are repeated. However, they do not reveal any obvious problems.

To fully rule out problems in the polarization extraction framework the measurement of the  $J/\psi$  polarization using data collected in pp collisions at  $\sqrt{s} = 7$  TeV [104] is repeated using the framework with all adaptations in place. The results of this measurement are shown in Fig. A.5 in comparison to the ones obtained from the data sample collected at  $\sqrt{s} = 8$  TeV during the 2012 data taking period. The results obtained from the data samples collected in 2011 do not exhibit the physically impossible trend at low  $p_T^{J/\psi}$ . Hence, also the possibility of a problem in the polarization extraction framework can be excluded.

### Reconstruction of $J/\psi$

Several different analysis groups use event samples containing inclusive  $J/\psi$  candidate events. Thus, it is possible to check the consistency of the reconstruction modules used by different groups to rule out the possibility of introducing a bug in the early stages of the analysis. No differences are found between the event samples obtained

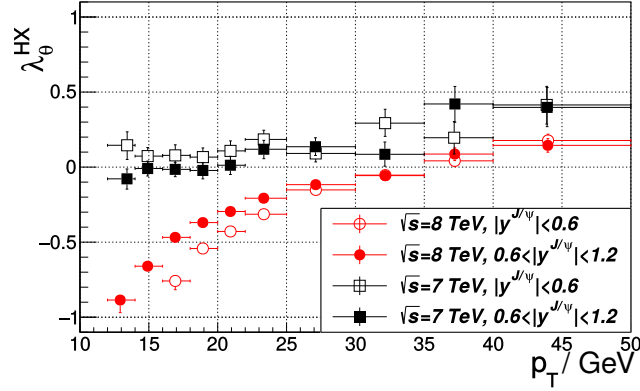


**Figure A.5:** Comparison of measured  $\lambda_{\vartheta}^{J/\psi}$  values using inclusive samples collected in 2011 ( $\sqrt{s} = 7$  TeV, black) and 2012 ( $\sqrt{s} = 8$  TeV, red) as a function of the  $J/\psi$  kinematics. The results have been obtained without applying  $\rho$  factor corrections.

from two different  $J/\psi$  reconstruction modules. Hence, the possibility of introducing a problem during the offline reconstruction can be excluded.

### Comparison of raw $J/\psi$ data

After excluding any problems in the analysis procedure the only conclusion that is left is that the observed angular decay distributions are different for the samples collected in the 2012 and 2011 data taking period. Since no problems are observed when the latter are used to measure the  $J/\psi$  polarization, these are used as the benchmark sample. Data samples collected during other data taking periods are compared to this benchmark sample. To minimize the possible influence of the event selection only very basic selection criteria are used that are aimed at removing combinatorial background and NP contaminations. The invariant dimuon mass must be within the range 3.025–3.175 GeV, the pseudo proper decay length must be below 0.05 mm and the dimuon vertex fit  $\chi^2$  probability must be larger than 1 %. All  $J/\psi$  candidate events must be in the range  $|y^{J/\psi}| < 1.2$ . For the single muons two different selections are in use: the *nominal* selection which requires  $p_T^\mu > 3.5$  GeV and the *strict* muon selection for which  $p_T^\mu > 5.5$  GeV. In both cases the muons must be within  $|\eta^\mu| < 1.6$ .

The ratios of the  $\cos \vartheta^{\text{HX}}$  distributions obtained from data samples collected during 2012 at  $\sqrt{s} = 8$  TeV and during 2016 at  $\sqrt{s} = 13$  TeV with respect to the distributions determined from data collected in 2011 at  $\sqrt{s} = 7$  TeV are shown in Fig. A.6 for different ranges of  $p_T^{J/\psi}$ . Since the polarization does not depend on the center-of-mass energy of the pp collisions these ratios can be used to detect differences between the different data taking periods at the “raw” data level.

As evident from Fig. A.6, there is a clearly visible difference in the low  $p_T^\mu$  part of the event samples. If the nominal muon selection is applied the ratios with respect to the 2011 distribution are flat only in the central part of the  $\cos \vartheta^{\text{HX}}$  range and drop



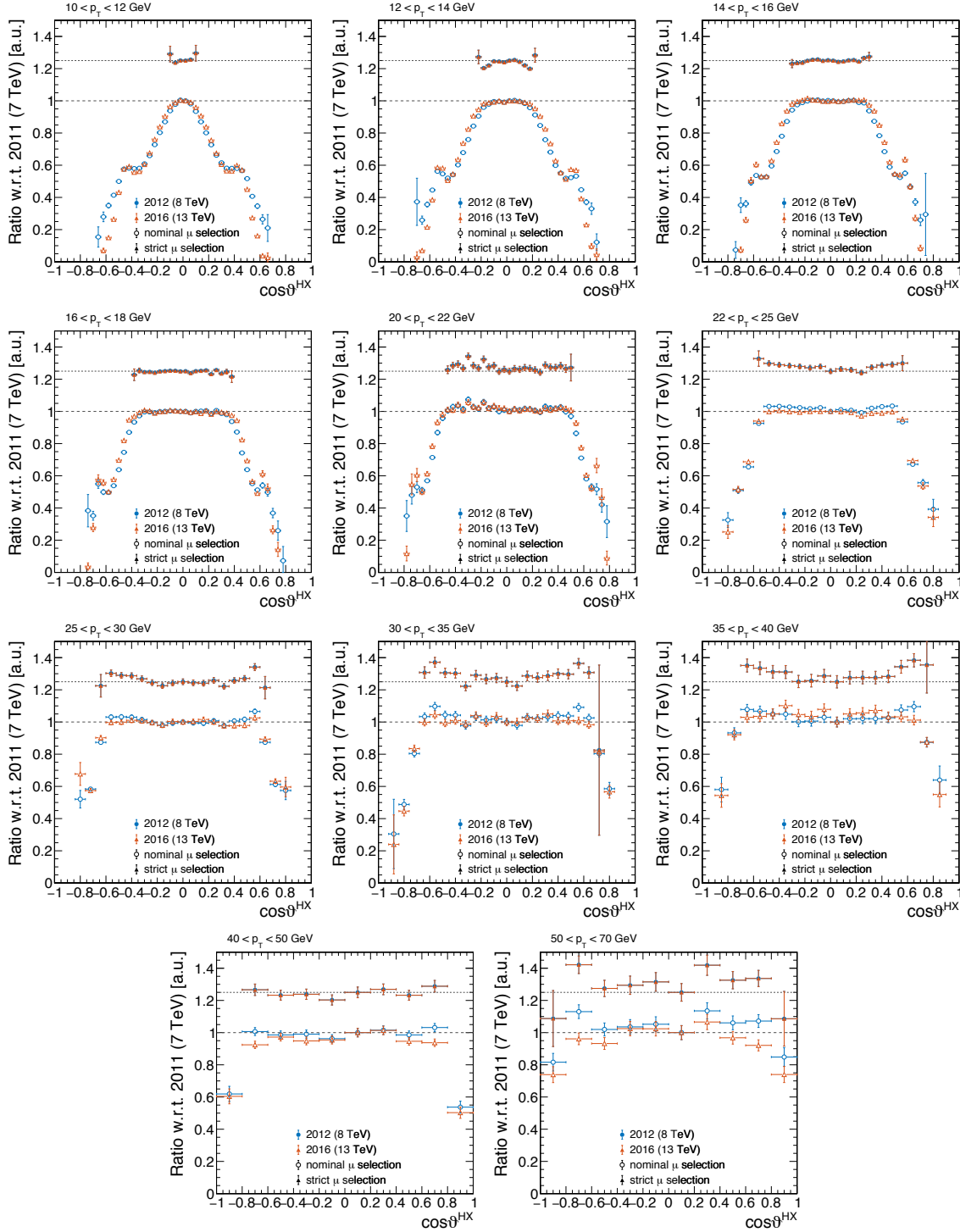


**Figure A.6:** “Raw”  $\cos\vartheta^{\text{HX}}$  distribution of inclusive  $J/\psi$  samples throughout the different data taking periods with respect to the distribution in the 2011 data taking period in different  $p_{\text{T}}^{J/\psi}$  ranges. The open (filled) symbols represent the ratios where the distributions have been obtained using nominal (strict) muon selection criteria (see text). The normalizations of the ratios have been adapted for better visibility and the values at  $\cos\vartheta = 0$  are represented by the horizontal lines.

steeply at the edges. With increasing  $p_T^{J/\psi}$  the central region gets broader, but only at very high  $p_T^{J/\psi}$  does the drop at the edges start to disappear. Contrary to this when using a stricter single muon selection with an increased  $p_T^\mu$  threshold, the ratios with respect to the 2011 distributions are flat. However, the coverage in  $\cos\vartheta^{\text{HX}}$  is also much narrower. This is clear evidence that the observed physically impossible  $\lambda_\vartheta$  values in the 2012 inclusive  $J/\psi$  samples are caused by a difference in the underlying data. These differences are not reflected in the change of single muon efficiencies.

### A.1.4 Gained insights

A physically impossible trend at low  $p_T^{J/\psi}$  of the polar anisotropy parameter,  $\lambda_\vartheta$ , has been discovered. Since it is not only found in results obtained from  $\chi_{c1}$  and  $\chi_{c2}$  mesons but also in results using inclusive  $J/\psi$  samples, a variety of possible sources of this behaviour have been investigated. In the end the cause was found already at the raw data level, where clear differences in the  $\cos\vartheta^{\text{HX}}$  distributions are observed in the data samples collected in 2012 and 2016 with respect to the ones collected in 2011. Even though some attempts have been made to understand the sources of these differences, no clear culprit has been found. Most likely, some implicit cut has been introduced between the 2011 and 2012 data taking periods, either already at trigger level or during the offline reconstruction.

Most importantly, it is evident that the effects of these changes are not reflected in the single muon efficiencies which are determined as a function of  $p_T^\mu$  and  $|\eta^\mu|$ . Hence, such effects are also not correctly taken into account in the polarization extraction framework. Studies show that these effects are only present at low  $p_T^\mu$  and that with sufficiently strict single muon  $p_T^\mu$  requirements a reliable polarization measurement should be possible. However, since the predictions of the  $\chi_{c1}$  and  $\chi_{c2}$  polarizations exhibit the largest differences at low  $p_T^{J/\psi}$ , such strict single muon requirements would make a measurement in the interesting kinematic region all but impossible.

Since the single muon reconstruction efficiencies do not reflect the observed effects on the angular distribution, another way has to be found to either properly determine the effect on the angular distribution or to eliminate the need for such inputs to the polarization measurement. A possible way to do the former is described briefly below, while the latter is what has in the end been adapted for the measurement of  $\chi_{c1}$  and  $\chi_{c2}$  polarizations presented in this thesis.

In order to ensure that the measurement presented in this thesis is not affected by this low  $p_T^\mu$  effect described above, the determination of the  $\chi_{c2}$  over  $\chi_{c1}$  yields as a function of  $|\cos\vartheta^{\text{HX}}|$  and  $\varphi^{\text{HX}}$  has been repeated with increasingly strict single muon cuts. The procedure is in fact the same that has been used for systematic checks of other selection criteria and has not revealed any systematic effects related to the single muon selection.

## A.2 Measurement relative to $J/\psi$ from $B^\pm \rightarrow J/\psi K^\pm$ decays

Since the single muon reconstruction efficiency corrections are not able to describe the sculpting of the  $\cos\vartheta^{\text{HX}}$  distribution, especially at low  $p_T^{J/\psi}$ , a different approach of determining the sculpting effects has to be found. Preferentially, the acceptance times efficiency effects on the angular decay distribution are determined directly from data. Otherwise the risk of having to rely on an accurate detector simulation in MC based approaches arises. One of the ways to determine the acceptance times efficiency effects on the angular decay distribution is to measure the observable angular decay distribution from a sample with known polarization.

### A.2.1 Measurement principle

In the decay  $B^\pm \rightarrow J/\psi K^\pm$ <sup>i</sup>, illustrated in Fig. A.7, the  $J/\psi$  is naturally longitudinally polarized if the polarization is measured along the  $J/\psi$  direction,  $z_0$ , in the B rest frame. This follows naturally from the fact that  $J_z(B) = J_z(J/\psi) + J_z(K)$  and  $J_z(B) = J_z(K) = 0$ .

However, if only the  $J/\psi$  in the B decay is reconstructed then the observable polarization of the  $J/\psi$  becomes zero, because its natural polarization axis  $z_0$  can have all possible directions with respect to the pp center-of-mass HX axis,  $z$ . The angle between  $z_0$  and  $z$ ,  $\cos\Theta$ , is equal to the emission angle of the  $J/\psi$  in the B rest frame. Since  $J(B) = 0$ , the B always decays isotropically and the fully longitudinal polarization of the  $J/\psi$  with respect to  $z_0$  becomes a zero polarization with respect to the  $z$  axis.

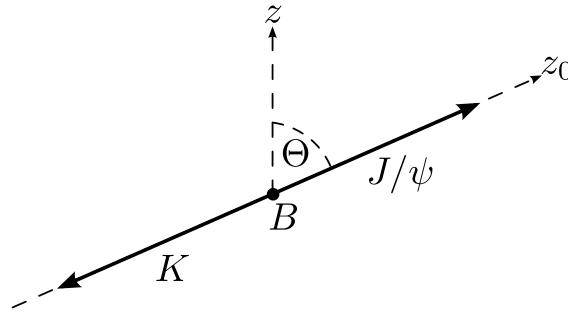


**Figure A.7:** Definition of the axes and the angle  $\Theta$  in the  $B \rightarrow J/\psi K$  decay in the B rest frame

The simple approach to derive acceptance times efficiency correction maps is now to measure the angular decay distribution of the  $J/\psi$  from  $B \rightarrow J/\psi K$  decays and divide the measured distribution by the angular decay distribution corresponding

<sup>i</sup>The charge superscripts will be dropped from here on and B and K denote  $B^\pm$  and  $K^\pm$  with implied proper charge combinations.

to the expected polarization. The major challenge that needs to be addressed is the fact that the expected angular decay distribution is sculpted by the kinematic selections that are used in the data analysis. While it is in principle possible to analytically calculate this effect using only kinematic arguments, it is simpler to calculate the observable polarization directly from the observed data distributions. The full angular decay distribution of the  $B \rightarrow J/\psi K$  and the subsequent  $J/\psi \rightarrow \mu\mu$  decay is

$$\begin{aligned} \tilde{W}(\cos \Theta, \Phi, \cos \vartheta, \varphi) \propto & 1 + \cos^2 \Theta \\ & + (1 - 3 \cos^2 \Theta) \cos^2 \vartheta \\ & - \sin^2 \Theta \cos 2\Phi \sin^2 \vartheta \cos 2\varphi \\ & - \sin 2\Theta \cos \Phi \sin 2\vartheta \cos \varphi, \end{aligned} \quad (\text{A.3})$$

where  $\Theta$  and  $\Phi$  are the emission angles of the  $J/\psi$  in the  $B$  rest frame and  $\vartheta$  and  $\varphi$  are the lepton emission angles in the  $J/\psi$  rest frame.

In the measurement the  $B$  decay is unobserved. Hence, to arrive at the observable angular decay distribution of the  $J/\psi$ , Eq. (A.3) has to be averaged over  $\cos \Theta$  and  $\Phi$ , resulting in

$$\begin{aligned} \tilde{w}(\cos \vartheta, \varphi) \propto & 1 + \langle \cos^2 \Theta \rangle \\ & + (1 - 3 \langle \cos^2 \Theta \rangle) \cos^2 \vartheta \\ & - \langle \sin^2 \Theta \cos 2\Phi \rangle \sin^2 \vartheta \cos 2\varphi \\ & - \langle \sin 2\Theta \cos \Phi \rangle \sin 2\vartheta \cos \varphi. \end{aligned} \quad (\text{A.4})$$

Here values in angle brackets represent averages calculated from the collected signal events. The predicted observable polarization parameters can be read from Eq. (A.4):

$$\begin{aligned} \lambda_\Theta &= \frac{1 - 3 \langle \cos^2 \Theta \rangle}{1 + \langle \cos^2 \Theta \rangle} \\ \lambda_\Phi &= - \frac{\langle \sin^2 \Theta \cos 2\Phi \rangle}{1 + \langle \cos^2 \Theta \rangle} \\ \lambda_{\Theta\Phi} &= - \frac{\langle \sin 2\Theta \cos \Phi \rangle}{1 + \langle \cos^2 \Theta \rangle} \end{aligned} \quad (\text{A.5})$$

Since only the observed events are used to calculate the averages, these polarization parameters already include the sculpting of the originally flat angular decay distribution. The only two conditions that need to be fulfilled are that, first, only signal events are used in the averaging procedure and, second, the smearing of  $\cos \Theta$  and  $\Phi$  is negligible. While the first condition can be met via an appropriate event selection, the second one is a standard assumption that is used in all CMS quarkonium polarization measurements.

With the knowledge of the observable polarization parameters two-dimensional acceptance times efficiency correction maps can be determined in the following steps:

1. For each kinematic  $J/\psi$  region of the measurement the observable polarization parameters  $\vec{\lambda}_{\text{obs}}$  are determined from a sample of  $B \rightarrow J/\psi K$  decays as defined in Eq. (A.5).

2. In each kinematic  $J/\psi$  region the background subtracted two-dimensional  $(\cos \vartheta, \varphi)$  distribution from the  $J/\psi$  from B decays is measured.
3. The expected observable angular decay distribution is calculated using the observable polarization parameters as  $W(\cos \vartheta, \varphi | \vec{\lambda}_{\text{obs}})$ .
4. The two-dimensional  $\cos \vartheta$  and  $\varphi$  dependent acceptance times efficiency correction map is obtained by dividing the the measured  $(\cos \vartheta, \varphi)$  distribution by the calculated expected angular decay distribution.

### A.2.2 Event selection and mass fitting

The identification of  $J/\psi$  coming from  $B \rightarrow J/\psi K$  decays closely follows the approach that has been taken for production cross section measurements of the  $B^\pm$  described in Refs. [180, 181]. Here only the main selection thresholds as well as a very basic description of the reconstruction of  $B^\pm$  candidate events will be given.

The  $J/\psi$  are reconstructed in the same way as for the nominal polarization measurement with the only difference being that  $J/\psi$  candidates are required to have an invariant dimuon mass in the range  $\pm 0.2$  GeV around the world average value [45]. Additionally, they must have a minimum  $p_T^{J/\psi} > 10$  GeV and be within the range  $|y^{J/\psi}| < 1.2$ . The charged tracks that are used as  $K^\pm$  candidates must satisfy the same high-purity track requirements as the ones used in the nominal analysis [160] and have a minimum  $p_T^{\text{tk}} > 1.2$  GeV. Combinations of  $J/\psi$  and one charged track are used in a KVF, where the mass of the  $J/\psi$  is constrained to the world average value and the charged track is assigned the  $K^\pm$  mass. Events with a resulting  $\chi^2$ -probability greater than 1 % are retained for the further analysis if the invariant mass of the  $J/\psi K$  system is in the range between 5 and 6 GeV.

To reduce the size of combinatorial background, consisting mainly of random  $J/\psi$  and charged track combinations, the cosine of the angle between the B meson momentum and the vector from the B decay vertex to the PV has to be larger than 0.95. Additionally, the distance in the transverse plane between the B decay vertex and the PV divided by its uncertainty has to be larger than 3 to suppress a possible contamination of prompt  $J/\psi$  decays.

The  $J/\psi$  candidates from B decays are identified using an unbinned maximum likelihood fit to the invariant  $J/\psi K$  mass distribution. Four superimposed contributions are considered during these fits. The  $B \rightarrow J/\psi K$  signal component is modeled using three Gaussian distributions centered at the same value but with different widths. A component from  $B^\pm \rightarrow J/\psi \pi^\pm$  decays, where the  $\pi$  track has been misidentified as K track is similarly modeled as a superposition of three Gaussian distributions. However, in this case all parameters are completely fixed to values obtained from simulated event samples. The combinatorial background component is modeled using a simple exponential function and an additional error function which describes  $B \rightarrow J/\psi K X$  decays, where the X has not been reconstructed. The result of this fit using all selected events is shown in Fig. A.8.

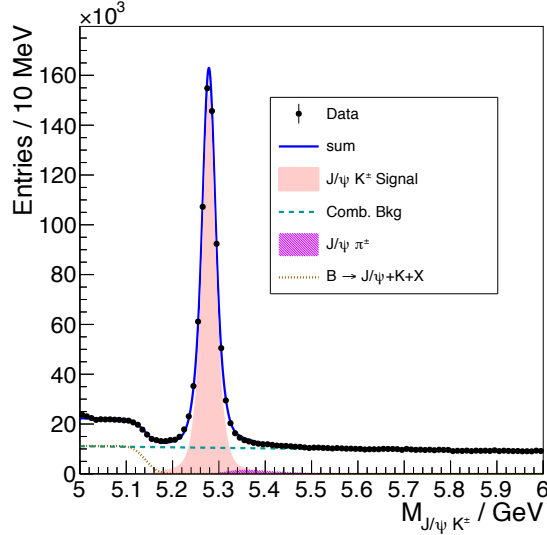


**Figure A.8:** Invariant  $J/\psi$  K mass distribution in the  $B \rightarrow J/\psi K$  candidate event sample collected in pp collisions at  $\sqrt{s} = 8$  TeV in 2012.

### A.2.3 Preliminary results

From the results of the fits a mass window can be defined to select mainly  $B \rightarrow J/\psi K$  events. Depending on the width of the mass window the fraction of background events varies between 9 %, if a very strict  $\pm 1\sigma$  window around the central value is used, up to 26 % for a loose  $\pm 5\sigma$  window. Using these signal windows and the  $(\cos\vartheta, \varphi)$  distributions in the sidebands, signal only  $(\cos\vartheta, \varphi)$  distributions can be determined using the same background subtraction technique that has already been used in the likelihood based polarization framework for the  $S$ -wave states (see Sec. A.1).

Figure A.9 shows a comparison of the polarization parameters that are obtained from the two-dimensional correction maps via a two-dimensional  $\chi^2$  fit to the angular decay distribution given in Eq. (2.3). Using different definitions of the signal mass window around the B peak for selecting the  $J/\psi$  samples allows to estimate the systematic effects related to the background contamination. While some differences are visible, especially for the  $\lambda_\vartheta$  parameter, no systematic effect related to the background contamination in the signal mass window, used to select  $J/\psi$  samples from  $B \rightarrow J/\psi K$  decays, is found.

The polarization parameters that are obtained from the correction maps show that mainly the polar anisotropy parameter,  $\lambda_\vartheta$ , is affected by the acceptance times efficiency corrections, while the other two parameters,  $\lambda_\varphi$  and  $\lambda_{\vartheta\varphi}$ , are only affected at low  $p_T^{J/\psi}$ . From the polarization parameters extracted from the correction maps it is already possible to deduce the effects on the measured polarization parameters. In case of  $\lambda_\vartheta$ , for example, the corrections will lead to significant corrections towards more positive values at low  $p_T^{J/\psi}$  and to some smaller corrections towards more negative values at high  $p_T^{J/\psi}$ .

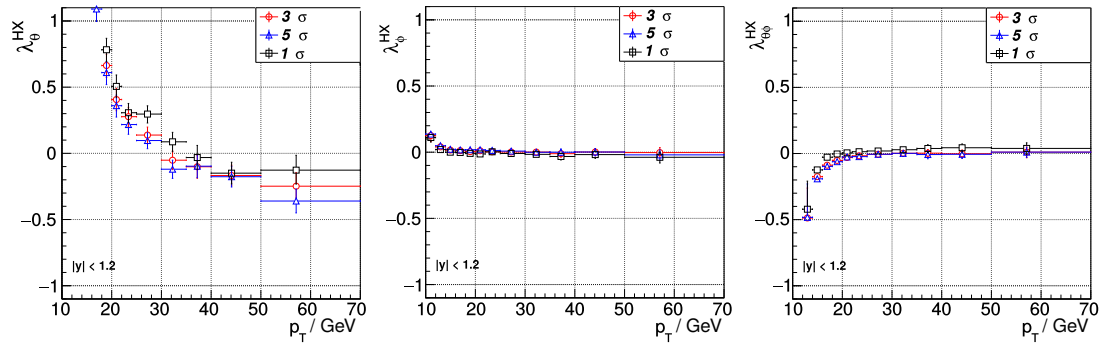


**Figure A.9:** Polarization parameters in the HX frame (from left to right:  $\lambda_\vartheta$ ,  $\lambda_\varphi$  and  $\lambda_{\vartheta\varphi}$ ) obtained from fitting the two-dimensional acceptance times efficiency correction maps as a function of  $p_T^{J/\psi}$  for differently sized mass windows around the B peak for selecting  $J/\psi$  events coming from  $B \rightarrow J/\psi K$  decays.

To assess the applicability of this approach to measure the  $\chi_{c1}$  and  $\chi_{c2}$  polarization preliminary studies are first done for the prompt  $J/\psi$  polarization using data collected in 2012. The main reasons for this are that the available data sample for prompt  $J/\psi$  events is about a factor 100 larger than the one available for  $\chi_c$  events and the ability to compare the results to the already published measurement [104].

In principle the approach should be more or less insensitive to the  $(\cos\vartheta, \varphi)$  binning that is used for the correction maps. However, as illustrated in Fig. A.10 the binning of the correction map has a significant influence on the resulting values of  $\lambda_\vartheta$ . The values for  $\lambda_\varphi$  and  $\lambda_{\vartheta\varphi}$  are only affected slightly when using different binnings for the correction maps. This unexpected behavior is further investigated by comparing the results obtained using correction maps determined from two exclusive subsamples of the  $B \rightarrow J/\psi K$  decay sample. The results are shown in Fig. A.11. The differences in the results for the correction maps using different subsamples are comparable in size to the ones for different binnings of the correction maps. Thus, the most likely conclusion is that the limited size of the reference sample that is used for the determination of the correction maps leads to large systematic effects in the measured polarization parameters. Considering the size of these systematic effects a precise measurement of the  $\chi_{c1}$  and  $\chi_{c1}$  polarizations is not possible with the available data samples for the 2012 data taking period.

#### A.2.4 Gained insights

The major insight from this approach is that it seems to be possible to determine acceptance times efficiency corrections from a reference sample with known polarization. However, no definite answer can be given on whether the observed issues have their main cause in the small size of the available reference sample or whether the approach has further systematic flaws that can only be detected with larger available reference samples.

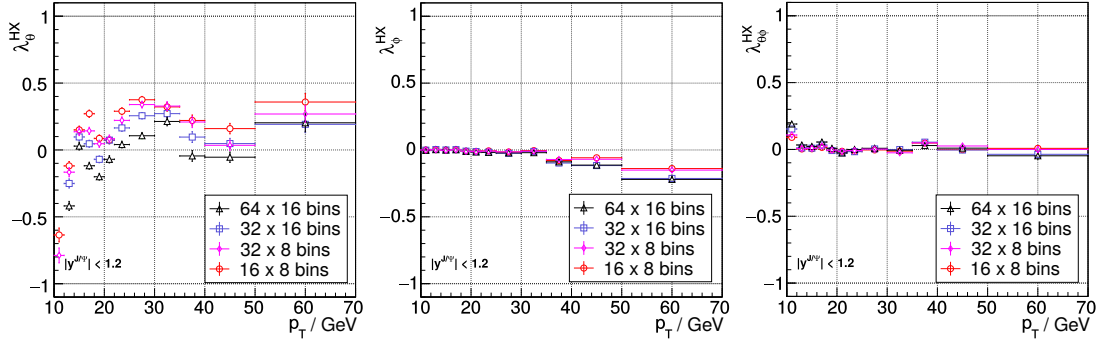


**Figure A.10:** Measured polarization parameters for different  $(\cos\vartheta, \varphi)$  binnings of the correction maps. The different sets of points correspond to different numbers of  $\cos\vartheta$  and  $\varphi$  bins.

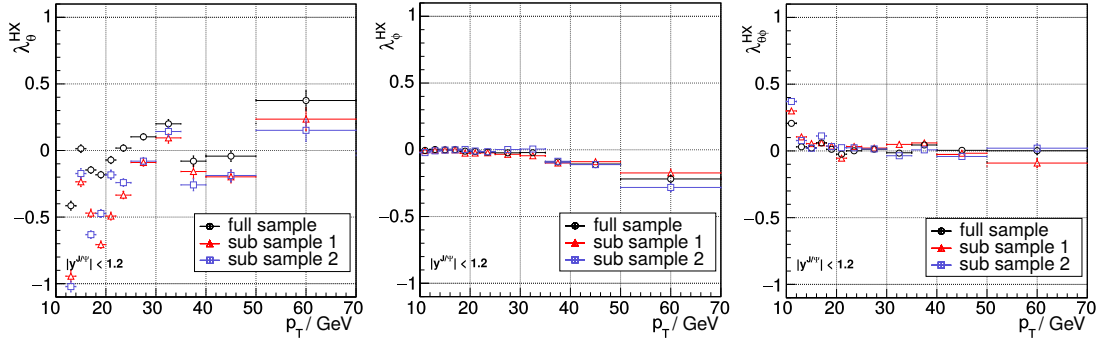


**Figure A.11:** Measured polarization parameters for correction maps obtained from different (exclusive) subsamples of the full  $B \rightarrow J/\psi K$  sample. The black points correspond to the results using a correction map obtained from the full sample, whereas the blue and red points correspond to results obtained using correction maps determined from splitting the full sample into two independent subsamples.



# Trigger Details for Run II

Some tables containing more detailed information about the available triggers and their selection criteria are presented. Tables B.1, B.2 and B.3 show the quarkonium related trigger paths that were in use for the 2016, 2017 and 2018 data taking period respectively.

**Table B.1:** Summary of the quarkonium trigger paths used for the 2016 data taking period, grouped by L1 seeds, and the integrated luminosity that was collected by each trigger path.

Trigger path / L1 seed expression	$\mathcal{L}_{\text{int}} / \text{fb}^{-1}$
L1_DoubleMu0er1p6_dEta_Max_1p8_0S	
HLT_Dimuon10_Jpsi_Barrel	4.7
HLT_Dimuon8_PsiPrime_Barrel	25.4
HLT_Dimuon8_Upsilon_Barrel	35.4
HLT_Dimuon0_Phi_Barrel	25.4
L1_DoubleMu10_0_dEta_Max1p8 OR L1_DoubleMu_11_4	
HLT_Dimuon16_Jpsi	25.4
HLT_Dimuon20_Jpsi	36.4
HLT_Dimuon13_PsiPrime	36.4
HLT_Dimuon13_Upsilon	36.4
L1_SingleMu14er OR L1_SingleMu16	
HLT_Mu16_TkMu0_dEta18_Onia	7.1
HLT_Mu16_TkMu0_dEta18_Phi	7.1
L1_SingleMu20 OR L1_SingleMu22 OR L1_SingleMu25 OR L1_SingleMu20er	
HLT_Mu25_TkMu0_dEta18_Onia	36.5

**Table B.2:** Summary of the quarkonium trigger paths used for the 2017 data taking period, grouped by L1 seeds, and the integrated luminosity that was collected by each trigger path.

Trigger path / L1 seed expression	$\mathcal{L}_{\text{int}} / \text{fb}^{-1}$
L1_DoubleMu0er1p5_SQ_OS_dRMax_1p4 OR L1_DoubleMuer1p4_SQ_OS_dRMax_1p4	
HLT_Dimuon20_Jpsi_Barrel_Seagulls	41.5
HLT_Dimuon10_PsiPrime_Barrel_Seagulls	41.5
HLT_Dimuon14_Phi_Barrel_Seagulls	41.5
L1_DoubleMu4p5er2p0_SQ_OS_Mass7to18	
HLT_Dimuon10_Upsilon_Barrel_Seagulls	41.5
HLT_Dimuon12_Upsilon_eta1p5	41.5
L1_DoubleMu4_SQ_OS_dRMax1p2 OR L1_DoubleMu4p5_SQ_OS_dRMax1p2 OR L1_DoubleMu0er1p5_SQ_OS_dRMax_1p4 OR L1_DoubleMuer1p4_SQ_OS_dRMax_1p4	
HLT_Dimuon25_Jpsi	41.5
HLT_Dimuon18_PsiPrime	41.5
L1_DoubleMu8_SQ	
HLT_Dimuon25_Jpsi_noCorrL1	27.1
HLT_Dimuon18_PsiPrime_noCorrL1	27.1
HLT_Dimuon24_Upsilon_noCorrL1	27.1
HLT_Dimuon24_Phi_noCorrL1	27.1
L1_SingleMu25 OR L1_SingleMu22 OR L1_SingleMu20er2p1 OR L1_SingleMu22er2p1	
HLT_Mu25_TkMu0_Onia	33.7
HLT_Mu30_TkMu0_Onia	41.5
L1_SingleMu16 OR L1_SingleMu18 OR L1_SingleMu20 OR L1_SingleMu16er2p1 OR L1_SingleMu18er2p1 OR L1_SingleMu20er2p1 OR L1_SingleMu22er2p1 OR L1_SingleMu25	
HLT_Mu20_TkMu0_Phi	36.1
HLT_Mu25_TkMu0_Phi	36.8

**Table B.3:** Summary of the quarkonium trigger paths used for the 2018 data taking period, grouped by L1 seeds, and the integrated luminosity that was collected by each trigger path.

Trigger path / L1 seed expression	$\mathcal{L}_{\text{int}} / \text{fb}^{-1}$
L1_DoubleMu0er1p5_SQ_OS_dRMax_1p4 OR L1_DoubleMuer1p4_SQ_OS_dRMax_1p4	
HLT_Dimuon20_Jpsi_Barrel_Seagulls <sup>a</sup>	5.4
HLT_Dimuon10_PsiPrime_Barrel_Seagulls <sup>a</sup>	5.4
HLT_Dimuon14_Phi_Barrel_Seagulls	61.3
L1_DoubleMu4p5er2p0_SQ_OS_Mass7to18	
HLT_Dimuon10_Upsilon_Barrel_Seagulls <sup>b</sup>	5.4
HLT_Dimuon12_Upsilon_eta1p5 <sup>b</sup>	5.4
HLT_Dimuon12_Upsilon_y1p4 <sup>b</sup>	55.9
L1_DoubleMu4_SQ_OS_dRMax1p2 OR L1_DoubleMu4p5_SQ_OS_dRMax1p2 OR L1_DoubleMu0er1p5_SQ_OS_dRMax_1p4 OR L1_DoubleMuer1p4_SQ_OS_dRMax_1p4	
HLT_Dimuon25_Jpsi	61.3
HLT_Dimuon18_PsiPrime	61.3
L1_DoubleMu8_SQ	
HLT_Dimuon25_Jpsi_noCorrL1	61.3
HLT_Dimuon18_PsiPrime_noCorrL1	61.3
HLT_Dimuon24_Upsilon_noCorrL1	61.3
HLT_Dimuon24_Phi_noCorrL1	61.3
L1_SingleMu25 OR L1_SingleMu22 OR L1_SingleMu20er2p1 OR L1_SingleMu22er2p1	
HLT_Mu30_TkMu0_Onia <sup>c</sup>	18.5
HLT_Mu30_TkMu0_Psi <sup>c</sup>	42.8
HLT_Mu30_TkMu0_Upsilon <sup>c</sup>	42.8
L1_SingleMu18 OR L1_SingleMu20 OR L1_SingleMu22 OR L1_SingleMu25	
HLT_Mu25_TkMu0_Phi	61.3

<sup>a</sup>The barrel trigger paths for the  $J/\psi$  and  $\psi(2S)$  were disabled shortly after the beginning of the data taking period due to too high rates.

<sup>b</sup>The two only slightly different paths covering the **Upsilon** mass regions were merged into only one path covering both use cases of the previously used paths.

<sup>c</sup>The mass window covered by **Onia** was split into two separate mass windows **Psi**, covering the  $J/\psi$  and  $\psi(2S)$ , and **Upsilon**, covering the  $\Upsilon(nS)$ , to reduce the rate.



Die approbierte gedruckte Originalversion dieser Dissertation ist an der TU Wien Bibliothek verfügbar.  
The approved original version of this doctoral thesis is available in print at TU Wien Bibliothek.

# Supplementary Information for the Data Analysis

## C.1 Studies using simulated events

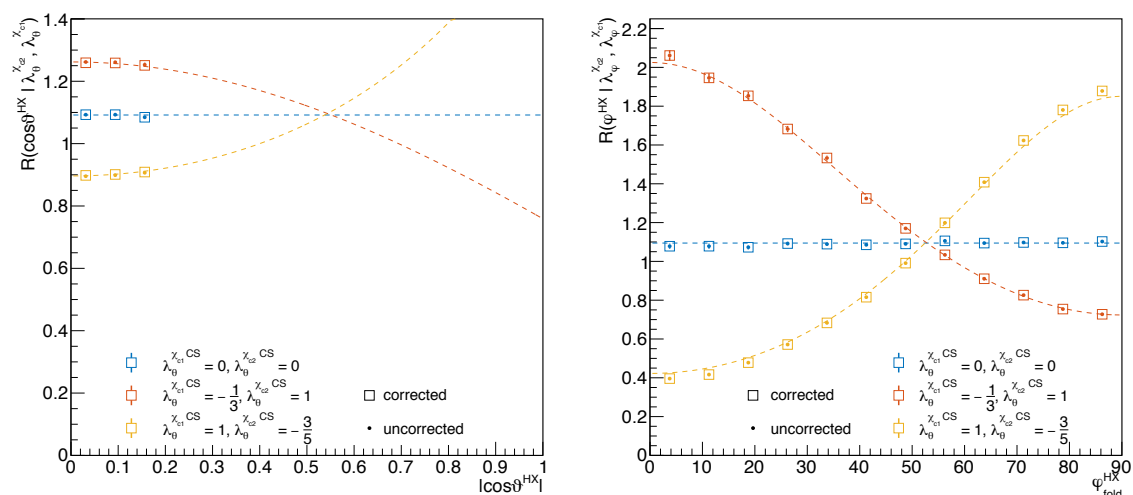


**Figure C.1:** Ratios of  $\chi_{c2}$  over  $\chi_{c1}$  yields as a function of  $|\cos\vartheta^{\text{HX}}|$  (left) and  $\varphi^{\text{HX}}$  (right) evaluated with event samples generated assuming the CS frame as natural frame and measured in the HX frame with and without acceptance times efficiency corrections to the analytically expected shapes (dashed lines), for the  $p_{\text{T}}^{J/\psi}$  range 8–9 GeV.

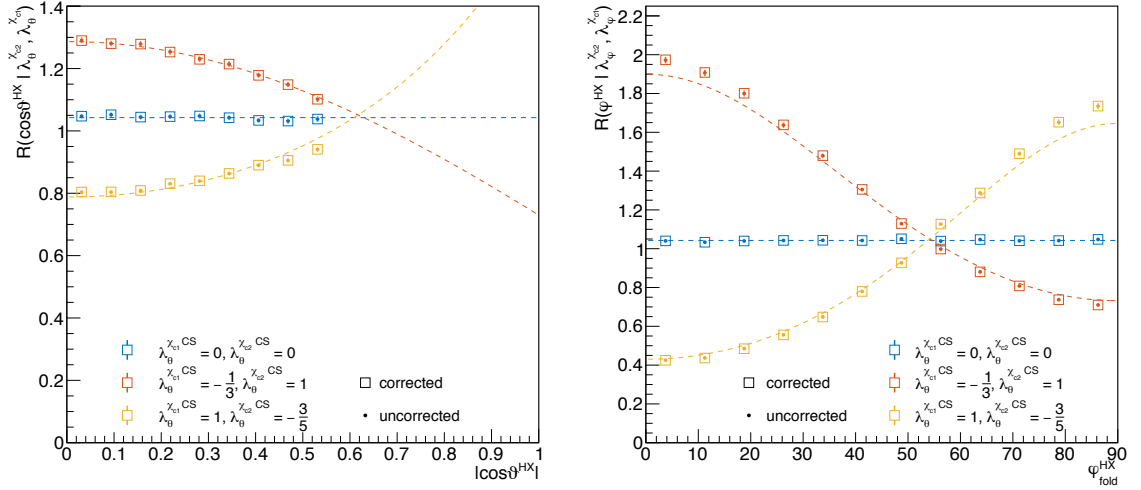


**Figure C.2:** Ratios of  $\chi_{c2}$  over  $\chi_{c1}$  yields as a function of  $|\cos\vartheta^{\text{HX}}|$  (left) and  $\varphi^{\text{HX}}$  (right) evaluated with event samples generated assuming the CS frame as natural frame and measured in the HX frame with and without acceptance times efficiency corrections to the analytically expected shapes (dashed lines), for the  $p_{\text{T}}^{\text{J}/\psi}$  range 16–20 GeV.

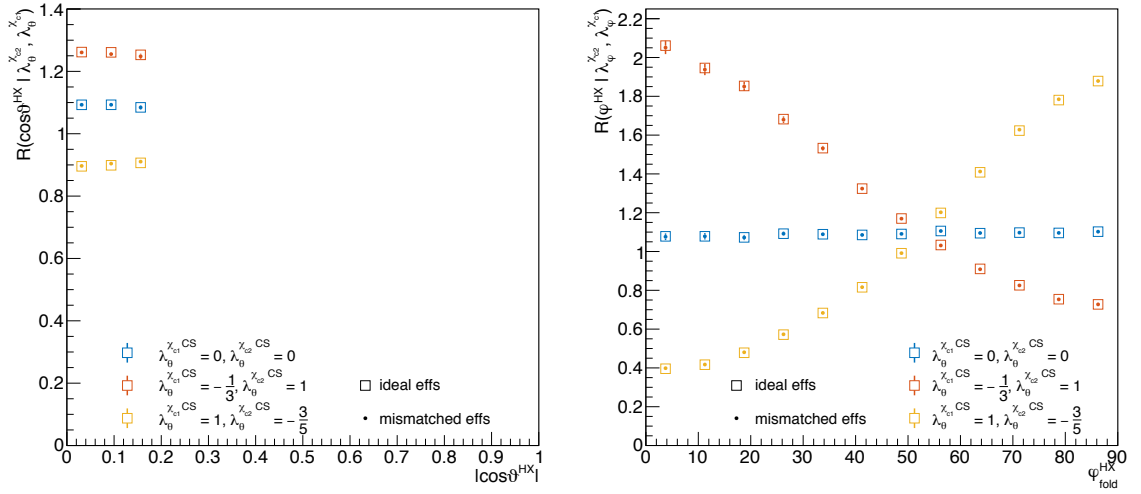


**Figure C.3:** Ratios of  $\chi_{c2}$  over  $\chi_{c1}$  yields as a function of  $|\cos\vartheta^{\text{HX}}|$  (left) and  $\varphi^{\text{HX}}$  (right) evaluated with corrections maps computed with different reconstruction efficiencies, for the  $p_{\text{T}}^{\text{J}/\psi}$  range 8–9 GeV. For the “ideal effs” the same efficiencies are used in the generation of the correction maps and the test samples whereas in case of the “mismatched effs” two different sets of efficiencies have been used.

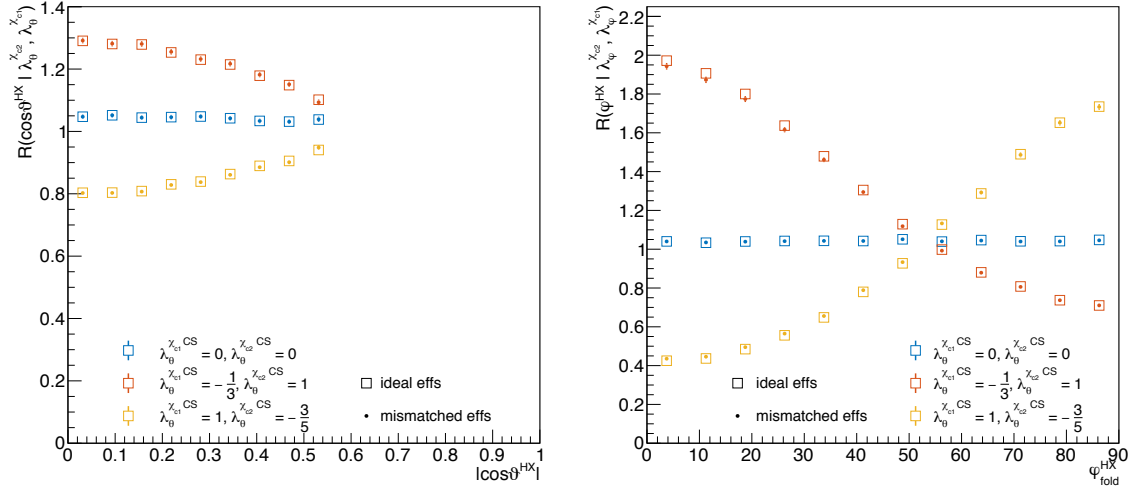


**Figure C.4:** Ratios of  $\chi_{c2}$  over  $\chi_{c1}$  yields as a function of  $|\cos\vartheta^{\text{HX}}|$  (left) and  $\varphi^{\text{HX}}$  (right) evaluated with corrections maps computed with different reconstruction efficiencies, for the  $p_{\text{T}}^{\text{J}/\psi}$  range 16–20 GeV. For the “ideal effs” the same efficiencies are used in the generation of the correction maps and the test samples whereas in case of the “mismatched effs” two different sets of efficiencies have been used.

## C.2 Simultaneous binned fits results

The following pages show all the invariant mass distributions with overlaid fit results in all  $|\cos\vartheta^{\text{HX}}|$  and  $\varphi^{\text{HX}}$  bins in the three  $p_{\text{T}}^{\text{J}/\psi}$  ranges. The  $|\cos\vartheta^{\text{HX}}|$  or  $\varphi^{\text{HX}}$  and the  $p_{\text{T}}^{\text{J}/\psi}$  ranges are indicated in the individual panels. The pull distributions, shown in the bottom panels, are calculated as the difference between the data points and the fitted curve divided by the uncertainty of the data points. The global  $\chi^2/\text{ndf}$  values stated in the top left corners are calculated from the invariant mass distributions in all  $|\cos\vartheta^{\text{HX}}|$  or  $\varphi^{\text{HX}}$  bins in each  $p_{\text{T}}^{\text{J}/\psi}$  range.

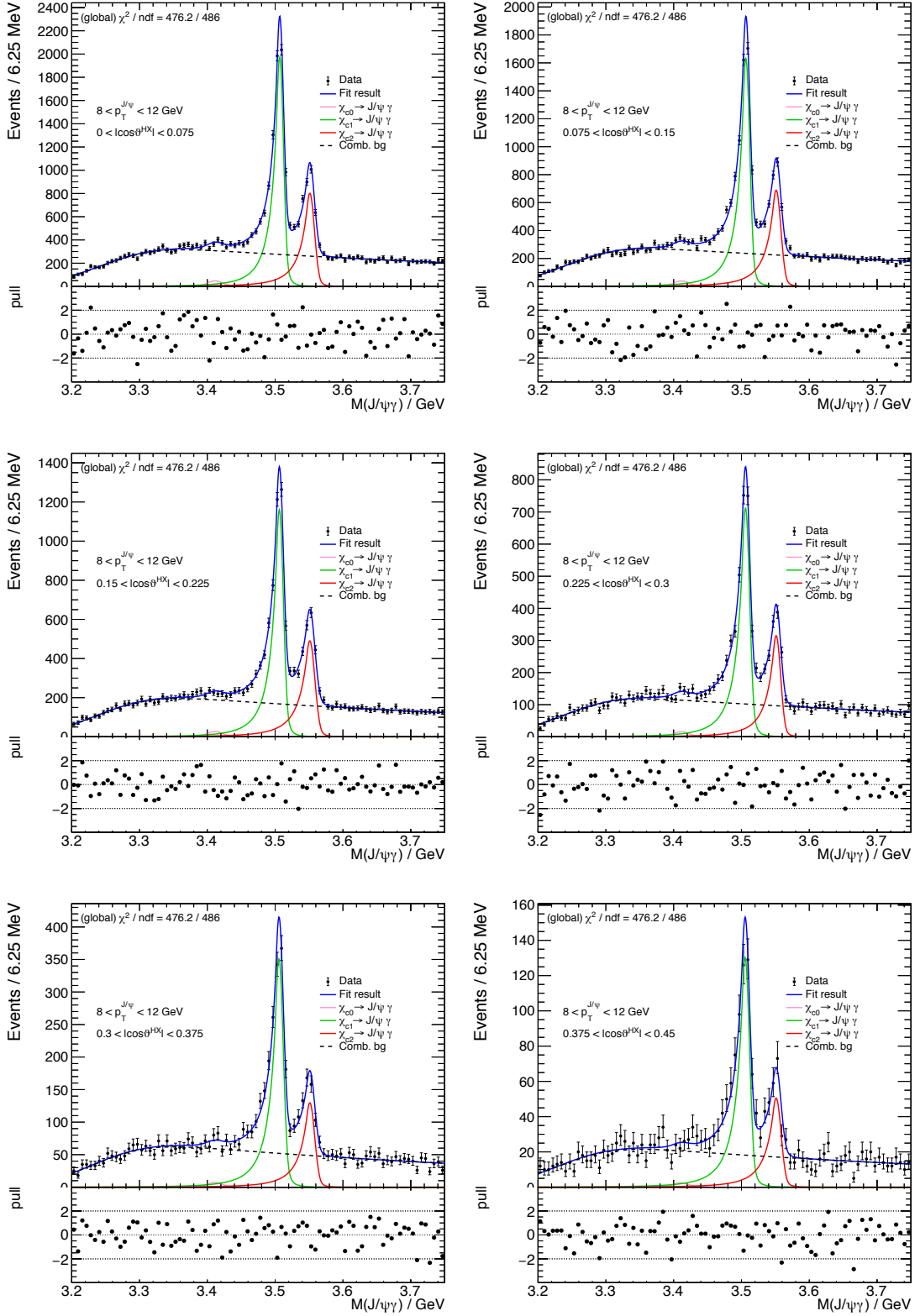


Figure C.5: Invariant mass distributions of the  $\chi_c$  candidates in different  $|\cos \vartheta^{\text{HX}}|$  bins for the 8–12 GeV  $p_{\text{T}}^{J/\psi}$  range with overlaid fit results.



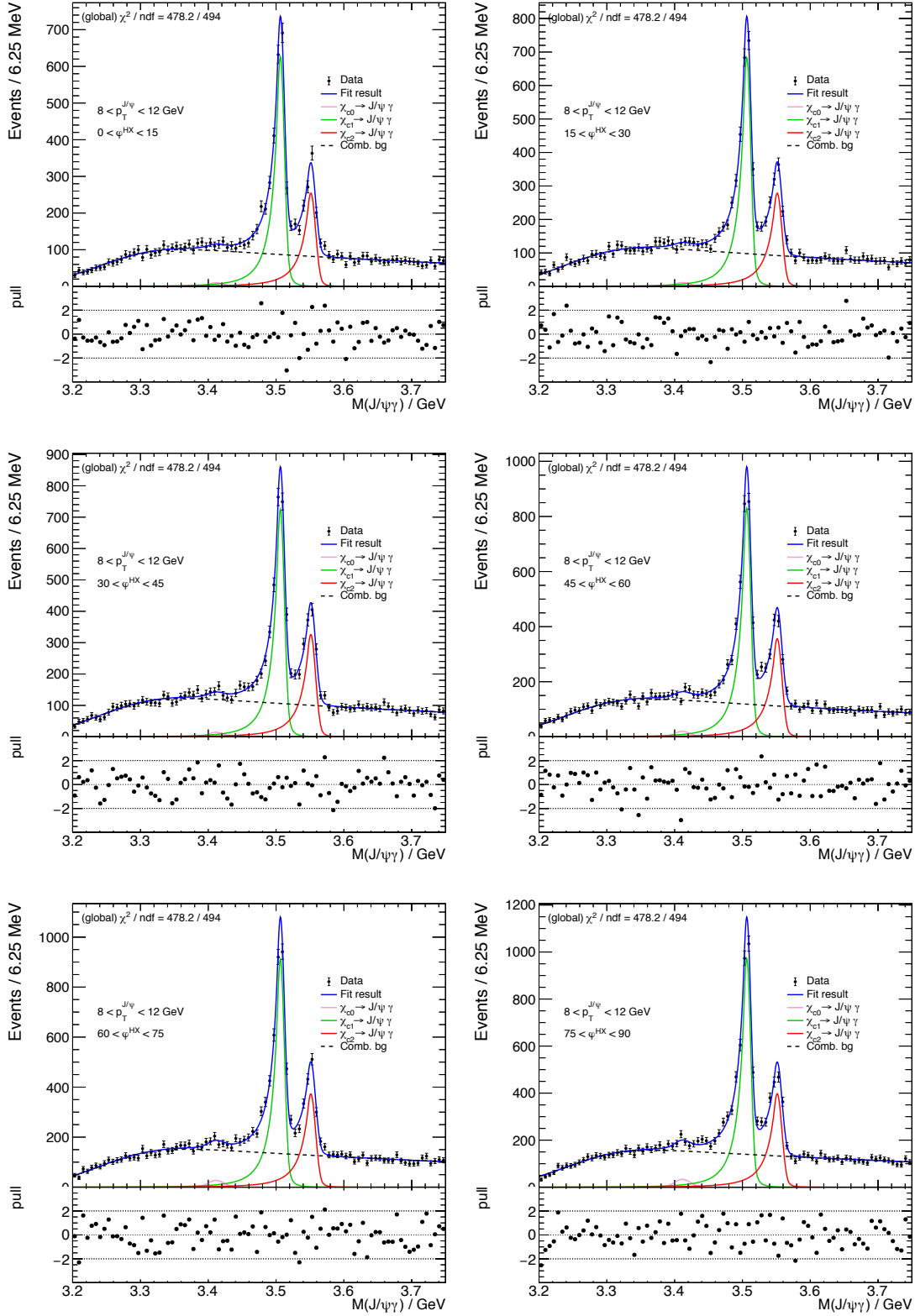
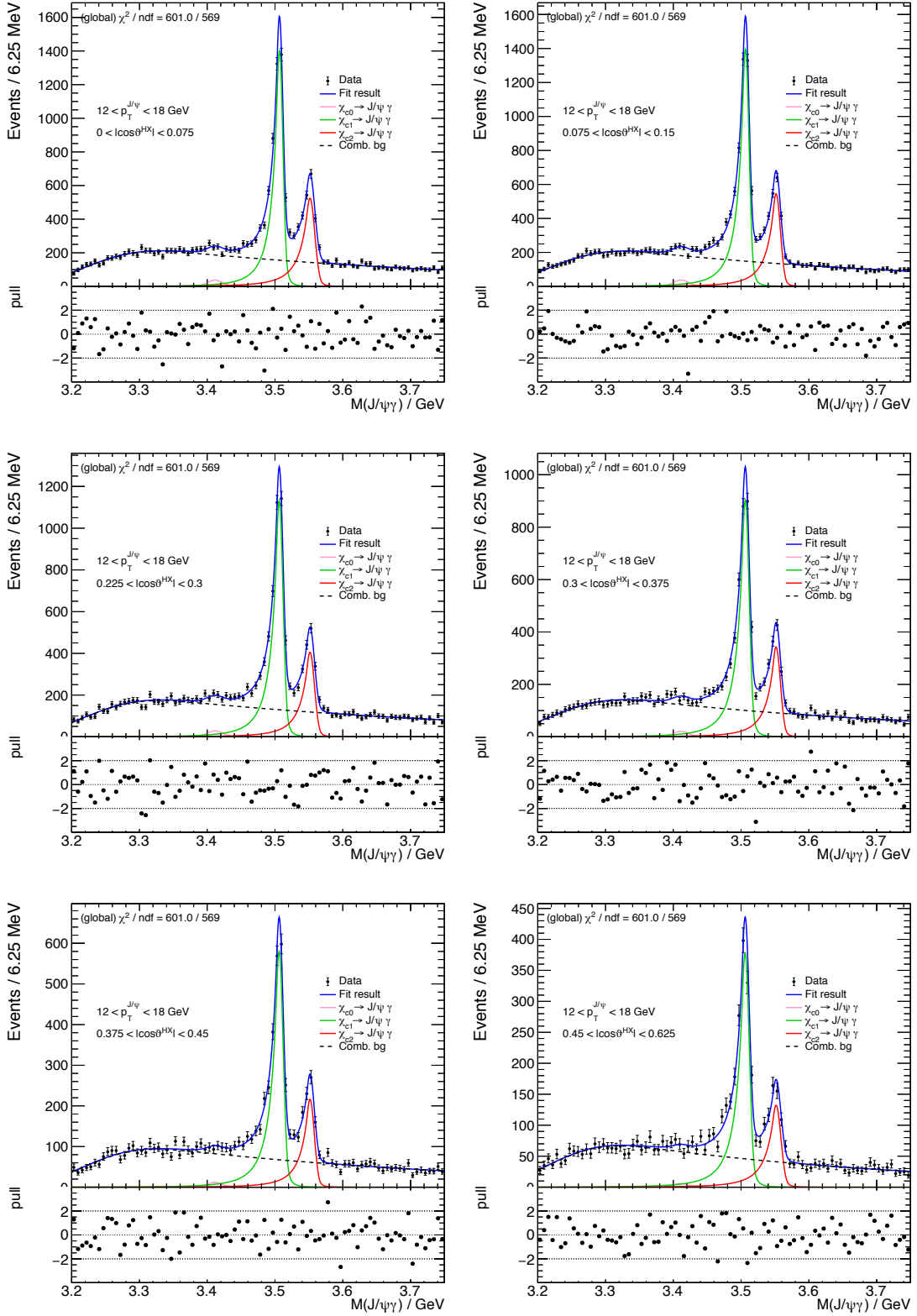


Figure C.6: Invariant mass distributions of the  $\chi_c$  candidates in different  $\varphi^{\text{HX}}$  bins for the 8–12 GeV  $p_T^{J/\psi}$  range with overlaid fit results.



**Figure C.7:** Invariant mass distributions of the  $\chi_c$  candidates in different  $|\cos \vartheta^{\text{HX}}|$  bins for the 12–18 GeV  $p_T^{J/\psi}$  range with overlaid fit results. The missing  $0.15 < |\cos \vartheta^{\text{HX}}| < 0.225$  range is shown in Fig. 5.13.

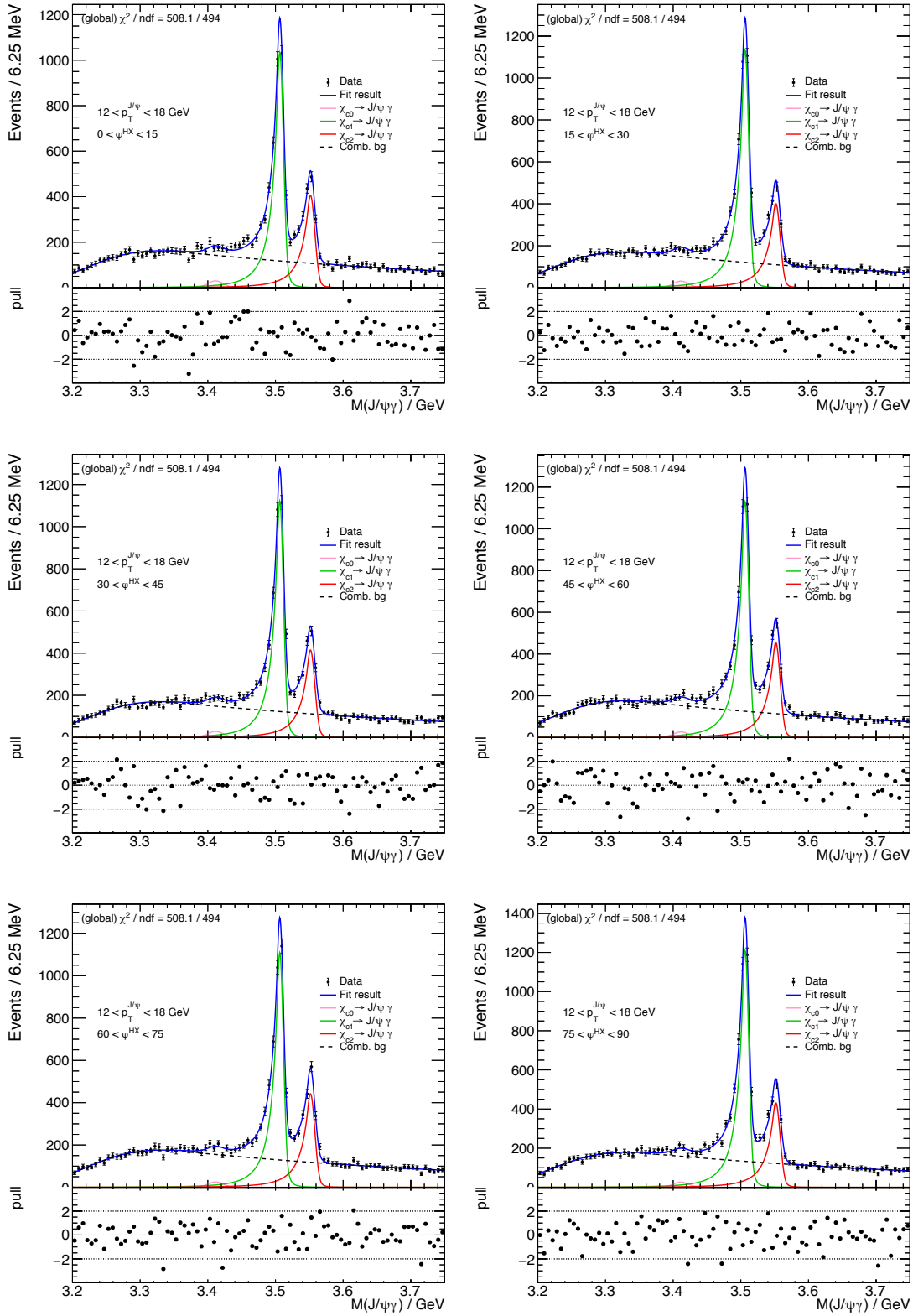
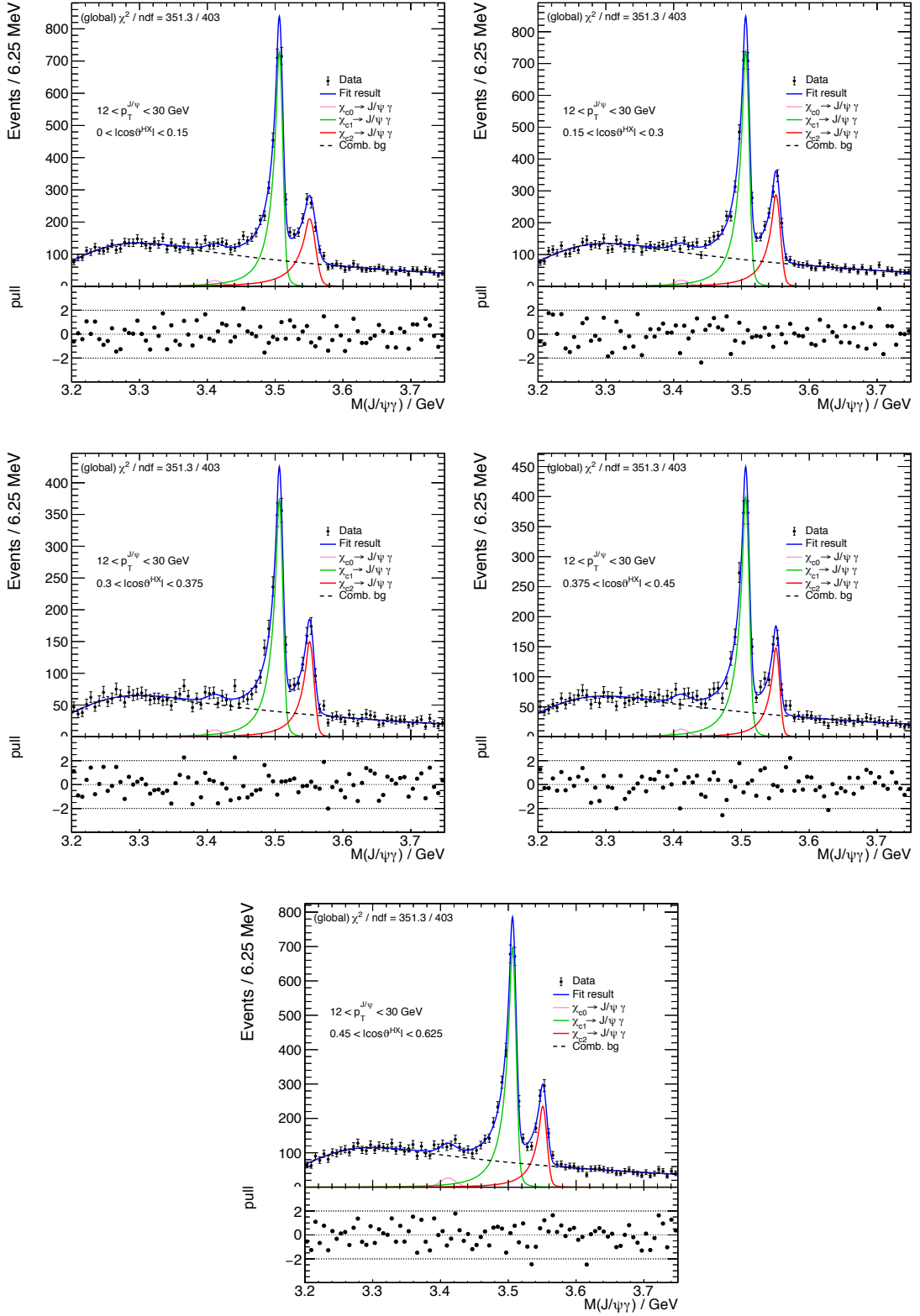


Figure C.8: Invariant mass distributions of the  $\chi_c$  candidates in different  $\varphi^{\text{HX}}$  bins for the 12–18 GeV  $p_T^{J/\psi}$  range with overlaid fit results.



**Figure C.9:** Invariant mass distributions of the  $\chi_c$  candidates in different  $|\cos \vartheta^{\text{HX}}|$  bins for the  $18-30 \text{ GeV}$   $p_{\text{T}}^{\text{J}/\psi}$  range with overlaid fit results.

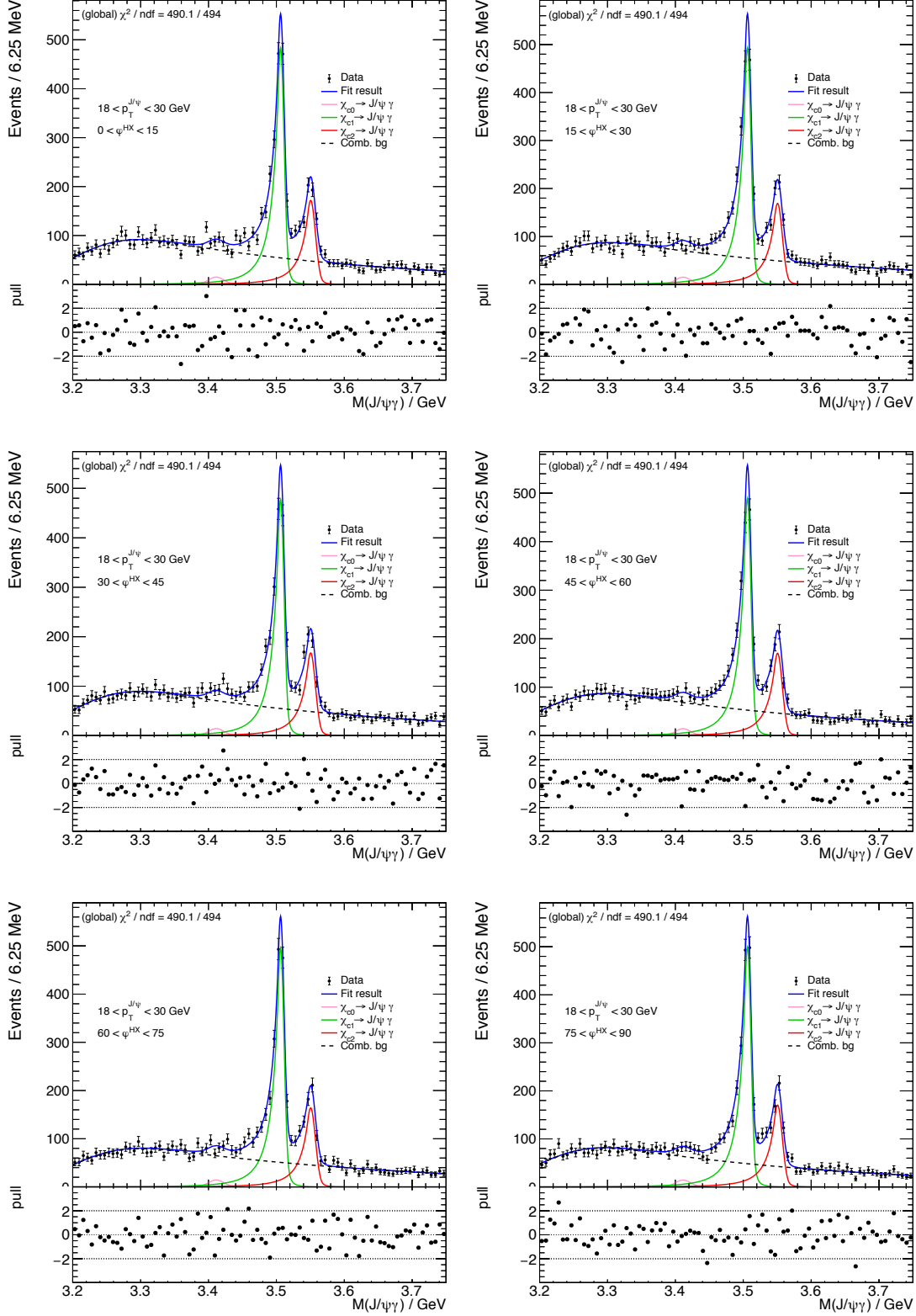


Figure C.10: Invariant mass distributions of the  $\chi_c$  candidates in different  $\varphi^{\text{HX}}$  bins for the 18–30 GeV  $p_T^{J/\psi}$  range with overlaid fit results.

### C.3 Systematic variations summary figures

The following few pages contain figures that give an overview over all the results that have been used in the systematic checks presented in Sec. 5.7. All figures have the same layout and show the results in a three-by-two matrix, where the rows correspond to different  $p_T^{J/\psi}$  ranges and the left column shows the results for the  $|\cos \vartheta^{\text{HX}}|$  direction, whereas the right column shows the results for the  $\varphi^{\text{HX}}$  direction.

Figures C.11–C.15 show the relative differences of the scaled  $\chi_{c2}$  over  $\chi_{c1}$  yield ratios obtained for the variations with respect to the nominally observed ratio. The results shown in these figures are not directly used to determine systematic uncertainties.

Figures C.16–C.20 show the differences in  $\Delta\lambda_\vartheta$  (left column) and  $\Delta\lambda_\varphi$  (right column) with respect to the nominal results obtained from the systematic variations. The red band represents the statistical uncertainties of the nominal results and the uncertainties on the individual variations are calculated assuming that the nominal results and the results obtained from the variations are fully correlated.

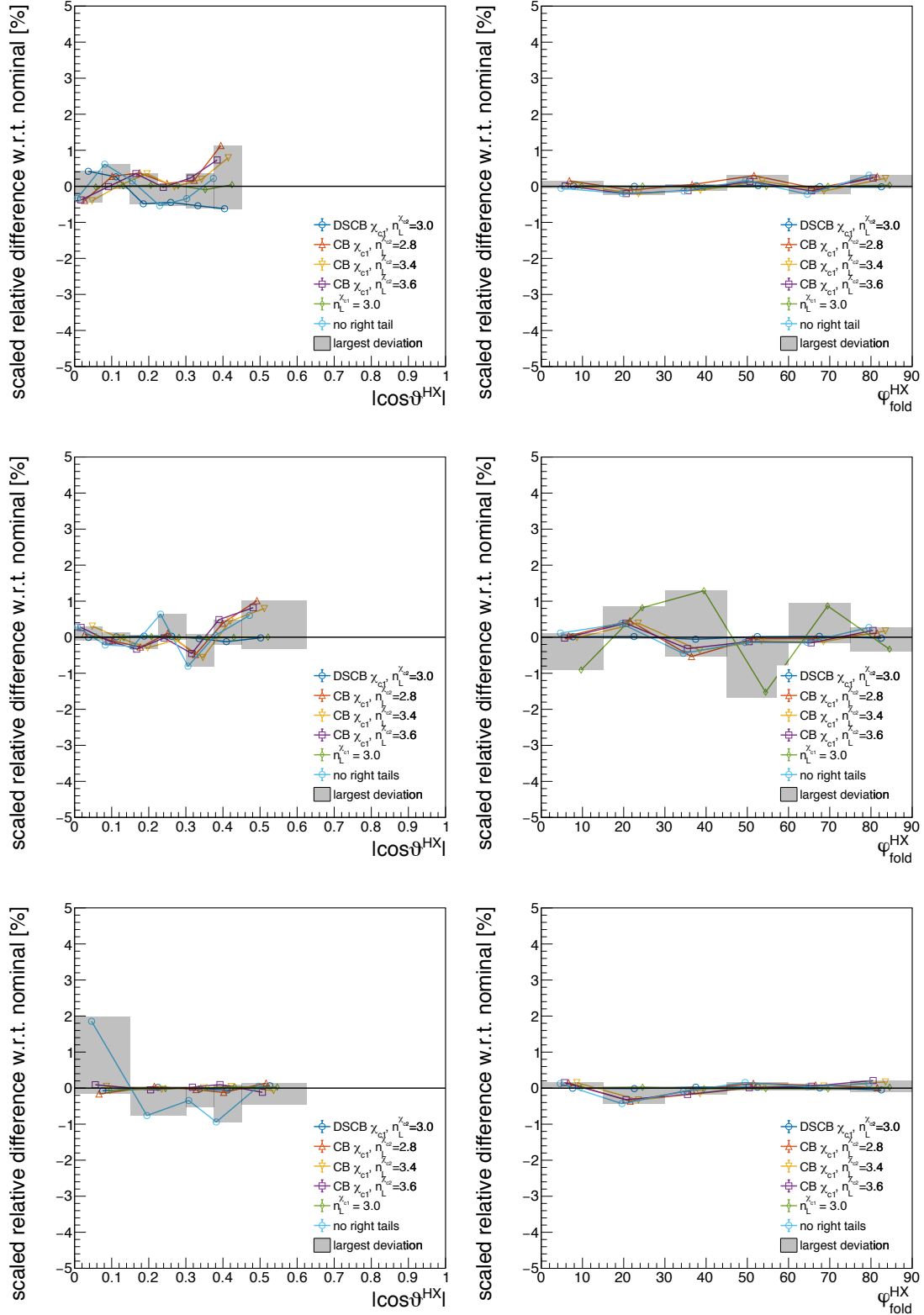


**Figure C.11:** Relative differences of the scaled variations of the signal peak fit model with respect to the nominal results for  $|\cos \vartheta^{\text{HX}}|$  (left) and  $\varphi^{\text{HX}}$  (right) for the three  $p_{\text{T}}^{J/\psi}$  ranges (top to bottom). Only a subset of all variations is shown for visibility reasons.

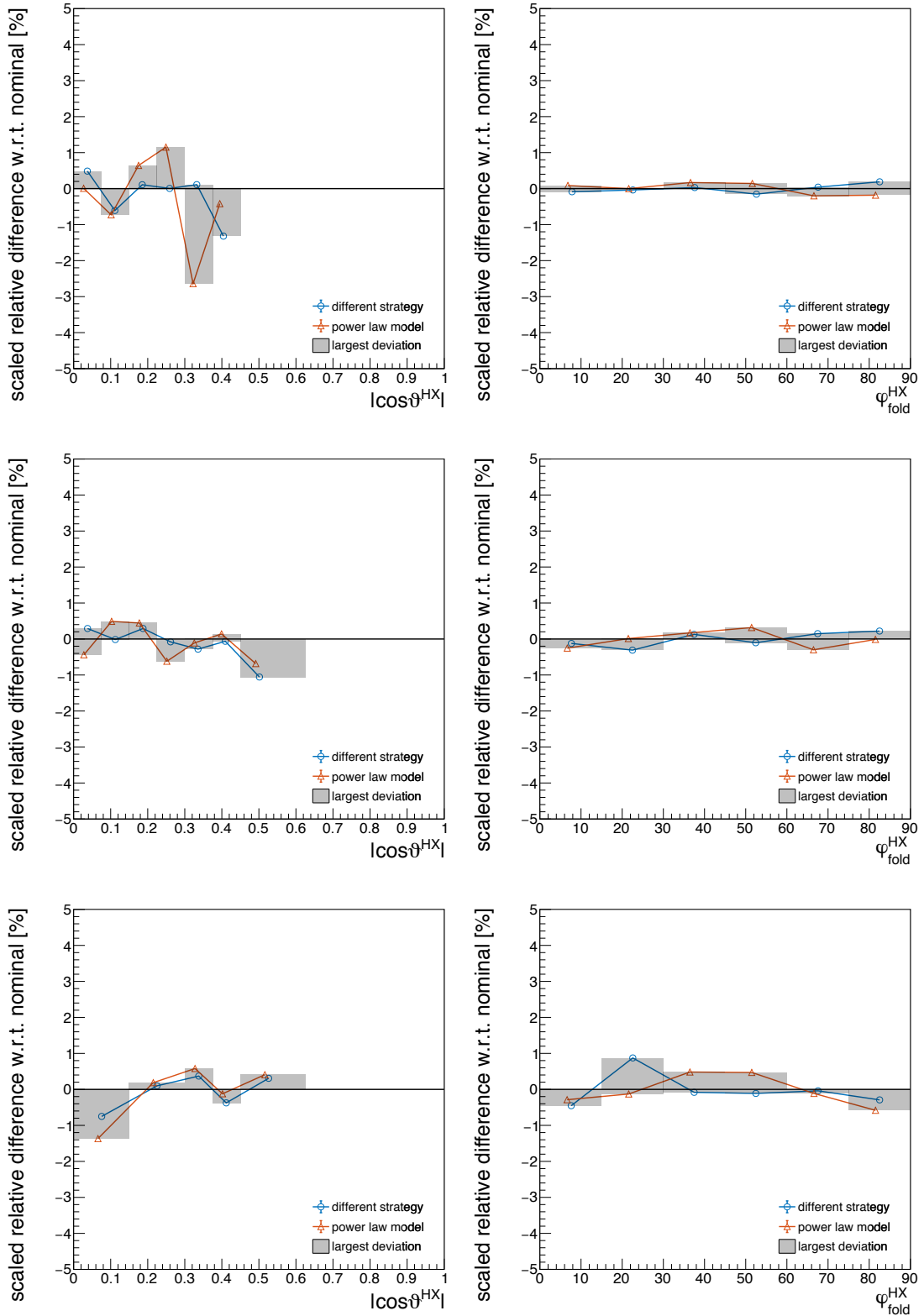


**Figure C.12:** Relative differences of the scaled variations of the continuum background fit model with respect to the nominal results for  $|\cos \vartheta^{\text{HX}}|$  (left) and  $\varphi^{\text{HX}}$  (right) for the three  $p_{\text{T}}^{J/\psi}$  ranges (top to bottom).



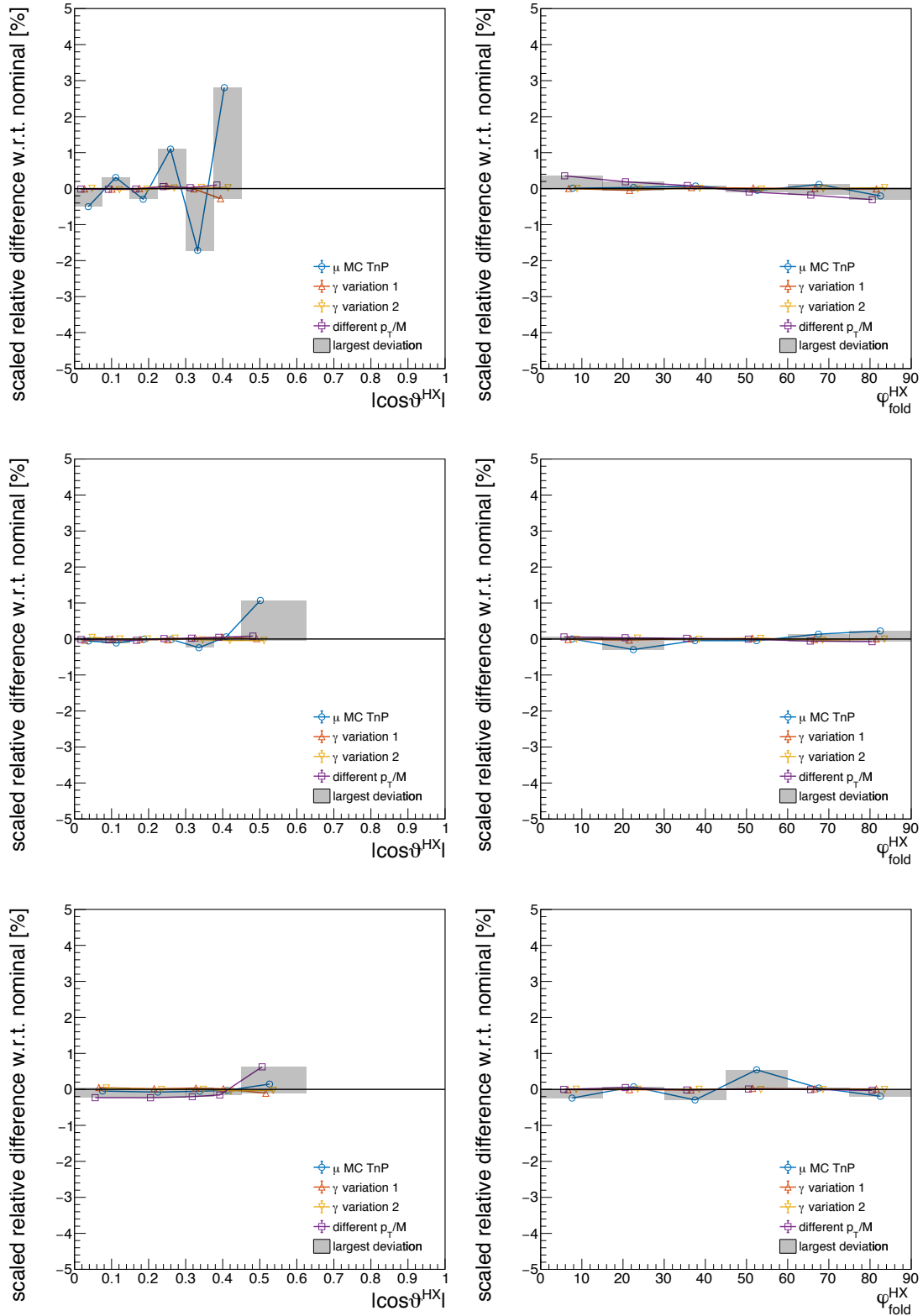


**Figure C.13:** Relative differences of the scaled variations of acceptance and efficiency corrections with respect to the nominal results for  $|\cos\theta^{\text{HX}}|$  (left) and  $\varphi^{\text{HX}}$  (right) for the three  $p_T^{J/\psi}$  ranges (top to bottom).

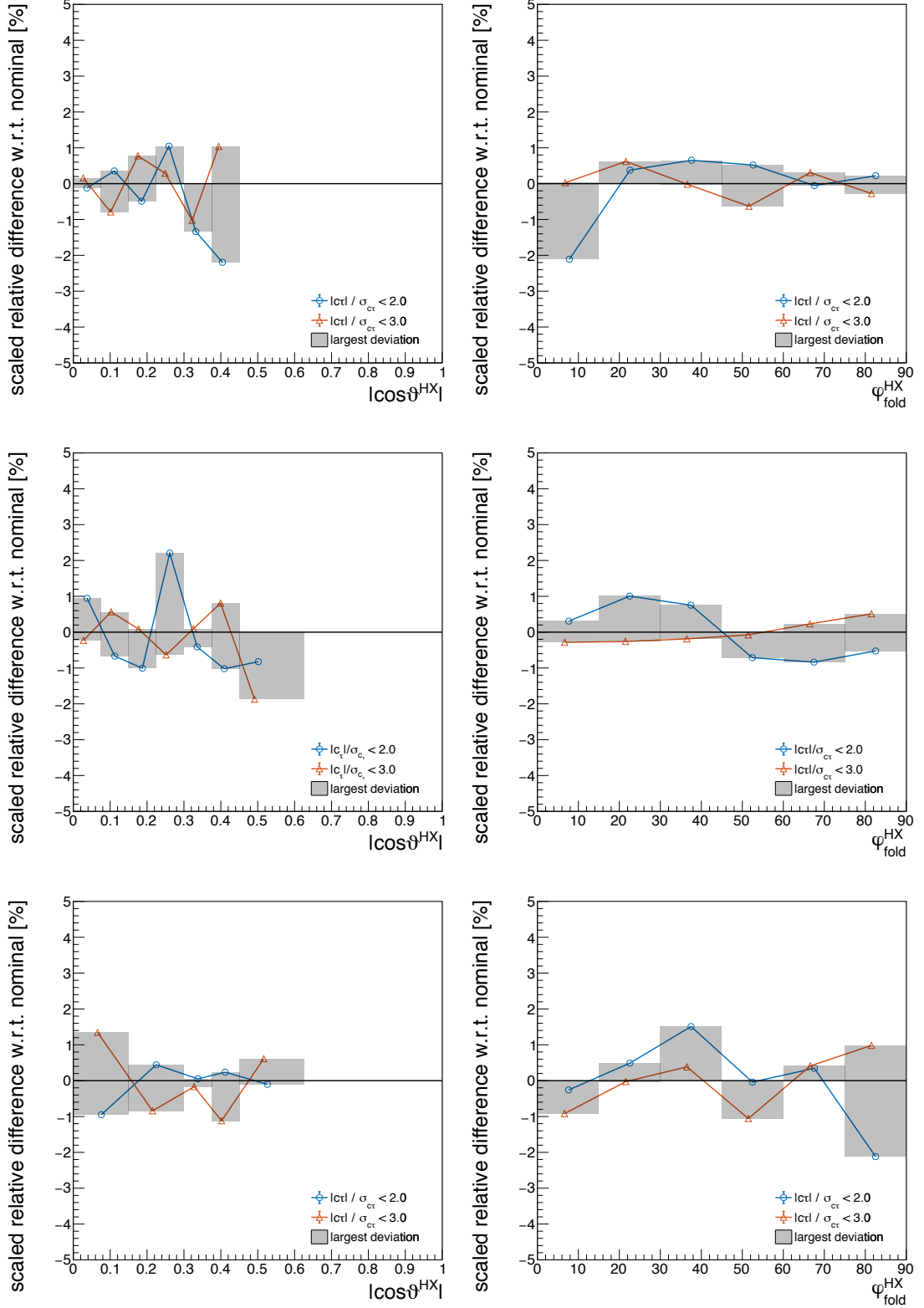


**Figure C.14:** Relative differences of the scaled variations of the cut value used to select promptly produced mesons with respect to the nominal results for  $|\cos \vartheta^{\text{HX}}|$  (left) and  $\varphi^{\text{HX}}$  (right) for the three  $p_{\text{T}}^{J/\psi}$  ranges (top to bottom).

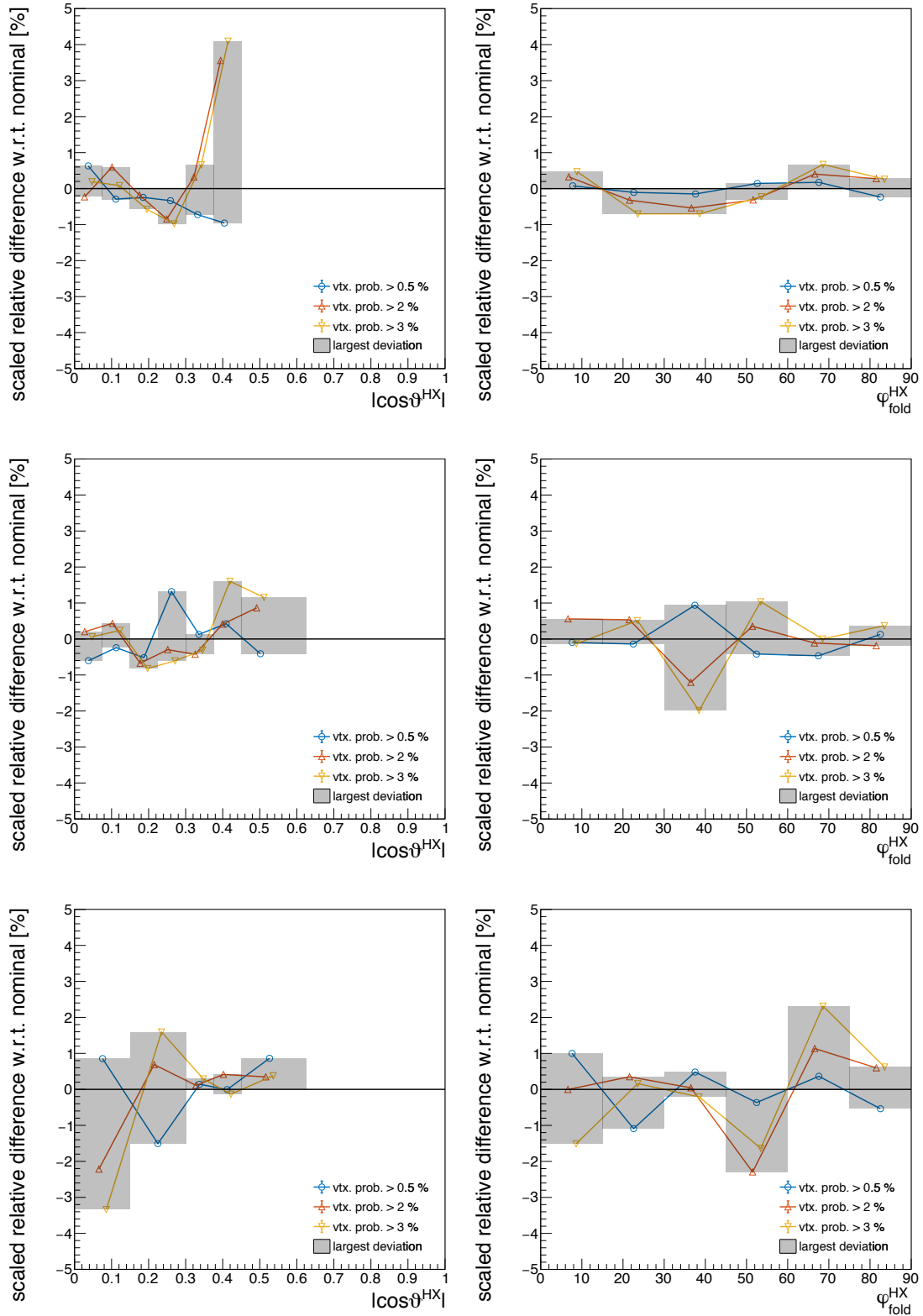


**Figure C.15:** Relative differences of the scaled variations of the KVF  $\chi^2$  probability cut with respect to the nominal results for  $|\cos\vartheta^{\text{HX}}|$  (left) and  $\varphi^{\text{HX}}$  (right) for the three  $p_T^{J/\psi}$  ranges (top to bottom).

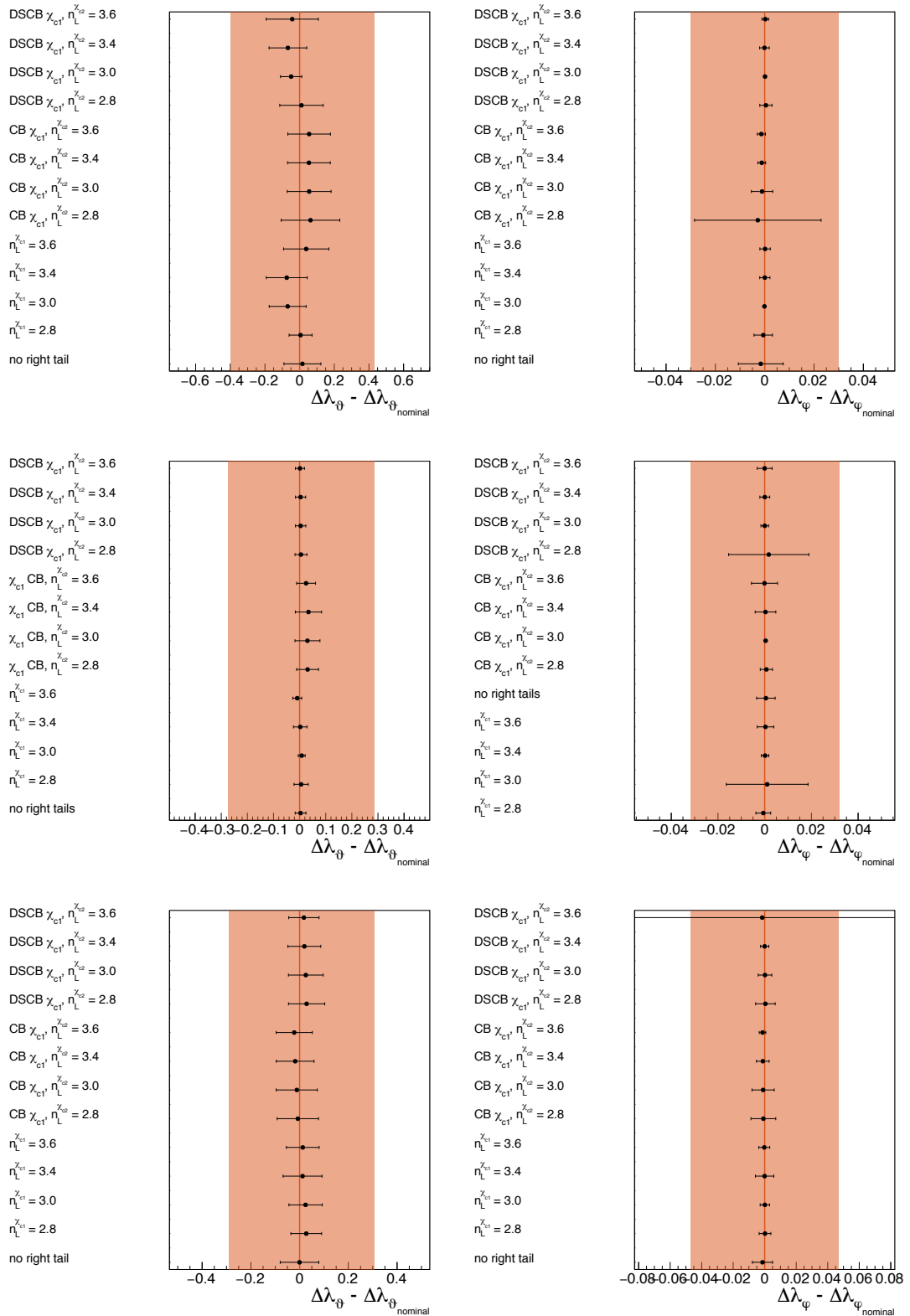


**Figure C.16:** Differences in central value and its uncertainty between the nominal results for  $\Delta\lambda_\theta$  (left) and  $\Delta\lambda_\phi$  (right) and variations of the signal peak fit model for the three  $p_T^{J/\psi}$  ranges (top to bottom).

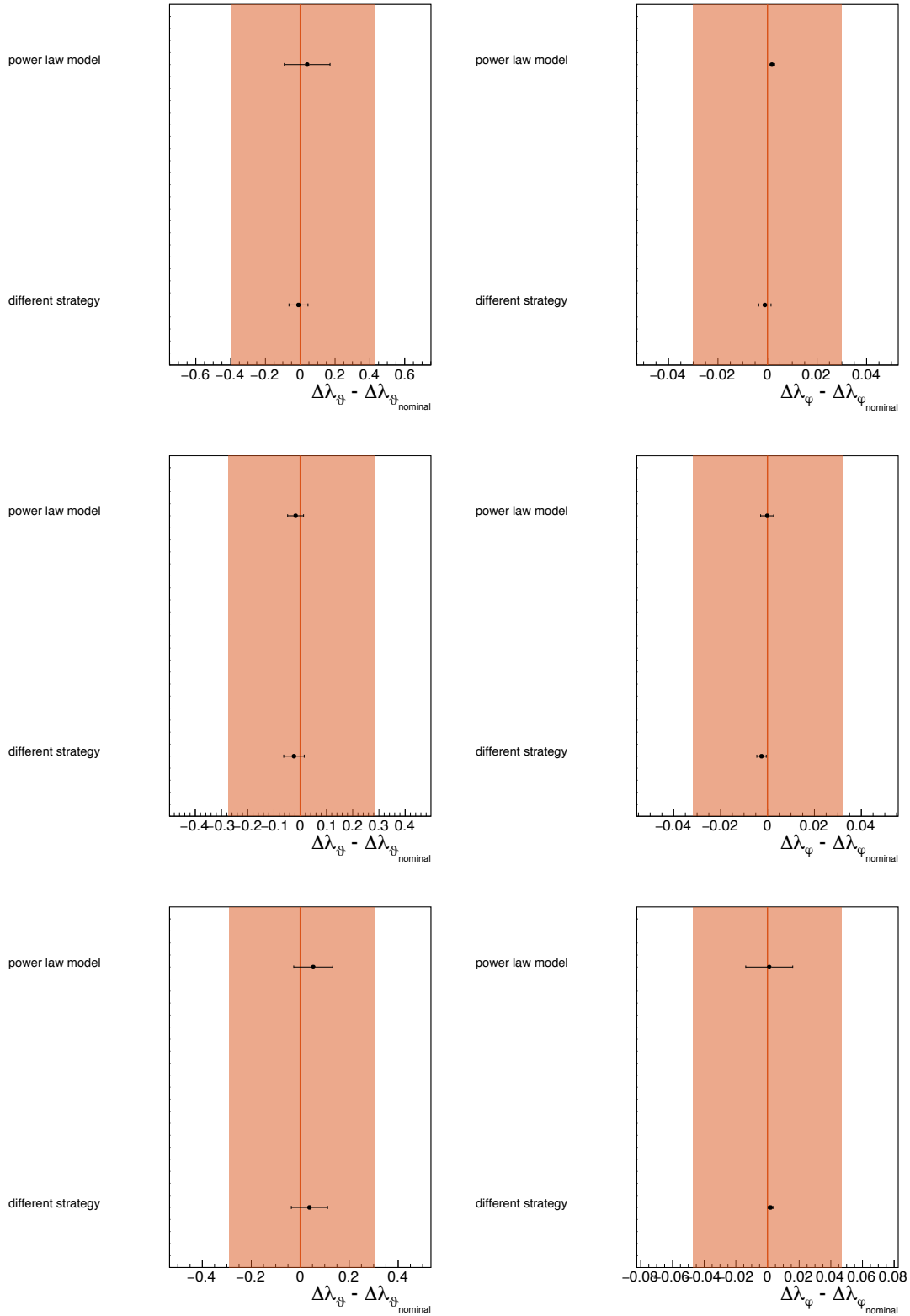


**Figure C.17:** Differences in central value and its uncertainty between the nominal results for  $\Delta\lambda_\theta$  (left) and  $\Delta\lambda_\phi$  (right) and variations of the continuum background fit model for the three  $p_T^{J/\psi}$  ranges (top to bottom).

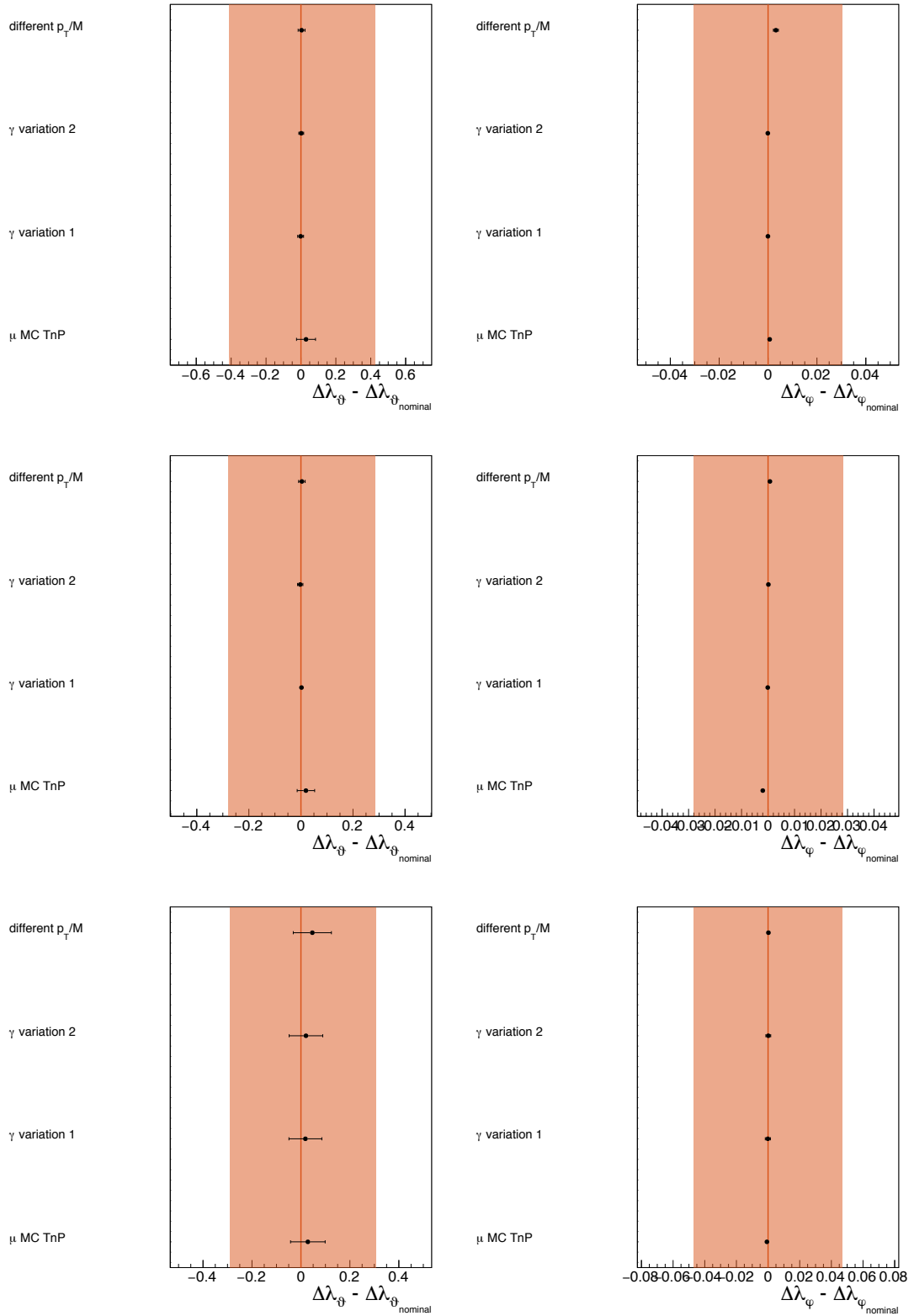


**Figure C.18:** Differences in central value and its uncertainty between the nominal results for  $\Delta\lambda_\theta$  (left) and  $\Delta\lambda_\psi$  (right) and variations of the acceptance times efficiency corrections for the three  $p_T^{J/\psi}$  ranges (top to bottom).

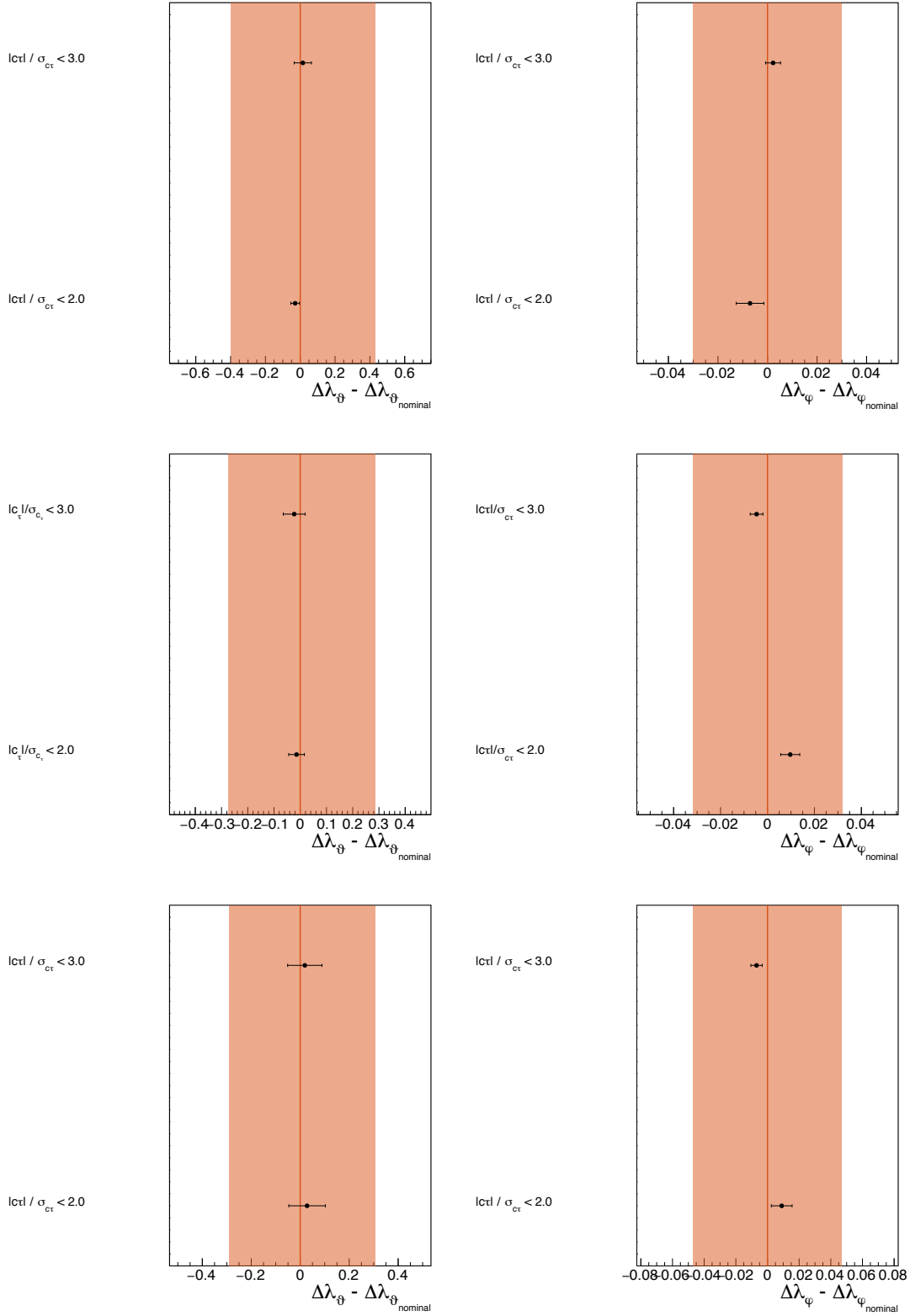


**Figure C.19:** Differences in central value and its uncertainty between the nominal results for  $\Delta\lambda_{\vartheta}$  (left) and  $\Delta\lambda_{\psi}$  (right) and variations of the lifetime significance cut value used to select prompt mesons for the three  $p_T^{J/\psi}$  ranges (top to bottom).

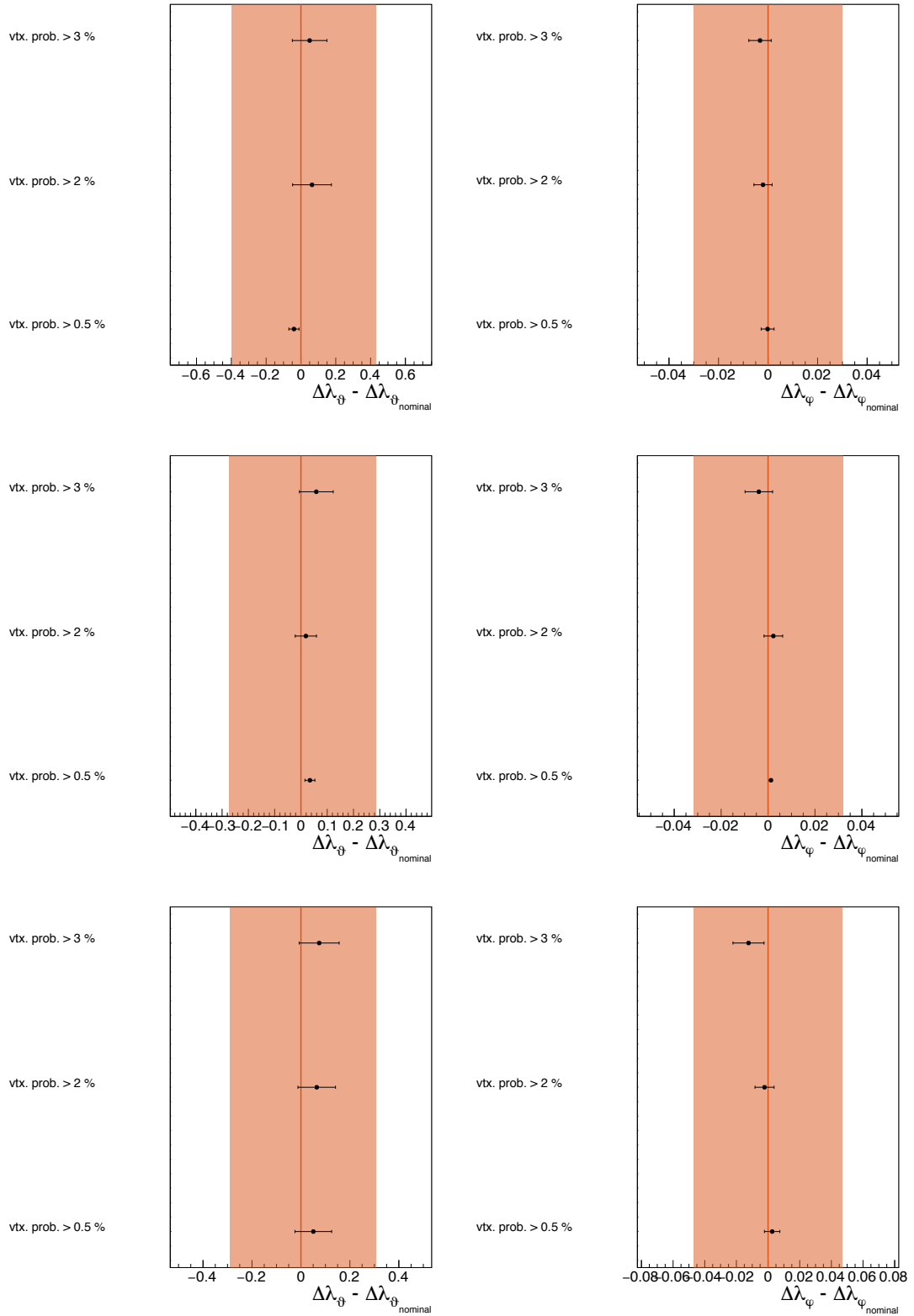


**Figure C.20:** Differences in central value and its uncertainty between the nominal results for  $\Delta\lambda_\theta$  (left) and  $\Delta\lambda_\psi$  (right) and variations of the KVF  $\chi^2$  probability cut value for the three  $p_T^{J/\psi}$  ranges (top to bottom).



# Bibliography

- [1] S. L. Glashow. “Partial symmetries of weak interactions”. *Nucl. Phys.* 22 (1961), pp. 579–588. DOI: [10.1016/0029-5582\(61\)90469-2](https://doi.org/10.1016/0029-5582(61)90469-2).
- [2] Steven Weinberg. “A Model of Leptons”. *Phys. Rev. Lett.* 19 (1967), pp. 1264–1266. DOI: [10.1103/PhysRevLett.19.1264](https://doi.org/10.1103/PhysRevLett.19.1264).
- [3] Abdus Salam. “Weak and Electromagnetic Interactions”. *8th Nobel Symposium Lerum, Sweden, May 19-25, 1968*. 1968, pp. 367–377. URL: <http://inspirehep.net/record/53083>.
- [4] CMS Collaboration. “Observation of a new boson at a mass of 125 GeV with the CMS experiment at the LHC”. *Phys. Lett.* B716 (2012), pp. 30–61. DOI: [10.1016/j.physletb.2012.08.021](https://doi.org/10.1016/j.physletb.2012.08.021). arXiv: [1207.7235 \[hep-ex\]](https://arxiv.org/abs/1207.7235).
- [5] ATLAS Collaboration. “Observation of a new particle in the search for the Standard Model Higgs Boson with the ATLAS detector at the LHC”. *Phys. Lett.* B716 (2012), pp. 1–29. DOI: [10.1016/j.physletb.2012.08.020](https://doi.org/10.1016/j.physletb.2012.08.020). arXiv: [1207.7214 \[hep-ex\]](https://arxiv.org/abs/1207.7214).
- [6] Andrew Purcell. “Go on a Particle Quest at the First CERN Webfest. Le Premier Webfest Du CERN Se Lance à La Conquête Des particules”. BULNA-2012-269. 35/2012 (Aug. 2012), p. 10. URL: <https://cds.cern.ch/record/1473657> (visited on 12/10/2019).
- [7] SNO Collaboration. “Measurement of the rate of  $\nu_e + d \rightarrow p + p + e^-$  interactions produced by  $^8B$  solar neutrinos at the Sudbury Neutrino Observatory”. *Phys. Rev. Lett.* 87 (2001), p. 071301. DOI: [10.1103/PhysRevLett.87.071301](https://doi.org/10.1103/PhysRevLett.87.071301). arXiv: [nucl-ex/0106015 \[nucl-ex\]](https://arxiv.org/abs/nucl-ex/0106015).
- [8] Super-Kamiokande Collaboration. “Evidence for oscillation of atmospheric neutrinos”. *Phys. Rev. Lett.* 81 (1998), pp. 1562–1567. DOI: [10.1103/PhysRevLett.81.1562](https://doi.org/10.1103/PhysRevLett.81.1562). arXiv: [hep-ex/9807003 \[hep-ex\]](https://arxiv.org/abs/hep-ex/9807003).
- [9] Douglas Clowe et al. “A direct empirical proof of the existence of dark matter”. *Astrophys. J.* 648 (2006), pp. L109–L113. DOI: [10.1086/508162](https://doi.org/10.1086/508162). arXiv: [astro-ph/0608407 \[astro-ph\]](https://arxiv.org/abs/astro-ph/0608407).
- [10] Peter W. Higgs. “Broken Symmetries and the Masses of Gauge Bosons”. *Phys. Rev. Lett.* 13 (1964), pp. 508–509. DOI: [10.1103/PhysRevLett.13.508](https://doi.org/10.1103/PhysRevLett.13.508).
- [11] F. Englert and R. Brout. “Broken Symmetry and the Mass of Gauge Vector Mesons”. *Phys. Rev. Lett.* 13 (1964), pp. 321–323. DOI: [10.1103/PhysRevLett.13.321](https://doi.org/10.1103/PhysRevLett.13.321).

- [12] G. S. Guralnik, C. R. Hagen, and T. W. B. Kibble. “Global Conservation Laws and Massless Particles”. *Phys. Rev. Lett.* 13 (1964), pp. 585–587. DOI: [10.1103/PhysRevLett.13.585](https://doi.org/10.1103/PhysRevLett.13.585).
- [13] H. Fritzsche, M. Gell-Mann, and H. Leutwyler. “Advantages of the color octet gluon picture”. *Physics Letters B* 47.4 (1973), pp. 365–368. DOI: [10.1016/0370-2693\(73\)90625-4](https://doi.org/10.1016/0370-2693(73)90625-4).
- [14] H. David Politzer. “Reliable Perturbative Results for Strong Interactions?” *Physical Review Letters* 30.26 (1973), pp. 1346–1349. DOI: [10.1103/physrevlett.30.1346](https://doi.org/10.1103/physrevlett.30.1346).
- [15] David J. Gross and Frank Wilczek. “Ultraviolet Behavior of Non-Abelian Gauge Theories”. *Physical Review Letters* 30.26 (1973), pp. 1343–1346. DOI: [10.1103/physrevlett.30.1343](https://doi.org/10.1103/physrevlett.30.1343).
- [16] N. Brambilla et al. “Heavy quarkonium: progress, puzzles, and opportunities”. *The European Physical Journal C* 71.2 (2011), p. 1534. DOI: [10.1140/epjc/s10052-010-1534-9](https://doi.org/10.1140/epjc/s10052-010-1534-9). arXiv: [1010.5827 \[hep-ph\]](https://arxiv.org/abs/1010.5827).
- [17] N. Brambilla et al. “QCD and Strongly Coupled Gauge Theories: Challenges and Perspectives”. *The European Physical Journal C* 74.10 (2014), p. 2981. DOI: [10.1140/epjc/s10052-014-2981-5](https://doi.org/10.1140/epjc/s10052-014-2981-5). arXiv: [1404.3723 \[hep-ph\]](https://arxiv.org/abs/1404.3723).
- [18] Geoffrey T. Bodwin, Eric Braaten, and G. Peter Lepage. “Rigorous QCD analysis of inclusive annihilation and production of heavy quarkonium”. *Physical Review D* 51.3 (1995), pp. 1125–1171. DOI: [10.1103/physrevd.51.1125](https://doi.org/10.1103/physrevd.51.1125). arXiv: [hep-ph/9407339 \[hep-ph\]](https://arxiv.org/abs/hep-ph/9407339). Erratum: PRD 55, 5853 (1997), <https://doi.org/10.1103/physrevd.55.5853>.
- [19] CDF Collaboration. “ $\Upsilon$  production in  $p\bar{p}$  collisions at  $\sqrt{s} = 1.8$  TeV”. *Phys. Rev. Lett.* 75 (1995), p. 4358. DOI: [10.1103/PhysRevLett.75.4358](https://doi.org/10.1103/PhysRevLett.75.4358).
- [20] CDF Collaboration. “ $J/\psi$  and  $\psi(2S)$  production in  $p\bar{p}$  collisions at  $\sqrt{s} = 1.8$  TeV”. *Phys. Rev. Lett.* 79 (1997), pp. 572–577. DOI: [10.1103/PhysRevLett.79.572](https://doi.org/10.1103/PhysRevLett.79.572).
- [21] CDF Collaboration. “Production of  $J/\psi$  Mesons from  $\chi_c$  Meson Decays in  $p\bar{p}$  Collisions at  $\sqrt{s} = 1.8$  TeV”. *Phys. Rev. Lett.* 79 (1997), pp. 578–583. DOI: [10.1103/PhysRevLett.79.578](https://doi.org/10.1103/PhysRevLett.79.578).
- [22] D0 Collaboration. “ $J/\psi$  production in  $p\bar{p}$  collisions at  $\sqrt{s} = 1.8$  TeV”. *Phys. Lett.* B370 (1996), pp. 239–248. DOI: [10.1016/0370-2693\(96\)00067-6](https://doi.org/10.1016/0370-2693(96)00067-6).
- [23] A. Sansoni. “Quarkonia production at CDF”. *Nucl. Phys.* A610 (1996), pp. 373C–385C. DOI: [10.1016/S0375-9474\(96\)00371-5](https://doi.org/10.1016/S0375-9474(96)00371-5).
- [24] CDF Collaboration. “Measurement of  $J/\psi$  and  $\psi(2S)$  polarization in  $p\bar{p}$  collisions at  $\sqrt{s} = 1.8$  TeV”. *Phys. Rev. Lett.* 85 (2000), pp. 2886–2891. DOI: [10.1103/PhysRevLett.85.2886](https://doi.org/10.1103/PhysRevLett.85.2886). arXiv: [hep-ex/0004027 \[hep-ex\]](https://arxiv.org/abs/hep-ex/0004027).

- [25] CDF Collaboration. “Polarization of  $J/\psi$  and  $\psi(2S)$  Mesons Produced in  $p\bar{p}$  Collisions at  $\sqrt{s} = 1.96$  TeV”. *Phys. Rev. Lett.* 99 (2007), p. 132001. DOI: [10.1103/PhysRevLett.99.132001](https://doi.org/10.1103/PhysRevLett.99.132001). arXiv: [0704.0638](https://arxiv.org/abs/0704.0638) [hep-ex].
- [26] D0 Collaboration. “Measurement of the polarization of the  $\Upsilon(1S)$  and  $\Upsilon(2S)$  states in  $p\bar{p}$  collisions at  $\sqrt{s} = 1.96$ -TeV”. *Phys. Rev. Lett.* 101 (2008), p. 182004. DOI: [10.1103/PhysRevLett.101.182004](https://doi.org/10.1103/PhysRevLett.101.182004). arXiv: [0804.2799](https://arxiv.org/abs/0804.2799) [hep-ex].
- [27] Eric Braaten, Bernd A. Kniehl, and Jungil Lee. “Polarization of prompt  $J/\psi$  at the Fermilab Tevatron”. *Physical Review D* 62.9 (2000), p. 094005. DOI: [10.1103/physrevd.62.094005](https://doi.org/10.1103/physrevd.62.094005). arXiv: [hep-ph/9911436](https://arxiv.org/abs/hep-ph/9911436) [hep-ph].
- [28] Pietro Faccioli et al. “ $J/\psi$  Polarization from Fixed-Target to Collider Energies”. *Physical Review Letters* 102.15 (2009), p. 151802. DOI: [10.1103/physrevlett.102.151802](https://doi.org/10.1103/physrevlett.102.151802).
- [29] Pietro Faccioli et al. “Towards the experimental clarification of quarkonium polarization”. *The European Physical Journal C* 69.3-4 (2010), pp. 657–673. DOI: [10.1140/epjc/s10052-010-1420-5](https://doi.org/10.1140/epjc/s10052-010-1420-5). arXiv: [1006.2738](https://arxiv.org/abs/1006.2738) [hep-ph].
- [30] Pietro Faccioli, Carlos Lourenço, and João Seixas. “New approach to quarkonium polarization studies”. *Physical Review D* 81.11 (2010), p. 111502. DOI: [10.1103/physrevd.81.111502](https://doi.org/10.1103/physrevd.81.111502). arXiv: [1005.2855](https://arxiv.org/abs/1005.2855) [hep-ph].
- [31] Pietro Faccioli, Carlos Lourenço, and João Seixas. “Rotation-Invariant Relations in Vector Meson Decays Into Fermion Pairs”. *Physical Review Letters* 105.6 (2010), p. 061601. DOI: [10.1103/physrevlett.105.061601](https://doi.org/10.1103/physrevlett.105.061601). arXiv: [1005.2601](https://arxiv.org/abs/1005.2601) [hep-ph].
- [32] Pietro Faccioli et al. “Model-independent constraints on the shape parameters of dilepton angular distributions”. *Physical Review D* 83.5 (2011), p. 056008. DOI: [10.1103/physrevd.83.056008](https://doi.org/10.1103/physrevd.83.056008). arXiv: [1102.3946](https://arxiv.org/abs/1102.3946) [hep-ph].
- [33] Pietro Faccioli et al. “Quarkonium production in the LHC era: A polarized perspective”. *Physics Letters B* 736.nil (2014), pp. 98–109. DOI: [10.1016/j.physletb.2014.07.006](https://doi.org/10.1016/j.physletb.2014.07.006). arXiv: [1403.3970](https://arxiv.org/abs/1403.3970) [hep-ph].
- [34] Pietro Faccioli et al. “Quarkonium production at the LHC: A data-driven analysis of remarkably simple experimental patterns”. *Physics Letters B* 773 (2017), pp. 476–486. DOI: [10.1016/j.physletb.2017.09.006](https://doi.org/10.1016/j.physletb.2017.09.006).
- [35] Pietro Faccioli et al. “From identical S- and P-Wave  $p_T$  spectra to maximally distinct polarizations: probing NRQCD with  $\chi$  states”. *The European Physical Journal C* 78.3 (2018), p. 268. DOI: [10.1140/epjc/s10052-018-5755-7](https://doi.org/10.1140/epjc/s10052-018-5755-7). arXiv: [1802.01106](https://arxiv.org/abs/1802.01106) [hep-ph].
- [36] Pietro Faccioli et al. “Universal kinematic scaling as a probe of factorized long-distance effects in high-energy quarkonium production”. *The European Physical Journal C* 78.2 (2018), p. 118. DOI: [10.1140/epjc/s10052-018-5610-x](https://doi.org/10.1140/epjc/s10052-018-5610-x). arXiv: [1802.01102](https://arxiv.org/abs/1802.01102) [hep-ph].

- [37] Pietro Faccioli and Carlos Lourenço. “NRQCD colour-octet expansion vs LHC quarkonium production: signs of a hierarchy puzzle?” *Eur. Phys. J. C* 79.6 (2019), p. 457. DOI: [10.1140/epjc/s10052-019-6968-0](https://doi.org/10.1140/epjc/s10052-019-6968-0). arXiv: [1905.09553](https://arxiv.org/abs/1905.09553) [hep-ph].
- [38] ATLAS Collaboration. “Measurement of  $\chi_{c1}$  and  $\chi_{c2}$  production with  $\sqrt{s} = 7$  TeV  $pp$  collisions at ATLAS”. *JHEP* 07 (2014), p. 154. DOI: [10.1007/JHEP07\(2014\)154](https://doi.org/10.1007/JHEP07(2014)154). arXiv: [1404.7035](https://arxiv.org/abs/1404.7035) [hep-ex].
- [39] CMS Collaboration. “Measurement of the relative prompt production rate of  $\chi_{c2}$  and  $\chi_{c1}$  in  $pp$  collisions at  $\sqrt{s} = 7$  TeV”. *Eur. Phys. J. C* 72 (2012), p. 2251. DOI: [10.1140/epjc/s10052-012-2251-3](https://doi.org/10.1140/epjc/s10052-012-2251-3). arXiv: [1210.0875](https://arxiv.org/abs/1210.0875) [hep-ex].
- [40] CMS Collaboration. “Measurement of the  $\chi_{c1}$  and  $\chi_{c2}$  polarizations in proton-proton collisions at  $\sqrt{s} = 8$  TeV” (2019). CERN-EP-2019-279, CMS-BPH-13-001, submitted to PRL. arXiv: [1912.07706](https://arxiv.org/abs/1912.07706) [hep-ex]. URL: <http://cds.cern.ch/record/2704573>.
- [41] J. J. Aubert et al. “Experimental Observation of a Heavy Particle J”. *Physical Review Letters* 33.23 (1974), pp. 1404–1406. DOI: [10.1103/physrevlett.33.1404](https://doi.org/10.1103/physrevlett.33.1404).
- [42] J. -E. Augustin et al. “Discovery of a Narrow Resonance In e+e- Annihilation”. *Physical Review Letters* 33.23 (1974), pp. 1406–1408. DOI: [10.1103/physrevlett.33.1406](https://doi.org/10.1103/physrevlett.33.1406).
- [43] A. De Rújula and S. L. Glashow. “Is Bound Charm Found?” *Physical Review Letters* 34.1 (1975), pp. 46–49. DOI: [10.1103/physrevlett.34.46](https://doi.org/10.1103/physrevlett.34.46).
- [44] S. W. Herb et al. “Observation of a Dimuon Resonance At 9.5 Gev in 400-gev Proton-Nucleus Collisions”. *Physical Review Letters* 39.5 (1977), pp. 252–255. DOI: [10.1103/physrevlett.39.252](https://doi.org/10.1103/physrevlett.39.252).
- [45] M. Tanabashi et al. “Review of Particle Physics”. *Physical Review D* 98.3 (2018), p. 030001. DOI: [10.1103/physrevd.98.030001](https://doi.org/10.1103/physrevd.98.030001).
- [46] ATLAS Collaboration. “Observation of a New  $\chi_b$  State in Radiative Transitions to  $\Upsilon(1S)$  and  $\Upsilon(2S)$  at ATLAS”. *Phys. Rev. Lett.* 108 (2012), p. 152001. DOI: [10.1103/PhysRevLett.108.152001](https://doi.org/10.1103/PhysRevLett.108.152001). arXiv: [1112.5154](https://arxiv.org/abs/1112.5154) [hep-ex].
- [47] D0 Collaboration. “Observation of a Narrow Mass State Decaying Into  $\Upsilon(1S) + \gamma$  in  $p\bar{p}$  Collisions At  $\sqrt{s} = 1.96$  TeV”. *Phys. Rev. D* 86 (2012), p. 031103. DOI: [10.1103/PhysRevD.86.031103](https://doi.org/10.1103/PhysRevD.86.031103). arXiv: [1203.6034](https://arxiv.org/abs/1203.6034) [hep-ex].
- [48] CMS Collaboration. “Observation of the  $\chi_{b1}(3P)$  and  $\chi_{b2}(3P)$  and Measurement of Their masses”. *Phys. Rev. Lett.* 121 (2018), p. 092002. DOI: [10.1103/PhysRevLett.121.092002](https://doi.org/10.1103/PhysRevLett.121.092002). arXiv: [1805.11192](https://arxiv.org/abs/1805.11192) [hep-ex].
- [49] P. Faccioli et al. “Study of  $\psi'$  and  $\chi_c$  decays as feed-down sources of  $J/\psi$  hadro-production”. *JHEP* 10 (2008), p. 004. DOI: [10.1088/1126-6708/2008/10/004](https://doi.org/10.1088/1126-6708/2008/10/004). arXiv: [0809.2153](https://arxiv.org/abs/0809.2153) [hep-ph].

- [50] A. Andronic et al. “Heavy-flavour and quarkonium production in the LHC era: from proton-proton to heavy-ion collisions”. *The European Physical Journal C* 76.3 (2016), p. 107. DOI: [10.1140/epjc/s10052-015-3819-5](https://doi.org/10.1140/epjc/s10052-015-3819-5). arXiv: [1506.03981](https://arxiv.org/abs/1506.03981) [nucl-ex].
- [51] R. Baier and R. Rückl. “Hadronic collisions: A quarkonium factory”. *Zeitschrift für Physik C Particles and Fields* 19.3 (1983), pp. 251–266. DOI: [10.1007/bf01572254](https://doi.org/10.1007/bf01572254).
- [52] Harald Fritzsche. “Producing heavy quark flavors in hadronic collisions-’ A test of quantum chromodynamics”. *Physics Letters B* 67.2 (1977), pp. 217–221. DOI: [10.1016/0370-2693\(77\)90108-3](https://doi.org/10.1016/0370-2693(77)90108-3).
- [53] F. Halzen. “CVC for Gluons and Hadroproduction of Quark Flavours”. *Physics Letters B* 69.1 (1977), pp. 105–108. DOI: [10.1016/0370-2693\(77\)90144-7](https://doi.org/10.1016/0370-2693(77)90144-7).
- [54] Zhong-Bo Kang, Jian-Wei Qiu, and George Sterman. “Heavy quarkonium production and polarization”. *Phys. Rev. Lett.* 108 (2012), p. 102002. DOI: [10.1103/PhysRevLett.108.102002](https://doi.org/10.1103/PhysRevLett.108.102002). arXiv: [1109.1520](https://arxiv.org/abs/1109.1520) [hep-ph].
- [55] Gouranga C. Nayak, Jian-Wei Qiu, and George F. Sterman. “Fragmentation, factorization and infrared poles in heavy quarkonium production”. *Phys. Lett. B* 613 (2005), pp. 45–51. DOI: [10.1016/j.physletb.2005.03.031](https://doi.org/10.1016/j.physletb.2005.03.031). arXiv: [hep-ph/0501235](https://arxiv.org/abs/hep-ph/0501235) [hep-ph].
- [56] Gouranga C. Nayak, Jian-Wei Qiu, and George F. Sterman. “Fragmentation, NRQCD and NNLO factorization analysis in heavy quarkonium production”. *Phys. Rev. D* 72 (2005), p. 114012. DOI: [10.1103/PhysRevD.72.114012](https://doi.org/10.1103/PhysRevD.72.114012). arXiv: [hep-ph/0509021](https://arxiv.org/abs/hep-ph/0509021) [hep-ph].
- [57] Pietro Faccioli. Usage of illustration kindly granted.
- [58] Gouranga C. Nayak, Jian-Wei Qiu, and George F. Sterman. “Nonrelativistic QCD factorization and velocity-dependence of NNLO poles in heavy quarkonium production”. *Phys. Rev. D* 74 (2006), p. 074007. DOI: [10.1103/PhysRevD.74.074007](https://doi.org/10.1103/PhysRevD.74.074007). arXiv: [hep-ph/0608066](https://arxiv.org/abs/hep-ph/0608066) [hep-ph].
- [59] Hua-Sheng Shao. “HELAC-Onia 2.0: an upgraded matrix-element and event generator for heavy quarkonium physics”. *Comput. Phys. Commun.* 198 (2016), pp. 238–259. DOI: [10.1016/j.cpc.2015.09.011](https://doi.org/10.1016/j.cpc.2015.09.011). arXiv: [1507.03435](https://arxiv.org/abs/1507.03435) [hep-ph].
- [60] Hua-Sheng Shao et al. “Polarizations of  $\chi_{c1}$  and  $\chi_{c2}$  in Prompt Production at the LHC”. *Physical Review Letters* 112.18 (2014), p. 182003. DOI: [10.1103/physrevlett.112.182003](https://doi.org/10.1103/physrevlett.112.182003). arXiv: [1402.2913](https://arxiv.org/abs/1402.2913) [hep-ph].
- [61] Kuang-Ta Chao et al. “ $J/\psi$  Polarization at Hadron Colliders in Nonrelativistic QCD”. *Phys. Rev. Lett.* 108 (2012), p. 242004. DOI: [10.1103/PhysRevLett.108.242004](https://doi.org/10.1103/PhysRevLett.108.242004). arXiv: [1201.2675](https://arxiv.org/abs/1201.2675) [hep-ph].

- [62] Eric Braaten and James Russ. “ $J/\psi$  and  $\Upsilon$  Polarization in Hadronic Production Processes”. *Annual Review of Nuclear and Particle Science* 64.1 (2014), pp. 221–246. DOI: [10.1146/annurev-nucl-030314-044352](https://doi.org/10.1146/annurev-nucl-030314-044352). arXiv: [1401.7352](https://arxiv.org/abs/1401.7352) [hep-ex].
- [63] Gerhard A. Schuler. “Quarkonium Production: Velocity-Scaling Rules and Long-Distance Matrix Elements”. *International Journal of Modern Physics A* 12.22 (1997), pp. 3951–3963. DOI: [10.1142/s0217751x97002103](https://doi.org/10.1142/s0217751x97002103).
- [64] Yan-Qing Ma and Ramona Vogt. “Quarkonium production in an improved color evaporation model”. *Physical Review D* 94.11 (2016), p. 114029. DOI: [10.1103/physrevd.94.114029](https://doi.org/10.1103/physrevd.94.114029).
- [65] Vincent Cheung and Ramona Vogt. “Polarization of prompt  $J/\psi$  and  $\Upsilon(1S)$  production in the color evaporation model”. *Physical Review D* 96.5 (2017), p. 054014. DOI: [10.1103/physrevd.96.054014](https://doi.org/10.1103/physrevd.96.054014).
- [66] Vincent Cheung and Ramona Vogt. “Polarized heavy quarkonium production in the color evaporation model”. *Physical Review D* 95.7 (2017), p. 074021. DOI: [10.1103/physrevd.95.074021](https://doi.org/10.1103/physrevd.95.074021).
- [67] Vincent Cheung and Ramona Vogt. “Production and polarization of prompt  $J/\psi$  in the improved color evaporation model using the  $k_T$ -factorization approach”. *Physical Review D* 98.11 (2018), p. 114029. DOI: [10.1103/physrevd.98.114029](https://doi.org/10.1103/physrevd.98.114029).
- [68] Vincent Cheung and Ramona Vogt. “Production and polarization of prompt  $\Upsilon(nS)$  in the improved color evaporation model using the  $k_T$ -factorization approach”. *Physical Review D* 99.3 (2019), p. 034007. DOI: [10.1103/physrevd.99.034007](https://doi.org/10.1103/physrevd.99.034007).
- [69] John C. Collins and Davison E. Soper. “Parton distribution and decay functions”. *Nuclear Physics B* 194.3 (1982), pp. 445–492. DOI: [10.1016/0550-3213\(82\)90021-9](https://doi.org/10.1016/0550-3213(82)90021-9).
- [70] John C. Collins and Davison E. Soper. “Angular distribution of dileptons in high-energy hadron collisions”. *Physical Review D* 16.7 (1977), pp. 2219–2225. DOI: [10.1103/physrevd.16.2219](https://doi.org/10.1103/physrevd.16.2219).
- [71] Pietro Faccioli et al. “Determination of  $\chi_c$  and  $\chi_b$  polarizations from dilepton angular distributions in radiative decays”. *Physical Review D* 83.9 (2011), p. 096001. DOI: [10.1103/physrevd.83.096001](https://doi.org/10.1103/physrevd.83.096001). arXiv: [1103.4882](https://arxiv.org/abs/1103.4882) [hep-ph].
- [72] CDF Collaboration. *Measurement of Upsilon(1S) Polarization*. CDF Public Note 9966. 2009. URL: [https://www-cdf.fnal.gov/physics/new/bottom/090903.blessed-Upsilon1S-polarization/cdf9966\\_ups\\_1s\\_pol\\_public.pdf](https://www-cdf.fnal.gov/physics/new/bottom/090903.blessed-Upsilon1S-polarization/cdf9966_ups_1s_pol_public.pdf) (visited on 21/08/2019).

- [73] CMS Collaboration. “Measurement of  $J/\psi$  and  $\psi(2S)$  Prompt Double-Differential Cross Sections in  $pp$  Collisions at  $\sqrt{s} = 7$  TeV”. *Phys. Rev. Lett.* 114.19 (2015), p. 191802. DOI: [10.1103/PhysRevLett.114.191802](https://doi.org/10.1103/PhysRevLett.114.191802). arXiv: [1502.04155](https://arxiv.org/abs/1502.04155) [hep-ex].
- [74] CMS Collaboration. “Prompt and non-prompt  $J/\psi$  production in  $pp$  collisions at  $\sqrt{s} = 7$  TeV”. *The European Physical Journal C* 71.3 (2011), p. 1575. DOI: [10.1140/epjc/s10052-011-1575-8](https://doi.org/10.1140/epjc/s10052-011-1575-8). arXiv: [1011.4193](https://arxiv.org/abs/1011.4193) [hep-ex].
- [75] CMS Collaboration. “Measurement of quarkonium production cross sections in  $pp$  collisions at  $\sqrt{s} = 13$  TeV”. *Phys. Lett.* B780 (2018), pp. 251–272. DOI: [10.1016/j.physletb.2018.02.033](https://doi.org/10.1016/j.physletb.2018.02.033). arXiv: [1710.11002](https://arxiv.org/abs/1710.11002) [hep-ex].
- [76] ATLAS Collaboration. “Measurement of the differential cross-sections of inclusive, prompt and non-prompt  $J/\psi$  production in proton-proton collisions at  $\sqrt{s} = 7$  TeV”. *Nucl. Phys.* B850 (2011), pp. 387–444. DOI: [10.1016/j.nuclphysb.2011.05.015](https://doi.org/10.1016/j.nuclphysb.2011.05.015). arXiv: [1104.3038](https://arxiv.org/abs/1104.3038) [hep-ex].
- [77] ATLAS Collaboration. “Measurement of the production cross-section of  $\psi(2S) \rightarrow J/\psi(\rightarrow \mu^+\mu^-)\pi^+\pi^-$  in  $pp$  collisions at  $\sqrt{s} = 7$  TeV at ATLAS”. *JHEP* 09 (2014), p. 079. DOI: [10.1007/JHEP09\(2014\)079](https://doi.org/10.1007/JHEP09(2014)079). arXiv: [1407.5532](https://arxiv.org/abs/1407.5532) [hep-ex].
- [78] ATLAS Collaboration. “Measurement of the differential cross-sections of prompt and non-prompt production of  $J/\psi$  and  $\psi(2S)$  in  $pp$  collisions at  $\sqrt{s} = 7$  and 8 TeV with the ATLAS detector”. *Eur. Phys. J.* C76.5 (2016), p. 283. DOI: [10.1140/epjc/s10052-016-4050-8](https://doi.org/10.1140/epjc/s10052-016-4050-8). arXiv: [1512.03657](https://arxiv.org/abs/1512.03657) [hep-ex].
- [79] LHCb Collaboration. “Measurement of  $J/\psi$  production in  $pp$  collisions at  $\sqrt{s} = 2.76$  TeV”. *JHEP* 02 (2013), p. 041. DOI: [10.1007/JHEP02\(2013\)041](https://doi.org/10.1007/JHEP02(2013)041). arXiv: [1212.1045](https://arxiv.org/abs/1212.1045) [hep-ex].
- [80] LHCb Collaboration. “Measurement of  $J/\psi$  production in  $pp$  collisions at  $\sqrt{s} = 7$  TeV”. *Eur. Phys. J.* C71 (2011), p. 1645. DOI: [10.1140/epjc/s10052-011-1645-y](https://doi.org/10.1140/epjc/s10052-011-1645-y). arXiv: [1103.0423](https://arxiv.org/abs/1103.0423) [hep-ex].
- [81] LHCb Collaboration. “Measurement of  $\psi(2S)$  meson production in  $pp$  collisions at  $\sqrt{s}=7$  TeV”. *Eur. Phys. J.* C72 (2012), p. 2100. DOI: [10.1140/epjc/s10052-012-2100-4](https://doi.org/10.1140/epjc/s10052-012-2100-4). arXiv: [1204.1258](https://arxiv.org/abs/1204.1258) [hep-ex].
- [82] LHCb Collaboration. “Production of  $J/\psi$  and  $\Upsilon$  mesons in  $pp$  collisions at  $\sqrt{s} = 8$  TeV”. *JHEP* 06 (2013), p. 064. DOI: [10.1007/JHEP06\(2013\)064](https://doi.org/10.1007/JHEP06(2013)064). arXiv: [1304.6977](https://arxiv.org/abs/1304.6977) [hep-ex].
- [83] LHCb Collaboration. “Measurement of forward  $J/\psi$  production cross-sections in  $pp$  collisions at  $\sqrt{s} = 13$  TeV”. *JHEP* 10 (2015), p. 172. DOI: [10.1007/JHEP10\(2015\)172](https://doi.org/10.1007/JHEP10(2015)172). arXiv: [1509.00771](https://arxiv.org/abs/1509.00771) [hep-ex]. Erratum: *JHEP* 05, 063 (2017), [https://doi.org/10.1007/JHEP05\(2017\)063](https://doi.org/10.1007/JHEP05(2017)063).
- [84] LHCb Collaboration. “Measurement of  $\psi(2S)$  production cross-sections in proton-proton collisions at  $\sqrt{s} = 7$  and 13 TeV”. *Submitted to: Eur. Phys. J.* (2019). arXiv: [1908.03099](https://arxiv.org/abs/1908.03099) [hep-ex].

- [85] ALICE Collaboration. “Rapidity and transverse momentum dependence of inclusive  $J/\psi$  production in  $pp$  collisions at  $\sqrt{s} = 7$  TeV”. *Phys. Lett.* B704 (2011), pp. 442–455. DOI: [10.1016/j.physletb.2011.09.054](https://doi.org/10.1016/j.physletb.2011.09.054). arXiv: [1105.0380](https://arxiv.org/abs/1105.0380) [hep-ex]. Erratum: *Phys. Lett.* B718, 692 (2012), <https://doi.org/10.1016/j.physletb.2012.10.060>.
- [86] ALICE Collaboration. “Measurement of prompt  $J/\psi$  and beauty hadron production cross sections at mid-rapidity in  $pp$  collisions at  $\sqrt{s} = 7$  TeV”. *JHEP* 11 (2012), p. 065. DOI: [10.1007/JHEP11\(2012\)065](https://doi.org/10.1007/JHEP11(2012)065). arXiv: [1205.5880](https://arxiv.org/abs/1205.5880) [hep-ex].
- [87] ALICE Collaboration. “ $J/\psi$  production as a function of charged particle multiplicity in  $pp$  collisions at  $\sqrt{s} = 7$  TeV”. *Phys. Lett.* B712 (2012), pp. 165–175. DOI: [10.1016/j.physletb.2012.04.052](https://doi.org/10.1016/j.physletb.2012.04.052). arXiv: [1202.2816](https://arxiv.org/abs/1202.2816) [hep-ex].
- [88] ALICE Collaboration. “Measurement of quarkonium production at forward rapidity in  $pp$  collisions at  $\sqrt{s} = 7$  TeV”. *Eur. Phys. J.* C74.8 (2014), p. 2974. DOI: [10.1140/epjc/s10052-014-2974-4](https://doi.org/10.1140/epjc/s10052-014-2974-4). arXiv: [1403.3648](https://arxiv.org/abs/1403.3648) [nucl-ex].
- [89] ALICE Collaboration. “Inclusive quarkonium production at forward rapidity in  $pp$  collisions at  $\sqrt{s} = 8$  TeV”. *Eur. Phys. J.* C76.4 (2016), p. 184. DOI: [10.1140/epjc/s10052-016-3987-y](https://doi.org/10.1140/epjc/s10052-016-3987-y). arXiv: [1509.08258](https://arxiv.org/abs/1509.08258) [hep-ex].
- [90] ALICE Collaboration. “Energy dependence of forward-rapidity  $J/\psi$  and  $\psi(2S)$  production in  $pp$  collisions at the LHC”. *Eur. Phys. J.* C77.6 (2017), p. 392. DOI: [10.1140/epjc/s10052-017-4940-4](https://doi.org/10.1140/epjc/s10052-017-4940-4). arXiv: [1702.00557](https://arxiv.org/abs/1702.00557) [hep-ex].
- [91] CDF Collaboration. “Cross Section for Forward  $J/\psi$  Production in  $p\bar{p}$  Collisions at  $\sqrt{s} = 1.8$  TeV”. *Phys. Rev.* D66 (2002), p. 092001. DOI: [10.1103/PhysRevD.66.092001](https://doi.org/10.1103/PhysRevD.66.092001).
- [92] CDF Collaboration. “Measurement of the  $J/\psi$  meson and  $b$ -hadron production cross sections in  $p\bar{p}$  collisions at  $\sqrt{s} = 1960$  GeV”. *Phys. Rev.* D71 (2005), p. 032001. DOI: [10.1103/PhysRevD.71.032001](https://doi.org/10.1103/PhysRevD.71.032001). arXiv: [hep-ex/0412071](https://arxiv.org/abs/hep-ex/0412071) [hep-ex].
- [93] CDF Collaboration. “Production of  $\psi(2S)$  mesons in  $p\bar{p}$  collisions at 1.96 TeV”. *Phys. Rev.* D80 (2009), p. 031103. DOI: [10.1103/PhysRevD.80.031103](https://doi.org/10.1103/PhysRevD.80.031103). arXiv: [0905.1982](https://arxiv.org/abs/0905.1982) [hep-ex].
- [94] D0 Collaboration. “Small angle  $J/\psi$  production in  $p\bar{p}$  collisions at  $\sqrt{s} = 1.8$  TeV”. *Phys. Rev. Lett.* 82 (1999), pp. 35–40. DOI: [10.1103/PhysRevLett.82.35](https://doi.org/10.1103/PhysRevLett.82.35). arXiv: [hep-ex/9807029](https://arxiv.org/abs/hep-ex/9807029) [hep-ex].
- [95] CMS Collaboration. “Measurements of the  $\Upsilon(1S)$ ,  $\Upsilon(2S)$ , and  $\Upsilon(3S)$  differential cross sections in  $pp$  collisions at  $\sqrt{s} = 7$  TeV”. *Phys. Lett.* B749 (2015), pp. 14–34. DOI: [10.1016/j.physletb.2015.07.037](https://doi.org/10.1016/j.physletb.2015.07.037). arXiv: [1501.07750](https://arxiv.org/abs/1501.07750) [hep-ex].



- [96] ATLAS Collaboration. “Measurement of upsilon production in 7 TeV pp collisions at ATLAS”. *Physical Review D* 87.5 (2013), p. 052004. DOI: [10.1103/physrevd.87.052004](https://doi.org/10.1103/physrevd.87.052004). arXiv: [1211.7255](https://arxiv.org/abs/1211.7255) [hep-ex].
- [97] LHCb Collaboration. “Measurement of  $\Upsilon$  production in  $pp$  collisions at  $\sqrt{s} = 2.76$  TeV”. *Eur. Phys. J. C* 74.4 (2014), p. 2835. DOI: [10.1140/epjc/s10052-014-2835-1](https://doi.org/10.1140/epjc/s10052-014-2835-1). arXiv: [1402.2539](https://arxiv.org/abs/1402.2539) [hep-ex].
- [98] LHCb Collaboration. “Measurement of  $\Upsilon$  production in pp collisions at  $\sqrt{s} = 7$  TeV”. *Eur. Phys. J. C* 72 (2012), p. 2025. DOI: [10.1140/epjc/s10052-012-2025-y](https://doi.org/10.1140/epjc/s10052-012-2025-y). arXiv: [1202.6579](https://arxiv.org/abs/1202.6579) [hep-ex].
- [99] LHCb Collaboration. “Forward production of  $\Upsilon$  mesons in  $pp$  collisions at  $\sqrt{s} = 7$  and 8 TeV”. *JHEP* 11 (2015), p. 103. DOI: [10.1007/JHEP11\(2015\)103](https://doi.org/10.1007/JHEP11(2015)103). arXiv: [1509.02372](https://arxiv.org/abs/1509.02372) [hep-ex].
- [100] LHCb Collaboration. “Measurement of  $\Upsilon$  production in  $pp$  collisions at  $\sqrt{s}=13$  TeV”. *JHEP* 07 (2018), p. 134. DOI: [10.1007/JHEP07\(2018\)134](https://doi.org/10.1007/JHEP07(2018)134). arXiv: [1804.09214](https://arxiv.org/abs/1804.09214) [hep-ex]. Erratum: *JHEP* 05,076(2019), [https://doi.org/10.1007/JHEP05\(2019\)076](https://doi.org/10.1007/JHEP05(2019)076).
- [101] CDF Collaboration. “Production of  $\Upsilon(1S)$  mesons from  $\chi_b$  decays in  $p\bar{p}$  collisions at  $\sqrt{s} = 1.8$  TeV”. *Phys. Rev. Lett.* 84 (2000), pp. 2094–2099. DOI: [10.1103/PhysRevLett.84.2094](https://doi.org/10.1103/PhysRevLett.84.2094). arXiv: [hep-ex/9910025](https://arxiv.org/abs/hep-ex/9910025) [hep-ex].
- [102] CDF Collaboration. “ $\Upsilon$  Production and Polarization in  $p\bar{p}$  Collisions at  $\sqrt{s} = 1.8$  TeV”. *Phys. Rev. Lett.* 88 (2002), p. 161802. DOI: [10.1103/PhysRevLett.88.161802](https://doi.org/10.1103/PhysRevLett.88.161802).
- [103] D0 Collaboration. “Measurement of Inclusive Differential Cross Sections for  $\Upsilon(1S)$  Production in  $p\bar{p}$  Collisions at  $\sqrt{s} = 1.96$  TeV”. *Phys. Rev. Lett.* 94 (2005), p. 232001. DOI: [10.1103/PhysRevLett.94.232001](https://doi.org/10.1103/PhysRevLett.94.232001). arXiv: [hep-ex/0502030](https://arxiv.org/abs/hep-ex/0502030) [hep-ex]. Erratum: *PRL* 100, 049902 (2008), <https://doi.org/10.1103/PhysRevLett.100.049902>.
- [104] CMS Collaboration. “Measurement of the prompt  $J/\psi$  and  $\psi(2S)$  polarizations in  $pp$  collisions at  $\sqrt{s} = 7$  TeV”. *Physics Letters B* 727.4-5 (2013), pp. 381–402. DOI: [10.1016/j.physletb.2013.10.055](https://doi.org/10.1016/j.physletb.2013.10.055). arXiv: [1307.6070](https://arxiv.org/abs/1307.6070) [hep-ex].
- [105] LHCb Collaboration. “Measurement of  $J/\psi$  polarization in  $pp$  collisions at  $\sqrt{s} = 7$  TeV”. *Eur. Phys. J. C* 73.11 (2013), p. 2631. DOI: [10.1140/epjc/s10052-013-2631-3](https://doi.org/10.1140/epjc/s10052-013-2631-3). arXiv: [1307.6379](https://arxiv.org/abs/1307.6379) [hep-ex].
- [106] LHCb Collaboration. “Measurement of  $\psi(2S)$  polarisation in  $pp$  collisions at  $\sqrt{s} = 7$  TeV”. *Eur. Phys. J. C* 74.5 (2014), p. 2872. DOI: [10.1140/epjc/s10052-014-2872-9](https://doi.org/10.1140/epjc/s10052-014-2872-9). arXiv: [1403.1339](https://arxiv.org/abs/1403.1339) [hep-ex].
- [107] ALICE Collaboration. “ $J/\psi$  polarization in  $pp$  collisions at  $\sqrt{s} = 7$  TeV”. *Phys. Rev. Lett.* 108 (2012), p. 082001. DOI: [10.1103/PhysRevLett.108.082001](https://doi.org/10.1103/PhysRevLett.108.082001). arXiv: [1111.1630](https://arxiv.org/abs/1111.1630) [hep-ex].

- [108] ALICE Collaboration. “Measurement of the inclusive  $J/\psi$  polarization at forward rapidity in pp collisions at  $\sqrt{s} = 8$  TeV”. *Eur. Phys. J.* C78.7 (2018), p. 562. DOI: [10.1140/epjc/s10052-018-6027-2](https://doi.org/10.1140/epjc/s10052-018-6027-2). arXiv: [1805.04374](https://arxiv.org/abs/1805.04374) [hep-ex].
- [109] CMS Collaboration. “Measurement of the  $\Upsilon(1S)$ ,  $\Upsilon(2S)$  and  $\Upsilon(3S)$  Polarizations in  $pp$  Collisions at  $\sqrt{s} = 7$  TeV”. *Phys. Rev. Lett.* 110.8 (2013), p. 081802. DOI: [10.1103/PhysRevLett.110.081802](https://doi.org/10.1103/PhysRevLett.110.081802). arXiv: [1209.2922](https://arxiv.org/abs/1209.2922) [hep-ex].
- [110] LHCb Collaboration. “Measurement of the  $\Upsilon$  polarizations in  $pp$  collisions at  $\sqrt{s} = 7$  and 8 TeV”. *JHEP* 12 (2017), p. 110. DOI: [10.1007/JHEP12\(2017\)110](https://doi.org/10.1007/JHEP12(2017)110). arXiv: [1709.01301](https://arxiv.org/abs/1709.01301) [hep-ex].
- [111] CDF Collaboration. “Measurements of Angular Distributions of Muons From  $\Upsilon$  Meson Decays in  $p\bar{p}$  Collisions at  $\sqrt{s} = 1.96$  TeV”. *Phys. Rev. Lett.* 108 (2012), p. 151802. DOI: [10.1103/PhysRevLett.108.151802](https://doi.org/10.1103/PhysRevLett.108.151802). arXiv: [1112.1591](https://arxiv.org/abs/1112.1591) [hep-ex].
- [112] Bin Gong et al. “Polarization for Prompt  $J/\psi$  and  $\psi(2S)$  Production at the Tevatron and LHC”. *Phys. Rev. Lett.* 110.4 (2013), p. 042002. DOI: [10.1103/PhysRevLett.110.042002](https://doi.org/10.1103/PhysRevLett.110.042002). arXiv: [1205.6682](https://arxiv.org/abs/1205.6682) [hep-ph].
- [113] CDF Collaboration. “Production of  $\chi_{c1}$  and  $\chi_{c2}$  in  $p\bar{p}$  Collisions at  $\sqrt{s} = 1.8$  TeV”. *Phys. Rev. Lett.* 86 (2001), pp. 3963–3968. DOI: [10.1103/PhysRevLett.86.3963](https://doi.org/10.1103/PhysRevLett.86.3963).
- [114] CDF Collaboration. “Measurement of  $\sigma_{\chi_{c2}}\mathcal{B}(\chi_{c2} \rightarrow J/\psi\gamma)/\sigma_{\chi_{c1}}\mathcal{B}(\chi_{c1} \rightarrow J/\psi\gamma)$  in  $p\bar{p}$  collisions at  $\sqrt{s} = 1.96$  TeV”. *Phys. Rev. Lett.* 98 (2007), p. 232001. DOI: [10.1103/PhysRevLett.98.232001](https://doi.org/10.1103/PhysRevLett.98.232001). arXiv: [hep-ex/0703028](https://arxiv.org/abs/hep-ex/0703028) [HEP-EX].
- [115] LHCb Collaboration. “Measurement of the cross-section ratio  $\sigma(\chi_{c2})/\sigma(\chi_{c1})$  for prompt  $\chi_c$  production at  $\sqrt{s} = 7$  TeV”. *Phys. Lett.* B714 (2012), pp. 215–223. DOI: [10.1016/j.physletb.2012.06.077](https://doi.org/10.1016/j.physletb.2012.06.077). arXiv: [1202.1080](https://arxiv.org/abs/1202.1080) [hep-ex].
- [116] LHCb Collaboration. “Measurement of the relative rate of prompt  $\chi_{c0}$ ,  $\chi_{c1}$  and  $\chi_{c2}$  production at  $\sqrt{s} = 7$  TeV”. *JHEP* 10 (2013), p. 115. DOI: [10.1007/JHEP10\(2013\)115](https://doi.org/10.1007/JHEP10(2013)115). arXiv: [1307.4285](https://arxiv.org/abs/1307.4285) [hep-ex].
- [117] CMS Collaboration. “Measurement of the production cross section ratio  $\sigma(\chi_{b2}(1P))/\sigma(\chi_{b1}(1P))$  in pp collisions at  $\sqrt{s} = 8$  TeV”. *Phys. Lett.* B743 (2015), pp. 383–402. DOI: [10.1016/j.physletb.2015.02.048](https://doi.org/10.1016/j.physletb.2015.02.048). arXiv: [1409.5761](https://arxiv.org/abs/1409.5761) [hep-ex].
- [118] LHCb Collaboration. “Measurement of the ratio of prompt  $\chi_c$  to  $J/\psi$  production in  $pp$  collisions at  $\sqrt{s} = 7$  TeV”. *Phys. Lett.* B718 (2012), pp. 431–440. DOI: [10.1016/j.physletb.2012.10.068](https://doi.org/10.1016/j.physletb.2012.10.068). arXiv: [1204.1462](https://arxiv.org/abs/1204.1462) [hep-ex].
- [119] LHCb Collaboration. “Measurement of the fraction of  $\Upsilon(1S)$  originating from  $\chi_b(1P)$  decays in  $pp$  collisions at  $\sqrt{s} = 7$  TeV”. *JHEP* 11 (2012), p. 031. DOI: [10.1007/JHEP11\(2012\)031](https://doi.org/10.1007/JHEP11(2012)031). arXiv: [1209.0282](https://arxiv.org/abs/1209.0282) [hep-ex].

- [120] LHCb Collaboration. “Study of  $\chi_b$  meson production in p p collisions at  $\sqrt{s} = 7$  and 8 TeV and observation of the decay  $\chi_b(3P) \rightarrow \Upsilon(3S)\gamma$ ”. *The European Physical Journal C* 74.10 (2014), p. 3092. DOI: [10.1140/epjc/s10052-014-3092-z](https://doi.org/10.1140/epjc/s10052-014-3092-z). arXiv: [1407.7734](https://arxiv.org/abs/1407.7734) [hep-ex].
- [121] LHCb Collaboration. “Measurement of the  $\chi_b(3P)$  mass and of the relative rate of  $\chi_{b1}(1P)$  and  $\chi_{b2}(1P)$  production”. *Journal of High Energy Physics* 2014.10 (2014), p. 88. DOI: [10.1007/jhep10\(2014\)088](https://doi.org/10.1007/jhep10(2014)088). arXiv: [1409.1408](https://arxiv.org/abs/1409.1408) [hep-ex].
- [122] Mathias Butenschoen and Bernd A. Kniehl. “ $J/\psi$  Polarization at the Tevatron and LHC: Nonrelativistic-QCD Factorization at the Crossroads”. *Phys. Rev. Lett.* 108 (2012), p. 172002. DOI: [10.1103/PhysRevLett.108.172002](https://doi.org/10.1103/PhysRevLett.108.172002). arXiv: [1201.1872](https://arxiv.org/abs/1201.1872) [hep-ph].
- [123] Mathias Butenschoen and Bernd A. Kniehl. “Next-to-leading-order tests of NRQCD factorization with  $J/\psi$  yield and polarization”. *Mod. Phys. Lett. A* 28 (2013), p. 1350027. DOI: [10.1142/S0217732313500272](https://doi.org/10.1142/S0217732313500272). arXiv: [1212.2037](https://arxiv.org/abs/1212.2037) [hep-ph].
- [124] Mathias Butenschoen and Bernd A. Kniehl. “ $J/\psi$  production in NRQCD: a global analysis of yield and polarization”. *Nucl. Phys. Proc. Suppl.* 222-224 (2012), pp. 151–161. DOI: [10.1016/j.nuclphysbps.2012.03.016](https://doi.org/10.1016/j.nuclphysbps.2012.03.016). arXiv: [1201.3862](https://arxiv.org/abs/1201.3862) [hep-ph].
- [125] HERA-B Collaboration. “A Measurement of the  $\psi'$  to  $J/\psi$  production ratio in 920 GeV proton-nucleus interactions”. *Eur. Phys. J. C* 49 (2007), pp. 545–558. DOI: [10.1140/epjc/s10052-006-0139-9](https://doi.org/10.1140/epjc/s10052-006-0139-9). arXiv: [hep-ex/0607046](https://arxiv.org/abs/hep-ex/0607046) [hep-ex].
- [126] Geoffrey T. Bodwin et al. “Fragmentation contributions to hadroproduction of prompt  $J/\psi$ ,  $\chi_{cJ}$ , and  $\psi(2S)$  states”. *Physical Review D* 93.3 (2016), p. 034041. DOI: [10.1103/physrevd.93.034041](https://doi.org/10.1103/physrevd.93.034041). arXiv: [1509.07904](https://arxiv.org/abs/1509.07904) [hep-ph].
- [127] CERN. *Our Member States*. Sept. 2019. URL: <https://home.cern/about/who-we-are/our-governance/member-states>.
- [128] UA2 Collaboration. “Evidence for  $Z^0 \rightarrow e^+e^-$  at the CERN  $\bar{p}p$  collider”. *Phys. Lett.* 129B (1983), pp. 130–140. DOI: [10.1016/0370-2693\(83\)90744-X](https://doi.org/10.1016/0370-2693(83)90744-X).
- [129] UA1 Collaboration. “Experimental observation of lepton pairs of invariant mass around 95 GeV/ $c^2$  at the CERN SPS collider”. *Phys. Lett.* 126B (1983), pp. 398–410. DOI: [10.1016/0370-2693\(83\)90188-0](https://doi.org/10.1016/0370-2693(83)90188-0).
- [130] UA2 Collaboration. “Observation of single isolated electrons of high transverse momentum in events with missing transverse energy at the CERN  $\bar{p}p$  collider”. *Phys. Lett.* 122B (1983), pp. 476–485. DOI: [10.1016/0370-2693\(83\)91605-2](https://doi.org/10.1016/0370-2693(83)91605-2).
- [131] UA1 Collaboration. “Experimental observation of isolated large transverse energy electrons with associated missing energy at  $s^{1/2} = 540$  GeV”. *Phys. Lett.* 122B (1983), pp. 103–116. DOI: [10.1016/0370-2693\(83\)91177-2](https://doi.org/10.1016/0370-2693(83)91177-2).

- [132] CERN. *A short history of the Web*. Sept. 2019. URL: <https://home.cern/science/computing/birth-web/short-history-web>.
- [133] Lyndon Evans and Philip Bryant. “LHC Machine”. *JINST* 3 (2008), S08001. DOI: [10.1088/1748-0221/3/08/S08001](https://doi.org/10.1088/1748-0221/3/08/S08001).
- [134] CMS Collaboration. “CMS Physics: Technical Design Report Volume I: Detector Performance and Software”. Technical Design Report CMS (2006). URL: <http://cds.cern.ch/record/922757>.
- [135] CMS Collaboration. “CMS Physics: Technical Design Report, Volume II: Physics Performance”. *J. Phys.* G34.6 (2007), pp. 995–1579. DOI: [10.1088/0954-3899/34/6/S01](https://doi.org/10.1088/0954-3899/34/6/S01).
- [136] CMS Collaboration. “The CMS Experiment at the CERN LHC”. *JINST* 3 (2008), S08004. DOI: [10.1088/1748-0221/3/08/S08004](https://doi.org/10.1088/1748-0221/3/08/S08004).
- [137] Michaela Schaumann et al. “First Xenon-Xenon Collisions in the LHC”. CERN-ACC-2018-126 (2018), MOPMF039. 4 p. DOI: [10.18429/JACoW-IPAC2018-MOPMF039](https://doi.org/10.18429/JACoW-IPAC2018-MOPMF039).
- [138] ALICE Collaboration. “The ALICE Experiment at the CERN LHC”. *JINST* 3 (2008), S08002. DOI: [10.1088/1748-0221/3/08/S08002](https://doi.org/10.1088/1748-0221/3/08/S08002).
- [139] ATLAS Collaboration. “The ATLAS Experiment at the CERN Large Hadron Collider”. *JINST* 3 (2008), S08003. DOI: [10.1088/1748-0221/3/08/S08003](https://doi.org/10.1088/1748-0221/3/08/S08003).
- [140] LHCb Collaboration. “The LHCb Detector at the LHC”. *JINST* 3 (2008), S08005. DOI: [10.1088/1748-0221/3/08/S08005](https://doi.org/10.1088/1748-0221/3/08/S08005).
- [141] Esma Mobs. “The CERN accelerator complex - August 2018. Complexe des accélérateurs du CERN - Août 2018” (Aug. 2018). General Photo. URL: <https://cds.cern.ch/record/2636343>.
- [142] Rende Steerenberg. “LHC Report: Protons: mission accomplished” (Oct. 2018). URL: <https://cds.cern.ch/record/2645638>.
- [143] CMS Collaboration. *CMS Luminosity - Public Results*. Oct. 2019. URL: <https://twiki.cern.ch/twiki/bin/view/CMSPublic/LumiPublicResults>.
- [144] Tai Sakuma and Thomas McCauley. “Detector and Event Visualization With SketchUp at the CMS Experiment”. *J. Phys. Conf. Ser.* 513 (2014), p. 022032. DOI: [10.1088/1742-6596/513/2/022032](https://doi.org/10.1088/1742-6596/513/2/022032). arXiv: [1311.4942](https://arxiv.org/abs/1311.4942) [physics.ins-det].
- [145] CMS Collaboration. *Cutaway diagrams of CMS detector*. May 2019. URL: <https://cds.cern.ch/record/2665537>.
- [146] CMS Collaboration. *Interactive Slice of the CMS detector*. URL: <https://cms-docdb.cern.ch/cgi-bin/PublicDocDB/ShowDocument?docid=4172> (visited on 10/10/2019).
- [147] A Dominguez et al. *CMS Technical Design Report for the Pixel Detector Upgrade*. Tech. rep. CERN-LHCC-2012-016. CMS-TDR-11. Sept. 2012. DOI: [10.2172/1151650](https://doi.org/10.2172/1151650).

- [148] P. Adzic et al. “Energy resolution of the barrel of the CMS electromagnetic calorimeter”. *JINST* 2 (2007), P04004. DOI: [10.1088/1748-0221/2/04/P04004](https://doi.org/10.1088/1748-0221/2/04/P04004).
- [149] CMS Collaboration. “Performance of photon reconstruction and identification with the CMS Detector in proton-proton collisions at  $\sqrt{s} = 8$  TeV”. *JINST* 10.08 (2015), P08010. DOI: [10.1088/1748-0221/10/08/P08010](https://doi.org/10.1088/1748-0221/10/08/P08010). arXiv: [1502.02702](https://arxiv.org/abs/1502.02702) [physics.ins-det].
- [150] CMS Collaboration. “Energy calibration and resolution of the CMS electromagnetic calorimeter in  $pp$  collisions at  $\sqrt{s} = 7$  TeV”. *JINST* 8 (2013), P09009. DOI: [10.1088/1748-0221/8/09/P09009](https://doi.org/10.1088/1748-0221/8/09/P09009). arXiv: [1306.2016](https://arxiv.org/abs/1306.2016) [hep-ex].
- [151] CMS Collaboration. “CMS TriDAS project: Technical Design Report, Volume 1: The Trigger Systems”. Technical Design Report CMS (2000). URL: <http://cds.cern.ch/record/706847>.
- [152] CMS Collaboration. “The CMS Trigger system”. *JINST* 12.01 (2017), P01020. DOI: [10.1088/1748-0221/12/01/P01020](https://doi.org/10.1088/1748-0221/12/01/P01020). arXiv: [1609.02366](https://arxiv.org/abs/1609.02366) [physics.ins-det].
- [153] CMS collaboration. *CMS Technical Design Report for the Level-1 Trigger Upgrade*. Tech. rep. CERN-LHCC-2013-011. CMS-TDR-12. June 2013. URL: <http://cds.cern.ch/record/1556311>.
- [154] CMS Collaboration. “Performance of CMS Muon Reconstruction in  $pp$  Collision Events at  $\sqrt{s} = 7$  TeV”. *JINST* 7 (2012), P10002. DOI: [10.1088/1748-0221/7/10/P10002](https://doi.org/10.1088/1748-0221/7/10/P10002). arXiv: [1206.4071](https://arxiv.org/abs/1206.4071) [physics.ins-det].
- [155] *Supplementary material to [39]*. URL: <https://twiki.cern.ch/twiki/bin/view/CMSPublic/PhysicsResultsBPH11010>.
- [156] CMS Collaboration. “CMS tracking performance results from early LHC operation”. *Eur. Phys. J.* C70 (2010), pp. 1165–1192. DOI: [10.1140/epjc/s10052-010-1491-3](https://doi.org/10.1140/epjc/s10052-010-1491-3). arXiv: [1007.1988](https://arxiv.org/abs/1007.1988) [physics.ins-det].
- [157] CMS Collaboration. *Studies of Tracker Material*. Tech. rep. CMS-PAS-TRK-10-003. 2010. URL: <http://cds.cern.ch/record/1279138>.
- [158] CMS Collaboration. *CMS web based monitoring*. 2019. URL: <https://cmswbm.cern.ch/>.
- [159] CMS Collaboration. *Muon ID performance: low- $p_T$  muon efficiencies*. CMS-DP-2014-020. 2014. URL: <http://cds.cern.ch/record/1712504>.
- [160] CMS Collaboration. “Description and performance of track and primary-vertex reconstruction with the CMS tracker”. *JINST* 9.10 (2014), P10009. DOI: [10.1088/1748-0221/9/10/P10009](https://doi.org/10.1088/1748-0221/9/10/P10009). arXiv: [1405.6569](https://arxiv.org/abs/1405.6569) [physics.ins-det].
- [161] Torbjorn Sjostrand, Stephen Mrenna, and Peter Z. Skands. “PYTHIA 6.4 Physics and Manual”. *JHEP* 05 (2006), p. 026. DOI: [10.1088/1126-6708/2006/05/026](https://doi.org/10.1088/1126-6708/2006/05/026). arXiv: [hep-ph/0603175](https://arxiv.org/abs/hep-ph/0603175) [hep-ph].

- [162] S. Agostinelli et al. “GEANT4: A Simulation toolkit”. *Nucl. Instrum. Meth.* A506 (2003), pp. 250–303. DOI: [10.1016/S0168-9002\(03\)01368-8](https://doi.org/10.1016/S0168-9002(03)01368-8).
- [163] CMS Collaboration. *Low  $p_T$  muon and dimuon efficiencies in the 2012 data*. CMS AN-2014-132, internal note (unpublished). 2016. URL: [http://cms.cern.ch/iCMS/jsp/db\\_notes/noteInfo.jsp?cmsnoteid=CMS%5C%20AN-2014/132](http://cms.cern.ch/iCMS/jsp/db_notes/noteInfo.jsp?cmsnoteid=CMS%5C%20AN-2014/132).
- [164] CMS Collaboration. *Low-energy photon conversion and reconstruction efficiencies*. CMS AN-2015-011, internal note (unpublished). 2015. URL: [http://cms.cern.ch/iCMS/jsp/db\\_notes/noteInfo.jsp?cmsnoteid=CMS%5C%20AN-2015/011](http://cms.cern.ch/iCMS/jsp/db_notes/noteInfo.jsp?cmsnoteid=CMS%5C%20AN-2015/011).
- [165] John Erthal Gaiser. “Charmonium Spectroscopy From Radiative Decays of the  $J/\psi$  and  $\psi'$ ”. Appendix F. PhD thesis. SLAC, 1982. URL: <https://slac.stanford.edu/pubs/slacreports/reports02/slac-r-255.pdf>.
- [166] Hirotogu Akaike. “Information theory and an extension of the maximum likelihood principle”. *Selected papers of Hirotugu Akaike*. Springer, 1998, pp. 199–213.
- [167] H. Akaike. “A new look at the statistical model identification”. *IEEE Transactions on Automatic Control* 19.6 (1974), pp. 716–723. DOI: [10.1109/tac.1974.1100705](https://doi.org/10.1109/tac.1974.1100705).
- [168] Gideon Schwarz. “Estimating the Dimension of a Model”. *The Annals of Statistics* 6.2 (1978), pp. 461–464. DOI: [10.1214/aos/1176344136](https://doi.org/10.1214/aos/1176344136).
- [169] Roger Barlow. “Systematic errors: Facts and fictions”. *Advanced Statistical Techniques in Particle Physics. Proceedings, Conference, Durham, UK, March 18-22, 2002*. 2002, pp. 134–144. arXiv: [hep-ex/0207026](https://arxiv.org/abs/hep-ex/0207026) [hep-ex]. URL: <http://www.ippp.dur.ac.uk/Workshops/02/statistics/proceedings/barlow.pdf>.
- [170] ATLAS Collaboration. “Measurement of the production cross section of prompt  $J/\psi$  mesons in association with a  $W^\pm$  boson in  $pp$  collisions at  $\sqrt{s} = 7$  TeV with the ATLAS detector”. *JHEP* 04 (2014), p. 172. DOI: [10.1007/JHEP04\(2014\)172](https://doi.org/10.1007/JHEP04(2014)172). arXiv: [1401.2831](https://arxiv.org/abs/1401.2831) [hep-ex].
- [171] ATLAS. “Measurement of  $J/\psi$  production in association with a  $W^\pm$  boson with  $pp$  data at 8 TeV” (2019). submitted to JHEP. arXiv: [1909.13626](https://arxiv.org/abs/1909.13626) [hep-ex].
- [172] ATLAS Collaboration. “Observation and measurements of the production of prompt and non-prompt  $J/\psi$  mesons in association with a  $Z$  boson in  $pp$  collisions at  $\sqrt{s} = 8$  TeV with the ATLAS detector”. *Eur. Phys. J.* C75.5 (2015), p. 229. DOI: [10.1140/epjc/s10052-015-3406-9](https://doi.org/10.1140/epjc/s10052-015-3406-9). arXiv: [1412.6428](https://arxiv.org/abs/1412.6428) [hep-ex].

- [173] Steven Weinberg. “The Making of the Standard Model”. *Eur. Phys. J. C* 34.hep-ph/0401010 (2003), 5–13. 21 p., streaming video. URL: <https://cds.cern.ch/record/799984>.
- [174] Stuart Firestein. *Failure: Why Science Is So Successful*. Oxford University Press, Oct. 2015. ISBN: 019939010X.
- [175] Eileen Parkes. *Scientific Progress Is Built on Failure*. 2019. URL: <https://www.nature.com/articles/d41586-019-00107-y> (visited on 22/11/2019).
- [176] Maryam Zaringhalam. *Failure in Science Is Frequent and Inevitable—and We Should Talk More About It*. URL: <https://blogs.scientificamerican.com/guest-blog/failure-in-science-is-frequent-and-inevitable-and-we-should-talk-more-about-it/> (visited on 22/11/2019).
- [177] Ilse Kratschmer. “Measurements of prompt  $J/\psi$  and  $\psi(2S)$  production and polarization at CMS”. PhD thesis. TU Wien, 2015. URL: <https://cds.cern.ch/record/2040539>.
- [178] Valentin Karl Knünz. “Measurement of Quarkonium Polarization to Probe QCD at the LHC”. PhD thesis. TU Wien, 2015. DOI: [10.1007/978-3-319-49935-2](https://doi.org/10.1007/978-3-319-49935-2).
- [179] W. K. Hastings. “Monte Carlo sampling methods using Markov chains and their applications”. *Biometrika* 57.1 (1970), pp. 97–109. ISSN: 0006-3444. DOI: [10.1093/biomet/57.1.97](https://doi.org/10.1093/biomet/57.1.97).
- [180] CMS. “Measurement of the  $B^+$  Production Cross Section in pp collisions at  $\sqrt{s} = 7$  TeV”. *Phys. Rev. Lett.* 106 (2011), p. 112001. DOI: [10.1103/PhysRevLett.106.112001](https://doi.org/10.1103/PhysRevLett.106.112001). arXiv: [1101.0131](https://arxiv.org/abs/1101.0131) [hep-ex].
- [181] CMS Collaboration. “Measurement of the total and differential inclusive  $B^+$  hadron cross sections in pp collisions at  $\sqrt{s} = 13$  TeV”. *Phys. Lett. B* 771 (2017), pp. 435–456. DOI: [10.1016/j.physletb.2017.05.074](https://doi.org/10.1016/j.physletb.2017.05.074). arXiv: [1609.00873](https://arxiv.org/abs/1609.00873) [hep-ex].



Die approbierte gedruckte Originalversion dieser Dissertation ist an der TU Wien Bibliothek verfügbar.  
The approved original version of this doctoral thesis is available in print at TU Wien Bibliothek.



# Acronyms

**ALICE** A Large Ion Collider Experiment.

**ASIC** Application Specific Integrated Circuit.

**ATLAS** A Toroidal LHC AparatuS.

**BNL** Brookhaven National Laboratory.

**BPH** B-physics.

**BS** beam spot.

**CB** Crystal Ball.

**CDF** Collider Detector at Fermilab.

**CEM** Color Evaporation Model.

**CERN** European Organization for Nuclear Research.

**CI** confidence interval.

**CL** confidence level.

**CMS** Compact Muon Solenoid.

**CO** color-octet.

**CPU** Central Processing Unit.

**CS** color-singlet.

**CSC** cathode strip chamber.

**CSM** Color-Singlet Model.

**CV** conversion vertex.

**DSCB** double-sided Crystal Ball.

**DT** drift tube.

**EB** ECAL Barrel.

- ECAL** Electromagnetic Calorimeter.
- EE** ECAL Endcap.
- FPGA** Field Programmable Gate Array.
- GMT** Global Muon Trigger.
- GT** Global Trigger.
- HCAL** Hadron Calorimeter.
- HLT** high-level trigger.
- ICEM** improved CEM.
- IP** interaction point.
- KVF** Kinematic Vertex Fit.
- L1** Level-1.
- LDMEs** Long-Distance Matrix Elements.
- LEP** Large Electron-Positron Collider.
- LHC** Large Hadron Collider.
- LHCb** Large Hadron Collider beauty.
- LINAC2** LINear ACcelerator 2.
- LO** leading order.
- LS** Long Shutdown.
- MC** Monte Carlo.
- MCMC** Markov Chain Monte Carlo.
- MPV** most probable value.
- NLO** next-to-leading order.
- NNLO** next-to-next-to-leading order.
- NP** non-prompt.
- NRQCD** Non-Relativistic Quantum Chromodynamics.

- PPD** posterior probability density.
- PR** prompt.
- PS** Proton Synchrotron.
- PSB** Proton Synchrotron Booster.
- PU** pile-up.
- PV** primary vertex.
- QCD** Quantum Chromodynamics.
- RPC** resistive plate chamber.
- SDCs** Short-Distance Coefficients.
- SLAC** Stanford Linear Accelerator Complex.
- SM** Standard Model of Particle Physics.
- SPS** Super Proton Synchrotron.
- SV** secondary vertex.
- TEC** Tracker Endcap.
- TIB** Tracker Inner Barrel.
- TID** Tracker Inner Disk.
- TnP** Tag-and-Probe.
- TOB** Tracker Outer Barrel.



Die approbierte gedruckte Originalversion dieser Dissertation ist an der TU Wien Bibliothek verfügbar.  
The approved original version of this doctoral thesis is available in print at TU Wien Bibliothek.

# List of Figures

1.1	Particles and forces described by the SM [6]. . . . .	2
2.1	Charmonium spectrum and a subset of decays of the CP-even states below the open-charm threshold. . . . .	8
2.2	Bottomonium spectrum and a subset of decays of the CP-even states below the open-bottom threshold. . . . .	8
2.3	Illustration of the assumed NRQCD factorization in quarkonium production . . . . .	12
2.4	SDCs and corresponding $\lambda_\vartheta$ in the helicity frame for the main contributions in the NRQCD factorization approach to directly produced $\psi$ mesons and for $J/\psi$ from $\chi_{c1}$ and $\chi_{c2}$ decays. . . . .	13
2.5	Coordinat system used to define the polar angle $\vartheta$ and the azimuthal angle $\varphi$ . . . . .	17
2.6	Definition of the production plane and the quantization axis $z$ for the HX and the CS frame. . . . .	18
2.7	Allowed regions for the polarization parameters of the dilepton angular decay distribution of $1^{--}$ and $J^{++}$ quarkonia. . . . .	19
2.8	Polarization parameters $\lambda_\vartheta$ , $\lambda_\varphi$ and $\lambda_{\vartheta\varphi}$ in the HX frame for prompt $J/\psi$ and $\psi(2S)$ mesons as a function of $p_T$ and $ y $ measured by the CMS collaboration at $\sqrt{s} = 7$ TeV. . . . .	23
2.9	Prompt cross sections at mid-rapidity as function of $p_T/M$ for different quarkonium states measured in pp collisions at $\sqrt{s} = 7$ TeV by ATLAS and CMS. . . . .	24
2.10	Polar anisotropy parameter $\lambda_\vartheta$ in the HX frame measured by CMS in pp collisions at $\sqrt{s} = 7$ TeV for prompt $J/\psi$ , $\psi(2S)$ and $\Upsilon(1S)$ . . . . .	26
2.11	$\chi_{c2}/\chi_{c1}$ cross section ratio measured by ATLAS and CMS with acceptance corrections for different polarization scenarios and predicted $\chi_{c1}$ and $\chi_{c2}$ $\lambda_\vartheta$ polarization parameter as a function of $p_T/M$ . . . . .	27
3.1	Overview of the CERN accelerator complex. . . . .	31
3.2	Peak instantaneous luminosity in pp collisions vs time for Run I and Run II. . . . .	32
3.3	Cumulative luminosity delivered by the LHC and recorded by CMS in pp collisions vs. time and pile-up distribution for different data taking periods. . . . .	33
3.4	Layout of the CMS experiment. . . . .	34
3.5	Illustration of particle identification in CMS. . . . .	34

3.6	Schematic layout of the inner tracking system before the Phase I upgrade of the pixel detector. . . . .	35
3.7	Conceptual layout comparing the disks and layers of the original and the upgraded pixel detector. . . . .	37
3.8	One quarter of the layout of the muon systems in CMS. . . . .	39
3.9	Architecture of the L1 trigger at CMS during LHC Run I. . . . .	42
3.10	Photon $p_T$ distribution observed in data collected during the 2012 data taking period and used in the analysis in Chapter 5 and convolution of conversion probability and reconstruction efficiency as function of photon $p_T$ estimated from simulations assuming 2011 CMS data taking conditions. . . . .	47
3.11	Spatial distribution of photon conversion vertices in the transverse plane. . . . .	49
4.1	Trigger rate as function of average PU for different trigger paths determined from special data samples collected in 2016 (left) and estimated trigger rates from extrapolation to expected conditions during the 2017 data taking period for different $p_T$ thresholds (right). . . . .	57
4.2	Invariant dimuon mass distribution (left) and $\Delta R$ distribution (right) for $J/\psi$ , $\psi(2S)$ and $\Upsilon(1S)$ mesons at the L1, obtained from simulated event samples. . . . .	58
4.3	L1 efficiencies of different L1 algorithms as a function of $\cos\vartheta^{\text{HX}}$ and $\varphi^{\text{HX}}$ for $J/\psi$ and $\Upsilon(1S)$ mesons. . . . .	59
4.4	Rate reduction factor by selecting only seagull dimuon decays at the HLT as function of the dimuon $p_T$ threshold. . . . .	61
4.5	Rates for three HLT paths vs. time of day during run 304144 of CMS data taking at the end of September 2017 [158]. . . . .	63
5.1	Dependence of polarization parameters $\vec{\lambda}^{\text{HX}}$ on $p_T^{J/\psi}$ and $ y^{J/\psi} $ for the polarization scenario corresponding to $\vec{\lambda}^{\text{CS}} = (-\frac{3}{5}, 0, 0)$ . . . . .	68
5.2	Illustration of how large values of $ \cos\vartheta^{\text{HX}} $ lead to imbalanced muon momenta in the center-of-mass laboratory frame whereas small values lead to muons with similar momenta. . . . .	70
5.3	Normalized $ \cos\vartheta^{\text{HX}} $ distributions for increasingly stricter $p_T^\mu$ requirements (left) and two-dimensional ( $ \cos\vartheta , \varphi$ ) angular distributions distributions in the HX (center) and CS (right) frame obtained from all candidate events in the $p_T^{J/\psi}$ range 12–18 GeV after applying all nominal event selection criteria (Sec. 5.2). . . . .	71
5.4	Invariant dimuon mass distribution and lifetime significance distribution after applying all selections but the lifetime significance. . . . .	73
5.5	Single muon reconstruction efficiencies (left) as a function of $p_T^\mu$ for two $ \eta^\mu $ ranges and ratios between the alternative and the nominal curve (right). . . . .	76
5.6	Photon reconstruction efficiencies (left) as a function of $p_T^\gamma$ and ratios between the alternative curves and the nominal curve (right). . . . .	76

5.7	Ratio $R(\cos\vartheta)$ obtained from a Full MC and a Fast MC sample generated assuming unpolarized $\chi_{c1}$ and $\chi_{c2}$ in three different $p_T^{\mu\mu}$ ranges (left to right): 8–12, 12–18 and 18–30 GeV. . . . .	77
5.8	Ratios of $\chi_{c2}$ over $\chi_{c1}$ yields as a function of $ \cos\vartheta^{\text{HX}} $ in the $p_T^{J/\psi}$ ranges 12–14 GeV (left) and 16–20 GeV (right) for three polarization scenarios with polar but no azimuthal anisotropies (different colors) in comparison with the shapes expected from analytic expressions. . . . .	79
5.9	Ratios of $\chi_{c2}$ over $\chi_{c1}$ yields as a function of $ \cos\vartheta^{\text{HX}} $ in the $p_T^{J/\psi}$ ranges 12–14 GeV (left) and 16–20 GeV (right) for three polarization scenarios with polar but no azimuthal anisotropies (different colors) comparing the values obtained with different single muon reconstruction efficiencies. . . . .	80
5.10	Ratios of $\chi_{c2}$ over $\chi_{c1}$ yields as a function of $ \cos\vartheta^{\text{HX}} $ in the $p_T^{J/\psi}$ ranges 12–14 GeV (left) and 16–20 GeV (right) for three polarization scenarios with polar but no azimuthal anisotropies (different colors) comparing the values obtained with different photon reconstruction efficiencies. . . . .	80
5.11	Ratios of $\chi_{c2}$ over $\chi_{c1}$ yields as a function of $ \cos\vartheta^{\text{HX}} $ (left) and $\varphi^{\text{HX}}$ (right) evaluated with event samples generated assuming the CS frame as natural frame and measured in the HX frame comparing the results with and without applying acceptance times efficiency corrections, for the $p_T^{J/\psi}$ range 12–14 GeV. . . . .	82
5.12	Several shape parameters of the model used to fit the mass distributions as determined from preliminary fits to mass spectra obtained from an enlarged data sample in the $p_T^{J/\psi}$ range 12–30 GeV. . . . .	87
5.13	Invariant mass distribution of the $\chi_c$ candidates in the range $0.15 <  \cos\vartheta^{\text{HX}}  < 0.225$ , for the 12–18 GeV $p_T^{J/\psi}$ range. . . . .	88
5.14	Ratios of $\chi_{c2}$ over $\chi_{c1}$ yields as a function of $ \cos\vartheta^{\text{HX}} $ (left) and $\varphi^{\text{HX}}$ (right) evaluated with corrections maps computed with different reconstruction efficiencies, for the $p_T^{J/\psi}$ range 12–14 GeV. . . . .	89
5.15	Ratios of $\chi_{c2}$ over $\chi_{c1}$ yields as a function of $ \cos\vartheta^{\text{HX}} $ (left) and $\varphi^{\text{HX}}$ (right) for the three $p_T^{J/\psi}$ ranges 8–12, 12–18 and 18–30 GeV (top to bottom). . . . .	90
5.16	One-dimensional projections of the 3D PPD onto the variables $\Delta\lambda_\vartheta$ (left) and $\lambda_\vartheta^{\chi_{c1}}$ (right) for the three different $p_T^{J/\psi}$ ranges. . . . .	93
5.17	One-dimensional projections of the 3D PPD onto the variables $\Delta\lambda_\varphi$ (left) and $\lambda_\varphi^{\chi_{c1}}$ (right) for the three different $p_T^{J/\psi}$ ranges. . . . .	93
5.18	Comparison of corrected yield ratio for different variations of the acceptance times efficiency corrections with and without scaling the variations to the nominal results. Relative difference between the scaled variations and the nominal results. . . . .	94
5.19	Comparison of the 1D projections of the 3D PPDs after shifting them by the nominal observed central value for $\Delta\lambda_\vartheta$ (left) and the resulting difference in central value and its uncertainty (right). . . . .	95
5.20	Values for $\Delta\lambda_\vartheta$ and $\Delta\lambda_\varphi$ as a function of $p_T^{J/\psi}$ . . . . .	99

5.21	Ratios of $\chi_{c2}$ over $\chi_{c1}$ yields as a function of $\varphi^{\text{HX}}$ (left) and $ \cos \vartheta^{\text{HX}} $ (right) for the three $p_{\text{T}}^{J/\psi}$ ranges in comparison with different polarization scenarios. . . . .	101
5.22	Two-dimensional contours for $\lambda_{\vartheta}^{\chi_{c2}}$ vs. $\lambda_{\vartheta}^{\chi_{c1}}$ , at the 68.3 %, 95.5 % and 99.7 % CLs, obtained from a simultaneous fit of the yield ratios as a function of $ \cos \vartheta^{\text{HX}} $ in all three $p_{\text{T}}^{J/\psi}$ ranges. . . . .	102
5.23	Measured $\lambda_{\vartheta}^{\chi_{c2}}$ values for different fixed values of $\lambda_{\vartheta}^{\chi_{c1}}$ in the three $p_{\text{T}}^{J/\psi}$ ranges. . . . .	103
5.24	Measured $\lambda_{\vartheta}^{\chi_{c2}}$ values as a function of $(p_{\text{T}}/M)^{J/\psi}$ for $\lambda_{\vartheta}^{\chi_{c1}}$ values fixed according to the unpolarized scenario (left) and the NRQCD scenario (right). . . . .	103
A.1	Pedagogical illustration of the mass-lifetime distribution and different mass and lifetime regions obtained from the data sample under study. . . . .	111
A.2	Polarization parameters in the HX frame ( $\lambda_{\vartheta}$ , $\lambda_{\varphi}$ and $\lambda_{\vartheta\varphi}$ from left to right) for the $\chi_{c1}$ (blue) and the $\chi_{c2}$ (red) as a function of $p_{\text{T}}^{\chi_c}$ . . . . .	113
A.3	Frame invariant parameter $\tilde{\lambda}$ determined in the HX and CS frame for the $\chi_{c1}$ (left) and the $\chi_{c2}$ (right) as a function of $p_{\text{T}}^{\chi_c}$ . . . . .	114
A.4	Comparison of the effects of different dimuon efficiencies on the measured values of $\lambda_{\vartheta}^{J/\psi}$ in the HX frame. . . . .	115
A.5	Comparison of measured $\lambda_{\vartheta}$ values using inclusive samples collected in 2011 ( $\sqrt{s} = 7$ TeV, black) and 2012 ( $\sqrt{s} = 8$ TeV, red) as a function of the $J/\psi$ kinematics. . . . .	116
A.6	“Raw” $\cos \vartheta^{\text{HX}}$ distribution of inclusive $J/\psi$ samples throughout the different data taking periods with respect to the distribution in the 2011 data taking period in different $p_{\text{T}}^{J/\psi}$ ranges. . . . .	117
A.7	Definition of the axes and the angle $\Theta$ in the $B \rightarrow J/\psi K$ decay in the B rest frame . . . . .	119
A.8	Invariant $J/\psi$ K mass distribution in the $B \rightarrow J/\psi K$ candidate event sample collected in pp collisions at $\sqrt{s} = 8$ TeV in 2012. . . . .	122
A.9	Polarization parameters in the HX frame (from left to right: $\lambda_{\vartheta}$ , $\lambda_{\varphi}$ and $\lambda_{\vartheta\varphi}$ ) obtained from fitting the two-dimensional acceptance times efficiency correction maps as a function of $p_{\text{T}}^{J/\psi}$ for differently sized mass windows around the B peak for selecting $J/\psi$ events coming from $B \rightarrow J/\psi K$ decays. . . . .	123
A.10	Measured polarization parameters for different $(\cos \vartheta, \varphi)$ binnings of the correction maps. . . . .	124
A.11	Measured polarization parameters for correction maps obtained from different (exclusive) subsamples of the full $B \rightarrow J/\psi K$ sample. . . . .	124



C.1	Ratios of $\chi_{c2}$ over $\chi_{c1}$ yields as a function of $ \cos \vartheta^{\text{HX}} $ (left) and $\varphi^{\text{HX}}$ (right) evaluated with event samples generated assuming the CS frame as natural frame and measured in the HX frame with and without acceptance times efficiency corrections to the analytically expected shapes (dashed lines), for the $p_{\text{T}}^{\text{J}/\psi}$ range 8–9 GeV. . . . .	129
C.2	Ratios of $\chi_{c2}$ over $\chi_{c1}$ yields as a function of $ \cos \vartheta^{\text{HX}} $ (left) and $\varphi^{\text{HX}}$ (right) evaluated with event samples generated assuming the CS frame as natural frame and measured in the HX frame with and without acceptance times efficiency corrections to the analytically expected shapes (dashed lines), for the $p_{\text{T}}^{\text{J}/\psi}$ range 16–20 GeV. . . . .	130
C.3	Ratios of $\chi_{c2}$ over $\chi_{c1}$ yields as a function of $ \cos \vartheta^{\text{HX}} $ (left) and $\varphi^{\text{HX}}$ (right) evaluated with corrections maps computed with different reconstruction efficiencies, for the $p_{\text{T}}^{\text{J}/\psi}$ range 8–9 GeV. . . . .	130
C.4	Ratios of $\chi_{c2}$ over $\chi_{c1}$ yields as a function of $ \cos \vartheta^{\text{HX}} $ (left) and $\varphi^{\text{HX}}$ (right) evaluated with corrections maps computed with different reconstruction efficiencies, for the $p_{\text{T}}^{\text{J}/\psi}$ range 16–20 GeV. . . . .	131
C.5	Invariant mass distributions of the $\chi_c$ candidates in different $ \cos \vartheta^{\text{HX}} $ bins for the 8–12 GeV $p_{\text{T}}^{\text{J}/\psi}$ range with overlaid fit results. . . . .	132
C.6	Invariant mass distributions of the $\chi_c$ candidates in different $\varphi^{\text{HX}}$ bins for the 8–12 GeV $p_{\text{T}}^{\text{J}/\psi}$ range with overlaid fit results. . . . .	133
C.7	Invariant mass distributions of the $\chi_c$ candidates in different $ \cos \vartheta^{\text{HX}} $ bins for the 12–18 GeV $p_{\text{T}}^{\text{J}/\psi}$ range with overlaid fit results. The missing $0.15 <  \cos \vartheta^{\text{HX}}  < 0.225$ range is shown in Fig. 5.13. . . . .	134
C.8	Invariant mass distributions of the $\chi_c$ candidates in different $\varphi^{\text{HX}}$ bins for the 12–18 GeV $p_{\text{T}}^{\text{J}/\psi}$ range with overlaid fit results. . . . .	135
C.9	Invariant mass distributions of the $\chi_c$ candidates in different $ \cos \vartheta^{\text{HX}} $ bins for the 18–30 GeV $p_{\text{T}}^{\text{J}/\psi}$ range with overlaid fit results. . . . .	136
C.10	Invariant mass distributions of the $\chi_c$ candidates in different $\varphi^{\text{HX}}$ bins for the 18–30 GeV $p_{\text{T}}^{\text{J}/\psi}$ range with overlaid fit results. . . . .	137
C.11	Relative differences of the scaled variations of the signal peak fit model with respect to the nominal results for $ \cos \vartheta^{\text{HX}} $ (left) and $\varphi^{\text{HX}}$ (right) for the three $p_{\text{T}}^{\text{J}/\psi}$ ranges (top to bottom). . . . .	139
C.12	Relative differences of the scaled variations of the continuum background fit model with respect to the nominal results for $ \cos \vartheta^{\text{HX}} $ (left) and $\varphi^{\text{HX}}$ (right) for the three $p_{\text{T}}^{\text{J}/\psi}$ ranges (top to bottom). . . . .	140
C.13	Relative differences of the scaled variations of acceptance and efficiency corrections with respect to the nominal results for $ \cos \vartheta^{\text{HX}} $ (left) and $\varphi^{\text{HX}}$ (right) for the three $p_{\text{T}}^{\text{J}/\psi}$ ranges (top to bottom). . . . .	141
C.14	Relative differences of the scaled variations of the cut value used to select promptly produced mesons with respect to the nominal results for $ \cos \vartheta^{\text{HX}} $ (left) and $\varphi^{\text{HX}}$ (right) for the three $p_{\text{T}}^{\text{J}/\psi}$ ranges (top to bottom). . . . .	142

C.15	Relative differences of the scaled variations of the KVF $\chi^2$ probability cut with respect to the nominal results for $ \cos\vartheta^{\text{HX}} $ (left) and $\varphi^{\text{HX}}$ (right) for the three $p_{\text{T}}^{\text{J}/\psi}$ ranges (top to bottom). . . . .	143
C.16	Differences in central value and its uncertainty between the nominal results for $\Delta\lambda_{\vartheta}$ (left) and $\Delta\lambda_{\varphi}$ (right) and variations of the signal peak fit model for the three $p_{\text{T}}^{\text{J}/\psi}$ ranges (top to bottom). . . . .	144
C.17	Differences in central value and its uncertainty between the nominal results for $\Delta\lambda_{\vartheta}$ (left) and $\Delta\lambda_{\varphi}$ (right) and variations of the continuum background fit model for the three $p_{\text{T}}^{\text{J}/\psi}$ ranges (top to bottom). . . . .	145
C.18	Differences in central value and its uncertainty between the nominal results for $\Delta\lambda_{\vartheta}$ (left) and $\Delta\lambda_{\varphi}$ (right) and variations of the acceptance times efficiency corrections for the three $p_{\text{T}}^{\text{J}/\psi}$ ranges (top to bottom). . . . .	146
C.19	Differences in central value and its uncertainty between the nominal results for $\Delta\lambda_{\vartheta}$ (left) and $\Delta\lambda_{\varphi}$ (right) and variations of the lifetime significance cut value used to select prompt mesons for the three $p_{\text{T}}^{\text{J}/\psi}$ ranges (top to bottom). . . . .	147
C.20	Differences in central value and its uncertainty between the nominal results for $\Delta\lambda_{\vartheta}$ (left) and $\Delta\lambda_{\varphi}$ (right) and variations of the KVF $\chi^2$ probability cut value for the three $p_{\text{T}}^{\text{J}/\psi}$ ranges (top to bottom). . . . .	148

# List of Tables

2.1	Properties of quarkonium states seen in Figs. 2.1 and 2.2 . . . . .	9
2.2	Relative scaling of the LDMEs $\langle \mathcal{O}^{\mathcal{Q}}(\{n\}) \rangle$ in powers of $v$ for different quantum states. . . . .	14
4.1	Overview of the selection criteria for different trigger paths encoded in the names. . . . .	54
4.2	Dimuon $p_T$ thresholds for the dimuon barrel HLT paths, respectively single muon $p_T$ thresholds for the single muon seeded dimuon HLT paths and their estimated total rates assuming 2017 data taking conditions. . . . .	62
5.1	Functional relations imposed on the shape parameters of the mass model described in Eq. (5.9) for the simultaneous fits in bins of $ \cos \vartheta^{\text{HX}} $ and $\varphi^{\text{HX}}$ . . . . .	86
5.2	Resulting $\chi^2/\text{ndf}$ for the simultaneous fits in bins of $ \cos \vartheta^{\text{HX}} $ and $\varphi^{\text{HX}}$ in the three $p_T^{\text{J}/\psi}$ ranges. . . . .	88
5.3	Systematic uncertainties on $\Delta\lambda_{\vartheta}$ and $\Delta\lambda_{\varphi}$ , for each of the three $p_T^{\text{J}/\psi}$ ranges. . . . .	98
5.4	Values for $\Delta\lambda_{\vartheta}$ and $\Delta\lambda_{\varphi}$ and their statistical and systematic uncertainties in the three different $p_T^{\text{J}/\psi}$ ranges. . . . .	99
5.5	Values for $\lambda_{\vartheta}^{\text{Xc}1}$ and $\lambda_{\vartheta}^{\text{Xc}2}$ obtained from evaluating the NRQCD prediction bands in Fig. 2.11 from Ref. [35] at the mean value of the observed $(p_T/M)^{\text{J}/\psi}$ in the three $p_T^{\text{J}/\psi}$ ranges. . . . .	100
B.1	Summary of the quarkonium trigger paths used for the 2016 data taking period, grouped by L1 seeds, and the integrated luminosity that was collected by each trigger path. . . . .	125
B.2	Summary of the quarkonium trigger paths used for the 2017 data taking period, grouped by L1 seeds, and the integrated luminosity that was collected by each trigger path. . . . .	126
B.3	Summary of the quarkonium trigger paths used for the 2018 data taking period, grouped by L1 seeds, and the integrated luminosity that was collected by each trigger path. . . . .	127

## Education

---

### Doctoral Program in Technical Sciences, Technical Physics

TU WIEN, INSTITUTE OF HIGH ENERGY PHYSICS, VIENNA

Jan 2016 - now

- Doctoral Thesis: "Measurement of the prompt  $\chi_{c1}$  and  $\chi_{c2}$  polarization at CMS"
- supervisor: Claudia Wulz
- Graduation planned in Dec 2019

### Master Program, Technical Physics (Dipl. Ing. / MSc.)

TU WIEN

Apr 2013 - Nov 2015

- Master Thesis: "Neural Network assisted track finding in the Belle II Silicon Vertex Detector"
- supervisor: Rudolf Frühwirth
- Graduation with distinction

### Bachelor Program, Technical Physics (BSc.)

TU WIEN

Sep 2009 - Mar 2013

- Bachelor Thesis: "Stability check of unbiasing and noise cancelling algorithms of MedAustrons Emittance Analysis Application"
- supervisor: Michael Benedikt
- Graduation with distinction

### Matura (School Leaving Exam)

SPORTGYMNASIUM DORNBIERN

Jun 2008

- Graduation with distinction

## Experience

---

### RESEARCH

#### Research for Doctoral Thesis

INSTITUTE OF HIGH ENERGY PHYSICS, VIENNA

Jan 2016 - ongoing

- Member of the CMS Collaboration
- Developed and applied statistical methods to measure the spin alignment (polarization) of the  $\chi_{c1}$  and  $\chi_{c2}$  mesons to probe hadron formation in quantum chromodynamics with the CMS experiment at the Large Hadron Collider (LHC) at CERN
- Implemented the necessary software tools, including an analysis framework and necessary preceding reconstruction steps running on the LHC computing grid
- Collaborated with scientists from various international institutions, including LIP, Lisbon and CERN, Geneva
- Several stays at CERN, Geneva

#### Research for Diploma Thesis

INSTITUTE OF HIGH ENERGY PHYSICS, VIENNA

Apr 2014 - Nov 2015

- Conducted feasibility studies for various supervised Machine Learning approaches for their application in track finding
- Contributed to the Belle II track finding software library
- Developed, applied and evaluated Machine Learning assisted approaches to track finding in the Belle II experiment

#### Research as short term project student

INSTITUTE OF THEORETICAL PHYSICS, TU WIEN

May 2013 - Dec 2013

- Performed first simulations of the interactions of a tungsten nano-tip with the electro-magnetic field of a two-color laser that were later experimentally tested and lead to the discovery of the surprising phenomena that the emitted charge depends on the phase shift between the two different colors of the laser field
- Implemented the two-color laser field into an already existing time-dependent density functional theory simulation framework
- Developed a simpler, semi-classical model, to be able to gain a first understanding of the observed phenomenon

#### Research for Bachelor Thesis

ATOMINSTITUT, TU WIEN

Apr 2012 - Jun 2012

- Developed tests to check the functionality of the noise cancelling algorithm of the Emittance Analysis Application (EAA) used by MedAustron
- Research conducted during a 2 month stay at CERN, Geneva

## WITHIN THE CMS EXPERIMENT

### L1Page developer and maintainer

Mar 2018 - Dec 2018

- Development and maintenance of new features for the L1Page which is the main interface for the trigger shifter monitoring the trigger operations in the CMS control room
- Responsible for testing and deploying new releases during the operation of the CMS experiment in 2018

### Software validation contact person for the B-physics group

Sep 2017 - Sep 2018

- Responsible for validating the consistency of the CMS software framework used between different releases

### Quarkonium triggers contact person

Jan 2017 - Dec 2018

- Responsible for the transition of the trigger strategy from Run I to Run II for the inclusive quarkonium triggers including the development of new trigger strategies to cope with the increased rate
- Communicating and coordinating between the corresponding analysis groups in the B-physics group and the CMS-wide Trigger Strategy Group

## TEACHING

### Co-supervisor of Master and Project students

INSTITUTE OF HIGH ENERGY PHYSICS, VIENNA

2017 - 2018

### Tutor

TU WIEN

Oct 2013 - Jul 2015

- Supervised experimental laboratory exercises (Bachelors course)
- Supervised calculation exercises in statistical physics (Masters course)

## FURTHER TRAINING

### CERN School of Computing 2017

UNIVERSIDAD POLITÉCNICA DE MADRID

Aug 2017 - Sep 2017

### ATHENS Program - Information Extraction and the Semantic Web

TÉLÉCOM PARISTECH

Mar 2014

## EXTRACURRICULAR EXPERIENCE

### Ski and snowboard instructor

SCHNEESPORTSCHULE AU-SCHOPPERNAU

Dec 2010 - Feb 2016 (seasonal)

- Instructing and supervising children of various age groups as well as adults

### Internship

BAUR PRÜF UND MESSTECHNIK, SULZ

Jul 2011 - Sep 2011

- Exchange of a software library in a report generation application

### Mandatory Civil Service

AUSTRIAN RED CROSS

Jul 2008 - Mar 2009

- Paramedic

## Skills

---

<b>Programming</b>	python, C++, bash, JavaScript, MATLAB, Fortran, Java
<b>Libraries / Frameworks</b>	ROOT (C++ framework prevalent in high-energy physics data analysis), NumPy, SciPy, pandas, CMSSW (C++ framework used by the CMS experiment), node.js, Polymer, PyTorch
<b>Data Science / Analysis</b>	Statistical modeling and model selection, maximum likelihood fitting, parameter and uncertainty estimation, hypothesis testing, supervised machine learning (shallow feedforward neural networks, Boosted Decision Trees and Gradient Boosting, ensemble methods)
<b>Physics / Mathematics</b>	Quantum mechanics, field theory, statistical physics, classical mechanics, computational physics, probability theory and statistics, linear algebra, analysis
<b>Operating systems</b>	Linux (Ubuntu, Scientific Linux, CentOS), MacOS
<b>Tools</b>	git, github/gitlab, Jupyter, SVN, LaTeX
<b>Languages</b>	German (mother tongue), English (excellent), French (intermediate), Italian (basic)

# Selected List of Publications and Contributions to Conferences

## JOURNAL ARTICLES

### Measurement of quarkonium production cross sections in pp collisions at $\sqrt{s} = 13$ TeV

CMS COLLABORATION

*Phys. Lett. B* 780 (2018) pp. 251–272

### Observation of the $\chi_{b1}$ (3P) and $\chi_{b2}$ (3P) and measurement of their masses

CMS COLLABORATION

*Phys. Rev. Lett.* 121 (2018) p. 092002

### High Visibility in Two-Color Above-Threshold Photoemission From Tungsten Nanotips in a Coherent Control Scheme

T. PASCHEN, M. FÖRSTER, M. KRÜGER, C. LEMELL, G. WACHTER, F. LIBISCH, T. MADLENER, J. BURGDÖRFER, P. HOMMELHOFF

*Journal of Modern Optics* 64.10-11 (2017) pp. 1054–1060

### Two-Color Coherent Control of Femtosecond Above-Threshold Photoemission From a Tungsten Nanotip

M. FÖRSTER, T. PASCHEN, M. KRÜGER, C. LEMELL, G. WACHTER, F. LIBISCH, T. MADLENER, J. BURGDÖRFER, P. HOMMELHOFF

*Physical Review Letters* 117.21 (2016) p. 217601

### Currently over 250 peer-reviewed publications as part of the CMS collaboration

- See <https://inspirehep.net/author/profile/T.Madlener.1> for a full list

## CONFERENCE PROCEEDINGS

### Results on B Hadron Properties in CMS

T. MADLENER

*EPJ Web of Conferences* 181 (2018) p. 01023

### The Track Finding Algorithm of the Belle II Vertex Detectors

T. BILKA, N. BRAUN, G. CASAROSA, O. FROST, R. FRÜHWIRTH, T. HAUTH, M. HECK, J. KANDRA, P. KODYS, P. KVASNICKA, J. LETTEN-

BICHLER, T. LÜCK, T. MADLENER, F. METZNER, M. NADLER, B. OBERHOF, E. PAOLONI, M. PRIM, M. RITTER, T. SCHLÜTER, M. SCHNELL,

B. SPRUCK, V. TRUSOV, J. WAGNER, C. WESSEL, M. ZIEGLER

*EPJ Web of Conferences* 150 (2017) p. 00007

## CONFERENCE TALKS

### Measurement of the $\chi_{c1}$ and $\chi_{c2}$ polarization at CMS

Paris (France)

CONGRES DES DOCTORANDS 2019

25-29 Mar 2019

- Invited talk as one of 10 students from different European universities

### Recent Measurements of P-wave quarkonia at CMS

Graz (Austria)

OEPG 2018: 68TH ANNUAL MEETING OF THE AUSTRIAN PHYSICAL SOCIETY

11-14 Sep 2018

### Results on B hadron properties in CMS

Vienna (Austria)

EXA2017: INTERNATIONAL CONFERENCE ON EXOTIC ATOMS AND RELATED TOPICS

11-15 Sep 2017

### Quarkonium production and polarization in pp collisions at CMS

Vienna (Austria)

OEPG 2016: 66TH ANNUAL MEETING OF THE AUSTRIAN PHYSICAL SOCIETY

27-29 Sep 2016

### Quarkonium cross sections in pp collisions with CMS

Richland, WA (USA)

QWG2016: 11TH INTERNATIONAL WORKSHOP ON HEAVY QUARKONIUM

6-10 Jun 2016

### Machine Learning assisted track finding in the Belle II SVD

Vienna (Austria)

CONNECTING THE DOTS 2016

22-24 Feb 2016